Chair of Structural and Functional Ceramics

# Doctoral Thesis

# Structure-Property Relationships in Substituted BaTiO₃: A Theoretical Study

Dipl.-Ing. Florian Mayer, BSc

May 2023

**MONTANUNIVERSITÄT LEOBEN**
www.unileoben.ac.at

## AFFIDAVIT

I declare on oath that I wrote this thesis independently, did not use other than the specified sources and aids, and did not otherwise use any unauthorized aids.

I declare that I have read, understood, and complied with the guidelines of the senate of the Montanuniversität Leoben for "Good Scientific Practice".

Furthermore, I declare that the electronic and printed version of the submitted theses are identical, both, formally and with regard to the content.

Date 03.05.2023

_____
Signature Author
Florian Mayer

# ACKNOWLEDGMENTS

First of all, I would like to thank everyone who supported, taught, and inspired me during my studies. During my time as a student at the Graz University of Technology and subsequently, at the Montanuniversität Leoben, I was not only able to expand my knowledge but also gain many important lessons for life.

This work would not have come to fruition if my supervisor Dr. Marco Deluca (Key Scientist, Material Center Leoben, MCL), had not convinced me of this project a few years ago. Originally hired as a potential experimentalist, it soon became apparent that my passion for theoretical models prevailed after all. I thank Marco for allowing me to work on the wonderful effective Hamiltonians and integrate this know-how at the MCL in Leoben. Thank you also for the ongoing support and essential inputs to my research and beyond. It was a pleasure to spend the last years in your research group.

I would also like to thank my mentor Prof. Dr. Peter Supancic (Montanuniversität Leoben), for his support over the past years. I appreciated the detailed questions about my work and benefitted greatly from them.

A special thanks also goes to my two colleagues (and co-supervisors), Dr. Jürgen Spitaler and Dr. Maxim Popov, from the MCL. Your immense dedication and unwavering support of my scientific work over the past years are greatly appreciated. I am grateful for the countless hours of fruitful discussions that have been a pleasure and will remain in my memory for a long time.

I would like to express my gratitude to Dr. Jiří Hlinka, Dr. Petr Ondrejkovič, Dr. Marek Paściak, and Dr. Mauro Gonçalves from the Czech Academy of Sciences for their invaluable collaboration, as well as to the many important discussions and ideas they have contributed.

Finally, I would like to express my gratitude to my family. I want to thank my mom and dad for enabling my study time and for their unwavering support during both favorable and challenging periods. Additionally, I would like to extend my appreciation to my siblings, Chrisi, Luki, and Kathi, for their constant love and unwavering encouragement. A heartfelt thank you also to my aunt and uncle, Edith and Friedl, for their continuous company and support.

# ABSTRACT

The development of energy-autonomous systems also requires the availability of high-performance energy storage devices. One method to store electrical energy rapidly and efficiently can be found in dielectric capacitors, provided the dielectric meets some relevant requirements. These are a high permittivity, a slim hysteresis curve, small leakage currents, and a high breakdown voltage. A class of materials that can fulfill many, if not all, of these requirements, is the so-called relaxor ferroelectrics (RF). Such RFs are created by the chemical substitution of ferroelectric materials and exhibit unique properties. These properties are not only relevant for energy storage but also for use in actuators, sensors, energy harvesting, or even novel computing devices. Despite efforts to understand RFs, the origins of their behavior are still not fully explained. This thesis aims to contribute to the discussion by using different theoretical approaches to describe RFs on an atomic level. Density functional theory (DFT) serves as the basis for all studies, allowing for the exploration of electronic structure, phonon properties, and structural deformations. As a prime example of two fundamentally different RFs, the homovalently substituted $Ba(Zr_xTi_{1-x})O_3$, BZT, and the heterovalently substituted $Ba(Nb_xTi_{1-x})O_3$, BNT, are studied. Using DFT and comparison to experiments, substitution effects such as local volume changes, potential changes as well as the formation of defects are investigated. To study properties at finite temperatures, first-principles-based effective Hamiltonians are used for molecular dynamics (MD) simulations. First, the formalism for describing the parent system barium titanate ($BaTiO_3$) is revised by including additional anharmonic couplings to higher-energy phonons, which yields a more accurate description of the potential energy surface. All associated parameters are parametrized using DFT calculations. Furthermore, the Hamiltonian extension's impact on various properties is studied using MD simulations, which result in a considerably better agreement with experimental data. The $BaTiO_3$ parameterization is used as a foundation for the inclusion of substituents. An alternative scheme for describing substituents in effective Hamiltonians is introduced, which is parametrized through DFT calculations. The ensuing MD simulations reveal a high degree of agreement with experimental data and offer a thorough understanding of the occurrence of RF behavior. The effective Hamiltonians for BZT and BNT are further utilized to assess the potential of these systems in neuromorphic computing applications. The study examines the response of the systems to ultrafast THz pulses and explores the occurrence of hidden phases and polarization integration, which is a must for the realization of artificial synapses. Additionally, the thesis presents further findings on energy density in substituted $BaTiO_3$, frequency-dependent susceptibility, and topological objects.

# TABLE OF CONTENTS

# 1  Introduction

The current level of global energy consumption [1] is creating significant environmental problems that make a transition to renewable energy sources essential to combat climate change, reduce carbon emissions, and create economic opportunities, including job creation and energy security. In parallel with the development of alternative energy sources, electrical energy storage is also becoming increasingly popular [2]. The storage media here scale from miniature applications in microelectronics to large systems for expanding the energy grid. In general, electrical energy storage can take many forms, including batteries, capacitors, supercapacitors, pumped hydro storage, and flywheel energy storage. In this thesis, the focus is mainly on materials for dielectric capacitors [3], targeting the application in energy-autonomous systems, whereby developing and investigating improved dielectrics is one of the main objectives. Such systems are associated with the so-called Internet of Things (IoT) [4–6], which has the potential to revolutionize the economy by enabling energy-autonomous systems that can optimize energy consumption and generation, reduce waste, and improve overall energy efficiency. The IoT refers to a system of interconnected physical objects, including vehicles, household appliances, and other devices equipped with software, electronics, sensors, and internet connections. This allows these objects to communicate with each other and exchange data. To ensure the reliable and efficient operation of networked devices in the IoT, energy storage is critical [7]. Although most IoT devices are low-power and energy-efficient, they still require a certain amount of energy to operate. This is where energy storage comes into play, as it allows devices to store excess harvested energy and use it when the power supply is inadequate or intermittent. A promising class of storage media for use in IoT applications can be found in dielectric capacitors [8]. Dielectric capacitors have several advantages, including relatively high energy density, fast charging and discharging, low internal resistance, long lifetime, and are safe and can be produced in an environmentally friendly way. Their fast charge and discharge times make them ideal for applications that require high power in a short time, such as in IoT wireless transceivers. Their low internal resistance allows them to deliver power quickly and efficiently, making them ideal for high power output applications, such as in electric vehicles. Their long lifetime and safety make them a cost-effective and reliable storage medium in the long term. However, the energy density of dielectric capacitors is a few orders of magnitude lower than that of batteries, so considerable efforts have been devoted to developing new dielectrics with improved storage properties [9]. A promising class of materials that exhibit excellent properties

for the storage of electrical energy in dielectric capacitors is so-called relaxor ferroelectrics (RF) [10–13]. To gain a better understanding of RFs, it is important to first mention their parent materials, which are ferroelectrics [14]. Ferroelectrics exhibit spontaneous polarization, which can be altered by applying external electric fields. The unique properties of these materials make them suitable for a wide range of applications, from actuators and sensors to memory storage. Prime examples of such ferroelectric materials are lead titanate ($PbTiO_3$) and barium titanate ($BaTiO_3$), with lead-free systems particularly gaining interest recently. This is due to a partial ban of lead-containing systems by various funding bodies. Characteristic properties of such ferroelectric materials, besides spontaneous polarization, are the occurrence of hysteresis, anisotropy of the crystal lattice, the possibility to switch between polarization states, and the property of piezoelectricity [15]. The latter means that electrical energy can be converted into mechanical energy and is mainly used for actuators, sensors, and energy harvesters. However, when it comes to storing electrical energy, these ferroelectric materials are only partially suitable, as significant losses occur, resulting in the recovery of only a portion of the stored energy [9]. These losses stem from the reorientation of ferroelectric domains, which are caused by the long-range correlation of dipoles in such materials. This is where RFs come into play, since in RFs this long-range correlation is disrupted by chemical substitution of the ferroelectric parent systems, and thus losses are greatly minimized [9,13,16]. Such RFs, in principle, can be described as a type of ferroelectric material that contains polar nanoregions (PNRs), which are regions of a nanoscale size where the polarization can fluctuate rapidly [10–13]. RFs have a high dielectric permittivity and low hysteresis, making them useful for applications such as capacitors and piezoelectric actuators [17]. The dielectric constant of an RF is dependent on the frequency of the applied electric field, a property known as dielectric dispersion [13]. These unique properties make them promising materials for a variety of applications, including energy storage, energy harvesting, sensors, actuators, and memory devices [17]. Although significant progress has been made in understanding the properties and potential applications of RFs, many unanswered questions and challenges remain to be addressed in this field [10–12,18]. Ongoing research is focused on developing more accurate models [11–13,18] and theories to describe their behavior and optimizing and controlling their properties to improve their performance for specific applications. New synthesis methods and processing techniques are also being developed to enhance their properties and performance [19]. Therefore, while RFs have been extensively explored, there is still much to be learned and developed in this area of research.

A central aim of this thesis is to enhance the existing knowledge of RFs and their properties by building upon previous research. Therefore, a crucial objective of the study is to develop

accurate theoretical models on an atomic level for homovalently and heterovalently substituted $BaTiO_3$. The key difference here is the oxidation state of the respective substituents. The selection of these two fundamentally different cases is intended to identify the different mechanisms responsible for the occurrence of RF behavior. For the homovalent case, the substitution with $Zr^{4+}$ at the B-site ($Ti^{4+}$) of $BaTiO_3$ is studied as a prime example. The corresponding chemical formula can be expressed by $Ba(Zr_xTi_{1-x})O_3$ (BZT). For the heterovalent case, $BaTiO_3$ is substituted with $Nb^{5+}$ at the B-site, where the chemical formula can be formulated as $Ba(Nb_xTi_{1-x})O_3$ (BNT). Remarkably, the manifestation of RF behavior is detected in this case at significantly different levels of substituent concentrations. Specifically, in the case of BZT, RF behavior arises when the concentration of Zr exceeds 30% [20], while for BNT, RF behavior is observed at a mere 7% of Nb concentration [21]. To delve into this discrepancy, various theoretical and experimental methods were pursued in this thesis, including density functional theory (DFT) calculations and effective Hamiltonian-based molecular dynamics (MD) simulations for the theoretical investigations. The core of this work is based on theoretical approaches aimed at describing various properties of the investigated materials. Density functional theory calculations are utilized to study electronic structures and structural relaxations. Moreover, they serve as the foundation for parameterizing potentials used in MD simulations. The potentials employed in this thesis are derived from effective Hamiltonians, which will be further elaborated upon. The fundamental concept behind these effective Hamiltonians is to employ a localized basis [22], defined within a subspace of the phonon band structure, to characterize the potential energy surface [23,24]. Initially used as a mean-field approach [23,24] for pure ferroelectrics like $BaTiO_3$, this method was later modified into a localized approach [25]. This approach was constantly extended over the course of time. For example, Nishimatsu et al. [26,27] extended the local self-energy up to the 8th order. Moreover, Paul et al. [28] showed an extension of the effective Hamiltonian by including additional phonon modes. Furthermore, various further developments have also been designed to describe substituted systems [29–33].

With the introduction above, the objectives of this dissertation can now be clearly defined. It is important to note that this is a cumulative dissertation, and as such, the core of this thesis is comprised of the four enclosed publications. Not only do these four publications build upon each other in terms of content, but they can also be viewed chronologically as a progression of established knowledge. The main objectives of this work can now be summarized as follows:

1. The aim of the first study is to investigate substitution effects on an atomic level, specifically focusing on homovalently ($Zr^{4+}$, BZT) and heterovalently ($Nb^{5+}$, BNT) substituted $BaTiO_3$. The objective is to identify fundamental differences between various substituents and, in combination with experiments, provide an improved understanding of RF behavior. Atomistic simulations, utilizing DFT, are used to describe the structural changes induced by substitution. Additionally, the effects on phonons are calculated through DFT, and the resulting data is compared with Raman spectroscopy. All the results of this study can be found in Publication 1.

2. The objective of the second study is to revise the formalism of the effective Hamiltonian for the pure $BaTiO_3$ system in order to provide an improved description of the potential energy surface. This involves revising the current formalism for the extension by additional phonons, followed by parameterization using DFT calculations. The resulting effective Hamiltonian for $BaTiO_3$ is thoroughly tested and compared with experimental data. The derivation of the alternative formalism, the parameterization by DFT calculations, and the results from the MD simulations can be found in Publication 2.

3. The objective of the third study is to extend the effective Hamiltonian so that it can describe substituted systems like those studied in the first publication (BZT and BNT). The extension should be flexible enough to incorporate different substituents while ensuring a local description on an atomic level. To achieve this, the effective Hamiltonian from the second publication shall serve as the basis for the extension's development, and parameterization is once again performed through DFT calculations. MD simulations are then carried out to verify the accuracy of the developed approach and to obtain important correlations that are relevant to the application of these materials. The details of the approach development, parameterization through DFT, and application through MD simulations are presented in Publication 3.

4. The fourth objective of this thesis is to showcase one possible application of the effective Hamiltonians for BZT and BNT developed in the third objective. Recent publications suggest the potential application of RF materials in neuromorphic computing systems, and thus the effective Hamiltonians are used to test the two materials for the required properties. This involves subjecting the respective materials to ultrafast THz pulses to verify the occurrence of hidden phases and other relevant

properties. The application of MD simulations, the lessons learned, and other results obtained from this study are presented in Publication 4.

The structure of this thesis is organized as follows. In Chapter 2, the fundamentals of ferroelectric materials and RF behavior are explained. Chapter 3 gives an overview of the state-of-the-art on simulations of ferroelectric materials and how the studies presented in this thesis contribute to progress in this subject. Chapter 4 provides a detailed description of the theoretical approaches used in this thesis, including density functional theory and the concept of effective Hamiltonians. Results from Publications 2 and 3 are also included to complete the theory behind effective Hamiltonians. Although the parameterization of effective Hamiltonians is described in detail in Publications 2 and 3, Chapters 5, 6, and 7 provide additional details. The core of this thesis is presented in Chapter 8, which lists Publications 1 to 4 in chronological order. Chapter 9 discusses additional results that have not yet been published. This thesis concludes with a summary and discussion in Chapter 10.

# 2 Lead-Free Relaxor Ferroelectrics

This chapter covers the fundamentals of ferroelectric materials, with a focus on barium titanate ($BaTiO_3$, BT) as the reference material for the work presented here. The chapter begins by presenting the basic properties of ferroelectric materials, followed by a discussion of homovalent and heterovalent substitution in BT. This discussion will inevitably introduce the concept of relaxor ferroelectrics (RF), including the properties exhibited by RFs and their theoretical description. Additionally, as this thesis explores energy storage based on the investigated materials, the third subchapter covers the basic quantities for dielectric capacitors.

## 2.1 Ferroelectrics

In general, ferroelectric materials [3,8,14] are characterized by permanent dipoles, which lead to spontaneous polarization of the system. A permanent dipole moment is caused by a non-symmetrical arrangement of charges. That implies that all molecules or crystals with inversion symmetry cannot exhibit a permanent dipole moment. An example of such a system is methane ($CH_4$), where no dipole moment occurs due to the symmetrical arrangement of the H atoms. However, if we look at $H_2O$, for example, a non-vanishing permanent dipole moment can be observed due to the arrangement of the atoms and their associated charges. The dipole moment can be determined directly from the charge distribution, as shown in Equation 1, where $\rho(\boldsymbol{r})$ represents the charge density and $\boldsymbol{r}$ the position vector. To obtain a dipole moment from Equation 1, both positive and negative charges must be present in the charge distribution. Furthermore, this equation is independent of the origin if overall charge neutrality is given.

$$\boldsymbol{p} = \int \rho(\boldsymbol{r})\boldsymbol{r}dr$$

(1)

The above example of the two molecules can also be applied to the charge distribution in crystals. Thus, crystal systems with an inversion center show no local dipole moment, whereas, in the absence of an inversion center, a local dipole moment occurs. Furthermore, the crystals without an inversion center exhibit one or more polar axes, whereas those crystals with a unique polar axis are also called ferroelectric crystals. If one or more polar axes are found, then one speaks of the piezoelectric effect. This means that all systems which are ferroelectric are automatically also piezoelectric. Piezoelectric materials do not necessarily have to exhibit spontaneous polarization, but external influences such as electric fields or stresses can induce electric polarization. A dipole moment can also be defined for the case of ferroelectric crystals, although here it is now referred to as a dipole moment per unit cell ($\boldsymbol{p}_{unitcell}$) due to the crystal structure. However, the concept of polarization is often used instead of dipole moment, which

can be simply calculated from the dipole moment and the volume of the unit cell ($V_{unitcell}$), as presented in Equation 2.

$$P = \frac{p_{unitcell}}{V_{unitcell}}$$

(2)

The polar axis plays an important role in ferroelectric systems and shall be discussed in more detail. In principle, to find the polar axis, one needs to investigate the crystal structure of the lattice and find the axis where polarization occurs. The polar axis is parallel to the direction of the occurring polarization within the crystal. Consequently, the polarization can be inverted and switched in the opposite direction. It is important to note that, in this case, the direction of the polarization changes, but the crystal structure remains the same. This change in the polarization state is directly connected with the displacements of atoms. Furthermore, it becomes clear that there are different positions of the atoms, which can create opposite polarization states. When changing from one polarization state to the other, a potential barrier must be overcome. Such a potential barrier is schematically illustrated in Figure 1 and indicates two local minima corresponding to the different polarization states. Such a double-well potential is often used to qualitatively explain the respective polarization states but also reflects the energetic landscape of such material in reality. The calculation of such a double-well potential can be done by quantum mechanical approaches, where reference is made to the work of Cohen and Krakauer [34]. This paper demonstrates in detail how density functional theory can be used to calculate the potential energy surfaces for the ferroelectric $BaTiO_3$. Such a double-well potential also indicates that by applying an external field, it is possible to switch between the two polarization states with different polarization directions.
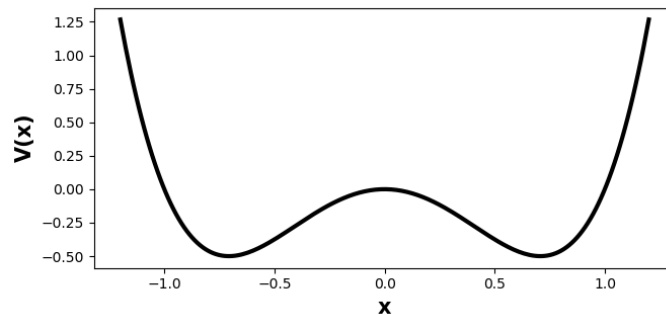


*Figure 1. Illustration of double well potential found in many ferroelectric materials. V(x) represents the energy, whereas x denotes a symbolic displacement.*

Another essential concept is the so-called spontaneous polarization which occurs in ferroelectric systems. This spontaneous polarization occurs in the material even without the

application of an external field and is based on the collective behavior of local permanent dipoles. To explain spontaneous polarization, the double-well potential can again be used, but the concept of phase transition must also be considered. Spontaneous polarization occurs analogously to a ferromagnetic material below a critical temperature $T_c$. At such temperatures, the local dipoles dwell in one of the minima of the double-well potential. Spontaneous polarization is caused when the local dipoles are correlated and, in the ferroelectric case, have the same direction. Of course, it must be taken into account that dipoles with the same orientation generate an electric field that also acts beyond the material. This field is not energetically beneficial and is minimized by forming randomly-oriented ferroelectric domains within the whole lattice. This is also referred to as a depolarization field. However, the correlation of the local dipoles can also be antiparallel, in which case we speak of anti-ferroelectric behavior. If the temperature rises above the critical temperature $T_c$, then the correlation of the local dipoles is lost, and one speaks of a paraelectric state. This is analogous to a transition between a ferromagnetic and paramagnetic state and can be described by a Curie-Weiss behavior. An alternative view can again be given by means of the double-well potential. The potential barrier is hard to overcome at temperatures below the critical temperature. At higher temperatures, however, enough energy is added that the potential barrier can be overcome, and the dipoles can fluctuate. The fluctuation of local dipoles leads to a paraelectric state. Of course, the above description is qualitative, and properties such as the coupling between displacements of the atoms and deformations of the unit cell must also be considered for the actual description of ferroelectric materials. Furthermore, ferroelectric materials can have several ferroelectric phases, which in turn can have different symmetries and, therefore, different polarization states. Therefore, the study of ferroelectric behavior and the resulting properties must be carefully performed for each material system.

In this work, primarily the ferroelectric material barium titanate ($BaTiO_3$, BT) and substituted versions of it are studied. Therefore, an overview of this material will be given here, and the main properties of BT will be discussed. The main preliminaries, BT exhibits four different phases, three of which are ferroelectric. The cubic phase (space group $Pm\overline{3}m$ [35]) is found at temperatures above 403 K and represents the paraelectric phase of BT [23,35]. The experimentally determined lattice constant for the cubic phase is $a = 4.010$ Å [28]. For temperatures below 403 K, a tetragonal phase (space group $P4mm$ [35]) is found. This phase is ferroelectric and displays polarization along the crystal directions <001> or also often referred to as c-axis. The spontaneous polarization along this direction, measured experimentally [23], amounts to a value of 0.27 $C/m^2$. The lattice constants for the tetragonal

structure were determined experimentally to be $a = 3.986$ Å and $a/c = 1.010$. The next phase transition occurs at 278 K from the tetragonal phase to an orthorhombic phase (space group $Amm2$ [35]). The polarization here is found along the <011> crystal directions and their symmetric counterparts. The polarization was determined here experimentally [23] with a value of 0.36 C/m². The experimental lattice constants [36] are $a = 4.041$ Å, $b = 3.982$ Å and $c = 4.065$ Å. The final phase transition occurs at a temperature of 183 K, where a transition from a orthorhombic phase to rhombohedral phase (space group $R3m$ [35]) is observed. In this phase the polarization is found along the directions <111>. The experimental value for the polarization along this direction is given as 0.33 C/m². Furthermore, the experimental lattice constants are found to be $a = 4.003$ Å and $\alpha = 89.84°$ [36]. The individual phases and the associated crystal structures can be seen schematically in Figure 2. The various possible polarization directions are also indicated here.
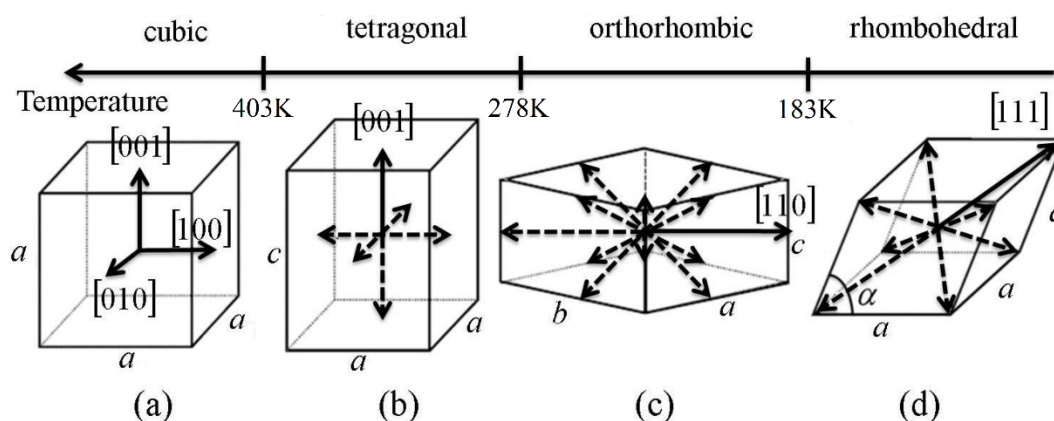


Figure 2. Illustration of the four phases of pure BT. The arrows indicate the possible directions for polarization. Plot was taken from Ref. [37] and adapted.

Due to the given number of phases, it becomes clear that BT is a rather complex system, where the description by a simple double-well potential is no longer satisfactory. Instead, the potential energy surface has different local minima, which can be assigned to the individual ferroelectric phases. The cubic phase represents a local maximum of the potential energy surface and can only be stabilized by enough applied thermal energy. The computation of the potential energy surface associated with BT represents a significant contribution to this work and is, therefore, discussed in detail in the subsequent chapters as well as in the attached publications. However, other important properties of BT will also be discussed here to explain the great popularity of this material. As already discussed in detail, BT is ferroelectric and piezoelectric, which makes this material interesting for many applications. For example, BT exhibits a very high relative permittivity, where this elevated permittivity is observed especially near the phase transitions. High permittivity is of particular interest in the application of ferroelectric materials in

capacitors. Furthermore, non-linear optical properties can be observed in BT, which is interesting for the application in frequency doubling in optical devices [38]. It should also be noted that BT has a high melting point of above 1600°C, which makes it suitable for high-temperature applications (albeit in the paraelectric phase).

Another important property of ferroelectric materials is their response to an applied external electric field. This leads to a hysteresis curve due to the spontaneous polarization and the associated alignment of the local dipoles. Such a curve is schematically outlined in Figure 3. Here, an external field $E$ is applied, and the response is monitored via the polarization $P$. For high electric fields, the polarization saturates to a value $P_s$. If the field is now reduced, the polarization also decreases but shows a non-linear behavior. At a field strength of zero, a non-vanishing polarization is observed, which is also called remnant polarization $P_r$. The polarization disappears only when the so-called coercivity $E_c$ is reached. Subsequently, the polarization changes its sign and approaches the saturation level at the other side again. The shapes of hysteresis curves can be quite different and are heavily dependent on the atomic structure of the ferroelectric systems being studied. Furthermore, the variables of temperature and the presence of stresses also influence the shape of the curves. In addition, the shape of the hysteresis can be controlled by substitution with impurity atoms, and thus desired properties can be achieved.
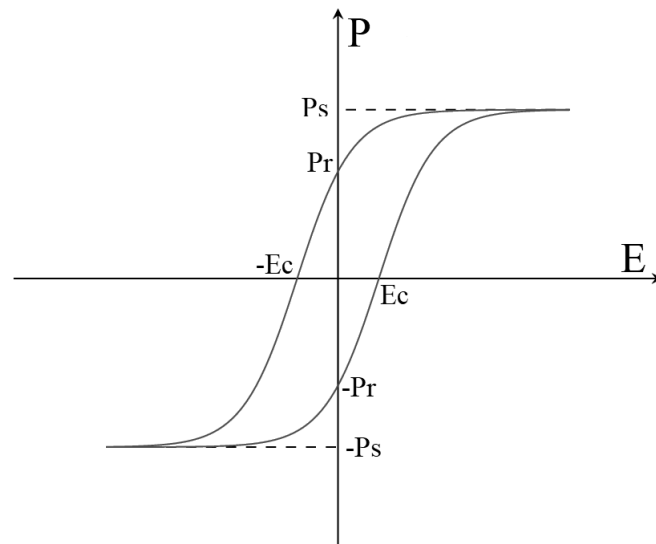


*Figure 3. Schematic representation of a ferroelectric hysteresis loop. P denotes the polarization and E the external electric field. $P_s$ represents the saturated polarization and $P_r$ the remnant polarization. $E_c$ corresponds to the coercive field strength.*

To conclude this chapter, the application areas of ferroelectric materials shall be discussed. Ferroelectric materials can be utilized in the fabrication of capacitors with medium to high

capacitance due to their relatively large permittivity. They are also employed in sensors for measuring temperature, pressure, and humidity. Non-volatile memories, or FeRAM, are another application of ferroelectric materials. Actuators based on ferroelectrics can be built due to their property of piezoelectricity, and they can be used for ultrasonic transducers in medicine. While energy harvesting is possible using ferroelectric materials, the gains achieved are typically quite small due to losses related to mechanical-mechanical and mechanical-electrical energy transfer [39].

## 2.2 Relaxor Ferroelectrics

Relaxor ferroelectrics (RFs) are a special class of ferroelectric materials that exhibit highly perturbed behavior in their ferroelectric response. In contrast to classical ferroelectric materials, which exhibit a well-defined and reproducible transition between non-polar and spontaneously polarized phases, RFs exhibit a highly diffuse and frequency-dispersed permittivity maximum in correspondence with the transition between a nonpolar and a relaxor state. The following explanation of relaxor behavior is based on the publications of Bokov and Ye [13], Shvartsman and Lupascu [10], as well as Kleemann, Samara, and Dec [18]. In order to explain RF behavior, one shall start with the occurrence of the paraelectric phase at high temperatures. This phase is analogous to the paraelectric phase of conventional ferroelectrics and is mainly characterized by fluctuations of dipoles. If the system is cooled down, no phase transition to a ferroelectric phase is observed. Instead, nanometer-sized regions with randomly distributed dipoles are formed. The formation of these regions is observed at the so-called Burns temperature $T_B$, which is far above the temperature $T_m$ associated with the maximum of the permittivity. However, this transition to the formation of nanometer-sized regions is not a conventional phase transition, since no structural changes are measurable here at the macroscopic level. Nevertheless, many properties change significantly at the Burns temperature, leading to the definition of a new state. The nanometer-sized regions are mobile around the Burns temperature and their behavior can be described as ergodic, i.e. an ergodic relaxor state. If the temperature of the system is decreased further, the dynamics of these regions drastically decrease. Once the temperature is low enough, a nonergodic state is reached at the so-called freezing temperature $T_f$. As the name suggests, the dynamics of the regions below $T_f$ are frozen, i.e. they become static. Interestingly, at these low temperatures, it is observed that the averaged symmetry of the system does not change and a macroscopic cubic state is still adopted. The nonergodic state is similar to that of a dipole glass, although this hypothesis is the subject of intense debate [13]. The loss of dynamics of the dipoles leads to a broad peak in the observed permittivity as a function of temperature. The magnitude of the broad peak is comparable to the permittivity

measured at the Curie point in conventional ferroelectrics. Furthermore, an interesting phenomenon is observed here, which is a shift of the peaks to higher temperatures when the frequency is increased (called frequency dispersion of permittivity). This behavior is illustrated in Figure 4, where the real and imaginary part of the permittivity is plotted as a function of temperature for different frequencies using the example of a lead-based RF [13]. The broad peak was often used to speak of a diffuse phase transition, although, of course, no real phase transition occurs here [13].
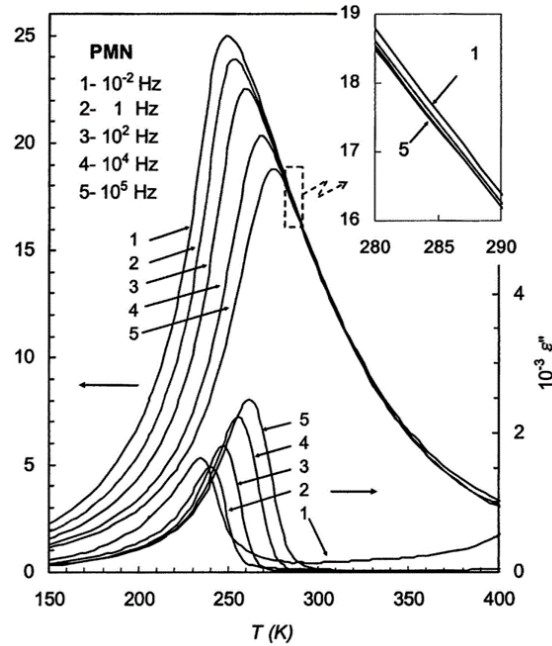


*Figure 4. Illustration of frequency dependence of permittivity in relaxor ferroelectrics on the example of Pb(Mg$_{1/3}$Nb$_{2/3}$)O$_3$ (PMN) taken from Ref. [13]. The plot shows the real and imaginary parts of the permittivity as a function of temperature measured at different frequencies.*

Another important feature of RFs is the transformation of the nonergodic state at low temperatures to a ferroelectric state upon application of a large enough external field. This transformation is irreversible and is different from dipole glasses, where such a feature does not occur. By increasing the temperature, the ferroelectric phase is transformed into an ergodic state, whereby this transformation occurs at a temperature $T_c$. This temperature $T_c$ is very close to the freezing temperature $T_f$. Furthermore, in many RFs, a spontaneous transformation of the ergodic state into a ferroelectric state can be observed at low temperatures, in which case the non-ergodic state is absent. Another fundamental condition for the occurrence of RF behavior is compositional disorder. That is, the irregular distribution of different ions on the same lattice site. The first materials where RF behavior has been reported are heterovalently substituted lead-based perovskites. Two prime examples are Pb(Mg$_{1/3}$Nb$_{2/3}$)O$_3$ (PMN) and Pb(Sc$_{1/2}$Ta$_{1/2}$)O$_3$ (PST), where a disorder of the B-site cations is observed [13]. For lead-free

materials, compositions based on BT can be mentioned here as examples. This includes the homovalently substituted system $Ba(Zr_xTi_{1-x})O_3$ (BZT), where the substitution via $Zr^{4+}$ takes place at the B-site. The occurrence of RF behavior is experimentally observed here at concentrations above 30% of Zr [20]. Another example can be found in heterovalently substituted $Ba(Nb_xTi_{1-x})O_3$ (BNT), where here $Nb^{5+}$ is substituted on the B-site. RF behavior is observed for this system at concentrations above 7%. Already here, it is obvious that the occurrence of RF behavior must depend on the different substituents and their distribution. For BNT, other defects also play an essential role since charge compensation becomes necessary due to the heterovalent substitution. For example, in BNT, such compensation is experimentally and theoretically proven to be provided by Ti vacancies [40]. As already mentioned, chemical disorder represents an important property in these RFs and will therefore be investigated in some detail. The basis for disorder in the system is the non-uniform distribution of ions on the respective lattice sites. In the general case at low temperatures, if the ratios of ions for the respective lattice site, for example, $Ba(Zr_{1/2}Ti_{1/2})O_3$, are equal, one would expect the ions to be ordered. This assumption is supported by the energy contributions of the elastic energy as well as the electrostatic interaction, which are the lowest in the ordered state [13]. At higher temperatures, however, the thermal fluctuations become high enough to allow the cations to diffuse, and thus disorder of the particular ion species becomes possible. The transition between ordered structure and disordered structure is a phase transition which is well known in metallic alloys. This means that at high temperatures the ions diffuse between the lattice sites, whereas at low temperatures such an exchange becomes almost impossible. However, there are also materials where an ordering of ions is not possible at all due to the long exchange times. For materials where an order can be established, the order can be prevented by rapid quenching. In summary, for the occurrence of RF behavior, it is necessary to achieve such a disorder in the materials, whether this disorder is given *a priori* or forced by quenching.

Another interesting property of RFs can be found in their response to an external electric field. For conventional ferroelectric materials, a hysteresis curve is obtained, as evident in Figure 3, where the associated characteristic quantities have already been discussed in detail in the previous chapter. The ferroelectric hysteresis curve usually exhibits a relatively large remnant polarization as well as coercivity. In the case of an RF, this curve is found to be much slimmer, as can be seen in Figure 5. The reason for this is the differences in the polar order of the respective systems. For ferroelectric systems, domains are formed in the order of tens of nanometers up to micrometers. These domains can be repolarized by the applied field only with some effort, and thus the remnant polarization, as well as the coercivity, is increased. In the

case of RFs, however, as already mentioned, so-called nanodomains are formed, which are much easier to align when an external field is applied compared to ferroelectric domains. The occurrence of such a slim hysteresis curve is directly associated with lower losses caused by the repolarization process and therefore offers interesting properties for various applications. A relevant application can be found in the storage of electrical energy, which will be discussed in detail in the next chapter on dielectric capacitors.
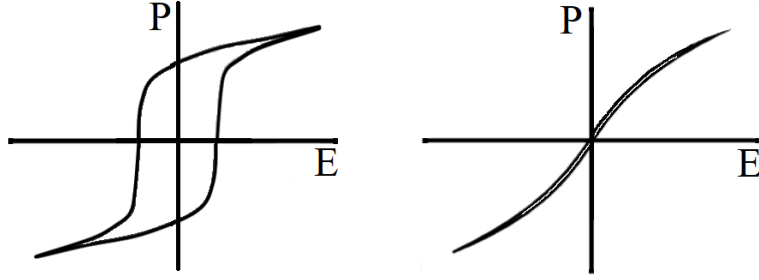


*Figure 5. Illustration of a hysteresis loop for a conventional ferroelectric (left) and an example of a slim hysteresis loop for relaxor ferroelectrics (right). P denotes the polarization and E the electric field.*

In the following, different concepts for the mathematical description of certain properties in RFs will be discussed. First, the observed dispersion of the broad peak caused by the presence of nanometer-sized regions and their respective dynamics will be discussed. It has already been mentioned that these nanometer-sized regions are mobile but lose their mobility entirely at a freezing temperature $T_f$ and adopt a nonergodic state. As this non-ergodic state is very similar to a dipolar glass (or spin glass), the phenomenological Vogel-Fulcher law [10] can be used to estimate $T_f$. The mathematical expression of this law, which was originally derived for studying glass transitions, is given in Equation 3. Here, $f_0$ represents the attempt frequency, $E_a$ denotes the activation energy, $k_B$ is the Boltzmann constant and $T_m$ is the temperature of the maximum in permittivity.

$$f = f_0 exp\left(\frac{E_a}{k_B(T_m - T_f)}\right)$$

(3)

The freezing temperature can thus be determined by Equation 3 and fitting the observed maxima in the permittivity. In the following, further approaches to the description of RF behavior shall be discussed. The basis is the broad peak in the permittivity, which is observed in RFs. To examine this peak from a different point of view, the example of substituted BT can be used. Here, when the pure system is considered, three sharp peaks in permittivity associated with the

14

phase transitions are observed [41]. The exact temperatures for the transitions can be taken from the previous chapter. To continue with the example, BT can now be substituted, for example, with Zr at the B-site [41]. The following trends in permittivity are observed. As the concentration of Zr is increased, the peaks begin to shift towards each other. At a concentration of about 15%, only one broad peak is visible, and the individual phase transitions have disappeared [41]. Furthermore, the temperature of the maximum in the permittivity decreases with increasing concentrations. For more details on this behavior of substituted BT, reference is made here to Publication 3, enclosed in this work. The occurrence of this merging of the individual phase transitions, and the associated broadening of the permittivity peak, are often referred to as a diffuse phase transition (DPT) [10]. Subsequently, a number of methods were developed to describe this DPT behavior mathematically. The first model to be presented was developed by Kirillov and Isupov [42]. The idea considers a spatial distribution of local compositions with different Curie points. The broad peak would be thus due to an average Curie temperature wrapped by a Gaussian function. The corresponding mathematical formulation of permittivity as a function of temperature can be found in Equation 4. Here, $\epsilon'$ is the real part of the complex permittivity, $\epsilon'_m$ denotes the maximum of the permittivity at a given frequency and $T_m$ is the temperature associated with the maximum in permittivity. The parameter $\delta$ defines the diffuseness of the transition.

$$\epsilon' = \epsilon'_\infty + \frac{\epsilon'_m}{1 + \frac{(T - T_m)^2}{2\delta^2}} \tag{4}$$

However, this equation is often inadequate to accurately describe the found behavior of the peaks, so an alternative approach was developed by Santos and Eiras [43]. The corresponding mathematical expression can be seen in Equation 5. Here, the parameters $T_m$ and $\delta$ are analogous to Equation 4. The new parameter $\gamma$ characterizes the phase transition. That is, the value of $\gamma = 1$ describes the phase transition of a conventional ferroelectric, whereas a value of $\gamma = 2$ represents a so-called complete diffuse transition. The values between these boundaries describe incomplete diffuse transitions. Furthermore, the Curie-Weiss behavior is the limiting case for both Equations 4 and 5, respectively. The above equations are suitable for describing DPT, but there is no shift of the peaks as a function of frequency. This is mainly the case at lower concentrations, such as 15% Zr-substituted BT. For higher concentrations, RF behavior is progressively exhibited, and a shift of the peaks is observed, which can be described by the already explained Vogel-Fulcher law.

$$\epsilon' = \frac{\epsilon'_m}{1 + \left(\dfrac{T - T_m}{\delta}\right)^\gamma}$$

(5)

Another model for describing RF behavior is the so-called random field model. Here, it is assumed that in RFs, localized random fields occur, which are caused by chemical substitution. This theory states that the ions in the system are subject to this interaction with the random fields, the strength of which plays a significant role in the occurrence of RF behavior. The fundamental principles of this theory were developed by Imry and Ma [44], and for more details, reference is made to their work [44]. Essentially, it must be stated that a variety of models have been developed over the years to describe the behavior of RFs phenomenologically. The approaches range from simple qualitative explanations to quite complex models. However, a generally accepted explanation of the phenomena occurring in RFs is still missing. One way to solve this puzzle is to simulate RFs on an atomic basis to better understand the effects that occur. In combination with the right experiments, another step towards a complete explanation can thus be made. In this work, the main contribution to the theoretical description of RF behavior is the development of suitable atomistic models. For more details on these models, reference is made here to the following chapters as well as to the enclosed publications.

In order to conclude this chapter on RFs, the possible areas of application shall be outlined. RFs generally exhibit excellent dielectric properties and therefore have a wide range of applications. Due to their high permittivity and their small dielectric losses, RFs are often used in capacitors. The capacitors are mainly used in electronic devices such as computers, cell phones, or other digital devices. Due to their good properties as piezoceramics, RFs are also used as piezoelectric transducers. With their help, electrical voltages can be converted into mechanical displacements and vice versa. Such transducers are used in medical analytics, sonar devices, and ultrasound equipment. RFs can also be used for sensors, for example, to measure temperature, pressure, and other quantities. Last and for this work very relevant field of application is the possibility of storing energy. Due to the slim hysteresis curves found in such materials, the recoverable energy is increased compared to conventional ferroelectrics, and thus larger amounts of electrical energy can be stored. The fundamentals of electrical energy storage via the application of RFs in dielectric capacitors will be discussed in detail in the next chapter.

## 2.3  Dielectric Capacitors

A capacitor is basically an electrical component that can store electrical energy. The structure of a capacitor consists of two electrical conductors separated by an insulator, whereby the latter

is often also called dielectric. If a voltage is applied to the two conductors, charges begin to accumulate on the surfaces of the conductors, causing a potential difference between the conductors. The electric field and the potential difference $V$ are directly proportional to the charge $Q$ that accumulates on the surface of the conductors. From this, as can be seen in Equation 6, the ratio between charge and the potential difference can be derived (called capacitance $C$), which indicates the charge storage capacity of the selected arrangement of conductors and dielectric. It should be noted that the obtained relation assumes small field strengths as well as a linear behavior of the dielectric.

$$C = \frac{Q}{V}$$

(6)

The above relation, though, does not give any information about the properties of the dielectric and the geometry of the capacitor. A simple example to explain the capacitance in more detail can be found in the parallel plate capacitor, where two electrical conductors simply face each other as plates. The capacitance of such an arrangement can be described by Equation 7. Here, $A$ is the area of the plates, $d$ is the spacing of the plates and $\epsilon_0$ is the vacuum permittivity. $\epsilon_r$ is the relative permittivity of the dielectric between the plates. Here it becomes clear that a large area, a small distance, and a large permittivity lead to a large capacitance. The first two requirements can be influenced by the design of the capacitor, but the last feature, permittivity, depends on the material used as the dielectric.

$$C = \epsilon_r \epsilon_0 \frac{A}{d}$$

(7)

The effect of a dielectric in a capacitor will also be briefly discussed here. If the capacitor is connected to a voltage source and, consequently, a dielectric is introduced into the capacitor, the accumulated charge on the surfaces increases by the factor $\epsilon_r$. This is due to the fact that an electric field is induced in the dielectric, which counteracts the external field. The induced field is caused by local dipole moments within the dielectric material, which align themselves by applying an external field, as already discussed in the chapter on ferroelectrics. A thorough description of dielectrics and capacitors can be found in the book of Tipler and Mosca [3]. Furthermore, if a dielectric is introduced into the capacitor and the voltage source is disconnected, the potential difference decreases by the factor $\epsilon_r$. This demonstrates that the dielectric in a capacitor is an essential component to achieve the desired capacitance. Another important quantity is the stored energy in a capacitor. For a linear dielectric, the relation in Equation 8 can be used to calculate the stored energy $W$. Here, $C$ is again the capacitance, and

17

$V$ is the applied voltage across the capacitor. It becomes clear that the storage capacity is directly dependent on the capacity and, thus, also on the above-mentioned characteristic quantities like geometry and relative permittivity. The geometry of the capacitors has been optimized over the years in such a way that a further increase in capacitance in today's applications can only be achieved through the development and use of new materials with higher permittivity. Of course, new materials may, in turn, require new geometries, which shows the complexity of the development of high-performance capacitors.

$$W = \frac{1}{2}CV^2 \tag{8}$$

In many cases, however, the behavior of dielectrics is non-linear and depends on the applied voltage, i.e., on the electric field. The most obvious example of this is ferroelectric materials, which show a hysteresis curve that deviates strongly from linear behavior. Subsequently, Equation 9 can be used to calculate the stored energy of a non-linear system, integrating over the polarization. The upper limit $P_{max}$ here is the maximum polarization reached. This energy includes all contributions needed to align the local dipole moments in the dielectric and therefore represents the total stored energy.

$$W = \int_0^{P_{max}} E dP \tag{9}$$

For energy storage applications, however, the energy portion that is recovered when the capacitor is discharged is of interest. Due to losses that occur during the repolarization of local dipole moments or in ferroelectric systems the repolarization of ferroelectric domains, the recoverable energy is not equal to the stored energy. The recoverable energy $W_{rec}$ can be calculated by a similar integral over the polarization, as can be seen in Equation 10. Here, however, the lower limit is set with the remnant polarization. Therefore, for high recoverable energy, the P-E hysteresis curve must be slim (small remnant polarization) yet have a high maximum polarization. Such a slim hysteresis curve, for example, is observed in RFs, as already discussed in the previous chapter.

$$W_{rec} = \int_{P_r}^{P_{max}} E dP \tag{10}$$

All in all, it can be stated that the stored energy in a capacitor can be determined via the shape of the P-E hysteresis curve. This curve depends on the respective material and differs considerably depending on the system under consideration. Ferroelectric systems show a pronounced hysteresis curve and exhibit high losses when the ferroelectric domains are

repolarized. Therefore, they are only partially useful for storing electrical energy. In contrast, RFs provide a much slimmer hysteresis curve due to the presence of nanodomains, and the recoverable energy is significantly increased. The influence of different chemical compositions in RFs on the shape of the P-E hysteresis curves is discussed in detail in the enclosed Publications 2 and 3.

# 3 State-of-the-Art and Impact of This Thesis

In this chapter, the state-of-the-art of homovalent and heterovalent substituted BaTiO$_3$ (BT) and theoretical models to describe such materials at the atomic scale will be elaborated. Furthermore, the impact of this thesis on the state-of-the-art will be highlighted. In the first subchapter, the state-of-the-art on Zr and Nb substituted BT is summarized, and open questions to explain the occurring effects are discussed. However, this subchapter is kept short because the main subject of this thesis is the method development for the theoretical description. Therefore, the state-of-the-art of simulations of ferroelectric materials and substituted versions thereof are discussed in the second subchapter. Here, an overview of different methods as well as their application will be given. Furthermore, the development of recent Hamiltonians will be discussed, and the areas of application for such simulations will be outlined.

## 3.1 Substituted BaTiO$_3$

Chemical substitution is an essential aspect of developing new compositions, as already highlighted in the introductory Chapter 2.2. Substituting elements can significantly impact various material properties, such as permittivity, polarization, and other characteristics [10,13,18]. Additionally, substitution can influence the behavior of materials. For instance, ferroelectric behavior is generally observed at low concentrations, but at higher concentrations, this can result in relaxor (RF) behavior or behavior similar to dipolar glasses [10,13,18]. This chapter will focus on discussing the primary distinctions between Zr and Nb substituted BT. The first fundamental difference between these substituents is the oxidation state. Zr$^{4+}$ (BZT) replaces the B-site cation Ti$^{4+}$ in homovalent substitution, while Nb$^{5+}$ (BNT) substitutes the B-site in heterovalent substitution. Moreover, these substituents differ in their ionic radii, with Zr$^{4+}$ having a radius of 0.72 Å and Nb$^{5+}$ having a radius of 0.64 Å, in comparison to Ti$^{4+}$'s ionic radius of 0.605 Å. An additional crucial distinction is the concentration range in which RF behavior occurs. For instance, in the case of BZT, the transition to RF behavior is experimentally [20] detected at a concentration exceeding 30%. Conversely, in BNT, RF behavior is already observed at a concentration exceeding 7.5% [21].

BZT is a well-studied form of substituted BT, and the research by Hennings et al. [41] deserves special recognition. They were the first to report on the diffuse phase transition (DPT) in BZT, which was a significant finding. Subsequent studies also demonstrated that polarization persists beyond T$_c$ (Curie temperature) for certain BZT concentrations. Additionally, some compositions exhibit a frequency-dependent permittivity as a function of temperature, such as when the concentration is 40% Zr, where the Vogel-Fulcher law from Chapter 2.2 applies. On

the other hand, some studies [45] propose a behavior resembling that of dipolar glasses, challenging the notion of collective dynamics among the polar nanoregions. Furthermore, neutron scattering [46] indicates that the substitution of $Ti^{4+}$ with larger $Zr^{4+}$ stabilizes local polar clusters in the form of polar nanoregions by displacing B-site $Ti^{4+}$ along the <111> direction. Kleemann et al. [47] proposed that weak random fields resulting from local strain effects exist and become effective in BZT at higher substitution content, influencing the distribution of local polar orders, which supports the neutron scattering findings. Further, in BZT below 50% Zr content, it seems appropriate to assume the presence of non-polar nanoregions embedded in a polar matrix since Zr-centered unit cells are nonpolar. Alternatively, one could assume that polar nanoregions have the size of a unit cell and are centered on Ti cations. This latter interpretation is indeed well-accepted and supported by the experimental findings.

In the case of heterovalently substituted BT, complex defect structures can be considered to suppress ferroelectric ordering due to the presence of different oxidation states. The mechanism is thus fundamentally different from the homovalent case, where size differences were the driving force for the disruption of long-range ferroelectricity. This work mainly focuses on heterovalently substituted BNT, where $Nb^{5+}$ is substituted at $Ti^{4+}$ sites. Here additional charges must be compensated to maintain charge neutrality in the lattice. Compensation mechanisms could include A- or B-cations or electrons. However, Veerapandiyan et al. [40] and the enclosed Publication 1 demonstrate through DFT calculations and Raman spectroscopy that the most probable charge compensation in BNT is via Ti vacancies. This implies that for every 4 Nb ions, one Ti vacancy is generated. Such complex defect structures can lead to random fields in the material, disrupting the long-range correlation and leading to DPT or RF behavior. Despite the extensive research [9,20,21,31,32,40,48–55] conducted on these two systems, the underlying cause of this difference has yet to be clearly explained. Relevant open questions are, for example, how the two substituents integrate into the structure of BT on an atomic basis and which effects are responsible for the disruption of the long-range correlation.

As part of this thesis, research was conducted on this matter, and the obtained results will be briefly summarized. A comprehensive analysis is available in Publications 1 and 3. A preliminary qualitative determination can be made by comparing ionic radii. This size difference causes a local expansion or contraction of the lattice, and randomly distributed strains occur. In the case of BNT, due to the similar ionic radius, such a local lattice change is not expected *a priori*. To validate these assumptions using DFT calculations, 5x5x5 supercells of

rhombohedral BT were created. Following, a small number of substituents were introduced for both BZT and BNT, and the structures were relaxed using DFT. Subsequently, the local volume change was calculated for each unit cell in the supercell. As predicted, substituting with Zr induces a local expansion of the lattice. Additionally, a volume change is observed for Nb, extending beyond the substituted unit cells. It should be noted that defects were also taken into account for charge compensation, as elaborated above. The local volume change also has a direct impact on the polar activity of the adjacent unit cells and induces preferred polarization directions, as described in the Supplemental Material of Publication 1. The volume change has already been discussed, but the effects on the electric potential were also explored. For that purpose, the same supercells described above were employed, and the potential change was determined using DFT with respect to the pure BT system. It was found that only a localized change in the electric potential occurs in the case of BZT. In contrast, BNT exhibits an induced change in the electric potential over several neighboring unit cells.

In summary, it can be concluded that both BZT and BNT systems exhibit local lattice changes. However, only BNT displays a non-local electrical potential change, indicating a more effective perturbation of the polar order. A detailed explanation of how these materials behave at finite temperatures will be presented in Publication 3. Furthermore, Publications 1 and 3 take a step forward in explaining the RF behavior of these systems, building on the state-of-the-art research presented in Refs. [9,10,13,18,21,32,40,41,55–57].

## 3.2   Effective Hamiltonians

The modeling of ferroelectric materials on the atomistic level can be done in different ways and depends on the properties to be investigated. If the atomic structure is to be investigated, first-principles calculations are inevitable. The most common method which is used here is density functional theory (DFT) calculations. Here, the time-dependent Schrödinger equation is solved, and thus the electronic structure of the system under consideration is calculated. From this, a variety of properties can be studied, such as the density of states, energy levels, total energy, or the occurring forces. Furthermore, DFT can also be used to relax the geometry of the initial structure or to calculate the vibrational properties. The application of DFT calculations to the study of ferroelectric materials is, therefore, almost unlimited and constantly provides new insights into the physical mechanisms. A relevant work here is the calculation of the well-known double-well potential of BT by Cohen and Krakauer [34] back in 1990. A steady increase of publications on DFT for the description of ferroelectric materials follows, which is also due to the ever-improving computing power. A paper that calculates and describes in detail the diverse properties of BT by means of DFT is that of King-Smith and Vanderbilt [24].

However, such DFT calculations can also be used for the calculation of substituted systems, as in the work of Levin et al. [55] on Zr-substituted BT. In summary, DFT calculations are a powerful tool for studying materials at the atomistic level and are indispensable in research today. A disadvantage of this method is that the calculations are performed at 0 K and are static when using pure DFT calculations. Of course, there are now methods that also allow finite temperatures, but such ab-initio molecular dynamic simulations are extremely computationally expensive. The keyword here is molecular dynamics (MD), which also allows to perform dynamic simulations by allowing the particles to move. The basis for such MD simulations is the so-called potentials, which describe the interaction between the particles. In this thesis, only MD simulations where particles represent atoms or entities associated with atoms are considered, but such simulations can be performed for various applications. Just to give an example, the potentials could describe the interaction between planets, and thus the dynamics of these could be simulated. But what can one imagine by such a potential? In principle, such a potential is nothing else than a mathematical construct that should describe the interaction between particles by suitable parameters. There is no limit to the variety of potentials, which differ more or less from each other. A very common class of potentials is so-called pair potentials. As the name suggests, such potentials describe the interactions of pairs of particles. Two well-known examples are the Lennard-Jones [58,59] potential and the Morse potential [60]. Often, however, it is not sufficient to consider only the pairwise interaction, and therefore, more elaborate methods have been developed, which are commonly known as many body potentials. Here, the interaction of more than two particles is considered for the construction of the potential. For the simulation of ferroelectric materials, so-called core-shell potentials are a suitable option. These potentials distinguish between the interaction of the core, i.e., the atomic nucleus, and the shell, i.e., the electron shell. Such potentials proved to be quite effective for the description of ferroelectric materials, and a wide variety of properties could be simulated [61–65]. Such simulations based on these potentials are less expensive compared to ab-initio MD simulations but still do not allow large-scale simulations. However, for substituted systems like Zr- or Nb-substituted BT, it is of relevance to allow large ensembles and long simulation times to better comprehend the dynamics of the local dipoles.

Therefore, in this thesis, an entirely different concept for the description of the interactions was selected. The chosen method is based on a description of the interactions by a local basis and is called the effective Hamiltonian. The idea behind this is to select a subspace of the phonon band structure, thereby defining a local basis and then parameterizing the interactions using this basis. The parameterization of the required parameters for the effective Hamiltonian can be

done entirely through DFT calculations [22–24]. A detailed explanation and derivation can be found in Chapter 4.3. The basis for the development of this method for describing ferroelectric materials was laid by the work of King-Smith, Vanderbilt, Zhong, Rabe, and Waghmare in the mid-1990s [22–24]. This method already allowed to reproduce properties of $BaTiO_3$ (BT) and $PbTiO_3$ (PT) astonishingly well by means of the effective Hamiltonian, which was still applied as a mean-field theory at that time. In 1997 this mean-field theory was extended to a local mode theory which also allowed a simulation of supercells. It was not long before this formalism was extended by Bellaiche et al. [29] to simulate substituted systems. In this work, it was impressively demonstrated how substituents could be taken into account by adding additional terms. Already in this early work, the phase diagram of $Pb(Zr_{1-x}Ti_x)O_3$ and associated piezoelectric constants were simulated. The method used by Bellaiche et al. [29] to parameterize the effective Hamiltonian is based on the Virtual Crystal approximation (VCA) [66] made within DFT. All necessary corrections for substituent incorporation are then referenced to this virtual crystal. Such an approach is well suited for larger substituent concentrations but leads to complications when small concentrations are considered. This was followed by a number of different parameterizations of substituted systems, such as $(Ba_{1-x}Sr_x)TiO_3$ (BST) [67] and $Pb(Sc_{0.5}Nb_{0.5})O_3$ (PSN) [68]. In 2008, Nishimatsu et al. [26] published a paper on simulations of thin films of BT. In association with this work, a very efficient implementation of the effective Hamiltonian using Fortran was also published. This implementation is extremely computationally efficient due to the intelligent use of fast Fourier transforms and allows large-scale simulations even on conventional workstations. The software and self-adapted versions are also used in this thesis. In the work of Nishimatsu et al. [27] in 2010, the approach was revised again, and certain energy terms were extended to provide an improved description of the potential energy surface. In another work by Nishimatsu et al. [33], it was shown for the BST system that parameterization by averaging and incorporating local deformations gives approximately the same results as using VCA. In 2017, parameterization by a newly developed exchange-correlation functional was demonstrated by Paul et al. [28]. Furthermore, the inclusion of anharmonic couplings [28] to higher energy phonons was presented. This inclusion of additional terms significantly increased the quality of the description of the phase transitions. Subsequently, this work also represents the inspiration for the approaches developed in this thesis to account for anharmonic couplings. Thus, this approach was completely revised, and a large number of couplings parameterized by DFT were incorporated into the effective Hamiltonian. The entire work on this topic can be found in detail in Publication 2 and its Supplemental Material. As a consequence, the description of the phase

transitions could be improved again. An alternative concept for the incorporation of substituents was published by Mentzer et al. [32] in 2019 for $Ba(Zr_xTi_{1-x})O_3$ (BZT). Here, BT was chosen as the basis, and the substitution effects were taken into account by means of a restoring force and an adaptation of the applied hydrostatic pressure. This approach made it possible to simulate the phase diagram for a larger concentration range and to achieve good agreement with experiments. The work of Mentzer et al. [32] and Akbarzadeh et al. [31] on BZT forms the starting point of this thesis for developing an extension of the effective Hamiltonian to describe substituted systems. Basically, the advantages and disadvantages of the two approaches were weighed, and then an alternative approach was formulated. The effective Hamiltonian from Publication 2 was chosen as the basis, which shows a favorable agreement of the phase transition temperatures compared to experiments. All corrections to describe substitution effects are referred to this basis. The corrections were designed following the work mentioned above and a general approach was derived from it. The parameterization and application in MD simulations shows good results compared to the reference simulations and experiments. The entire derivation and results from the MD simulations can be found in Publication 3 and its Supplemental Material.

Recently, further interesting results have been published using effective Hamiltonians. These works investigate ferroelectric materials for properties that could be relevant for application in neuromorphic computing systems. Of particular note is the work of Prosandeev et al. [69–72], who investigated relaxor ferroelectrics using ultrafast THz pulses. The pulses are applied to the respective materials using MD simulations, and the response of the system is studied. Such pulses can induce phases in $Pb(Mg_{1/3}Nb_{1/3})O_3$ (PMN) which are hidden in the equilibrium state. Subsequently, these phases are also called hidden phases. When a train of pulses is applied, the integration of the polarization over the hidden phases is observed. These and other results show promising properties for application in neuromorphic computing systems. In Publication 4 of this thesis, an analogous study is performed for both $Ba(Zr_xTi_{1-x})O_3$ (BZT) and $Ba(Nb_xTi_{1-x})O_3$ (BNT) systems, examining for possible similar phenomena.

Overall, the following can be concluded on the state-of-the-art in simulations of ferroelectric materials: There are plenty of different methods for describing effects on the atomic level. Density functional theory is one of the most important and relevant methods for characterizing materials at the atomic level. For simulations of finite temperatures, molecular dynamics simulations are inevitable and different potentials can be used. If the positions of the atoms shall be directly accessible, core-shell potentials are preferable, for example. However, if large

supercells and long simulation times are to be realized, effective Hamiltonians are a suitable choice. Although these have a certain complexity, they provide outstanding results if parameterized correctly. To conclude this chapter, an example of the performance of such effective Hamiltonian simulations is given. For a supercell measuring 100x100x100 and comprising 5 million atoms to be simulated for 200 ps, a standard workstation with 18 cores is adequate, and the computation is finalized in under an hour. Achieving such high accuracy and performance with other potentials is almost implausible.

# 4 Computational Methods

In this chapter, all computer-aided methods used in this thesis shall be described in detail. First of all, quantum mechanical methods mainly based on density functional theory (DFT) are considered. This method finds wide applicability in the simulation of effects on the atomic level and is, so to say, the foundation of the whole presented work. Therefore, a detailed description of the methodology is given, and the main components of DFT are explained. Since DFT is mainly related to static and 0 Kelvin properties, the basics of molecular dynamics (MD) simulations are also explained in the course of this chapter. Such simulations allow finite temperatures to be simulated and provide deep insight into the dynamics of atoms and their collective behavior. The range of possible properties to be simulated extends from local lattice effects to the simulation of permittivity as a function of frequency. First, the basics of MD simulations will be explained, and different thermostats will be discussed. As a basis for such simulations, one needs potentials for the description of the potential energy surface. Such potentials are mathematical constructs to describe the interaction between particles. There is a wide range of different approaches for this, but in this work, as previously stated, the well-tried method of effective Hamiltonians is extended and used. Such effective Hamiltonians are based on the idea of parameterizing the potential energy surface by means of so-called local modes. Since such potentials have a complex structure, first, the underlying theory is explained, and then the individual energy contributions are elaborated in detail. The required parameters for such an effective Hamiltonian can be determined entirely by means of DFT calculations. Owing to the fact that the parametrization is rather complex, the procedure of obtaining the parameters is explained in individual chapters for each of the investigated systems.

## 4.1 Density Functional Theory

In modern times, the application of quantum mechanical methods for the characterization of materials is indispensable. The basis for this is the so-called Schrödinger equation, which describes atoms, molecules, and crystal systems at the quantum mechanical level. The solution of this equation gives information about the energetic states of the system and allows to predict a variety of properties. Besides wave-function-based methods like Hartree-Fock, the application of DFT is predominant nowadays. This method is not only used by physicists and chemists but also by engineers, material scientists, geologists, and other scientists in related disciplines. The continuous development of high-performance computing centers makes it possible to describe even larger systems at the atomic level or to study a large number of different systems. This chapter will begin by explaining the basis of DFT, starting with the quantum mechanical description of many-particle systems, followed by an explanation of the

most important assumptions for DFT. The application of the Kohn-Sham formalism will be discussed, and a brief overview of plane-wave basis sets will be given. Additionally, the description of exchange-correlation energies will be presented, and the most important corresponding functionals will be discussed.

### 4.1.1  Many Body Hamiltonian

In order to understand DFT, the fundamental basis must first be laid at the quantum mechanical level. A system of different particles can be described energetically by a so-called many-particle Hamiltonian. In our case, we want to restrict ourselves to many-particle systems consisting of electrons and atomic nuclei. Such a system with $M$ atomic nuclei and $N$ electrons can be described by the Hamiltonian presented in Equation 11. Here $\hbar$ is the reduced Planck constant. $M_j$ the mass of the respective atomic nuclei. $M_e$ is the mass of the electrons. $R_{ij}$ and $r_{ij}$ represent the distances of the individual particles. $Z_i$ describes the charge of the atomic nuclei and $e$ the elementary charge. The first term in Equation 11 denotes the kinetic energy of the atomic nuclei. The second term describes the Coulomb interaction between atomic nuclei. It follows the Coulomb interaction between atomic nuclei and electrons. The fourth term represents the kinetic energies of the electrons. The last term accounts for the electron-electron interaction. In principle, such a Hamiltonian fully describes a many-particle system at the quantum mechanical level. However, there are some challenges to overcome in order to actually obtain useful results from this quantum mechanically sound description.

$$\hat{H} = -\sum_{j}^{M} \frac{\hbar^2}{2M_j} \nabla_j^2 + \sum_{j}^{M}\sum_{i \neq j}^{M} \frac{Z_i Z_j e^2}{R_{ij}} - \sum_{j}^{M}\sum_{i}^{N} \frac{Z_j e^2}{r_{ij}} - \sum_{i}^{N} \frac{\hbar^2}{2M_e} \nabla_i^2 + \sum_{j}^{N}\sum_{i \neq j}^{N} \frac{e^2}{r_{ij}}$$

(11)

The above-mentioned many-particle Hamiltonian can now be used to formulate the time-independent nonrelativistic Schrödinger equation as stated in Equation 12. Here, the Hamiltonian acts on the total wave function of the system. The total wave function is a function of all degrees of freedom, including the spatial coordinates of electrons and nuclei. Furthermore, the obtained equation represents an eigenvalue problem that has to be solved by searching for the wave function $\Psi(\mathbf{R}_1 \dots \mathbf{R}_M, \mathbf{r}_1 \dots \mathbf{r}_N)$ and the associated eigenvalue $E$.

$$\hat{H}\Psi = E\Psi$$

(12)

At this point, we already encounter the first problem: an analytical solution to this equation is only possible for very simple problems like the hydrogen atom. All systems with several atomic nuclei and electrons require a numerical solution, but also, here, certain assumptions have to be

made, as will be seen in the next chapter. Most of the difficulties in this equation come from the electron-electron interaction, where the complexity increases strongly with increasing electron number. Furthermore, the expressions exchange energy, as well as correlation energy, get significance here, which carry special importance for a physically correct description of the total system. More about this topic can be found in the following chapters.

### 4.1.2 Born Oppenheimer Approximation

A step toward a solution to the above-mentioned Schrödinger equation is the application of the so-called Born-Oppenheimer approximation. The fact that electrons have a much smaller mass compared to the nuclei allows separating the electronic part from the nuclear part. That is, we can separate the contribution of electrons from the contribution of nuclei and obtain a new Hamiltonian which describes the electronic part of the system. The corresponding Hamiltonian for the electronic problem is stated in Equation 13. Here, three energy contributions are present. The kinetic energies of electrons as denoted by the first term. The electron-electron interactions are stated via the second term. The last term represents the interaction with an external potential, which in our case, is the interaction between electrons and nuclei. It becomes clear that the coordinates of the nuclei are also present in the electronic part of the Hamiltonian, but here they are only to be considered as parameters.

$$\widehat{H}_{el} = -\sum_i^N \frac{\hbar^2}{2M_e} \nabla_i^2 + \sum_j^N \sum_{i \neq j} \frac{e^2}{r_{ij}} - \sum_j^M \sum_i^N \frac{Z_j e^2}{r_{ij}}$$

(13)

This Hamiltonian can now be used to formulate the Schrödinger equation for the electronic part of a given system, as stated in Equation 14. The spin coordinate is omitted here to simplify the notation and focus the discussion on the main features of DFT. The electronic wave function $\Psi_{el}(\boldsymbol{r}_1 \dots \boldsymbol{r}_N)$ differs from the total wave function $\Psi(\mathbf{R}_1 \dots \mathbf{R}_M, \mathbf{r}_1 \dots \mathbf{r}_N)$ from above and includes only the spatial coordinates of the N electrons. $E$ represents the ground-state energy of the electronic Hamiltonian. Since the ground-state of this equation is independent of time, we can also speak here of the time-independent Schrödinger equation of the electronic part.

$$\widehat{H}_{el}\Psi_{el} = E\Psi_{el}$$

(14)

The electronic Schrödinger equation from above represents the central point of modern quantum chemistry. A variety of different theories have been developed to solve this equation numerically as efficiently and accurately as possible. Even though in the following section the

focus will be on DFT, alternative approaches for solving this equation based on wave functions shall be discussed first. The simplest approach would be to write the electronic wave function as a product of individual single electron wave functions. Such an approach is also called Hartree product. However, the assumption to write the wave functions as a product would only be valid if the interaction between the electrons were switched off. But exactly this interaction is of great importance for the physically correct description. For further progress, we have to consider that electrons are subject to the Pauli principle, and therefore, the wave function must be antisymmetric. The Hartree product is anything but antisymmetric and thus cannot fulfill this requirement. A solution to this problem can be found in the construction of the wave function by means of a so-called Slater determinant. The construction again assumes individual single electron wave functions but forms an antisymmetric overall electronic wave function. This approach is the foundation for the Hartree-Fock method. Starting from the Slater construction, a formalism is derived to obtain a solution to the Schrödinger equation. The difficulty for this and all other solutions lies, as already mentioned, in the electron-electron interaction. Since the electrons influence each other and the potential is, therefore, always a function of the respective other electrons, the solution to this term is exceedingly complicated. Hartree and Fock provide a solution to this problem by introducing a new operator. The so-called Fock operator. In simple words, the electrons no longer interact in pairs but with a field generated by all other electrons on average. This formalism represents a significant step toward a useful solution of the electronic Schrödinger equation and is still used in many quantum chemistry simulations today. A major advantage of this method is the exact calculation of the exchange energy of the system. However, the Hartree-Fock method does not properly account for the correlation between electrons. Therefore, in the course of time, additional methods have been developed which are based on Hartree-Fock and aim to take into account the correlation effects of the electrons. Examples are the configuration interaction (CI) method or the coupled cluster method.

However, certain disadvantages of wave-function-based methods shall also be discussed here. A major challenge for the solution of the Schrödinger equation is the dimensionality of the corresponding wave function. For example, if we consider the molecule $C_2H_6$, we get a wave function with 54 dimensions (for each of the 18 electrons, 3 dimensions have to be considered). If we want to calculate 100 Au atoms, we get a function with more than 24000 dimensions. This means that wave-function-based methods are well suited for molecules and smaller ensembles of atoms but fail as soon as larger systems are to be calculated. In addition, such wave functions cannot be determined experimentally as a function of spatial coordinates. Nevertheless, there is

a quantity that can, in principle, be observed experimentally, namely the so-called electron density. The corresponding probability density is directly related to the wave-function and reads $\Psi_{el}^*(r_1 ... r_N)\Psi_{el}(r_1 ... r_N)$. Here, the asterisk denotes the complex conjugate of the wave-function. From that, it is possible to derive the electron density of a given system as stated in Equation 15, where $N$ represents the number of electrons.

$$n(r) = N \int dr_2 ... \int dr_N |\Psi_{el}(r, r_2 ... r_N)|^2$$

(15)

The electron density is a key concept in quantum mechanics, as it reveals the likelihood of finding electrons in an infinitesimal element of space. What's intriguing is that the wave-function determines the electron density and, as a result, provides abundant information about the system's fundamentals. However, while the wave-function has a 3N dimension, the electron density is simply a function of three coordinates. This disparity confers a significant advantage when employing the electron density as the focal point for addressing the Schrödinger equation.

### 4.1.3 Hohenberg Kohn Theorems

DFT is used in many fields nowadays, but the basis for it was already provided by Hohenberg and Kohn in the 1960s. The entire theoretical description can be traced back to two important Hohenberg-Kohn theorems [73,74]. For the actual application of these theorems, however, the so-called Kohn-Sham equations are needed, which will be discussed in the next chapter. The first fundamental theorem of Hohenberg and Kohn reads:

*"The ground-state energy from Schrödinger's equation is a unique functional of the electron density."* [75]

Consequently, the first theorem states that there is a direct connection between the ground state wave-function and the ground-state electron density. The connection between these two quantities is a so-called functional. A functional is defined by the application to a function whereby a number is returned as an answer. That means the ground state energy can be written as a functional of the electron density $E[n(r)]$. This theorem contains a very powerful statement, namely that by the ground state electron density, the properties of the ground state are uniquely determined. That is, a 3-dimensional function, the electron density, determines the ground state of the entire electronic system. Unfortunately, this theorem only states the existence of this functional but does not give any information about the actual form of the functional. In fact, this is part of the research, and much effort is being put into finding such a

functional, or at least developing good approximations, for any material or compound. The second fundamental theorem of Hohenberg and Kohn reads as follows:

*"The electron density that minimizes the energy of the overall functional is the true electron density corresponding to the full solution of the Schrödinger equation."* [75]

This theorem contains an important property of the functional from the first theorem. It says that the functional provides the lowest energy if, and only if, the actual ground state density is put into the functional. In principle, this is nothing more than the so-called variational principle. That is, the electron density is varied until the minimum energy is reached. The corresponding mathematical expression is stated in Equation 16.

$$E_0 \leq E[n(\boldsymbol{r})]$$

(16)

In summary, these two theorems form the basis of DFT. The first theorem declares the existence of a universal functional, while the second one conveys the uniqueness of the ground state density. This framework is very powerful from the theoretical side, but it requires additional approaches and methods for actual applicability. Also, in this case, the electron-electron interaction causes the biggest problems. With some assumptions, however, it is possible to derive a formalism that allows an accurate calculation of quantum mechanical systems.

### 4.1.4 Kohn Sham Equations

A theory is only as good as its applicability. For DFT, the fundamental principles have been explained, but the question arises of how this formalism can be used to actually calculate the properties of a many-particle system. The answer can be found in the so-called Kohn-Sham equations. The idea of Kohn-Sham is based on a fictitious system of non-interacting particles which produce the same electron density as the interacting system. Here, analogous to the Hartree-Fock approach, the introduction of individual wave-functions $\Psi_i$ is used. In this context, these individual wave functions are often referred to as Kohn-Sham orbitals. The total electronic wave-function is constructed by using the Slater determinant approach as introduced before. Furthermore, it is possible to calculate the corresponding electron density as stated in Equation 17. The summation includes all individual wave-functions occupied by electrons. The factor of two arises from the fact that electrons can occupy each individual wave-function if they have opposite spins.

$$n(\boldsymbol{r}) = 2 \sum_{i} \Psi_i^*(\boldsymbol{r}) \Psi_i(\boldsymbol{r})$$

(17)

The total energy of the system can now be formulated as a functional of the individual energy contributions, as evident in Equation 18. The first term is the kinetic energy of the system, followed by the interaction with an external potential. The third term is the so-called Hartree potential. The last term represents the exchange-correlation energy of the electrons.

$$E[n(\boldsymbol{r})] = T[n(\boldsymbol{r})] + \int V_{ext}(\boldsymbol{r})n(\boldsymbol{r})d\boldsymbol{r} + E_H[n(\boldsymbol{r})] + E_{xc}[n(\boldsymbol{r})]$$

(18)

The next step is to provide a more detailed explanation of the individual energy contributions. The kinetic energy of the system can be expressed via the Kohn-Sham orbitals as stated below:

$$T[n(r)] = -\frac{\hbar^2}{2M_e} \sum_{i} \int \Psi_i^* \nabla^2 \Psi_i d^3 r$$

(19)

The interaction with an external potential is to be calculated as indicated by the second term in Equation 18. The Hartree potential, in turn, can be expressed by Equation 20. The Hartree potential is determined directly from the electrostatic potential of the electron density.

$$E_H[n(\boldsymbol{r})] = \frac{e^2}{2} \int \int \frac{n(\boldsymbol{r})n(\boldsymbol{r}')}{|\boldsymbol{r} - \boldsymbol{r}'|} d^3 r d^3 r'$$

(20)

The previous energy terms are known and can be determined by the above equations. The last remaining term stands for the exchange-correlation energy. This term contains all quantum mechanical effects which are not considered by the first terms. Unfortunately, no analytical form can be derived for this energy contribution, and approximations are required to account for these effects. Let us assume we can provide a useful term for this energy. The question then arises as to how we obtain a solution to the problem formulated in the Schrödinger equation. Kohn and Sham provided the answer by establishing a set of equations that allowed them to find the correct electron density for the underlying problem. The Kohn-Sham equations are presented in Equation 21. These equations are based on the wave-functions, but in contrast to the conventional Schrödinger equation, the sums over the individual spatial coordinates are missing. This was achieved by using the single-electron wave-functions (Kohn-Sham orbitals) instead of the total electronic wave function.

$$\left[\frac{\hbar^2}{2M_e}\nabla^2 + V(\boldsymbol{r}) + V_H(\boldsymbol{r}) + V_{XC}(\boldsymbol{r})\right]\Psi_i(\boldsymbol{r}) = \epsilon_i\Psi_i(\boldsymbol{r})$$

$$(21)$$

The potentials of the Kohn-Sham equations are defined as follows. $V(\boldsymbol{r})$ represents the interactions of an electron with the potential of the atomic nuclei. This potential is also found in the conventional Schrödinger equation. The second term $V_H(\boldsymbol{r})$ is the Hartree potential. It accounts for the electrostatic repulsion between electrons and the total electron density. This term also includes a self-interaction since a considered electron is also part of the total electron density. Such an effect is unphysical and is therefore considered in the last term. This last term $V_{XC}(\boldsymbol{r})$ accounts for all effects not accounted for by the previous terms, such as exchange and correlation energies that occur due to the interaction of electrons. Formally, this potential can be written as a derivative with respect to the electron density, as evident in Equation 22.

$$V_{XC}(\boldsymbol{r}) = \frac{\delta E_{XC}(\boldsymbol{r})}{\delta n(\boldsymbol{r})}$$

$$(22)$$

Assuming there is an expression for the exchange-correlation energy, a complete procedure for solving the Kohn-Sham equations can now be established. First, an input electron density is generated. Subsequently, the Kohn-Sham equations can be solved by means of this electron density. This results in new Kohn-Sham orbitals. These orbitals can be used again to calculate a new electron density. Afterward, this electron density is compared with the initial electron density. If both are (almost) identical, then the electron density is the ground state density and can be used to calculate the total energy. If the densities do not match, the density is updated in a predetermined way, and the procedure starts again. Such a procedure is also called a self-consistent procedure.

However, there are still some open questions. For example, how is the exchange-correlation energy approximated, and what are the state-of-the-art approximations? Furthermore, the question of which functions can be used for the Kohn-Sham orbitals has to be answered. The answers to this question will be presented in the next two chapters.

### 4.1.5 Exchange-Correlation Functionals

An essential part of DFT is the description of the exchange-correlation energy. An exact determination of this energy is not yet achieved, and therefore, research in this area is of great interest. In the present time, however, there are a number of different approximations which allow an accurate solution of the Schrödinger equation for a wide range of molecules and materials. A well-known class of approximations is the so-called local-density approximation

(LDA) [76]. The obtained approximation for the exchange-correlation energy depends only on the value of the electron density at a given point in space. A common definition of the LDA approach can be found in Equation 23. Here, $\epsilon_{XC}$ is the exchange-correlation energy per particle of a homogenous electron gas with $n(\boldsymbol{r})$ representing the electron density of the system. Hence, the exchange-correlation energy per particle at a given point $\boldsymbol{r}$ is approximated by considering the exchange-correlation energy of a homogeneous electron gas of the same density $n(\boldsymbol{r})$. The LDA is a surprisingly effective estimate for the exchange-correlation energy and is still commonly utilized today. However, in the course of time, more sophisticated approximations based on LDA have been devised to enhance the description of the exchange-correlation energy [77].

$$E_{XC}^{LDA}[n(\boldsymbol{r})] = \int \epsilon_{XC}(n)n(\boldsymbol{r})d^3r$$

(23)

An approximation that builds upon the LDA can be introduced by the inclusion of the gradient of the electron density. The gradient allows to include also non-local changes in the electron density. Such an approximation is generally called generalized gradient approximation (GGA) [78–80] and has a wide range of applications in quantum chemistry. A formal definition of such a GGA functional can be seen in Equation 24. Here, the spin coordinate and its different electron densities have been omitted. Well-known examples of such GGA functionals would include Perdew-Wang (PW91) [78], Perdew-Burke-Enzerhof (PBE) [81], and revised PBE for solids (PBEsol) [82].

$$E_{XC}^{GGA}[n(\boldsymbol{r})] = \int \epsilon_{XC}(n, \nabla n)n(\boldsymbol{r})d^3r$$

(24)

A commonly known problem of LDA and GGA functionals is the underestimation of bandgaps in semiconductors and insulators. To solve this problem and others, the available functionals are constantly evolving. For example, there are so-called meta-GGA functionals in which the second derivative of the electron density is also taken into account. Furthermore, the determination of an accurate exchange energy is often a challenge. This can be remedied by including a certain part of the exact exchange energy obtained within the Hartree-Fock approximation. Such functionals are generally called hybrid functionals.

### 4.1.6 Plane Wave Basis Sets

Not yet addressed is the question of how the electronic wavefunction in the framework of DFT should be formulated mathematically to obtain reasonable results. The choice of these functions is also called the choice of a basis set. Basically, there are two fundamentally different

approaches. Either the basis set is expressed by localized functions like atomic orbitals, or one chooses non-localized functions, which are also called plane waves. The former method is commonly utilized in quantum chemistry and is frequently selected for Hartree-Fock methods as well as DFT. The advantage of the localized basis functions is the description of core electrons and, therefore, is also called an all-electron method. If one uses a plane-wave basis set, such core electrons are difficult to describe, and so-called pseudopotentials are needed. The plane-wave basis sets are often used in the calculation of periodic structures. The reason for this is explained further below. However, it should also be mentioned that localized basis functions can also be used for periodic systems with the help of a Bloch construction. Since in this work mainly periodic structures are worked with, and the applied DFT packages are all based on plane-wave basis sets, this method shall be explained in more detail below.

The foundation for plane-wave basis functions is the so-called Bloch theorem [83]. The theorem tells about the type of solutions of the stationary Schrödinger equation for a periodic potential. The solutions, thereby, are of the shape represented in Equation 25. Here, $k$ is a wave vector and $u_k(r)$ is a periodic function with the period $u_k(r + R)$, where $R$ denotes a translational vector.

$$\phi_k(r) = e^{ikr} u_k(r)$$

(25)

As a further step, the periodic functions $u_k(r)$ can now be expressed by a set of plane waves. This leads to Equation 26, where the coefficients $c_G^k$ have been introduced, and the reciprocal translational vector $G$ has been added. The functions obtained in this way have the following properties. They are periodic, orthonormal, and complete. Such a definition also requires that the Schrödinger equation must be solved for each chosen k-point in the reciprocal space.

$$\phi_k(r) = \sum_G c_G^k e^{i(k+G)r}$$

(26)

The reciprocal translation vector $G = m_1 b_1 + m_2 b_2 + m_3 b_3$ is defined by the reciprocal lattice vectors $b_i$ and integer multiples $(m_1, m_2, m_3)$ thereof. The definition of the plane-wave basis set and the summation over all possible $G$ vectors involved implies that the calculation of the solution of the Schrödinger equation requires an infinite sum. However, this cannot be implemented in reality, and thus a trade-off must be accepted. A common method to get rid of the infinite sum is to restrict the kinetic energy of the solutions. Since low-energy solutions are more important than high-energy solutions, such a constraint is acceptable. The so-called cutoff

energy can be found in Equation 27. That is, only wave-functions up to a certain energy under the limiting $G_{cut}$ vector are considered.

$$E_{cutoff} = \frac{\hbar^2}{2M_e} G_{cut}^2$$

(27)

The introduction of the cutoff energy limits the infinite sum, and only a finite number of wave functions are taken into account in the Schrödinger equation, as seen in the equation below:

$$\phi_k(r) = \sum_{|G+k|<G_{cut}} c_G^k e^{i(k+G)r}$$

(28)

The introduction of cutoff energy, however, also has certain effects on the solution of the Schrödinger equation. For example, valence electrons can still be described very accurately using the cutoff, but the description of electrons close to the nucleus becomes worse or even impossible. To solve this problem, so-called pseudopotentials are used. These pseudopotentials replace the electron density of the electrons close to the nucleus with the help of an effective potential. It is important that the pseudopotential is defined in a way that the physical and mathematical properties of the core electrons are captured. Therefore, only well-parameterized pseudopotentials lead to a meaningful solution of the Schrödinger equation.

In summary, the following important aspects of a DFT calculation can be enumerated. The choice of the k-grid and, thus, the number of points in the reciprocal space at which the Schrödinger equation is solved is of particular importance. This number is not known a priori and must be determined by a convergence test. Which value or property is to converge is thereby due to the respective use of the results. For example, that could include a convergence test considering the total energy. Furthermore, the choice of correct cutoff energy is an important criterion. Here, convergence must also be checked, and a suitable value must be found according to requirements. Finally, the applied pseudopotentials play a decisive role and are usually included in a solid DFT package.

## 4.2 Molecular Dynamics

In this chapter, the theoretical basis of molecular dynamics simulations will be presented. The idea of such simulations is based on the description of interacting atoms with the help of Newton's equations of motion. The result is a time-resolved trajectory from which the desired physical properties can be derived. The beauty of this method is that such simulations are very similar to experiments. Different ensembles can be studied, different temperatures or pressures

can be applied, or external fields can be added. An important role is assigned to the so-called potentials, which describe the interaction of the atoms on a mathematical level. In this work, an effective Hamiltonian operator is used as potential. Such an effective Hamiltonian differs from conventional potentials since the smallest unit is no longer the atom but the unit cell. More details on this model can be found in Chapter 4.3. Even though the potential used no longer has the atom as its smallest unit, the general methodology of molecular dynamics simulations can be applied here as well. Therefore, the following description of the fundamentals is based on a conventional (i.e. atomic-based) potential.

### 4.2.1 Newton's Equations of Motion

The foundation of molecular dynamics simulations is the solution of Newton's equations of motion, as illustrated in Equation 29. Here, $\boldsymbol{F}$ is the force acting on the i-th particle. $m_i$ represents the corresponding mass and $\boldsymbol{r}_i$ is the position vector of the particles. This equation is a second-order differential equation. To obtain a time-dependent trajectory for the individual particles, this equation must be integrated. The particles considered here do not play a role in the solution of the equations. It can be an ensemble of atoms, which are considered in a classical way. But also, whole galaxies can be simulated by such a description. It is only important that the boundary conditions, as well as the interactions among the particles, are determined.

$$\boldsymbol{F}_i = m_i \frac{d^2 \boldsymbol{r}_i(t)}{dt^2}$$

(29)

The integration of the equations of motion represents the central point of molecular dynamics simulations. Therefore, two common and quite simple methods for integration will be discussed here. These are called Verlet [84] and Leap-Frog [85] algorithms. Both can be used to simulate a microcanonical ensemble. That is, constant particle number $N$, constant volume $V$, and constant energy $E$, in short $NVE$-ensemble. For the simulation of canonical ensembles, a thermostat is also needed, which will be described in the next chapter. The integration of the equations of motion in a simulation is done over discrete time steps $\tau$. This means that, for each time step, the particle positions, the velocity, and the forces acting on the particles have to be determined. The basis for the Verlet algorithm is a Taylor expansion of the spatial coordinate of the particles, which is terminated after the 3$^{rd}$ order. The resulting relationship between the new and old position of the particles can be seen in Equation 30. The Verlet algorithm does not rely on updating the velocity, as it only utilizes the velocity at the first time step.

$$\boldsymbol{r}(t + \tau) = 2\boldsymbol{r}(t) - \boldsymbol{r}(t - \tau) + \tau^2 \ddot{\boldsymbol{r}}(t)$$

(30)

The Verlet algorithm is the basis for the more robust Leap-Frog algorithm. The name for this method comes from the fact that the spatial coordinate and the velocity are updated at different times. That is, as shown in Equation 31, the spatial coordinate is calculated at each time step $\tau$.

$$r(t + \tau) = r(t) + \tau v\left(t + \frac{\tau}{2}\right)$$
(31)

The Leap-Frog algorithm also includes the velocity, but the computation of the new velocity takes place at time steps shifted by $\tau/2$, as can be seen in the definition below:

$$v\left(t + \frac{\tau}{2}\right) = v\left(t - \frac{\tau}{2}\right) + \tau \ddot{r}(t)$$
(32)

The velocity for the first iteration can be calculated by using the following equation:

$$v\left(\frac{\tau}{2}\right) = v(0) + \frac{\tau}{2}\ddot{r}(0)$$
(33)

An important point for integration in a simulation is the choice of the time step. The latter must be chosen in such a way that the underlying physics is reproduced accurately. However, care must also be taken that the time step is not chosen too small. Otherwise, the total times to be simulated will be greatly reduced. In most cases, tests are necessary to select a suitable time step.

### 4.2.2 Canonical Ensemble

The integration methods shown in the previous chapters are based on a microcanonical ensemble. However, it is often necessary to keep variables other than the number of particles, volume, or energy constant. For example, many experiments are temperature dependent, and one would therefore want to simulate systems at a particular temperature. Such a system is also called a canonical ensemble, short NVT ensemble. However, one may also want to simulate a constant temperature and pressure. This leads to an isothermal-isobaric (NPT) ensemble. For this work, the canonical ensemble is mainly used and will therefore be explained in more detail. The canonical ensemble covers all possible states of a system in thermal equilibrium at a constant temperature that interacts with a heat bath. Energy can be exchanged between the system and the heat bath, i.e., the energy is no longer constant in this case. The absolute temperature is introduced as a new constant variable in addition to the number of particles and the volume. The temperature $T(t)$ of an ensemble of particles at a given time can be calculated using Equation 34. Here $k_B$ is the Boltzmann constant, and $N_f$ is the number of degrees of

freedom. $m_i$ is the mass and $v_{i,\alpha}$ the velocity of the individual particles. $\alpha$ denotes the Cartesian component of the velocity vector.

$$T(t) = \frac{1}{k_B N_f} \sum_{i,\alpha} m_i v_{i,\alpha}^2(t)$$

(34)

For the canonical ensemble, it is important to keep the temperature constant. The methods used for this purpose are also called thermostats. In the following, different thermostats and their basic principles will be presented. The first thermostat can be realized by scaling the velocity of the particles, which is therefore called velocity scaling. For this purpose, a scaling factor $\lambda$ is introduced, which scales the velocities of the system. The corresponding mathematical expression for the temperature is given in Equation 35.

$$T^{new} = \frac{1}{k_B N_f} \sum_{i,\alpha} m_i \left(\lambda v_{i,\alpha}(t)\right)^2$$

(35)

The difference between scaled temperature and old temperature can be represented by the following relation:

$$\Delta T = (\lambda^2 - 1)T(t)$$

(36)

The value for the scaling factor can be calculated using the relationship evident in Equation 37. Here, $T_0$ is the desired temperature, and $T(t)$ is the actual temperature of the time step $t$.

$$\lambda = \sqrt{\frac{T_0}{T(t)}}$$

(37)

This thermostat is very simple to implement, but it does not allow fluctuations in temperature. However, these are part of the canonical ensemble, and thus the velocity scaling algorithm cannot sample the canonical ensemble. Another thermostat can be found in the so-called Nose-Poincare method [86,87]. This approach is based on the introduction of additional degrees of freedom, which belong to the heat bath and allow fluctuations of the energy of the system. The basis for this is the work of Nose [88,89], who introduced one additional degree of freedom. This enables sampling analytically from the canonical ensemble in an ergodic system. Based on the work of Nose, different approaches have been developed over the years [86,87,89,90], including the Nose-Poincare Hamiltonian [86]. Here, based on the Hamiltonian defined by Nose [88,89], a new Hamiltonian is constructed without using a Poincare time transformation [91,92]. This new Hamiltonian allows for keeping the temperature constant and

also ensures a correct sampling in the canonical ensemble. Since the derivation goes far beyond the knowledge required here, only the basic principles will be discussed. The Nose-Poincare Hamiltonian is presented in Equation 38. $\tilde{p}_i$ is the canonical momentum of the particles, where the tilde is used to distinguish it from the real momentum. $q$ is the associated position variable. $m_i$ represents the mass of the particles and $Q$ denotes an artificial mass corresponding to an extended position variable $s$. $\pi$ is introduced as canonical momenta associated with the variable $s$. $k_B$ stands for the Boltzmann constant and $T$ states the temperature of the system. $g$ represents the degrees of freedom of the real system. $H_0$ denotes a constant where the value is chosen so that $H$ is zero when evaluated at initial conditions.

$$H = \left( \sum_i \frac{\tilde{p}_i}{2m_i s^2} + V(q) + \frac{\pi^2}{2Q} + gk_B T ln(s) - H_0 \right) s$$

(38)

As evident in Equation 38, additional degrees of freedom are introduced here to implement the exchange with the heat bath. A detailed description of the approach can be found in the work of Bond et al. [86]. The implementation of such an approach for the application in molecular dynamics simulations is very well described in the work of Kleinerman et al. [87].

### 4.2.3 Statistical Quantities

In this chapter, the statistical quantities which can be calculated from molecular dynamics simulations will be described. First of all, it must be stated that the result of such a simulation is a trajectory of positions along the simulation time. However, since, in our case, effective Hamiltonians are used as a basis, the quantities of the simulation are somewhat different. A detailed explanation of the basic quantities for effective Hamiltonians will be given in Chapter 4.3. In contrast to the trajectory of atomic positions, simulations using effective Hamiltonians consider the amplitude of so-called local modes [23,25,26]. This amplitude is directly connected to the atomic displacements by the eigenvectors of the phonon modes. That is, for a supercell of $N$ unit cells, a vector $\boldsymbol{u}(\boldsymbol{R})$ is defined for the amplitude of the local mode in each cell [26,27]. Here, $\boldsymbol{R}$ denotes the position of the unit cell within the supercell. Of course, there are also other variables in this context, but they are not relevant for the calculation of the following properties. Furthermore, the dipole moment can be calculated with the local mode and its amplitude. Here, the Born effective charge $Z^*$ associated with the local mode are used. Thus, for a local unit cell in the supercell, the dipole moment is given by $p(\boldsymbol{R}) = Z^*\boldsymbol{u}(\boldsymbol{R})$. In other words, the result of a simulation is a data set of amplitudes $\boldsymbol{u}_t(\boldsymbol{R})$ in a supercell for each time step $t$ considered. This collection of amplitudes can now be used to calculate statistical quantities for relevant properties. The first important quantity that can be calculated is the

expectation value of the amplitude for the entire unit cell averaged over time. The corresponding mathematical expression is given in Equation 39. Here, the average is first taken over the supercell and then the time average is determined. $N$ is the number of time steps over which is averaged. $N_t$ is the number of time steps and $N$ is the number of unit cells used to calculate the mean value. $\alpha$ denotes the Cartesian component of the amplitude vector.

$$\langle u_\alpha \rangle = \frac{1}{N_t} \sum_t^{N_t} \frac{1}{N} \sum_R^N u_{\alpha,t}(\boldsymbol{R})$$

(39)

This temporal and local mean value now also allows to directly calculate the temporally and spatially averaged dipole moment of the supercell. The corresponding mathematical expression for the Cartesian components of the dipole moment $p_\alpha$ is provided in Equation 40. Here, $N$ is again the number of unit cells in the supercell and $V$ the volume of the entire supercell.

$$p_\alpha = \frac{NZ^*}{V} \langle u_\alpha \rangle$$

(40)

The molecular dynamics simulations performed in this work are mainly aimed at determining the dielectric properties of ferroelectric materials. An essential quantity here is the so-called susceptibility, which specifies the ability of polarization of the material upon application of an electric field. This quantity is a tensor of rank two and can be determined in different ways. The first method used in this work is based on the response of a system when an external field is applied. The relation between polarization and an electric field is given by $\boldsymbol{P} = \chi \epsilon_0 \boldsymbol{E}$. Here, $\epsilon_0$ stands for the vacuum permittivity. This relation can be transformed under the condition that the applied electric field is small, which allows the response of the system and, thus, the susceptibility to be calculated. The expression for this calculation, using the fact that the susceptibility is a rank two tensor, can be found in Equation 41. $\alpha$ and $\beta$ denote the Cartesian components of the vectors. $\langle u_\alpha \rangle_{ext}$ represents the averaged amplitude of the supercell when applying an external electric field $E_{ext,\beta}$. Since in this work, mainly ferroelectric materials are investigated, and these materials can exhibit spontaneous polarization, a reference simulation has to be performed for the determination of the susceptibility as well. The reference simulation is performed without an electric field and then subtracted from the response of the excited simulation. The associated averaged amplitude is denoted by $\langle u_\alpha \rangle_{ref}$. For the further course of this work, this method is also called the direct method and represents the static limit of the susceptibility [31].

$$\chi_{\alpha\beta}^{direct} = \frac{NZ^*\left(\langle u_\alpha \rangle_{ext} - \langle u_\alpha \rangle_{ref}\right)}{V\epsilon_0 E_{ext,\beta}} \tag{41}$$

Another important method for determining the susceptibility can be obtained from the fluctuations of the dipoles. The method uses the correlation functions of the amplitudes to determine the susceptibility, which can be found in Equation 42. Here, $T$ represents the temperature and $k_B$ the Boltzmann constant. This susceptibility can also be referred to as the low-frequency (nearly-static) susceptibility [31] of a system.

$$\chi_{\alpha\beta}^{CF} = \frac{(NZ^*)^2}{V\epsilon_0 k_B T}\left(\langle u_\alpha u_\beta \rangle - \langle u_\alpha \rangle \langle u_\beta \rangle\right) \tag{42}$$

For many applications, the susceptibility as a function of frequency is of interest. Furthermore, this quantity also plays an important role in the investigation of material properties. This way, the response of the system at different excitation frequencies can be studied. The calculation of this quantity requires somewhat more effort. On the one hand, the required equation is a bit more complicated. On the other hand, the simulations have to be adjusted for the desired frequency range as well. Basically, this means that the lower the considered frequency shall be, the longer the underlying simulation has to be performed. For example, if a frequency window of 1 GHz to 1 THz is to be investigated, the simulation must last at least for 1 ns, and the finite time step must be much smaller than 1 ps. From the trajectory, the frequency-dependent susceptibility can then be calculated using Equation 43. Here, $f$ represents the frequency, and $i$ denotes the imaginary unit. The first term in the parenthesis is already known from Equation 42 and gives the nearly static case of the susceptibility. The second term includes two important components. First, the autocorrelation function of the amplitudes and second, the Fourier transform of it. The autocorrelation function describes the correlation of the dipoles with itself at an earlier time and can be easily implemented by using fast Fourier transforms (FFTs). As the Fourier transform of the autocorrelation is also calculated on discrete sampling points, FFT can be applied here as well.

$$\chi_{\alpha\beta}(f) = \frac{(NZ^*)^2}{V\epsilon_0 k_B T}\left[\langle u_\alpha(t)u_\beta(t) \rangle + i2\pi f \int_0^\infty e^{i2\pi f t}\langle u_\alpha(t)u_\beta(0) \rangle dt\right] \tag{43}$$

A quantity related to susceptibility is permittivity. The permittivity is used, for example, to describe the polarizability of a dielectric. Consequently, the electrical capacitance of a material also depends directly on the permittivity. Thus, if the energy storage properties of dielectrics are required, the permittivity provides a straightforward indication of their storage capability.

The permittivity can be calculated by the relation to the susceptibility shown below, where $\delta_{\alpha\beta}$ denotes the Kronecker delta:

$$\epsilon_{\alpha\beta} = \delta_{\alpha\beta} + \chi_{\alpha\beta}$$

(44)

The meaning of the calculated susceptibility or permittivity should also be discussed here. Basically, these quantities are composed of different contributions. The contributions which are included here refer mainly to the ionic polarization. The contributions from the displacements of the electronic shells are indirectly included in the calculation of the local dipole moments via the Born effective charges. The latter was obtained by first-principles calculations in the parameterization of the effective Hamiltonian. However, these contributions are not actively considered in the simulations, and therefore no electronic resonances can be observed in the frequency-dependent susceptibility. For this work, this is of no consequence since the investigated phenomena in the studied systems are caused by the relaxation of dipoles, and these are described very well by the effective Hamiltonian.

## 4.3 Effective Hamiltonians

As already mentioned in the chapter about molecular dynamics simulations, potentials describing the interactions between the particles are needed for the application of such simulations. There is a wide range of different approaches to formulate the interaction mathematically. On an atomic basis, these include pair potentials, many-particle potentials, or so-called force fields. A very well-known pair potential is, for example, the Lennard-Jones [58,59] potential which consists of an attractive and a repulsive term. In the course of time, however, much more complex models have been developed to provide a more accurate description of the interaction. All these potentials are based on an atomistic basis, i.e., the interaction between individual atoms is described. In this work, a fundamentally different approach is used. The approach is based on so-called effective Hamiltonians for the mathematical description of the potential energy surface. The basic idea is the formulation of a potential that does not use the atoms as a basis but a local basis defined by a subspace of the phonon band structure. The associated parameters can be entirely determined by DFT calculations. The foundation for defining such a Hamiltonian was established in the 1990s by the works of Rabe and Waghmare [22] as well as Zhong, Vanderbilt, and Rabe [23]. In the beginning, this approach was a mean-field theory which was later extended to a local-mode theory [25]. Having proved its effectiveness over time, this approach was revised in the works of Nishimatsu et al. [26,27], with certain terms being innovated. In addition to numerous

applications for the simulation of pure [26–28] and substituted systems [29,30,32], work has also been done to increase the accuracy of the description of the potential energy surface. The work of Paul et al. [28] demonstrates the inclusion of anharmonic couplings to higher energy phonons, which have a positive effect on several simulated properties. This work serves as the foundation for the expansion of the approach outlined in this thesis, which incorporates an even greater number of anharmonic terms. Full details on this extension can be found further below and in the enclosed publications. In this chapter, the foundation for effective Hamiltonians via the so-called Lattice Wannier functions shall first be laid. This is followed by the definition of an effective Hamiltonian for the application to perovskite structures. Subsequently, all accompanying energy contributions are explained in detail, and the advantages and disadvantages of this approach are pointed out.

### 4.3.1 Lattice-Wannier Functions

The fundamental idea of effective Hamiltonians is based on the description of the potential energy surface by a local basis set. In principle, a subspace of the phonon band structure is represented where this subspace should contain the contributions important for the lattice distortion. Analogous to electronic Wannier functions, a local basis can also be constructed for phonons. In the following, this local basis set is also called Lattice-Wannier functions (LWF). The derivation here is based on the application of group theory and the decomposition of the ionic displacement space into invariant subspaces. Since the derivation goes far beyond the aim of this paper, only the most important points are explained. For more details, please refer to the valuable work of Rabe and Waghmare [22]. This work also provides the basis for the derivation presented here.

After the decomposition of the ionic displacement space into invariant subspaces spanned by one or more branches of the phonon band structure, basis vectors can be defined for each subregion. These basis vectors combined represent the whole ionic displacement space. The basis vectors can be expressed by real numbers $\xi_{\Lambda l R_i}$ and represent the coordinates of a certain configuration. Here $\Lambda$ represents the index of the band subspace and $n_s$ it the total number of band subspaces. $l$ is the index which gives information about the multiplicity of the subspace and $\boldsymbol{R}_i$ are the lattice vectors. These basis vectors are the analog of electronic Wannier functions. In further consequence, a Taylor expansion of the lattice energy can now be performed. The quadratic term of this expansion around a reference structure can be seen in Equation 45. Here, the conventional coordinates are already replaced by the local basis

functions. The sum runs over all subspaces $n_s$. An important feature of this expansion is that there are no cross-terms between the individual band subspaces.

$$H_{lat}\left(\{\xi_{\Lambda l R_i}\}\right) = \sum_{\Lambda}^{n_s} H_{\Lambda}\left(\{\xi_{\Lambda l R_i}\}\right)$$

(45)

The expression for the contributions of the individual subspaces is provided in Equation 46. Here, the number of branches $n_{\Lambda}$ in each subspace is summed. The second sum is over the number of unit cells $N$. The newly introduced quantity $a_{lil'j}^{\Lambda}$ represents associated coefficients.

$$H_{\Lambda}\left(\{\xi_{\Lambda l R_i}\}\right) = \sum_{l,l'}^{n_{\Lambda}} \sum_{i,j}^{N} a_{lil'j}^{\Lambda} \, \xi_{\Lambda l R_i} \xi_{\Lambda l' R_j}$$

(46)

Based on these equations, an effective Hamiltonian can now be developed. First of all, a subspace must be chosen as a symmetry-invariant subspace. In this invariant subspace, the effective Hamiltonian acts. In principle, this subspace should be chosen as small as possible, but consider all modes that are important for the energetic description of low energy configurations. The choice of the modes usually includes unstable modes, which are responsible for driving the structural phase transitions of the system. In this context, higher orders of the branches must be taken into account in order to describe these transitions correctly. Subsequently, the effective Hamiltonian is assumed to act on a single subspace $\Lambda_0$ and thus the following approximation can be derived for the lattice energy:

$$H_{lat} \approx H_{eff}\left(\{\xi_{\Lambda_0 l R_i}\}\right) + \sum_{\Lambda \neq \Lambda_0} H_{\Lambda}\left(\{\xi_{\Lambda l R_i}\}\right)$$

(47)

An important property of this approximation is that anharmonic terms are present only in the effective part. Furthermore, no cross-terms occur between the selected subspace $\Lambda_0$ and the other subspaces. This has the implication that the degrees of freedom which do not appear in the effective part can be integrated analytically. The question now arises of how an effective Hamiltonian can be derived from this approximation, which can actually be used in a simulation. For this purpose, a Taylor expansion with respect to the symmetry invariant combinations of the basis-functions must be carried out. How such an expansion looks and how an effective Hamiltonian for perovskite structures can be derived from it will be described in detail in the next chapter.

### 4.3.2 General Definition

In the course of this chapter, the fundamental approaches already derived will be used to formulate an effective Hamiltonian. The basis of the first part of the explanations presented here is the work of King-Smith and Vanderbilt [24]. This work shows a systematic derivation of a theoretical approach to describe the potential energy surface by choosing an appropriate local basis. Even if the actual effective Hamiltonians are based on a local-mode theory and the original formalism is a mean-field theory, it does not harm to sketch parts of the original idea first. Further below, a detailed description of actual Hamiltonians and their corresponding energy contributions is given. The starting point of the original formalism is the idea that the lattice energy of a cubic $ABO_3$ perovskite can be described by the 15 displacement coordinates $v_\alpha^\tau$ and six additional strain variables $\eta_i$. Here, $\tau$ denotes the index of the atoms, and $\alpha$ represents the Cartesian component of the displacement. An important property in an inversion symmetric structure is the following relationship: $E(\{\eta_i\}, \{v_\alpha^\tau\}) = E(\{\eta_i\}, \{-v_\alpha^\tau\})$. This relation states that the energy is the same when an atom is displaced in a positive or negative direction from the nominal position. Consequently, the lattice energy of the system can be divided into four principal contributions, as evident in Equation 48. Here, $E_0$ is the energy of the undistorted reference structure. $E^{disp}$ denotes the energy change purely from atomic displacements. $E^{elas}$ accounts for energy contributions exclusively from strain and $E^{int}$ includes all interactions between displacements and strain.

$$E = E^0 + E^{disp}(\{v_\alpha^\tau\}) + E^{elas}(\{\eta_i\}) + E^{int}(\{\eta_i\}, \{v_\alpha^\tau\}) \tag{48}$$

The elastic energy for a cubic system can be simply described up to the second order by the expression given in Equation 49. Here, $B_{11}$, $B_{12}$ and $B_{44}$ are the elastic constants multiplied by the volume of the unit cell.

$$E^{elas}(\{\eta_i\}) = \frac{1}{2}B_{11}(\eta_1^2 + \eta_2^2 + \eta_3^2) + B_{12}(\eta_1\eta_2 + \eta_2\eta_3 + \eta_3\eta_1)$$
$$+ \frac{1}{2}B_{44}(\eta_4^2 + \eta_5^2 + \eta_6^2) \tag{49}$$

As a next step, the energy of the displacements is to be considered. This contribution can be expressed by a Taylor expansion where Equation 50 illustrates the lowest term of the expansion. The matrix $D_{\alpha,\beta}^{\tau,\tau'}$ is the so-called second-order force-constant matrix.

$$E^{disp}(\{v_\alpha^\tau\}) \approx \frac{1}{2} \sum_{\tau,\tau',\alpha,\beta} \frac{\partial E}{\partial v_\alpha^\tau \partial v_\beta^{\tau'}} v_\alpha^\tau v_\beta^{\tau'} = \frac{1}{2} \sum_{\tau,\tau',\alpha,\beta} D_{\alpha,\beta}^{\tau,\tau'} v_\alpha^\tau v_\beta^{\tau'}$$

$$(50)$$

The force-constant matrix can now be used to formulate an eigenvalue problem with eigenvalues $\lambda(j)$ and eigenvectors $\xi_\alpha^\tau(j,\gamma)$, as stated in Equation 51. The index $j$ numbers the solutions of the eigenvalue problem. This eigenvalue problem should not be confused with the solution of the dynamical matrix, where, unlike here, the masses are also considered. The eigenvectors of the eigenvalue problem presented in Equation 51 represent, in principle, the local basis functions from the previous chapter. Therefore, they are of utmost importance for the construction of the effective Hamiltonian.

$$\sum_{\beta\tau'} D_{\alpha,\beta}^{\tau,\tau'} \xi_\beta^{\tau'}(j,\gamma) = \lambda(j)\xi_\alpha^\tau(j,\gamma)$$

$$(51)$$

To continue with the derivation of the formalism, another important relation has to be established first. The displacements $v_\alpha^\tau$ can be expressed by the amplitudes $u_\alpha^j$ of the eigenmodes where the relation is made via the eigenvectors $\xi_\alpha^\tau(j,\alpha)$. The corresponding mathematical expression is stated below:

$$u_\alpha^j = \sum_\tau \xi_\alpha^\tau(j,\alpha) v_\alpha^\tau$$

$$(52)$$

This relation can now be used to express the displacement energy in a straightforward manner by the eigenvalues and amplitudes as presented in Equation 53.

$$E^{disp} = \frac{1}{2} \sum_j \lambda(j) \sum_\alpha u_\alpha^j u_\alpha^j$$

$$(53)$$

Equations 52 and 53 lead to an important point that was already mentioned in the previous chapter, namely, which subspace of phonons should be used for the construction of the Hamiltonian. For this purpose, the phonon modes present in the cubic $ABO_3$ structure must first be discussed. Due to the cubic symmetry, the solutions of the eigenvalue problem reduce from 15 to 5 eigenvalues and eigenvectors. These five eigenvalues are degenerate and therefore yield the same values for the Cartesian directions $(x,y,z)$. The occurring phonon modes can be characterized by their symmetry. One of the five degenerate modes is the acoustic mode with zero frequency in the Brillouin zone center. It is followed by a mode with $\Gamma_{25}$ symmetry. Finally, there are three modes, with $\Gamma_{15}$ symmetry. Without further information, it is difficult to predict which of these phonon modes have the largest influence on structural distortions of the

system. Experimentally it is observed in such systems that the $\Gamma_{15}$ modes are responsible for ferroelectric transitions [24]. If one relies on pure theory, DFT calculations can help. For example, if $BaTiO_3$ is found that one of these $\Gamma_{15}$ modes has an imaginary frequency, indicating instability of the system [23,24,28]. It also shows an overlap of the eigenvector with the structural changes in the system [28]. Such an imaginary frequency mode is also often called a soft-mode. Consequently, this mode can be identified as the main cause of structural deformation and thus used as the basis for developing the effective Hamiltonian. For the theoretical description of the model, however, the choice of the mode plays a subordinate role but only finds its importance in the parameterization by DFT.

To continue with the derivation of the effective Hamiltonian, one of these modes $\lambda_0$ is formally selected, and thus the energy of the displacements can be rewritten and expanded via the mathematical expressions of $\kappa = \frac{1}{2}\lambda_0$ and $u_\alpha = u_\alpha^0$. The energy of the displacements developed up to the fourth order in $u_\alpha$ can now be expressed by Equation 54. Third-order terms are forbidden due to symmetry. Here, the new parameters $\alpha$ and $\beta$ were introduced, which are in relation to the higher-order derivatives of the energy by Equations 55 and 56.

$$E^{disp}(\{u_\alpha\}) = \kappa u^2 + \alpha u^4 + \gamma(u_x^2 u_y^2 + u_y^2 u_z^2 + u_z^2 u_x^2) \tag{54}$$

$$\alpha = \frac{1}{24} \frac{\partial^4 E}{\partial u_x^4}\bigg|_0 \tag{55}$$

$$\gamma = \frac{1}{12}\left(3 \frac{\partial^4 E}{\partial u_x^2 \partial u_y^2}\bigg|_0 - \frac{\partial^4 E}{\partial u_x^4}\bigg|_0\right) \tag{56}$$

The remaining term to be explained in Equation 48 is the interaction between displacements and deformation, also called strain-phonon coupling. This term may also include any couplings to other phonons. The general way to account for this term is to calculate the magnitudes of $\tilde{\eta}$ and $\tilde{u}$ which minimize the total energy. The renormalized total energy of the system is denoted by $\tilde{E}(\{u_\alpha\})$. It can be shown that the decisive term for minimization is the lowest-order term in $E^{int}$. This allows a matrix equation to be set up as presented in Equation 57. Here, both the elastic constants $B_{ij}$ and the coupling terms $B_{i\alpha\beta}$ find application. Furthermore, it can be shown

that due to the cubic symmetry, only three non-zero elements can occur. These elements are the parameters $B_{1xx}$, $B_{1yy}$ and $B_{4yz}$.

$$\sum_j B_{ij}\tilde{\eta}_i + \frac{1}{2}\sum_{\alpha\beta} B_{i\alpha\beta}u_\alpha u_\beta = 0 \tag{57}$$

By solving the above matrix equation, a new term for the lattice energy can be formulated as presented in Equation 58. For the derivation of this equation, reference is made here to the work of King-Smith and Vanderbilt [24]. Furthermore, this equation can be taken as a starting point for further reformulation of the lattice energy as a function of known quantities. The lattice energy can thus be written as a function of the displacement energy and quantities such as the bulk modulus or shear moduli. The corresponding mathematical expression can be found in Equation 16 in Ref. [24].

$$\tilde{E}(\{u_\alpha\}) = E^0 + E^{disp}(\{u_\alpha\}) - \frac{1}{8}\sum_{ij}\sum_{\alpha\beta mn} u_\alpha u_\beta B_{i\alpha\beta}[B^{-1}]_{ij} B_{jmn}u_m u_n \tag{58}$$

In the following, an interesting feature can be exploited to further simplify the lattice energy. The corrections which become effective by the contributions of the interaction energy have the same form as the displacement energy up to the fourth order. Therefore, the associated parameters can be summarized, and a final form of the lattice energy is obtained in Equation 59. This energy represents the energy of the lattice renormalized by strain-phonon coupling. Here, the new parameters $\alpha'$ and $\gamma'$ were introduced, which are related to the already known parameters $\alpha$ and $\gamma$ via Equations 60 and 61. The additional parameters in these relations are, for example, the bulk modulus ($B$), shear moduli ($\nu_t$,$\nu_r$) and the analogous expressions which can be defined for the interaction between strain and phonons ($C, \mu_t, \mu_r$). A detailed listing and description of the individual parameters can be found in Ref. [24].

$$\tilde{E}(\{u_\alpha\}) = E^0 + \kappa u^2 + \alpha'u^4 + \gamma'\left(u_x^2 u_y^2 + u_y^2 u_z^2 + u_z^2 u_x^2\right) \tag{59}$$

$$\alpha' = \alpha - \frac{1}{24}\left(\frac{C^2}{B} + 4\frac{\nu_t^2}{\mu_t}\right) \tag{60}$$

$$\gamma' = \gamma + \frac{1}{2}\left(\frac{\nu_t^2}{\mu_t} - \frac{\nu_r^2}{\mu_r}\right) \tag{61}$$

The expression presented in equation 59 is the final lattice energy of the effective Hamiltonian defined by King-Smith and Vanderbilt [24] for the description of $ABO_3$ perovskites. However, this formulation is based on a mean-field theory and is not, for example, designed for a supercell with different amplitudes of the local modes. In the following, this formalism was used as the basis for the development of a local mode theory. The first revision to such a theory was done already one year later by Zhong, Vanderbilt, and Rabe [23]. Another important work for the reformulation was published by Waghmare and Rabe [25] in 1997. Here, the theory was explained in detail and expanded, with the parameterization for $PbTiO_3$ demonstrated as an example. After many publications based on such effective Hamiltonians, the formalism was revised again in 2008 by Nishimatsu et al. [26], and a freely available software [26,27,93] was released that allows simulation with such models. In this thesis, this effective Hamiltonian of Nishimatsu et al. [26,27] is predominantly used, and therefore, the related theory will be explained in detail.

The starting point for the derivation of the local-mode theory is the description of the lattice energy from Equation 59. In this equation, the lattice energy was derived via a Taylor expansion up to the fourth order. The final energy term also includes renormalization due to the interaction between strain and displacements. Furthermore, the chosen variables are given by $\{u_\alpha\}$, where here the bracket $\{\}$ represents a set of amplitudes with Cartesian directions $x$, $y$, and $z$. As only the amplitudes of a unit cell are used here, we also speak of a mean-field theory. To develop a local-mode theory from this approach, the selected variables must be defined for a number of unit cells in a supercell. For this purpose, the bracket $\{\}$ is used again, where $\{\boldsymbol{u}\}$ denotes a set of amplitudes defined for each of the unit cells within a supercell. The $\boldsymbol{u}$ is written in bold because it is an amplitude vector $\boldsymbol{u}$ for each unit cell. The total energy of the system defined for a supercell using the newly introduced variables can be expressed as presented in Equation 62. The variables $\eta_i$ are the strain components of the supercell in Voigt notation. The energy contributions entering Equation 62 can be described as follows: $V^{self}$ is the so-called local-mode self-energy. $V^{dpl}$ denotes the dipole-dipole interaction. $V^{short}$ represents the short-range interaction between the local-modes. $V^{elas}$ contains all strain-related energies and $V^{int}$ accounts for interactions between local modes and local strains. For further details on the derivation of Equation 62, reference is made here to the work of Zhong, Vanderbilt, and Rabe [23], as well as the work of Nishimatsu et al. [26]. The individual energy contributions are also described in detail in the following chapters.

$$E^{tot} = V^{self}(\{\boldsymbol{u}\}) + V^{dpl}(\{\boldsymbol{u}\}) + V^{short}(\{\boldsymbol{u}\}) + V^{elas}(\eta_1, \dots, \eta_6)$$
$$+ V^{int}(\{\boldsymbol{u}\}, \eta_1, \dots, \eta_6) \tag{62}$$

Due to the importance, the relation between the amplitudes of the local modes and the displacements of the atoms shall be pointed out again. This relation is given by the eigenvectors of the respective mode, whereby the relation in Equation 63 can be stated. Here $\boldsymbol{\nu}_\alpha$ is the displacement vector of the atoms, $u_\alpha$ the amplitude and $\boldsymbol{\xi}_\alpha$ the corresponding eigenvector. $\alpha$ denotes here again the Cartesian direction of the vectors. It is self-explanatory that this definition was derived for the $ABO_3$ structure. The index of the eigenvector components indicates the value for the respective atoms at the A-site, the B-site, and the three oxygen positions.

$$\boldsymbol{\nu}_\alpha = u_\alpha \begin{pmatrix} \xi_\alpha^A \\ \xi_\alpha^B \\ \xi_\alpha^{O_1} \\ \xi_\alpha^{O_2} \\ \xi_\alpha^{O_3} \end{pmatrix} \tag{63}$$

The model in Equation 62 allows the description of the potential energy surface of the system under investigation and can be used quite straightforwardly for Monte Carlo simulations. In this work, however, molecular dynamics simulations are to be applied, and therefore, a suitable formalism of an effective Hamiltonian defined by Nishimatsu et al. [26,27] is described in further detail. The corresponding expression of the adopted Hamiltonian is presented in Equation 64. The Hamiltonian is a function of a set of local-mode amplitudes $\{\boldsymbol{u}\}$ and the strain variables $\eta_i$ in Voigt notation. In addition, the variables $\boldsymbol{w}$ have been introduced, with a set of these variables defined for each unit cell in the supercell $\{\boldsymbol{w}\}$. These dimensionless variables are used to account for local strains. A detailed description of these variables can be found in Chapter 4.3.7 about elastic energies. $\boldsymbol{R}$ represents a translational vector between the unit cells within the supercell. $\alpha$ indicates the Cartesian components of the individual vectors. $M_i^*$ denote effective masses associated with the local-mode $\boldsymbol{u}$ and variables $\boldsymbol{w}$. $Z^*$ is the Born effective charge corresponding to the local-mode $\boldsymbol{u}$. Furthermore, kinetic energies for the local-mode $\boldsymbol{u}$ and the dimensionless variables $\boldsymbol{w}$ were also introduced in Equation 64. The remaining energy contributions are analogous to those defined in Equation 62, but the elastic energies and the interaction energy have been divided into homogeneous and inhomogeneous components. The last term is employed to enable the application of an external electric field. All associated variables, parameters, and the details of the individual energy contributions are discussed in depth in the following chapters.

$$H^{eff} = \frac{M^*_{dipole}}{2} \sum_{R,\alpha} \dot{u}^2_\alpha(\boldsymbol{R})$$

$$+ \frac{M^*_{acoustic}}{2} \sum_{R,\alpha} \dot{w}^2_\alpha(\boldsymbol{R}) + V^{self}(\{\boldsymbol{u}\}) + V^{dpl}(\{\boldsymbol{u}\})$$

$$+ V^{short}(\{\boldsymbol{u}\}) + V^{elas,homo}(\eta_1, \dots, \eta_6) + V^{elas,inho}(\{\boldsymbol{w}\})$$

$$+ V^{coupl,homo}(\{\boldsymbol{u}\}, \eta_1, \dots, \eta_6) + V^{coupl,inho}(\{\boldsymbol{u}\}, \{\boldsymbol{w}\})$$

$$- Z^* \sum_R \epsilon \cdot u(\boldsymbol{R}) \tag{64}$$

The effective Hamiltonian from Equation 64 builds on all previously discussed foundations and represents the basis for all following simulations as well as extensions. Included in this formulation is the choice of a local basis by the selected eigenvectors associated with the used local-mode variable $\boldsymbol{u}$. Furthermore, for the derivation, certain symmetry conditions arising from the $ABO_3$ structure were exploited. The applicability of the formalism also depends strongly on the considered systems and must be examined for each case individually. The most important point, however, is the parameterization of the effective Hamiltonian by first-principles calculations based on DFT calculations. Only a complete and reasonable parameter set allows an accurate description of the underlying system. The parameterization is a major part of this theory and is therefore discussed in detail in chapters on parameterization as well as in the enclosed publications.

### 4.3.3 Kinetic Energies

The first two terms in Equation 64 are the kinetic energies of the local-mode $\boldsymbol{u}$ and of the dimensionless variable $\boldsymbol{w}$. The quantities entering this equation are the derivatives of the respective variables with respect to time, which is implied by the dot in the accent. Furthermore, the corresponding effective masses $M^*_{dipole}$ and $M^*_{acoustic}$ were also introduced. The masses basically refer to the displacement of the atoms according to the respective eigenvectors and represent an effective mass of the corresponding modes. The calculation of the effective mass for the local mode can be accomplished as presented in Equation 65. Here, the quantities $m_A$, $m_B$ and $m_O$ are the atomic masses of the respective A-site and B-site atoms and the mass of the oxygen atoms. These masses are multiplied by the respective squared components of the associated eigenvector. Due to the cubic symmetry, the eigenvectors are equivalent in their respective Cartesian directions, denoted by $\alpha$.

$$M_{dipole}^* = m_A(\xi_\alpha^A)^2 + m_B(\xi_\alpha^B)^2 + m_O\left(\xi_\alpha^{O_1}\right)^2 + m_O\left(\xi_\alpha^{O_2}\right)^2 + m_O\left(\xi_\alpha^{O_3}\right)^2$$

(65)

The calculation of the effective mass $M_{acoustic}^*$ for the dimensionless variables $\boldsymbol{w}$ is to be carried out analogously. However, here the eigenvector for the acoustic branch in the center of the Brillouin zone has to be used, which in this case, represents a simple translation. These kinetic energies are required for use in MD simulations [26,27] but are not needed in Monte Carlo simulations as originally conducted by Zhong, Vanderbilt, and Rabe [23].

### 4.3.4  Local-Mode Self-Energy

The next key energy contribution is the so-called local-mode self-energy. This energy is comparable with the displacement energy from Equation 54. However, here, a change from a mean-field theory to a local-mode theory is adopted, and thus the local-mode self-energy is defined for each unit cell in the supercell. In principle, this energy represents the isolated local displacements of the atoms with respect to the initial position, which in this case is the cubic phase of the $ABO_3$ structure. In order to describe the system accurately, this energy contribution should include both harmonic and anharmonic terms. The first and consequently often used definition of this energy was provided by the fourth-order theory of King-Smith and Vanderbilt [24]. A reformulation into a local mode theory was conducted shortly thereafter by Zhong, Vanderbilt, and Rabe [23]. Over the years, however, it became apparent that for many cases, the description using polynomials up to the fourth order was not sufficient. Therefore, in 2010, the local-mode self-energy was extended by further terms up to the eighth order in $\boldsymbol{u}$ in the work of Nishimatsu et al. [27]. The corresponding mathematical expression for the local-mode self-energy is given in Equation 66. Here, the sum over each unit cell is used to determine the total energy resulting from the isolated local modes. To note, due to the cubic reference structure, only even terms have a non-vanishing contribution. Furthermore, additional parameters $\kappa_2$, and $k_1$ to $k_4$ were introduced to the already known parameters $\alpha$ and $\gamma$. The parameter $\kappa_2$ is related to the parameter $\kappa$ but is calculated by a correction during parameterization in order not to change the potential energy surface. A detailed description of how this parameter is calculated can be found in Chapter 4.3.6 on short-range interaction. The local-mode self-energy represents a central point in this thesis and will be discussed further in detail in the chapters on parameterization. Additionally, in the following subchapter and in the attached Publication 2, the possibility of extending this energy for additional phonon modes is also shown, and the implications for the quality of the potential energy surface are discussed.

$$V^{self}(\{\boldsymbol{u}\}) = \sum_{\boldsymbol{R}} \Big\{ \kappa_2 u^2(\boldsymbol{R}) + \alpha u^4(\boldsymbol{R})$$

$$+ \gamma \big[ u_y^2(\boldsymbol{R}) u_z^2(\boldsymbol{R}) + u_z^2(\boldsymbol{R}) u_x^2(\boldsymbol{R}) + u_x^2(\boldsymbol{R}) u_y^2(\boldsymbol{R}) \big] + k_1 u^6(\boldsymbol{R})$$

$$+ k_2 \big( u_x^4(\boldsymbol{R}) * \big[ u_y^2(\boldsymbol{R}) + u_z^2(\boldsymbol{R}) \big] + u_y^4(\boldsymbol{R}) * \big[ u_z^2(\boldsymbol{R}) + u_x^2(\boldsymbol{R}) \big]$$

$$+ u_z^4(\boldsymbol{R}) * \big[ u_x^2(\boldsymbol{R}) + u_y^2(\boldsymbol{R}) \big] \big) + k_3 u_x^2(\boldsymbol{R}) u_y^2(\boldsymbol{R}) u_z^2(\boldsymbol{R})$$

$$+ k_4 u^8(\boldsymbol{R}) \Big\} \tag{66}$$

### 4.3.4.1 Expansion for Higher-Energy Phonons

In this chapter, an extension of the local-mode self-energy developed in this thesis will be explained. A detailed description of the derivation as well as the application of the approach for BaTiO$_3$ can be found in Publication 2. However, for the completeness of the theoretical part, the basic concept shall be explained here. The idea for an extension was based on the work of Paul et al. [28], which contains a detailed study of anharmonic couplings. In [28], it is demonstrated that an extension of the local-mode self-energy leads to an improved description of the potential energy surface and, thus, to improved results of the simulations compared to experiments. Basically, in their paper, the local-mode self-energy was extended for higher energy phonons, although the extension was only done up to the 2$^{nd}$ order for these additional phonons. In this thesis, a more general approach was developed, and a variety of anharmonic couplings to higher energy phonons are included. The fundamental basis for the expansion is the local-mode self-energy from Equation 66. This equation can be used to evaluate the energy in the high-symmetric directions <001>,<011>, and <111> by substituting the expressions $\boldsymbol{u} = (0,0,u)$, $\boldsymbol{u} = (0,u,u)$ and $\boldsymbol{u} = (u,u,u)$ for the local amplitude $\boldsymbol{u}$. The local-mode self-energy in <001> directions reads as stated below:

$$E_{001}(u) = \kappa u^2 + \alpha u^4 + k_1 u^6 + k_4 u^8 \tag{67}$$

It follows the local-mode self-energy in <011> direction:

$$E_{011}(u) = \kappa u^2 + \left( \alpha + \frac{1}{4}\gamma \right) u^4 + \left( k_1 + \frac{1}{4}k_2 \right) u^6 + k_4 u^8 \tag{68}$$

Finally, the corresponding expression for the energy in <111> direction:

$$E_{111}(u) = \kappa u^2 + \left( \alpha + \frac{1}{3}\gamma \right) u^4 + \left( k_1 + \frac{2}{9}k_2 + \frac{1}{27}k_3 \right) u^6 + k_4 u^8 \tag{69}$$

The above equations represent a central point for the parameterization by first-principles calculations and are used to determine the associated parameters by fitting. So far, however,

these equations are a function purely of the local amplitude $u$, whereas, in the parameterization, a suitable phonon mode must be chosen as the basis. In many cases, the parameterization and formulation via one phonon mode is already a very good approximation for the description of the potential energy surface. However, as described in detail in Publication 2, it can be shown that other phonon modes can also contribute a non-negligible amount to the structural phase transitions. In this case, the inclusion of these additional modes is essential for an improved description of the phase transitions. In the following, the local-mode self-energy shall be expanded to include two additional phonon modes, where the amplitudes of these modes are denoted by $v_1$ and $v_2$. That means an expression for the energy $E_{001}^{anh}(u, v_1, v_2)$ must be found, which includes the three local mode amplitudes $u$, $v_1$ and $v_2$. In this thesis, the derivation is concentrated on the <001> direction, whereas the other directions are to be considered analogously. This also implies that the local amplitudes ($u$, $v_1$ and $v_2$) in the subsequent derivation are not vectors but represent components in the <001> direction. For the expansion of the local-mode self-energy, a multivariate Taylor expansion is now applied, where $u$ is expanded up to the 8th order and $v_1$ and $v_2$ up to the 6th order. The corresponding mathematical expression can be seen in Equation 70, where the expansion is done around a reference of $u_0$, $v_{1,0}$ and $v_{2,0}$, respectively. The reference can be chosen as for the conventional effective Hamiltonian with the perfect cubic $ABO_3$ structure.

$$E_{001}^{anh}(u, v_1, v_2) =$$

$$\sum_{n_1}^{8} \sum_{n_2}^{6} \sum_{n_3}^{6} \frac{(u - u_0)^{n_1}(v_1 - v_{1,0})^{n_2}(v_2 - v_{2,0})^{n_3}}{n_1! \, n_2! \, n_3!} \left( \frac{\partial^{n_1+n_2+n_3} E(u, v_1, v_2)}{\partial u^{n_1} \partial v_1^{n_2} \partial v_2^{n_3}} \right) (u_0, v_{1,0}, v_{2,0})$$

$$(70)$$

The evaluation of this multivariate Taylor expansion can be found in the Supplemental Material of Publication 2. Here it becomes clear that the evaluation contains all mathematical terms, also the ones that are forbidden due to symmetry. The reason for this is the choice of the cubic reference, which does not allow odd orders of the summed powers of the local amplitudes. An alternative derivation of the expanded local-mode self-energy in <001> direction can be found in the ISOTROPY tool [94]. This allows the automatic output of polynomials describing order parameters when the correct symmetries are entered. The order parameters, in this case, are the local amplitudes of the selected modes. Both methods can be used to derive an expression for the local-mode self-energy, including just allowed terms, as shown in Equation 71. The description of the local amplitudes $u$ was restricted to the parameters $c_1$ to $c_4$ to be consistent with the definition from Equation 67. It follows the parameters $a_1$ to $a_{12}$ which contain the terms for the phonon mode $v_1$ as well as the anharmonic couplings to individual other modes.

Analogously, the parameters $b_1$ to $b_{12}$ are defined for the phonon mode $v_2$. The parameters $d_1$ to $d_{22}$ describe the couplings between the three included phonon modes. It becomes clear that a significant number of parameters are required to describe the local-mode self-energy under the chosen conditions. For low orders, these parameters can be determined quite easily by explicit first-principles calculations [28]. For higher orders, however, this endeavor becomes increasingly difficult or impossible. In this thesis, therefore, an approach was pursued to allow all parameters to be determined at once by fitting to a large set of first-principles calculations. The details of this approach, as well as its application to $BaTiO_3$, can be found in Publication 2.

$$
\begin{aligned}
E_{001}(u, v_1, v_2) = {} & c_0 + c_1 u^2 + c_2 u^4 + c_3 u^6 + c_4 u^8 + a_1 u v_1 + a_2 v_1^2 + a_3 u^3 v_1 \\
& + a_4 u^2 v_1^2 + a_5 u v_1^3 + a_6 v_1^4 + a_7 u^5 v_1 + a_8 u^4 v_1^2 \\
& + a_9 u^3 v_1^3 + a_{10} u^2 v_1^4 + a_{11} u v_1^5 + a_{12} v_1^6 + b_1 u v_2 + b_2 v_2^2 \\
& + b_3 u^3 v_2 + b_4 u^2 v_2^2 + b_5 u v_2^3 + b_6 v_2^4 + b_7 u^5 v_2 + b_8 u^4 v_2^2 \\
& + b_9 u^3 v_2^3 + b_{10} u^2 v_2^4 + b_{11} u v_2^5 + b_{12} v_2^6 + d_1 v_1 v_2 + d_2 u^2 v_1 v_2 \\
& + d_3 u v_1^2 v_2 + d_4 u v_1 v_2^2 + d_5 v_1^3 v_2 + d_6 v_1^2 v_2^2 + d_7 v_1 v_2^3 \\
& + d_8 u^4 v_1 v_2 + d_9 u^3 v_1^2 v_2 + d_{10} u^3 v_1 v_2^2 + d_{11} u^2 v_1^3 v_2 \\
& + d_{12} u^2 v_1^2 v_2^2 + d_{13} u^2 v_1 v_2^3 + d_{14} u v_1^4 v_2 + d_{15} u v_1^3 v_2^2 \\
& + d_{16} u v_1^2 v_2^3 + d_{17} u v_1 v_2^4 + d_{18} v_1^5 v_2 + d_{19} v_1^4 v_2^2 + d_{20} v_1^3 v_2^3 \\
& + d_{21} v_1^2 v_2^4 + d_{22} v_1 v_2^5
\end{aligned}
\tag{71}
$$

In summary, Equation 71 is an expansion of the local-mode self-energy of the effective Hamiltonian by two additional phonon modes. Subsequently, all terms which depend on $u$ would have to be extended for the additional modes $v_1$ and $v_2$. However, careful tests showed that certain contributions, like the coupling of $v_1$ and $v_2$ with strain are only minor compared to the coupling of $u$ with strain. Therefore, as a good approximation, the corresponding extension can be omitted. Furthermore, the long-range interaction would also have to be modified for the new modes, but even in this case, the contribution obtained is negligible. Publication 2 and the associated attached Supplemental Material can be consulted to justify these assumptions. Rather, in the course of the development of this extension, emphasis was put on preserving the efficiency of the effective Hamiltonian. That is, a big advantage of such simulations is the speed as well as the thereby favorable computational effort. In order to not lose this advantage, the following approach was chosen for the inclusion of the couplings to the additional phonon modes. First, the local-mode self-energy from Equation 71 is parameterized by first-principles calculations. Then, the amplitudes of $v_1$ and $v_2$ which minimize the total energy to a given $u$ are determined. Substituting the minimizing amplitudes $v_{1,min}(u)$ and

$v_{2,min}(u)$ into Equation 71 lead to a new term for the local-mode self-energy $E_{001}\big(u, v_{1,min}(u), v_{2,min}(u)\big)$, which again is a function purely depending on the local amplitude $u$. This new expression, which indirectly contains a large number of anharmonic couplings, can now be used in the conventional effective Hamiltonian without further modification. It should also be mentioned that, due to the complexity of Equation 71, an analytical solution for the minimizing amplitudes $v_{1,min}(u)$ and $v_{2,min}(u)$ is not feasible, and thus, numerical minimization must be performed. This numerical minimization can be done on discrete amplitudes of $u$, and subsequently, the local-mode self-energy from Equation 67 must be re-fitted. Also, on this topic, reference is made here to Publication 2, where such a numerical approach is applied. Furthermore, the effects of the extension on phase transitions and dielectric properties are also discussed in this publication.

### 4.3.5 Long-Range Interaction

The long-range interactions [23,26,27] between the individual unit cells will be discussed next. To lay the foundation for the physical description of this quantity, it must first be repeated that the fundamental unit of the effective Hamiltonian is the unit cell. The central variable defined for each unit cell is the amplitude of the local mode $\boldsymbol{u}$. Through the amplitude of the local mode, the dipole moment of the unit cell can be directly calculated via the Born effective charges $Z^*$. That is, for the long-range interaction, the interaction between dipoles in the supercell becomes decisive. The associated dipole-dipole interaction can be expressed by Equation 72. Here, the sums over $i$ and $j$ run respectively over the total number of unit cells in the supercell. The subscripts $\alpha$ and $\beta$ indicate the Cartesian directions of the amplitude vectors.

$$V^{dpl}(\{\boldsymbol{u}\}) = \frac{1}{2} \sum_{i,\alpha,j,\beta} u_\alpha(\boldsymbol{R}_i) \Phi_{\alpha\beta}(\boldsymbol{R}_{ij}) u_\beta(\boldsymbol{R}_j) \tag{72}$$

The remaining term in Equation 72 is the interaction matrix which is defined in Equation 73. Here, $Z^*$ is the Born effective charge associated with the local mode $\boldsymbol{u}$. $\epsilon_\infty$ denotes the optical dielectric constant. $\delta_{\alpha\beta}$ represents the Kronecker delta. Furthermore, $\boldsymbol{R}_{ij}$ are translational vectors between single unit cells within the supercell. Finally, $\boldsymbol{n}$ represent translational vectors between the supercells. The expressions $\big(\boldsymbol{R}_{ij} + \boldsymbol{n}\big)_{\alpha,\beta}$ have to be normalized.

$$\Phi_{\alpha\beta}(\boldsymbol{R}_{ij}) = \frac{Z^{*2}}{\epsilon_\infty} \sum_n \frac{\delta_{\alpha\beta} - 3\big(\boldsymbol{R}_{ij} + \boldsymbol{n}\big)_\alpha \big(\boldsymbol{R}_{ij} + \boldsymbol{n}\big)_\beta}{\big|\boldsymbol{R}_{ij} + \boldsymbol{n}\big|^3} \tag{73}$$

The Born effective charge $Z^*$ associated with the local mode $\boldsymbol{u}$ can be calculated using the eigenvector $\boldsymbol{\xi}_\alpha$ and the respective effective charges of the atoms $Z_i^*$ as shown in Equation 74. The choice of the Cartesian direction $\alpha$ is redundant since, due to the cubic symmetry, the effective charge is the same in all Cartesian directions.

$$Z^* = Z_A^*\xi_\alpha^A + Z_B^*\xi_\alpha^B + Z_{O_1}^*\xi_\alpha^{O_1} + Z_{O_2}^*\xi_\alpha^{O_2} + Z_{O_3}^*\xi_\alpha^{O_3} \tag{74}$$

It is obvious from the above equations that the dipole-dipole interaction can be calculated quite straightforwardly by matrix multiplication. The interaction matrix contains no variables as well as the translation vectors are fixed in the given case. This means that the matrix can be calculated at the beginning of the simulation and does not change consecutively. However, the calculation of the interaction matrix is increasingly complex due to the sum over different supercells. The problem represents the convergence of the matrix elements to be computed given by the sum over the supercells. In theory, this sum would have to be continued infinitely since periodic boundary conditions are used for the systems considered here. A widely used method to accurately and faster calculate the interaction matrix for such boundary conditions is found in the Ewald summation [95,96]. This method uses a trick that allows splitting the interactions into two parts. The first part is the so-called real space contribution, and the second part is the reciprocal space contribution. The real space contribution contains the short-range terms which converge very fast in real space. In contrast, the reciprocal contribution contains all parts of the long-range interaction. Since this term is evaluated in the reciprocal space, all long ranges are to be found at small $\boldsymbol{k}$-vectors due to the definition. Here, the $\boldsymbol{k}$-vector represents a reciprocal lattice vector. Accordingly, the $\boldsymbol{k}$-vectors are summed and the sum again converges quickly. For more details on the long-range interaction in effective Hamiltonians as well as the implementation of it, the reader is referred to the work of Nishimatsu et al. [26,27].

### 4.3.6 Short-Range Interaction

The next energy contribution for the effective Hamiltonian is the so-called short-range interaction [23,26,27]. This energy gives the interaction of adjacent unit cells as a function of local modes. Considering the total energy only as a function of the local modes, the energy contributions can be characterized as follows. The local-mode self-energy gives the isolated displacement energy at the zone center. The long-range and short-range interactions give the contributions to the total energy away from the zone center. Combining these energies, the phonon band structure can be reproduced for the chosen local basis. More details will be given in the course of this chapter. Nevertheless, the short-range energy can be expressed by Equation 75, where again, the local amplitudes $\boldsymbol{u}$ are used. Here, the sum over $i$ includes all unit cells in

the supercell. The sum for $j$ runs over the adjacent unit cells up to the third nearest neighbor shell. The sums exclude terms with the same index since these contributions are taken into account in the local-mode self-energy. The associated parameters are expressed by the coupling matrix $J_{ij,\alpha\beta}$.

$$V^{short}(\{\boldsymbol{u}\}) = \frac{1}{2}\sum_{i\neq j}\sum_{\alpha\beta}u_\alpha(\boldsymbol{R}_i)J_{ij,\alpha\beta}u_\beta(\boldsymbol{R}_j)$$

(75)

In order to calculate and understand the entries of the coupling matrix $J_{ij,\alpha\beta}$, Figure 6 can be considered. Here new parameters $j_1$-$j_7$ have been introduced, which will be called inter-site parameters in the course of this thesis. Each of these parameters represents a certain arrangement of adjacent local modes up to the third nearest neighbor shell. For example, the first parameter $j_1$ indicates the interaction between local modes when they are direct neighbors and have a parallel displacement. However, the displacement of the local modes is perpendicular to the connection vector. Consequently, such a parameter can be defined for several different configurations.
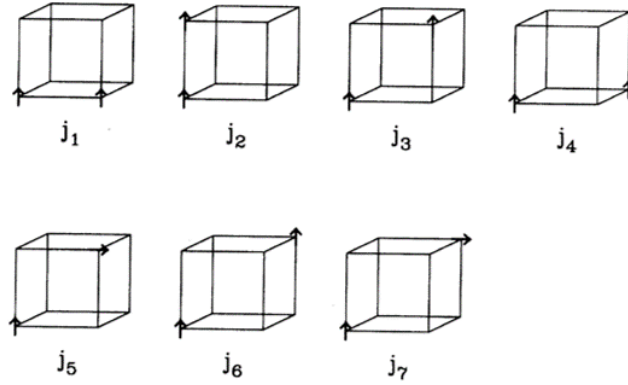


*Figure 6. Schematic diagram to illustrate how the individual inter-site parameters $j_1$-$j_7$ are defined* [23]. *The associated parameters allow a description up to the third nearest neighbor shell.*

These inter-site parameters $j_1$-$j_7$ can now be used to construct the coupling matrix $J_{ij,\alpha\beta}$. A different mathematical expression is needed for the different shells of the neighbors. For the interactions between unit cells which are directly next to each other (first nearest neighbor shell), the following relation can be formulated:

$$J_{ij,\alpha\beta} = \left(j_1 + (j_2 - j_1)|\hat{R}_{ij,\alpha}|\right)\delta_{\alpha\beta}$$

(76)

For the second nearest neighbor shell, the relation reads:

$$J_{ij,\alpha\beta} = \left(j_4 + \sqrt{2}(j_3 - j_4)\left|\hat{R}_{ij,\alpha}\right|\right)\delta_{\alpha\beta} + 2j_5\hat{R}_{ij,\alpha}\hat{R}_{ij,\beta}\left(1 - \delta_{\alpha\beta}\right) \tag{77}$$

Finally, the entries of the coupling matrix for the third nearest neighbor shell are given by:

$$J_{ij,\alpha\beta} = j_6\delta_{\alpha\beta} + 3j_7\hat{R}_{ij,\alpha}\hat{R}_{ij,\beta}\left(1 - \delta_{\alpha\beta}\right) \tag{78}$$

In these equations, $\delta_{\alpha\beta}$ represents the Kronecker delta and $\hat{R}_{ij}$ are normalized translational vectors between the adjacent unit cells. In the following, the determination of the inter-site parameters shall be discussed in more detail. In principle, there are two different approaches. The first approach is based on the application of the corresponding eigenvector of the local mode $\boldsymbol{u}$. This eigenvector can be used to generate high symmetry configurations by constructing the displacements manually. Subsequently, first-principles calculations can be employed to compute the energies and determine the inter-site parameters from them [23]. However, a much more elegant method is to calculate the full phonon band structure and determine the parameters using highly symmetric points in reciprocal space. These points represent in real space nothing else than highly symmetric displacements of atoms. Therefore, in the following, a superposition of the inter-site parameters can be used to construct an equation for the phonon energy for different configurations. The chosen points in the reciprocal space for this purpose are: $\Gamma\,(0,0,0)$, $X\left(\frac{\pi}{a},0,0\right)$, $M\left(\frac{\pi}{a},\frac{\pi}{a},0\right)$, $R\left(\frac{\pi}{a},\frac{\pi}{a},\frac{\pi}{a}\right)$, $\Sigma\left(\frac{\pi}{4},\frac{\pi}{4},0\right)$. Here $a$ symbolically represents a lattice parameter. The atomic displacements associated with these points are also those that must be manually constructed for the first method. If, instead, the entire phonon band structure or the required parts of it are calculated, the associated energies for these points are already included. Further details on these highly symmetric points and the reasons for their selection can be found in the work of Zhong, Vanderbilt, and Rabe [23] as well as Nishimatsu et al. [26,27]. Next, the energies associated with the highly symmetric points $\boldsymbol{k}_i$ can now be expressed by a combination of local energy, short-range contribution, and long-range interaction. Thus, Equations 79 to 85 can be constructed for each of the selected points. Here, $\kappa(\boldsymbol{k}_i)$ represent half of the eigenvalues associated with the reciprocal point $\boldsymbol{k}_i$. The first term in each equation specifies the contribution of the long-range interaction. The new parameter $a_0$ represents the lattice constant of the unit cell. The second term is expressed by the parameter $\kappa_2$ and denotes the respective local contribution to the total energy. This parameter is also used in the self-energy, however, a small correction must be applied here to ensure the correct description of the potential energy surface. The correction for this parameter is $\kappa_2 = \kappa_2 + [\kappa - \kappa(\Gamma_{TO})]$, where $\kappa$ here stems from the isolated displacement energy and

$\kappa(\Gamma_{TO})$ represents half of the eigenvalue at the zone center. This correction is applied to raise the dispersion of the band structure to align it with the self-energy. The further terms in Equations 79 to 85 are now the already known inter-site parameters $j_1$-$j_7$ which are applied according to the associated configuration. The derivation can simply be done via the definition of the respective parameters shown in Figure 6.

$$\kappa(\Gamma_{TO}) = -\frac{2}{3}\pi\frac{Z^*}{\epsilon_\infty a_o^3} + \kappa_2 + 2j_1 + j_2 + 4j_3 + 2j_4 + 4j_6 \tag{79}$$

$$\kappa(X_1) = 4.84372\frac{Z^*}{\epsilon_\infty a_o^3} + \kappa_2 + 2j_1 - j_2 - 4j_3 + 2j_4 - 4j_6 \tag{80}$$

$$\kappa(X_5) = -2.42186\frac{Z^*}{\epsilon_\infty a_o^3} + \kappa_2 + j_2 - 2j_4 - 4j_6 \tag{81}$$

$$\kappa(M_{3\prime}) = -2.67679\frac{Z^*}{\epsilon_\infty a_o^3} + \kappa_2 - 2j_1 + j_2 - 4j_3 + 2j_4 + 4j_6 \tag{82}$$

$$\kappa(M_{5\prime}) = 1.33839\frac{Z^*}{\epsilon_\infty a_o^3} + \kappa_2 - j_2 - 2j_4 + 4j_6 \tag{83}$$

$$\kappa(R_{25\prime}) = \kappa_2 - 2j_1 - j_2 + 4j_3 + 2j_4 - 4j_6 \tag{84}$$

$$\kappa(\Sigma_{LO}) = 2.93226\frac{Z^*}{\epsilon_\infty a_o^3} + \kappa_2 + j_1 - 2j_5 - 4j_7 \tag{85}$$

In summary, using the above equations, the inter-site parameters can be determined by first-principles calculations. From these results, the coupling matrix can then be constructed. However, it remains to be clarified how the different energy contributions represent the band structure of the system. As can be seen in the results for $BaTiO_3$ from the work of Nishimatsu et al. [27], a band structure can be obtained purely for the long-range interaction. Adding now the contributions of the short-range interaction yields the band structure for the selected local basis. The offset which occurs between the real band structure and the added contributions of

short- and long-range interaction is given by the local energy, expressed by $\kappa_2$. Therefore, a correction of the parameter $\kappa_2$ can be performed without further ado, since $\kappa_2$ only shifts the absolute values of the energy but has no influence on the dispersion itself.

The implementation of the different energy contributions shall now be discussed. The local-mode self-energy can be implemented quite efficiently, as shown in Equation 66. For the long-range energy and the short-range interaction, a transformation and evaluation in the reciprocal space can be considered due to their mathematical form. That can increase the performance of the code considerably through the utilization of Fourier transformations. Therefore, such a transformation into the reciprocal space shall be addressed. For more details, please refer to the work of Nishimatsu et al. [26,27]. Following, all energy contributions that have a quadratic term in $\boldsymbol{u}$ can be combined and a new mathematical expression can be stated as evident in Equation 86. This equation also includes the quadratic term of the local-mode self-energy from Equation 66. In addition, the sum over the reciprocal vectors $\boldsymbol{k}$ is introduced.

$$V^{quad}(\{\boldsymbol{u}\}) = \frac{1}{2}\sum_{\boldsymbol{k}}\sum_{\alpha\beta}\tilde{u}_\alpha^*(\boldsymbol{k})\,\widetilde{\Phi}_{\alpha\beta}^{quad}(\boldsymbol{k})\tilde{u}_\beta(\boldsymbol{k})$$

(86)

The variable $\tilde{u}_\alpha(\boldsymbol{k})$ entering Equation 86 is the Fourier-transformed amplitude of the local modes. Such a Fourier transform for $\boldsymbol{u}(\boldsymbol{R})$ is stated in Equation 87. In addition, the transformed interaction matrix $\widetilde{\Phi}_{\alpha\beta}^{quad}(\boldsymbol{k})$ is introduced, which contains all quadratic contributions.

$$\tilde{u}_\alpha(\boldsymbol{k}) = \sum_{\boldsymbol{R}} u_\alpha(\boldsymbol{R})\exp(-i\boldsymbol{k}\cdot\boldsymbol{R})$$

(87)

All previous energy contributions were pure functions of the local amplitude $\boldsymbol{u}$ and thus, only atomic displacements were considered without the deformation of the unit cell. However, especially for ferroelectric systems, it is of utmost relevance to include also the deformations and the couplings between displacements of the atoms and deformations. In the next two chapters, these energy contributions will be discussed in detail, and the formulation of the effective Hamiltonian will be completed.

### 4.3.7  Elastic Energies

In this chapter, the contributions to the energy originating from the elastic deformations shall be described. First of all, it can be stated that elastic energy can be divided into two contributions, i.e., homogeneous $V^{elas,homo}$ and inhomogeneous strain $V^{elas,inho}$. The description of the homogenous part correct to the second order can be conducted by

Equation 88. Here, $\eta_{H,l}$ represent homogenous strain variables in Voigt notation. It should be noted that these strain variables allow for homogenous deformations of the entire supercell. Furthermore, the modified elastic constants $B_{11}$, $B_{12}$ and $B_{44}$ are used. The relation of these parameters to the conventional elastic constants is given by: $B_{11} = a_0^3 C_{11}$, $B_{12} = a_0^3 C_{12}$ and $B_{44} = a_0^3 C_{44}$. $a_0$ denotes the lattice constant of the cubic reference system. The parameter $N$ represents the number of unit cells in the supercell.

$$V^{elas,homo}(\eta_{H,1}, \dots, \eta_{H,6}) = \frac{N}{2} B_{11}(\eta_{H,1}^2 + \eta_{H,2}^2 + \eta_{H,3}^2)$$
$$+ N B_{12}(\eta_{H,2}\eta_{H,3} + \eta_{H,3}\eta_{H,1} + \eta_{H,1}\eta_{H,2})$$
$$+ \frac{N}{2} B_{44}(\eta_{H,4}^2 + \eta_{H,5}^2 + \eta_{H,6}^2) \tag{88}$$

The calculation of the inhomogeneous contribution to the elastic energy is somewhat more complex. For this purpose, the already known but not explained variables $w$ have to be introduced first. Such a vector $w$ is defined for each unit cell in the supercell. It should be noted that these vectors are defined in units of the lattice constants and, therefore, dimensionless. In principle, they give the local displacement, by definition, using an A-centered basis. Furthermore, inhomogeneous strain variables $\{\eta_{I,l}\}$ for each of the unit cells can be introduced. To establish the relationship between local inhomogeneous strain $\eta_{I,l}(R)$ and the dimensionless variables $w$, the six averaged differential displacements over Equations 89 and 90 must first be calculated. The remaining four expressions can be derived by cyclic permutation. Here $x,y$ and $z$ are unit vectors and indicate the translation to adjacent unit cells in these same directions. $d$ represents an additional translational vector.

$$\Delta w_{xx} = \sum_{d=0,y,z,y+z} [w_x(R_i - d - x) - w_x(R_i - d)] \tag{89}$$

$$\Delta w_{xy} = \sum_{d=0,y,z,y+z} [w_y(R_i - d - x) - w_y(R_i - d)] \tag{90}$$

From the results of the above equations, the local inhomogeneous strain variables can now be calculated by $\eta_{I,1}(R_i) = \Delta w_{xx}/4$, $\eta_{I,4}(R_i) = (\Delta w_{yz} + \Delta w_{zy})/4$, etc. For more details on the derivation of these relations, see the work of Zhong, Vanderbilt, and Rabe [23]. The total strain thus results from the amounts of homogeneous and inhomogeneous deformations, which can

be simply added: $\eta_l(\boldsymbol{R}) = \eta_{H,l}(\boldsymbol{R}) + \eta_{I,l}(\boldsymbol{R})$. As a next step, it will be explained how the dimensionless variables $\boldsymbol{w}$ are taken into account in the effective Hamiltonian. These variables are used in the inhomogeneous part of the elastic energy and in the coupling between phonons and strain. The mathematical expression for the inhomogeneous elastic energy can be found in Equation 91. Again, the transformation of the potential into reciprocal space was performed to speed up the calculation. Here, the variables $\widetilde{w}_\alpha(\boldsymbol{k})$ are the Fourier transformed dimensionless variables $w_\alpha(\boldsymbol{R})$ analogous to Equation 87.

$$V^{elas,inho}(\{\boldsymbol{w}\}) = \frac{1}{2}\sum_{\boldsymbol{k}}\sum_{\alpha\beta}\widetilde{w}_\alpha^*(\boldsymbol{k})\widetilde{\Phi}_{\alpha\beta}^{elas,inho}(\boldsymbol{k})\widetilde{w}_\beta(\boldsymbol{k})$$

(91)

The quantity $\widetilde{\Phi}_{\alpha\beta}^{elas,inho}(\boldsymbol{k})$ represents the Fourier transformed force-constant matrix, whereby the long-wavelength approximation can be applied. Using this approximation, the diagonal elements of the matrix result as evident below:

$$\widetilde{\Phi}_{\alpha\beta}^{elas,inho}(\boldsymbol{k}) = \frac{1}{N}\left[k_x^2 B_{11} + k_y^2 B_{44} + k_z^2 B_{44}\right]$$

(92)

The off-diagonal elements of the force-constant matrix in reciprocal space are given by the following expression:

$$\widetilde{\Phi}_{\alpha\beta}^{elas,inho}(\boldsymbol{k}) = \frac{1}{N}\left[k_x k_y B_{12} + k_x k_y B_{44}\right]$$

(93)

An alternative formulation of this energy contribution in real space and more details on the derivation can be found in the work of Zhong, Vanderbilt, and Rabe [23]. A detailed description of the transformation to reciprocal space and its implementation can be found in the work of Nishimatsu et al. [26,27].

### 4.3.8  Strain-Phonon Coupling

The final term which is employed in the effective Hamiltonian from Equation 64 is the coupling of the local mode with strain [26,27]. This coupling represents a central point since the atomic displacements from the reference structure are accompanied by deformations of the unit cell. In this case, the coupling energy can again be divided into homogeneous and inhomogeneous contributions. The homogeneous coupling between local mode and strain can be calculated via Equation 94. Here, both the strain variables $\eta_{H,l}$ and the local modes $\boldsymbol{u}$ are involved.

$$V^{coup,homo}(\{\boldsymbol{u}\}, \eta_{H,1}, \dots, \eta_{H,6}) = \frac{1}{2}\sum_{\boldsymbol{R}}\sum_{i=1}^{6}\sum_{j=1}^{6}\eta_{H,i}C_{ij}y_j(\boldsymbol{R})$$

(94)

To simplify the notation of the above equation, the new variables $y_j(\boldsymbol{R})$ were introduced for the local amplitudes. The definitions of the respective products of local amplitudes can be seen below:

$$y_1(\boldsymbol{R}) = u_x^2(\boldsymbol{R}), \qquad y_2(\boldsymbol{R}) = u_y^2(\boldsymbol{R}), \qquad y_3(\boldsymbol{R}) = u_z^2(\boldsymbol{R})$$

$$y_4(\boldsymbol{R}) = u_y(\boldsymbol{R})u_z(\boldsymbol{R}), \qquad y_5(\boldsymbol{R}) = u_z(\boldsymbol{R})u_x(\boldsymbol{R}), \qquad y_6(\boldsymbol{R}) = u_x(\boldsymbol{R})u_y(\boldsymbol{R}) \quad (95)$$

The relationship between local modes and strain can be determined by the coupling matrix $C_{ij}$, as illustrated by Equation 96. The entries of this matrix are based on three different parameters $B_{1xx}$, $B_{1yy}$ and $B_{4yz}$ due to the cubic reference structure. These parameters specify the interaction between the local displacement of the atoms and the corresponding deformation of the unit cell. The calculation of these parameters can be done in different ways and is discussed in detail in the parameterization chapters and in the enclosed publications. For more details on the derivation of this energy contribution as well as the exact definition of the coupling parameters, the work of King-Smith and Vanderbilt can be referred to [24].

$$C = \begin{pmatrix} B_{1xx} & B_{1yy} & B_{1yy} & 0 & 0 & 0 \\ B_{1yy} & B_{1xx} & B_{1yy} & 0 & 0 & 0 \\ B_{1yy} & B_{1yy} & B_{1xx} & 0 & 0 & 0 \\ 0 & 0 & 0 & 2B_{4yz} & 0 & 0 \\ 0 & 0 & 0 & 0 & 2B_{4yz} & 0 \\ 0 & 0 & 0 & 0 & 0 & 2B_{4yz} \end{pmatrix} \quad (96)$$

The next and final term is the coupling of the local modes with the inhomogeneous strain. The associated potential is again expressed in the reciprocal space, as shown in Equation 97. Here, both the local amplitudes $\boldsymbol{u}$ and the dimensionless variables $\boldsymbol{w}$ are involved. The local amplitudes are specified here again by $y_j(\boldsymbol{R})$, where the relations to the actual amplitudes are listed in Equation 95. However, since the calculation is done in reciprocal space, the Fourier transformed quantities have to be used for both variables. These are denoted here by $\widetilde{w}_\alpha^*(\boldsymbol{k})$ and $\tilde{y}_i(\boldsymbol{k})$, where for $\widetilde{w}_\alpha^*(\boldsymbol{k})$ the complex conjugate version has to be adopted.

$$V^{coup,inho}(\{\boldsymbol{u}\}, \{\boldsymbol{w}\}) = \frac{1}{2} \sum_{\boldsymbol{k}} \sum_{\alpha} \sum_{i=1}^{6} \widetilde{w}_\alpha^*(\boldsymbol{k})\tilde{B}_{\alpha i}(\boldsymbol{k})\tilde{y}_i(\boldsymbol{k}) \quad (97)$$

The interaction between local modes and inhomogeneous strain can again be expressed by a coupling matrix $\widetilde{\boldsymbol{B}}(\boldsymbol{k})$. The corresponding illustration of the matrix can be found in Equation 98, where $N$ represents the number of unit cells in the supercell. The parameters found are the same

as in Equation 96 and describe the deformation as a function of local amplitudes. Furthermore, the long-wavelength approximation was also applied in this case.

$$\widetilde{\boldsymbol{B}}(\boldsymbol{k}) = \frac{1}{N}\begin{pmatrix} k_x B_{1xx} & k_x B_{1yy} & k_x B_{1yy} & 0 & 2k_z B_{4yz} & 2k_y B_{4yz} \\ k_y B_{1yy} & k_y B_{1xx} & k_y B_{1yy} & 2k_z B_{4yz} & 0 & 2k_x B_{4yz} \\ k_z B_{1yy} & k_z B_{1yy} & k_z B_{1xx} & 2k_y B_{4yz} & 2k_x B_{4yz} & 0 \end{pmatrix} \tag{98}$$

### 4.3.9 Summary of Derivation

As a whole, this chapter forms the basis of this thesis and can be summarized as follows. At the beginning, the fundamental basis was demonstrated by so-called Lattice Wannier functions. Subsequently, the original mean-field theory was presented, whereby here, the description of the lattice energy was carried out up to the fourth order. This approach served as a basis for the extension to a local-mode theory, where the application of the formalism to a supercell was demonstrated. The general form of the effective Hamiltonian was first explained, followed by a detailed discussion of the individual energy contributions. The derivations of the energy contributions and the effective Hamiltonian presented here are mostly based on existing works from the literature. In this thesis, however, extensions for the effective Hamiltonian have been developed, which were introduced in Chapter 4.3.4.1 and will be further discussed in the following chapters and in the enclosed publications. That includes a completely revised scheme for including a large number of anharmonic couplings to higher energy phonons as well as alternative ways to parametrize the effective Hamiltonian, as discussed in detail in Publication 2. Furthermore, the next chapter will also lay the foundation for the extension of the effective Hamiltonian to describe substituted systems.

### 4.4 Effective Hamiltonians for Substituted Systems

In this chapter, the extension of the effective Hamiltonian formalism for the inclusion of substituents in a perovskite structure will be discussed. In literature, one finds a variety of different approaches, whereby these are fundamentally different from each other. The main common feature of these approaches is the formalism of Zhong, Vanderbilt, and Rabe [23]. This Hamiltonian has already been described in detail in the previous chapter and allows the simulation of pure systems like $BaTiO_3$ (BT). The most chosen approach to model substituents is to introduce a perturbation of a well-defined base system. Here, it must already be determined which system is to be perturbed. The work of Bellaiche et al. [29–31] describes a perturbation of a basis system parameterized by Virtual Crystal Approximation (VCA) [66]. Basically, a sort of averaged system is used here, and the respective different species at the A- and B-sites in the perovskite lattice are considered perturbations with respect to the base system. The applied perturbation terms were constructed to account for changes in the local-mode self-energy as

well as a correction to the local strain variables. Using this framework, several systems, such as $Pb(Zr_{1-x}Ti_x)O_3$ (PZT) [29] and $Ba(Zr_{1-x}Ti_x)O_3$ (BZT) [31] were parameterized, and the subsequent Monte Carlo and MD simulations showed good agreement with experimentally observed properties. A disadvantage of this approach is that the parameterization must be performed specifically for each composition, and therefore, results have only been published for selected concentrations. Furthermore, the application of the VCA method for small concentrations of substituents is debatable. In the work of Nishimatsu et al. [33], a different approach was followed, whereby the parameterization was first performed for the two binary systems (e.g. $BaTiO_3$ and $SrTiO_3$ for $Ba_{1-x}Sr_xTiO_3$, BST) in parallel. Then the parameters were simply averaged, and it was shown that these averaged parameters were very similar to those of the VCA parameterization. Furthermore, the averaged system was used as a basis, and the further perturbation terms were related to it. The chosen perturbation terms here refer to a hydrostatic pressure correction as well as a modulation for the local strain variables. The resulting findings for BST provided good agreement with experimental data and demonstrated the applicability of this approach. In addition, a wide range of concentrations was simulated. A different approach was provided by the work of Mentzer et al. [32], which takes pure BT as the base system and relates the perturbation by substituents to this system. The perturbation induced by the B-site substitution by Zr ions is performed here by means of a restoring force. Furthermore, a hydrostatic pressure correction is applied for the influence of strain. The results obtained by this approach reproduce the phase diagram of BZT very well and also provide good agreement of hysteresis curves with experiments. Only the local description of effects like local deformations is somewhat neglected by such an approach.

Overall, it can be concluded here that the integration of impurity atoms can be accomplished by a wide diversity of methods, with the respective approaches having to be adapted for different systems. In the following chapters, the approach developed in this thesis will be discussed based on literature and new ideas.

### 4.4.1 General Definition via Perturbation

In this chapter, the basic idea for the integration of substituent atoms, which was developed in this thesis, will be described. The basis of this chapter is the framework developed in Publication 3, though additional details will be provided here. Following the work done in this thesis on an accurate Hamiltonian for pure BT, as discussed in Publication 2, this Hamiltonian was chosen as the starting point for further development. This choice is further motivated by the excellent agreement of the phase transition temperatures as well as the reproducibility of other experimental data. The associated phase diagram and parameterization details can be

found in Publication 2. The idea of incorporating substituents is based on inspirations from the above-mentioned methods and is intended to provide an alternative scheme to the existing approaches from the literature. The starting point is the effective Hamiltonian $H_{BTO}^{eff}$, which is extended by a perturbation term $H^{peturb.}$. The total Hamiltonian $H_{total}^{eff}$ can be seen in Equation 99, where the definition for $H_{BTO}^{eff}$ can be found in Publication 2. The used variables here are the local-mode amplitudes $\boldsymbol{u}$, the dimensionless variables $\boldsymbol{w}$, the strain variables in Voigt notation $\eta_i$, and a newly introduced variable $\sigma$. The latter is used to distinguish between different species at the A or B lattice sites. In contrast to methods in the literature where this variable also has a quantitative value, $\sigma$ denotes here a symbolic variable.

$$H_{total}^{eff}(\{\boldsymbol{u}\},\{\boldsymbol{w}\},\eta_i,\{\sigma\}) = H_{BTO}^{eff}(\{\boldsymbol{u}\},\{\boldsymbol{w}\},\eta_i) + H^{peturb.}(\{\boldsymbol{u}\},\{\boldsymbol{w}\},\{\sigma\})$$

(99)

The foundation for the description of substituents is the additional term $H^{peturb.}$, which contains the perturbation of the pure BT system. The construction of this term was inspired by already established methods from the literature as well as by own ideas. Basically, this term consists of four different energy contributions, as evident in Equation 100. The first contribution $\Delta T$ is a correction of the kinetic energies to account for the different masses of the ions. The second contribution $\Delta V^{self}$ adapts the local-mode self-energy due to the different ions at the lattice sites. This is followed by a correction to the long-range interaction $\Delta V^{dpl}$ to compensate for different effective charges. The last term $V^{aux}$ accounts for short-range interactions between the different local modes and includes a correction for the local strains. An additional adaptation is made for the homogeneous strain, which is not included in Equation 100. All of these contributions are explained in more detail in the following subchapters as well as an explanation of the underlying physical principles is given.

$$H^{peturb.} = \Delta T(\{\boldsymbol{u}\},\{\boldsymbol{w}\},\{\sigma\}) + \Delta V^{self}(\{\boldsymbol{u}\},\{\sigma\}) + \Delta V^{dpl}(\{\boldsymbol{u}\},\{\sigma\})$$
$$+ V^{aux}(\{\boldsymbol{u}\},\{\boldsymbol{w}\},\{\sigma\})$$

(100)

The perturbation term contains two contributions that were adopted directly from the literature. These are the adaptation of the local-mode self-energy and the short-range correction. The other two corrections may have been used occasionally but, to the author's knowledge, not in conjunction with the other corrections. All in all, the perturbation term in this work has been designed to ensure the most flexible application to different types of substituents. This includes the description of homovalently and heterovalently substituted systems, where different defects types (e.g. due to charge compensation) can also be considered.

### 4.4.2 Adaptation of Local-Mode Self-Energy

The first correction, which shall be explained in more detail, is an adaptation of the local-mode self-energy. The local-mode self-energy is defined as the local displacement energy at the Γ-point of the 1st Brillouin zone. Originally, a polynomial up to the fourth order was used by Zhong, Vanderbilt, and Rabe [23] for the mathematical description. Subsequently, this term was extended to the 8th order in the local amplitude $\boldsymbol{u}$ by Nishimatsu et al. [27]. In the Hamiltonian $H_{BTO}^{eff}$, which serves as a basis, the formulation of Nishimatsu et al. [27] is applied, which makes a correction of all associated parameters necessary. Such a correction, although only up to the fourth order, was first proposed by Bellaiche et al. [29] for the description of PZT. In this work, this approach has been adapted, and a correction up to the 8th order is applied. The corresponding mathematical expression for this adaptation can be seen in Equation 101. Basically, this equation is analogous to the original local-mode self-energy, but new parameters have been introduced. The first new parameter is $\sigma$ to distinguish between different species at the A or B lattice sites. Following, the parameters $\Delta\kappa_{2,\sigma}$, $\Delta\alpha_\sigma$, $\Delta\gamma_\sigma$ and $\Delta k_{1,\sigma}$ to $\Delta k_{4,\sigma}$ have been applied, which are used to adapt the shape of the local-mode self-energy. Here it is important to define these parameters in such a way that the description of the correction refers to the parent system $H_{BTO}^{eff}$. This means that all correction parameters must be parameterized in such a way that the energetic differences are related to the base system. More details on the parameterization by first-principles calculations can be found in Publication 3 and in Chapter 6 and 7.

$$\Delta V^{self}(\{\boldsymbol{u}\},\{\sigma\})$$
$$= \sum_R \{\Delta\kappa_{2,\sigma}u^2(\boldsymbol{R}) + \Delta\alpha_\sigma u^4(\boldsymbol{R})$$
$$+ \Delta\gamma_\sigma\left[u_y^2(\boldsymbol{R})u_z^2(\boldsymbol{R}) + u_z^2(\boldsymbol{R})u_x^2(\boldsymbol{R}) + u_x^2(\boldsymbol{R})u_y^2(\boldsymbol{R})\right]$$
$$+ \Delta k_{1,\sigma}u^6(\boldsymbol{R}) + \Delta k_{2,\sigma}(u_x^4(\boldsymbol{R}) * \left[u_y^2(\boldsymbol{R}) + u_z^2(\boldsymbol{R})\right] + u_y^4(\boldsymbol{R})$$
$$* \left[u_z^2(\boldsymbol{R}) + u_x^2(\boldsymbol{R})\right] + u_z^4(\boldsymbol{R}) * \left[u_x^2(\boldsymbol{R}) + u_y^2(\boldsymbol{R})\right])$$
$$+ \Delta k_{3,\sigma}u_x^2(\boldsymbol{R})u_y^2(\boldsymbol{R})u_z^2(\boldsymbol{R}) + \Delta k_{4,\sigma}u^8(\boldsymbol{R})\}$$

$$(101)$$

The purpose of this correction of the local-mode self-energy shall also be discussed shortly. In principle, this correction allows the adaptation of the potential energy surface considering the displacive energy connected to the local amplitudes $\boldsymbol{u}$. For example, a formation of a double-well potential can result here for the parent system. The correction can change this potential arbitrarily within the mathematical boundary conditions. Thus, the influence of substituents on

the local amplitudes $u$ can be calculated relatively straightforwardly. However, as already mentioned, this correction only affects the local amplitudes and does not include interactions with neighboring unit cells. To apply corrections also away from this local adaptions, additional corrections of the potential energy surface are required.

### 4.4.3 Auxiliary Spring System

The next modification, which shall be explained in more detail, is for interactions between different unit cells containing different species of ions on the respective lattice sites. It is based on the work of Bellaiche et al. [29], which proposes a term that adapts the local amplitudes $u$ and the dimensionless variables $w$. The correction proposed in the work of Bellaiche et al. [29] was derived up to the first order in $u$ and $w$, although an extension to higher orders can be carried out analogously if necessary. In this thesis, this approach has been adopted one-to-one and can be seen in Equation 102. Also, in this equation, the symbolic parameter $\sigma$ is used to distinguish between unit cells with different substituted ions. The first term in Equation 102 is used to account for the influence of differently substituted unit cells on the neighboring unit cells with respect to the local amplitude $u$. Here, $Q_{T,R}(\sigma_T)$ is an interaction matrix containing the parameters for the interaction between the unit cells. $R$ denotes a translational vector between the unit cells. The sum over $R$ runs over all unit cells in the supercell. $T$ represents a further translational vector between unit cells. The sum over $T$ is set so that interactions up to the third nearest neighbor shell are taken into account. $e_{T,R}$ is a unit vector joining the site $T$ with the center of $u(R)$. The application of such a unit vector contains a substantial advantage over other approaches like a pure definition by matrices. By projecting $u(R)$ onto the unit vector $e_{T,R}$, only contributions that are different from zero are taken into account. All other contributions in the respective Cartesian directions, which are zero due to symmetry, are automatically neglected. An analogous term can now be applied to the dimensionless variables $w$ as shown in Equation 102. This term is used to account for changes in the local strain induced by substituents. That is, with the help of this correction, it is possible to influence the local deformation of unit cells. Also, in this case, an interaction matrix is defined that takes into account the influence of the different ions at the respective lattice sites on their neighbors. Here, $f_{T,R}$ denotes again a unit vector joining the site $T$ with the center of $w(R)$. The translation vectors and the respective sums are analogous to those described for the correction applied for $u$. It should be noted that the particular unit vectors must be defined to match the respective chosen basis for the local mode $u$ and the dimensionless variable $w$. For example, in the case of BT, a B-centered basis is chosen for the local mode $u$ and an A-centered basis is chosen for

the dimensionless variables $\boldsymbol{w}$ during the parametrization of the effective Hamiltonian. More on this topic on the local basis can be found in Publication 2 and the instructive paper by Waghmare and Rabe [25].

$$
V^{aux}(\{\boldsymbol{u}\}, \{\boldsymbol{w}\}, \sigma)
$$

$$
= \sum_R \sum_T Q_{T,R}(\sigma_T) \boldsymbol{e}_{T,R} \cdot \boldsymbol{u}(\boldsymbol{R}) + \sum_R \sum_T S_{T,R}(\sigma_T) \boldsymbol{f}_{T,R} \cdot \boldsymbol{w}(\boldsymbol{R}) \tag{102}
$$

Altogether, this correction for the local amplitudes $\boldsymbol{u}$ and the dimensionless variables $\boldsymbol{w}$ is an important part of the perturbation of the parent system. Only with the application of this correction, it is possible to take into account the influence of substitution on the neighboring unit cells. The required parameters can be determined again by first-principles calculations. Also, here, the parameters have to account for the interactions with reference to the parent system. Furthermore, the interaction matrices $Q_{T,R}(\sigma_T)$ and $S_{T,R}(\sigma_T)$ can be calculated quite straightforwardly using supercells and considering the occurring forces due to substitution. More about the parametrization using DFT can be found in Publication 3 and in Chapters 6 and 7.

### 4.4.4 Hydrostatic Pressure Correction

As a next step, a correction for the change of the lattice volume due to substitution will be discussed. In the previous chapter, it was shown how the influence on the local strain could be taken into account, but this correction does not provide a change in the homogeneous strain. For many systems, however, substitution by impurity atoms does induce a change in the lattice, either by expansion or contraction. To introduce this contribution to the effective Hamiltonian, the application of a hydrostatic pressure was considered. The idea for such a correction goes back to the work of Nishimatsu et al. [33] as well as Mentzer et al. [32], whereby the underlying effective Hamiltonians are different. Also, the effective Hamiltonian used in this work differs from the literature since, here, the effects of substitution are considered differently. This means that the correction via the hydrostatic pressure must be chosen to be harmonized with the other applied corrections. Therefore, in this thesis, the following approach was adopted to account for induced volume changes. Initially, first-principles calculations were performed with different concentrations of substituents, and the change in the lattice constants was observed. It was found that, in most cases, a linear dependence of the lattice volume on the concentration can be assumed. For more details, the Supplemental Material of Publication 3 is referred to. Thus, a pressure correction can be written as in Equation 103, where $x$ denotes the concentration of the impurity atoms and $p_0$ a constant. If a non-linear dependence of the pressure occurs, this relation can simply be extended by further orders of $x$ and fitted to the first-principles

calculations. It must also be mentioned here that the pressure correction refers to the parent system, which for example, in this thesis, is BT.

$$p_{eff} = x \cdot p_0 \tag{103}$$

Such a pressure correction causes an expansion or contraction of the entire supercell, and of course, the volumes of local unit cells change accordingly. However, this change is an averaged expansion or contraction of all unit cells and is not dependent on the particular chemical composition of each unit cell. Nevertheless, in order to take into account this local deformation in dependence on the chemical composition of the unit cell, the second term from Equation 102 is essential. This term allows, despite the averaged change of the unit cell volume, to ensure a correct description of the local deformations. In order to make this feasible, though, the interaction matrix $S_{T,R}(\sigma_T)$ must be determined in such a way that the changes in the local unit cells already take into account the averaged change in the volume. This, in turn, implies that for each concentration, the interaction matrix $S_{T,R}(\sigma_T)$ would have to be re-parameterized. As the Hamiltonian constructed in this thesis should be as flexible as possible for a wide concentration range, a re-parameterization of the interaction matrix is omitted. This assumption is reasonable, especially for small concentrations of impurity ions, whereas for larger concentrations, an overestimation of local distortions can occur.

### 4.4.5 Adaptation of Kinetic Energies

A further adjustment for the description of substituents can be made in the kinetic energies of the effective Hamiltonian. As evident in Equation 64, effective masses and associated kinetic energies are used for the effective Hamiltonian of the parent system. If other species are substituted at certain lattice sites, these effective masses must be adapted to the respective atomic masses. It should be mentioned again that the effective masses used are associated with the local modes. That is, the atomic masses are multiplied by the quadratic entries of the respective eigenvectors, as can be seen in Equation 65. For the inclusion of substituents, an effective mass is calculated analogously, which takes into account the respective atomic mass at the A or B lattice site. Which eigenvector is taken for the computation must be decided individually, but the choice of the eigenvector used as the basis for the parametrization of the parent system is a good approximation. This adaptation of the effective masses allows to directly influence the dynamics of the respective local modes. Such an adjustment of kinetic energies has not yet been applied to the author's knowledge and will therefore be further discussed in Publication 3.

### 4.4.6 Adaptation of Long-Range Interaction

As a final correction, the long-range interaction between the local dipoles is adapted. The basis for the calculation of this interaction has already been discussed in detail in Chapter 4.3.5. After the calculation of the interaction matrix, this energy contribution can be simply calculated by matrix multiplication, as shown in Equation 72. If different atoms are now substituted, the Born effective charges also change as defined in Equation 74. That is, for an adaptation of the dipole interaction, the Born effective charges of the impurity ions must be calculated first, and then an effective charge associated with the local mode must be calculated according to Equation 74. Also, for this case, a suitable eigenvector must be used for the calculation of the effective charge. The eigenvector used for the parameterization of the parent system can be used as an approximation. A more complex method would be to calculate the associated phonons in a supercell, where the coupling between the eigenvector of the parent system and the substituted system must be investigated. Subsequently, an approximation can be found for the eigenvector of the local unit cell containing the substituted ions with respect to the parent system. Such an approximation can also be used for the calculation of effective masses from the previous chapter. Whether an application of long-range interaction adaptation should be included in the extended effective Hamiltonian must be decided specifically for each substituted system considered.

# 5 Parametrization of BaTiO₃

In this chapter, the parameterization of the effective Hamiltonian for pure $BaTiO_3$ (BT) will be discussed, with the results shown referring to Publication 2 and the associated Supplemental Material. Nevertheless, the parameterization will be summarized here, and any additional details will be revealed. The basis of the parameterization is DFT calculations, using the DFT package VASP [97–100] for all the following calculations. The calculations with VASP are based on so-called projector-augmented wave potentials [101]. The valence electronic configurations of $5s^2\,5p^6\,6s^2$ for Ba (10 valence electrons), $3s^2\,3p^6\,4s^2\,3d^2$ for Ti (12 valence electrons), and $2s^2\,2p^4$ for O (6 valence electrons) were used within the DFT calculations. Furthermore, the PBEsol [82] functional was used as an exchange-correlation functional. As a first step, convergence tests for the k-grid and the cutoff energy were performed. Cubic BT was considered, and the size of the k-grid was varied to determine which size yielded converging results. It was found that a k-grid of size 8x8x8 was sufficient for the 5-atom unit cell calculations. An analogous study was performed for the cutoff energy, and here a cutoff of 520 eV was adopted for the calculations. Larger cutoff energies were also considered for relaxations, where only minimal differences in lattice constants were observed. For the convergence of the SCF (self-consistent field) cycle, the EDIFF tag within VASP was set to $10^{-8}$ eV for all calculations.

## 5.1 Lattice Constant

The lattice constant of cubic BT plays a crucial role in the parameterization since this structure forms the basis for the effective Hamiltonian. Therefore, the optimization of the lattice constant by DFT calculations should be carried out with great care. In this work, a cubic structure of BT was first prepared and relaxed by DFT and the PBEsol functional. The k-grid, as well as the cutoff energy, were varied here to obtain a converged lattice constant. The final settings for the relaxation were a k-grid of size 8x8x8 and a cutoff energy of 520 eV. The criteria for the SCF cycle within the relaxation were set to a value for EDIFF of $10^{-8}$ eV, and for the maximal residual forces, a value of $10^{-4}$ eV/Å was chosen. As a result, a cubic lattice constant for BT of $a_0 = 3.987$ Å can be reported. Compared to the experimental lattice constant [23] of $a_0 = 4.01$ Å, the PBEsol functional slightly underestimates the lattice constant. The same procedure was also used to investigate the remaining phases of BT and the corresponding lattice parameters are presented in Table 1. These results are complementary to Publication 2 and are in good agreement with results from the literature [28].

*Table I. Summary of lattice constants for different phases of $BaTiO_3$ obtained from DFT relaxations using the PBEsol functional.*

|  | a [Å] | b [Å] | c [Å] | $\alpha$ [°] | $\beta$ [°] | $\gamma$ [°] |
|---|---|---|---|---|---|---|
| **Cubic** | 3.987 | 3.987 | 3.987 | 90.00 | 90.00 | 90.00 |
| **Tetragonal** | 3.971 | 3.971 | 4.065 | 90.00 | 90.00 | 90.00 |
| **Orthorhombic** | 4.027 | 4.027 | 3.965 | 90.00 | 90.00 | 90.21 |
| **Rhombohedral** | 4.007 | 4.007 | 4.007 | 89.86 | 89.86 | 89.86 |

## 5.2 Local-mode self-energy

The parameterization of the local-mode self-energy is a central point of this thesis and is described in detail in Publication 2 and its Supplemental Material. Therefore, only the foundation of this parameterization will be discussed in this chapter. The starting point for the calculation of the required parameters is the cubic phase of BT obtained from the previous chapter. This structure is used to calculate the phonons at the Γ-point by means of DFT. The calculation can be done either by a finite-difference method or by density-functional-perturbation theory (DFPT). In this thesis, both approaches were used, and only minimal differences in the calculated eigenvectors and eigenvalues were observed. The results for the eigenvectors are presented in Publication 2. A comparison between different exchange-correlation functionals can be found in the Supplemental Material of Publication 2. The results of the phonon calculation result in a total of 15 modes, whereby these modes are threefold degenerate [23,26–28]. This means that the displacement associated with an eigenvalue is equivalent for each of the respective Cartesian directions. Therefore, only five distinct modes result. These five modes include one acoustic mode, three modes with $\Gamma_{15}$ symmetry and one mode with $\Gamma_{25}$ symmetry. Interestingly, one of the $\Gamma_{15}$ modes has an imaginary frequency, indicating instability of the cubic phase. This mode is also called soft-mode and plays a special role in the parameterization. It can be shown that the structural change of the lattice is due to displacements based on the eigenvector of the soft-mode. See Publication 2 for more details. For the parameterization, as already explained in detail in the theoretical part, a phonon mode must be chosen as a basis. Since the eigenvector of the soft mode significantly overlaps with the structural change, this mode is the obvious choice for the basis of the effective Hamiltonian. In terms of Lattice Wannier functions, the eigenvector of the soft mode would now correspond to the local basis.

### 5.2.1 Conventional Hamiltonian

The parameterization of the local-mode self-energy is rather simple to perform after choosing the local basis by the eigenvector of the soft-mode. For the conventional effective Hamiltonian, it is sufficient to construct displacements of the atoms using the eigenvector in the highly symmetric directions <001>, <011>, and <111>. The displacements of the atoms are given by the local amplitude $\boldsymbol{u}$ and the eigenvector components, as evident in Equation 63. Then DFT can be used to calculate the associated total energies for a discrete set of amplitudes $\boldsymbol{u}$. By fitting Equations 67, 68, and 69, the required parameters for the local-mode self-energy can be determined. Here it is important to choose the discrete set in order to fit the local minima as well as the anharmonic contributions in the best possible way. An illustration of the obtained local-mode self-energy for BT is given in the Supplemental Material of Publication 2. It should be further noted that this energy refers purely to the displacement of the atoms at the $\Gamma$-point and does not include any changes in the unit cell. The changes due to deformation are taken into account via the other terms of the effective Hamiltonian. In addition, an alternative method for the determination of the local-mode self-energy shall be discussed here. This approach is called the valley tracing method (VTM) and originates from the work of Hashimoto et al. [102] and Nishimatsu et al. [27]. The approach involves a redefinition of the local amplitude by the displacements of the individual atoms, as can be seen in Equation 104. Here, $u_\alpha$ is the local amplitude in the Cartesian direction $\alpha$. $v_\alpha^i$ represents the displacement of atom $i$.

$$u_\alpha = \sqrt{(v_\alpha^A)^2 + (v_\alpha^B)^2 + \left(v_\alpha^{O_1}\right)^2 + \left(v_\alpha^{O_2}\right)^2 + \left(v_\alpha^{O_3}\right)^2} \qquad (104)$$

The basic proposition of the approach is that the eigenvector is not constant along the displacement of the atoms from the cubic phase toward the local minima. That is, a new eigenvector $\boldsymbol{\xi}(\boldsymbol{u})$ should be calculated for each displacement $\boldsymbol{u}$. The realization of this calculation of $\boldsymbol{\xi}(\boldsymbol{u})$ is achieved by minimizing the energy with respect to the change in atomic displacements at a fixed local amplitude $\boldsymbol{u}$. In this thesis, this approach was tested, and the results are comparable to literature values. However, due to the newly developed approach to include multiple phonon modes, the conventional approach was preferred in the remainder of the thesis. The reason for this is simply that by the VTM method, the local basis by clearly defined eigenvectors is no longer given. However, this basis is essential for the description of different phonon modes, and therefore, such a basis must be used for further parameterization.

### 5.2.2 Revised Hamiltonian

A major part of this thesis is the development of an extension of the effective Hamiltonian to incorporate additional phonon modes. A detailed description of the derivation, as well as the

parameterization, can be found in Publication 2 and its Supplemental Material. An overview of the developed approach is additionally given in Chapter 4.3.4.1. In this chapter, complementary to Publication 2, additional details on the parameterization will be discussed. The idea of including additional phonon modes in the effective Hamiltonian came from the fact that the two $\Gamma_{15}$ modes besides the soft mode also have an overlap with the structural deformation. In Publication 2, using a projection of the eigenvectors onto the structural deformation, the contribution of these modes is discussed in detail. Subsequently, the local-mode self-energy was expanded, yielding Equation 70 by applying a multivariate Taylor expansion. The formula for the local-mode self-energy in the <001> direction, cleaned of disallowed terms, can be seen in Equation 71. This equation has to be parameterized by DFT calculations, where a large number of different parameters have to be determined. For further progress, the three included phonon modes are denoted by the amplitudes $u$, $v_1$, and $v_2$, with the associated eigenvectors given in Publication 2. Basically, for the parametrization of Equation 71, a set of DFT calculations has to be found, which allows the accurate determination of all parameters. For this purpose, a Python script was written that takes over the construction of different structures based on atomic displacements. A very helpful module for the construction of these structures is the *pymatgen* module, which allows to create input files for the VASP calculations. Subsequently, the script was programmed to apply a superposition of the respective displacements based on the eigenvectors. Since three different modes are used here, the considered range of the corresponding amplitudes increases enormously. In the course of the parameterization, a discrete range for the soft-mode amplitude $u$ was defined. This range was chosen to cover the local minima and to consider the anharmonic part as best as possible. The definition of this discrete range for $u$ is, in principle, analogous to the parameterization of the conventional local-mode self-energy. In order to consider the additional modes $v_1$ and $v_2$, structures have to be created which contain a finite amplitude of all three modes. First, a range of discrete grid points was defined for each amplitude, where each grid point must be combined with the grid points of the other amplitudes. If the number of grid points is denoted by $N_u, N_{v_1}$ and $N_{v_2}$, the total number of structures to be created is $N_u N_{v_1} N_{v_2}$. Here it is obvious that if a dense grid is chosen, the number of structures to be calculated increases significantly. However, due to symmetry, the choice of amplitudes can already be reduced. Furthermore, to ensure a suitable choice of grids, the calculation was divided into patches, and then the fitting process was performed with different sizes of the dataset. Thereby, the convergence of the individual parameters as a function of the dataset size could be observed systematically. The final parameterization, therefore, includes a dataset of over 2500 DFT calculations with different

amplitudes. In fact, however, over 4000 DFT calculations were performed. Details of the fit process with various fit algorithms can be found in Publication 2 and its Supplemental Material. Furthermore, the stability of the fit and the final parameters for the effective Hamiltonian are also presented in Publication 2. Another important point is that the local-mode self-energy parameterized by Equation 71 is not directly used in the effective Hamiltonian. As already discussed in detail in Chapter 4.3.4.1 and Publication 2, this energy term is again transformed back to a function purely of $u$. This transformation is performed by calculating the amplitudes $v_{1,min}(u)$ and $v_{2,min}(u)$ which minimize the total energy. Since equation 71 does not allow a feasible analytical solution for the calculation of $v_{1,min}(u)$ and $v_{2,min}(u)$, numerical methods have to be used. That means, as a result, a data set of local-mode self-energies over a discrete set of amplitudes $u_i$ is obtained. However, this set indirectly includes all calculated couplings between the individual phonon modes. Furthermore, this set is used to refit the conventional local-mode self-energy from Equation 67. For the refit, not all parameters are redetermined. Only the parameters $k_1$ and $k_4$. This choice is discussed in Publication 2 and can be further motivated by the work of Paul et al. [28]. The final parameters used in the revised effective Hamiltonian are denoted by $k_1'$ and $k_4'$.

In the course of this thesis, the inclusion of the other two directions, <011> and <111>, was also investigated. Here, an expansion of the local-mode self-energy analogous to the <001> direction must first be performed. This expansion can basically be done in two different ways. Either each direction is considered separately, and a multivariate Taylor expansion is applied, or the formulation is carried out with the vectors $u$, $v_1$, and $v_2$. Both approaches give essentially the same result, except that any pre-factors must be considered carefully. In the Supplemental Material of Publication 2, the expansion for both these directions is discussed in detail as well as the associated parametrization is demonstrated. However, it turns out that the chosen approach for the back-transformation of the local-mode self-energy as well as the accompanying refitting of the conventional approach, reaches its limits. In detail, for the refitting of the directions <011> and <111> only the two parameters $k_2'$ and $k_3'$ are available, which strongly limits the flexibility of the mathematical function. But even if all available parameters are used for the refit process, the energy to be fitted can only be described in a partially acceptable manner. The reason for refitting has already been mentioned and is simply to maintain the efficiency of the effective Hamiltonian. For the solution to the above-mentioned problem, two approaches can be pursued. First, the effective Hamiltonian is revised, and all phonon modes are actively considered, which, however, leads to a loss of computational

efficiency. Second, Equations 67, 68, and 69 used for the refit are extended by additional terms, which allows greater flexibility for the fitting process. The latter is currently in progress and will be covered in a possible future publication.

## 5.3 Elastic Constants

In this chapter, the calculation of the elastic constants will be explained in more detail. In Supplemental Material of Publication 2, a comparison of the elastic constants for different exchange-correlation functionals is given, but the theoretical basis for the calculation is not discussed. Therefore, the required DFT calculations, as well as the subsequent fit processes, shall be described at this point. The approach adopted here to determine the constants is based on the work of Nishimatsu et al. [27]. In general, the three constants $B_{11}$, $B_{12}$ and $B_{44}$ are needed for the effective Hamiltonian. These constants are the elastic constants $C_{11}$, $C_{12}$ and $C_{44}$ multiplied by the volume of the unit cell. Furthermore, these elastic constants relate to the cubic structure used as the basis for the effective Hamiltonian. The first constant to be calculated is the bulk modulus of the system, which is not directly used in the Hamiltonian but is needed for the determination of the other constants. To calculate the bulk modulus, starting from the cubic structure, the strain tensor from Equation 105 is applied. Thus, the total energies at different volumes of the unit cell can be calculated by means of DFT.

$$\epsilon = \begin{pmatrix} \delta & 0 & 0 \\ 0 & \delta & 0 \\ 0 & 0 & \delta \end{pmatrix} \tag{105}$$

The bulk modulus $B_0$ can now be determined by fitting a Murnaghan [16] equation of state as shown in Equation 106. Here $E(V)$ is the total energy of the system as a function of the unit cell volume $V$. $B_0'$, $V_0$ and $E_0$ represent further constants which are also estimated during the fitting. The unit of the bulk modulus depends here on the input variables, of course, but the unit always amounts to pressure. To be consistent with the other variables $B_{11}$, $B_{12}$ and $B_{44}$, $B_0$ must be multiplied by the volume of the unit cell. Furthermore, it is also possible to calculate the bulk modulus using the Birch-Murnaghan [103] equation of state, although no relevant change in bulk modulus was observed for the case of BT. That is, the value for cubic BT with the Murnaghan approach yields $B_0 = 177.43$ GPa, whereas the Burch-Murnaghan equation of state leads to a value of $B_0 = 177.67$ GPa. The corresponding fit of the DFT data can be seen in Figure 7a.

$$E(V) = \frac{B_0 V}{B_0'(B_0' - 1)} \left( B_0' \left( 1 - \frac{V_0}{V} \right) + \left( \frac{V_0}{V} \right)^{B_0'} - 1 \right) + E_0 \tag{106}$$

The next constant to be determined is $B_{11}$. For this purpose, the strain tensor from Equation 107 must first be applied to the cubic structure. Such a deformation of the cubic cell leads to a tetragonal lattice structure. Subsequently, the constructed structures are calculated via DFT to obtain the corresponding total energy as a function of $\delta$.

$$\epsilon = \begin{pmatrix} 0 & 0 & 0 \\ 0 & 0 & 0 \\ 0 & 0 & \delta \end{pmatrix} \tag{107}$$

In order to estimate the constant $B_{11}$, Equation 108 is fitted to the above-mentioned set of DFT calculations. The corresponding fit for the case of BT can be found in Figure 7b. The associated value for the constant is provided in Publication 2.

$$E(\delta) = E_0 + \frac{1}{2}B_{11}\delta^2 + O(\delta^4) \tag{108}$$

From the two constants $B_0$ and $B_{11}$, the constant $B_{12}$ can now be calculated using the relation below. Here, the bulk modulus from Equation 106 must be multiplied by the volume of the unit cell to be consistent with the units.

$$B_{12} = \frac{3B_0 a_0^3 - B_{11}}{2} \tag{109}$$

Finally, the constant $B_{44}$ can be determined by the following procedure. First, the strain tensor from Equation 110 has to be applied to the cubic structure. Following, the constructed structures are calculated by DFT to obtain the total energies.

$$\epsilon = \begin{pmatrix} 0 & \delta & \delta \\ \delta & 0 & \delta \\ \delta & \delta & 0 \end{pmatrix} \tag{110}$$

From the set of DFT data, the constant $B_{44}$ can then be determined by fitting Equation 111. An illustration of the fit for the case of BT is given in Figure 7c.

$$E(\delta) = E_0 + \frac{3}{2}B_{44}\delta^2 + O(\delta^4) \tag{111}$$

All required parameters for the effective Hamiltonian for BT can be found in Publication 2. Furthermore, it should be mentioned that the calculation of the elastic constants can, of course, be done in different ways. For example, many DFT packages provide a direct output of the elastic constants when the phonon properties are calculated. However, it is advantageous if the direct results from DFT are checked with such classical approaches. Furthermore, a comparison to experimental values, as given in the Supplemental Material of Publication 2, is also helpful in estimating the quality of the calculation.
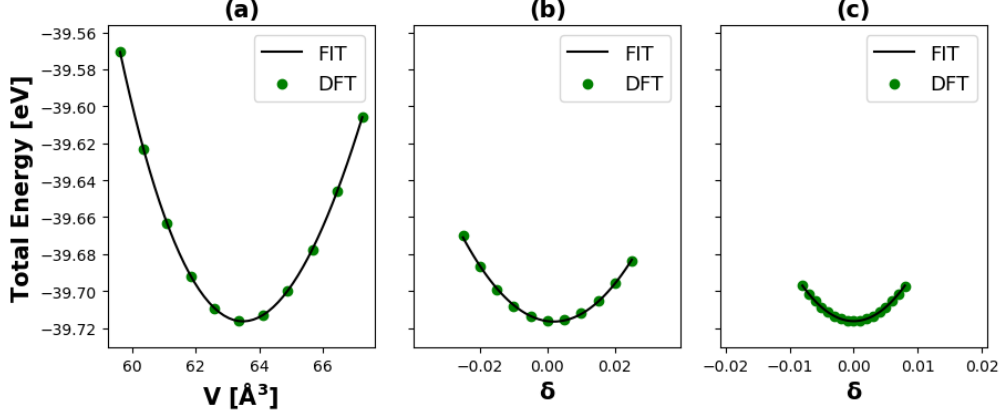
*Figure 7. Illustration of fitting the elastic constants from DFT calculations. (a) shows the fit of the Murnaghan equation of state to obtain the bulk modulus. (b) shows the fit to determine the constant $B_{11}$. (c) shows the fit to extract the constant $B_{44}$.*

## 5.4 Strain-Phonon Coupling

Next, the parametrization of the strain-phonon coupling parameters will be described in more detail. The approach for this is based on the work of Nishimatsu et al. [27], but different methods are used for the required DFT calculations. The approach shown in the work of Nishimatsu et al. [27] is related to the application of the VTM method, where the relaxation of the unit cell is taken into account for the calculation of the local-mode self-energy. Using this approach, the final parameters of the local-mode self-energy have to be re-calculated by excluding the contributions from strain. In the case of the VTM method, the calculation of the strain-phonon coupling can be performed directly from the corresponding DFT calculations. In this work, however, the local-mode self-energy was parameterized in a conventional way by applying displacements according to the eigenvectors. For the calculation of the strain-phonon coupling, additional DFT calculations are now necessary, which take into account the dependence of the local amplitude on the deformation of the unit cell. The approach chosen here is described in detail in Publication 2 and its associated Supplemental Material, although the theoretical foundations will be supplemented here. The standard approach for the calculation of the strain-phonon coupling parameters $B_{1xx}$, $B_{1yy}$ and $B_{4yz}$ is a simultaneous displacement by the local amplitude $\boldsymbol{u}$ and application of different deformations of the unit cell. In this thesis, this approach was first followed, and viable parameters were extracted, as evident in Publication 2. However, this approach is based on predefined deformations of the unit cell and does not allow for additional relaxations of the unit cell. Therefore, in the course of this thesis, another approach was developed, which should provide an improved description of the strain-phonon coupling. The basis for the revised method is the ISIF=6 relaxation in VASP, which allows a full relaxation of the unit cell with fixed internal coordinates of the atoms.

Subsequently, relaxed unit cells for a particular displacement according to a local amplitude $\boldsymbol{u}$ can be calculated. Therefore, in the case of BT, structures with different amplitudes of $\boldsymbol{u}$ in <011> direction were first constructed and then calculated using VASP and the ISIF=6 tag. Subsequently, the approach developed by Nishimatsu et al. [27] can be applied to calculate the coupling parameters. To use this approach, the parameters $a_{xx}$, $a_{xy}$, and $a_{zz}$ must first be determined from the Equations 112, 113, and 114 by fitting. This is the quadratic dependence on the local amplitude $u$ of the strain. The local amplitudes $u$ in these equations correspond to the <011> direction. The calculation of the strain values $e_{xx}$, $e_{xy}$ and $e_{zz}$ can be done from the relaxed structures of the DFT calculations. The required amplitudes $u$ can be calculated analogously considering the atomic displacements and the applied eigenvectors. A visualization of such fits to the DFT data for the case of BT can be found in the Supplemental Material of Publication 2.

$$e_{xx} = a_{xx}u^2 \tag{112}$$

$$e_{xy} = a_{xy}u^2 \tag{113}$$

$$e_{zz} = a_{zz}u^2 \tag{114}$$

Once the parameters $a_{xx}$, $a_{xy}$, and $a_{zz}$ are determined, the strain-phonon coupling parameters $B_{1xx}$, $B_{1yy}$ and $B_{4yz}$ can be calculated by Equations 115, 116, and 117. Here, the elastic constants from the previous chapter are used. As listed in Publication 2, the application of the ISIF=6 method yields slightly different coupling constants. However, since this method takes into account the full relaxation of the unit cell, these values are relied upon for application in the effective Hamiltonian.

$$B_{1xx} = -4B_{11}a_{xx} + 2(B_{11} - 2B_{12})a_{zz} \tag{115}$$

$$B_{1yy} = -4B_{12}a_{xx} - 2B_{11}a_{zz} \tag{116}$$

$$B_{4yz} = -2B_{44}a_{xy} \tag{117}$$

## 5.5 Short-Range and Long-Range Interactions

Finally, the parameterization of the short-range and long-range interactions will be discussed. For the calculation of the long-range interaction, in general, just the determination of the Born effective charge associated with the local mode $\boldsymbol{u}$ is required. The basis for this is Equation 74, where the Born effective charges of the atoms and the eigenvector of the local mode $\boldsymbol{u}$ are used to calculate an effective charge for the mode. The required Born effective charges for the individual atoms can be determined by DFT calculations. Here, again, two approaches can be used. First, a finite-difference method can be employed by IBRION=6 in VASP. Second, the charges can also be determined via the tag IBRION=8 by density functional perturbation theory (DFPT). Both methods give results with excellent agreement. However, for the values in this thesis, the results of the DFPT method were used. The value of the Born effective charge associated with the local mode $\boldsymbol{u}$ is listed in Publication 2. The calculation of the short-range parameters is a somewhat more complex task since the phonon band structure must be evaluated at different reciprocal points. The basis for the determination of the inter-site parameters $j_1$ to $j_7$ is provided by Equations 79 to 85. Chapter 4.3.6 also describes the reciprocal points required for the parameterization. To calculate the band structure for these points, the *phonopy* [104,105] package was used. This package allows quite straightforwardly to compute the entire phonon band structure by the employment of supercells. The starting point is the cubic structure of BT represented by the 5-atom unit cell. Using the *phonopy* package, a supercell of size 2x2x2 was constructed based on this unit cell. Subsequently, the force constants have to be calculated for this supercell. These can be calculated either by the finite-difference method (IBRION=6) or by DFPT (IBRION=8). Furthermore, a k-grid of size 4x4x4 was employed for the DFPT calculation. The resulting force constants are then used to calculate the band structure using *phonopy*. Here, it is of utmost importance to set the masses of the respective atoms to one to be consistent with the definition of the effective Hamiltonian. For details on the derivation and definition of the effective Hamiltonian, please refer to Chapter 4.3.2. Actually, not the whole phonon band structure has to be calculated by *phonopy*, but only the highly symmetric points in the reciprocal space defined in Chapter 4.3.6. Subsequently, the eigenvalues which are applied in Equations 79 to 85 can be extracted from the DFT data. Again, the correct unit of the eigenvalues must be ensured. Once the eigenvalues have been calculated, the inter-site parameters $j_1$ to $j_7$ can be determined by solving the linear problem given by Equations 79 through 85. The parameters for BT applying the procedure from above are listed in Publication 2. Furthermore, a value for the parameter $\kappa_2$ is determined by solving the linear

equation system. This parameter is used for the local-mode self-energy but has to be corrected first, as described in Chapter 4.3.6. The correction ensures that the potential energy surface is described consistently by all involved energy terms. As explained in the theoretical part, Chapter 4.3.6, the calculation of all quadratic terms is performed by a redefined potential $\widetilde{\Phi}_{\alpha\beta}^{quad}(\boldsymbol{k})$ in reciprocal space. This potential contains the quadratic term of the local-mode self-energy, the short-range interaction as well as the long-range interaction. It is now possible to calculate the eigenvalues of this potential and to evaluate the dispersion along the highly symmetric directions in the reciprocal space. The result is shown in Figure 8, where half the value of the eigenvalues is plotted. Here, in principle, the subspace of the phonon band structure is mapped, which is given by choice of the local basis in the effective Hamiltonian. Furthermore, a minimum of the band structure is found at the Γ-point, which indicates the ferroelectric behavior of BT.
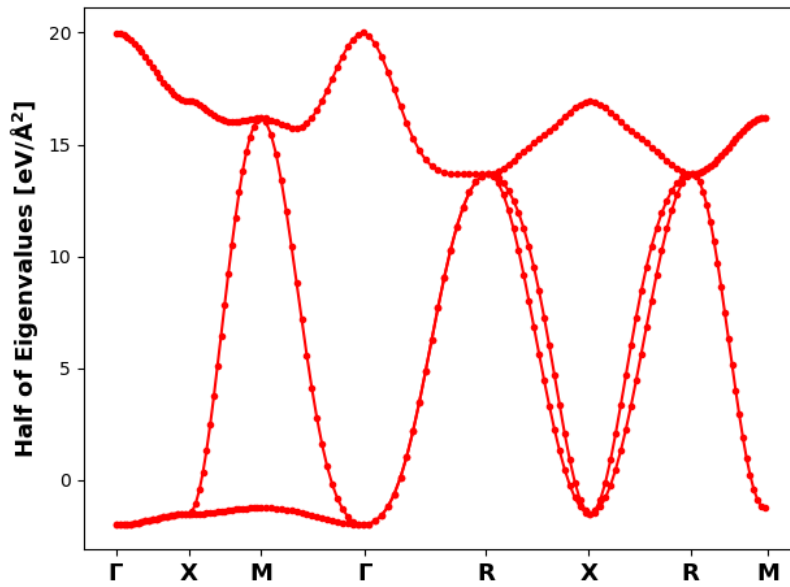


*Figure 8. Visualization of half of the eigenvalues associated with the quadratic interaction matrix $\widetilde{\Phi}_{\alpha\beta}^{quad}(\boldsymbol{k})$ for the case of BT. The dispersion shows the subspace of the phonon band structure taken into account by choice of the local basis within the effective Hamiltonian.*

# 6 Parametrization of Ba(Zr$_x$Ti$_{1-x}$)O$_3$

In this chapter, the parameterization of Zr substituted BT (Ba(Zr$_x$Ti$_{1-x}$)O$_3$, BZT) will be discussed. Such a substitution is called homovalent substitution since Zr$^{4+}$ is substituted for Ti$^{4+}$ at the B-site of BT. Essentially, Publication 3 and its Supplemental Material cover the parameterization and application of the extended effective Hamiltonian. However, any additional details of the parameterization which were not covered in Publication 3 will be discussed here. The basis for the parameterization is, again, DFT calculations using the VASP package. The valence electronic configurations of the species Ba, Ti, and O are the same as explained in Chapter 5. For the species Zr, a configuration of 4s$^2$ 4p$^6$ 5s$^2$ 4d$^2$ (12 valence electrons) was used. Furthermore, convergence tests were first performed to obtain suitable values for the k-grid size and cutoff energy. For the cutoff energy, convergence tests revealed that a value of 520 eV is sufficient for all required calculations. Furthermore, convergence tests were also performed for the k-grid, and the following values were determined for the different supercells. For calculations of the primitive 5-atom unit cell, a k-grid of size 8x8x8 was determined. For supercells of size 2x2x2, a k-grid of size 4x4x4 was applied. Finally, for calculations with supercells of size 3x3x3, a k-grid of size 3x3x3 was chosen. For the stop criterion of the SCF (self-consistent field) cycle, the EDIFF tag within VASP was set to $10^{-8}$ eV for all calculations.

## 6.1 Kinetic Energies

The first correction which is applied in the extended effective Hamiltonian is the adaptation of the kinetic energies via the effective masses. The effective mass can be calculated for the chosen local mode $\boldsymbol{u}$ by Equation 65 by multiplication with the squared entries of the corresponding eigenvector. For the case of the extended effective Hamiltonian, an adapted effective mass can now be calculated as a function of the local chemical composition. For the case of pure BT, an effective mass associated with the local mode $\boldsymbol{u}$ of $M^*_{dipole}(Ti) = 38.148$ a.m.u. results, as listed in Publication 2. For the effective mass associated with the acoustic mode, a value of $M^*_{acou}(Ti) = 46.638$ a.m.u. is obtained. Here, the corresponding eigenvector used for the computation is related to a pure translation. In order to account for substituted unit cells, an alternative effective mass can be calculated. For the case of Zr substituted at the B-site of BT, the effective mass related to the local mode $\boldsymbol{u}$ results to $M^*_{dipole}(Zr) = 64.148$ a.m.u. Analogously, the effective mass for the acoustic mode can be estimated and yields $M^*_{acou}(Zr) = 55.309$ a.m.u. For the effective masses associated with the acoustic mode, the calculation is unambiguous since the eigenvector is the same in both cases. However, the choice for the calculation of the effective masses associated with the local mode $\boldsymbol{u}$ must be discussed.

It should be noted that the determination of the effective mass for pure BT is unambiguous due to the eigenvector of the local mode $\boldsymbol{u}$. However, if Zr is substituted, the corresponding eigenvector changes and an unambiguous determination is no longer trivial. Two approaches can be followed here to determine an effective mass. The first and simplest approach is to use the eigenvector of $\boldsymbol{u}$, which results from the parent system. This is a good approximation and describes, in principle, the mass change related to pure BT. This method was adopted in this thesis. A more elaborate method would be to calculate a supercell with substituted unit cells and to investigate the eigenvectors. Here, it can be filtered out how the local unit cell containing Zr couples with the surrounding Ti unit cells to the local mode $\boldsymbol{u}$. From that investigation, an adapted mass can be calculated from the subspace of the total eigenvector of the supercell. However, also here, the choice of the eigenvector is not unique and is subject to the observer. All in all, the approach adopted here delivers reasonable results, as described in detail in Publication 3.

## 6.2 Adapted Local-Mode Self-Energy

The next correction for which the parameters are to be determined is the local-mode self-energy. The theoretical basis for this correction has already been explained in detail in Chapter 4.4.2, where the parameters $\Delta\kappa_{2,\sigma}$, $\Delta\alpha_\sigma$, $\Delta\gamma_\sigma$ and $\Delta k_{1,\sigma}$ to $\Delta k_{4,\sigma}$ have been introduced. In principle, for this correction, the change of the local-mode self-energy upon substitution of different species at specific lattice sites is considered with respect to the parent system BT. For the case of Zr substituted at the B-site of BT, the following DFT calculations can now be applied for the parameterization. The conventional parameterization for the parent system is performed with displacements of the atoms from the initial cubic phase by using the eigenvector of the local mode $\boldsymbol{u}$. For the estimation of the correction parameters, the same eigenvector has to be applied in order to relate the energy difference to the parent system. For that purpose, a 5-atom unit cell of cubic BT is constructed first. The lattice parameters amount to those of the cubic BT. Then, the B-site is replaced by Zr, and different displacements of the atoms in the <001>, <011>, and <111> directions are constructed. The displacements are calculated using the eigenvector of the local mode $\boldsymbol{u}$ from Publication 2. Following, the generated structures are calculated using DFT, and the total energies are extracted. The total energies can, in turn, be used to determine the parameters by fitting Equations 67, 68, and 69. The parameters obtained are listed in Publication 3 and its Supplemental Material. The corresponding DFT data, as well as the fits, are presented in Figure 9. Here it can be seen that, in contrast to BT, no double-well potential is formed upon substitution by Zr. Rather, a strong increase in energy is observed with increasing displacement by means of the eigenvector. That is, if a Zr ion is placed instead of Ti,

this Zr ion intends to remain in the center of the unit cell. This observation is in excellent agreement with the results of Mentzer et al. [32], who take advantage of this fact in the construction of their effective Hamiltonian. It is also intuitive that $Zr^{4+}$ does not cause polar B-site displacements, if its larger size compared to $Ti^{4+}$ (0.72 Å for $Zr^{4+}$ vs. 0.605 Å for $Ti^{4+}$). Furthermore, it is also observed that the displacements in the different directions <001>, <011>, and <111> are equivalent. Another important point is the correct application of the parameter $\Delta\kappa_{2,\sigma}$ which has to be chosen in a way that the potential energy surface is described consistently. For this purpose, a calculation via DFPT can be performed to adjust the values for the phonon band structure. More about this calculation will be discussed in the next chapter.
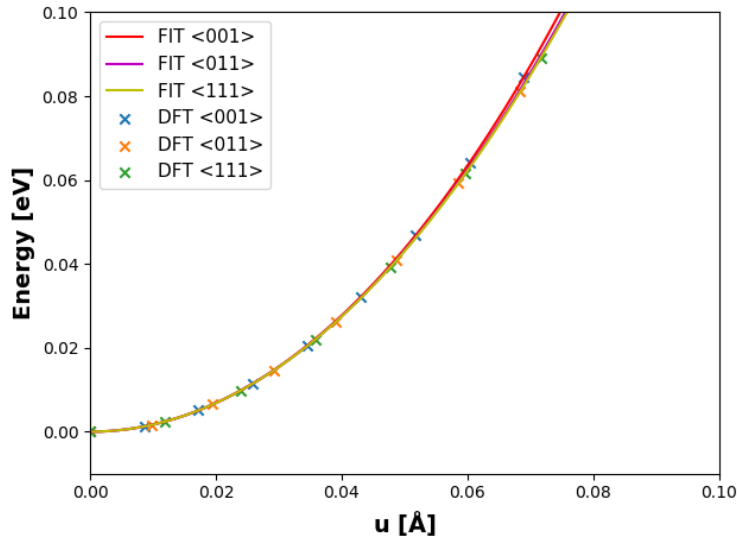


*Figure 9. Visualization of local-mode self-energy when B-site is substituted with Zr. The plot shows the obtained total energies from DFT and the respective fits to estimate the correction parameters.*

## 6.3 Modified Long-Range Interaction

In this chapter, the determination of Born effective charges to describe the correction of long-range interactions will be discussed. In general, a dipole-dipole interaction is used in the effective Hamiltonian to describe the long-range interaction. The only parameter which can be adapted for a correction is the Born effective charge associated with the local mode $\boldsymbol{u}$. That means, if instead of Ti at the B-site, Zr is substituted, a new effective charge has to be calculated. In principle, there is a lot of leeway for its determination since it is not clearly defined how this new effective charge is to be calculated. For example, the unit cell of the parent system or the relaxed unit cell containing the substituted atom can be used as the initial structure. Furthermore, supercells could also be used to determine the effective charges. In this thesis, however, the approach chosen is to relate all corrections to the parent system BT and its cubic phase. Therefore, the parent cubic structure is also used to calculate the new Born effective

charges. That is, a 5-atom unit cell with the lattice parameters for pure cubic BT was chosen as the initial structure. Then, the B-site was replaced by Zr, and a supercell of size 2x2x2 was constructed. This supercell was calculated by means of DFPT to obtain the Born effective charges. Furthermore, the entire phonon band structure along the high-symmetry directions was also calculated, as described in Chapter 5.5. The Born effective charges of the individual atoms can now be used to calculate a new effective charge by Equation 74 using the eigenvector associated with the local mode $\boldsymbol{u}$. The choice of eigenvector was made to relate the correction to the parent system. The estimated value for the Born-effective charge for a Zr-containing unit cell is listed in the Supplemental Material of Publication 3. Furthermore, the phonon band structure can be used to solve the linear system of equations from Chapter 4.3.6. Here, the choice of the input eigenvalues has to be done in such a way as to be consistent with the chosen modes of the base system. In principle, the symmetry of the individual modes must be analyzed and compared with the original parameterization. Afterward, analogous to Chapter 5.5, the short-range parameters $j_1$-$j_7$ as well as the parameter $\Delta\kappa_{2,\sigma}$ can be calculated. This parameter now represents the adapted correction parameter for the local-mode self-energy. The short-range parameters obtained here describe, in principle, the interaction between Zr unit cells in a system with 100% Zr content. However, these parameters are not used in the following since these corrections are taken into account via the auxiliary spring system.

## 6.4 Auxiliary Spring System

The most time-consuming part of the parameterization of the extended effective Hamiltonian is the determination of the parameters for the auxiliary spring system. The mathematical description of this term has been discussed in detail in Chapter 4.4.3, and now the necessary DFT calculations for the parameterization shall be discussed. In general, the parameterization of this term is described in detail in Publication 3 and its Supplemental Material. However, more details and some challenges of parameterization shall be explained at this point. Fundamentally, supercells must be used for the parameterization, and these must be calculated with different arrangements of the substituents. In contrast to parameterizations in the literature [29–31], 3x3x3 supercells are used here instead of 2x2x2 supercells. This has the advantage that an improved description of the interactions can be achieved within the periodic boundary conditions. First of all, the determination of the parameters $Q_{T,R}(\sigma_T)$ for the corrections to the local mode $\boldsymbol{u}$ will be discussed. The basis for all calculations is, again, the cubic structure of BT. In principle, it is sufficient for the 1$^{st}$ order terms in Chapter 4.4.3 to construct supercells with different arrangements of substituents and to determine the occurring forces by DFT. Thus, the required parameters can be extracted rather straightforwardly. In this

thesis, however, a more elaborate way was chosen, and also the displacement of the atoms from their original positions was considered. Such an approach has the advantage that also higher order terms can be included analogously. That is, first, for example, a Ti atom was replaced by a Zr atom in the supercell. Consequently, the local unit cell, which is located as a direct neighbor to the Zr atom, was displaced by means of the eigenvector of the local mode $\boldsymbol{u}$. Since a B-centered basis was chosen for the local mode, the displacement of the atoms can be performed as follows. For Ti at the B-site, the full displacement due to the chosen amplitude is used. For the oxygen atoms, which are each adjacent to a directly neighboring unit cell and thus shared, half the amplitude is applied. For Ba atoms located at the A-site, one-eighth of the amplitude must be applied since these atoms are adjacent to eight neighboring unit cells. This procedure averages the local displacement of the atoms, which is a good approximation for the actual displacement. The displacement of the atoms of the local unit cell is carried out in the direction in which the substituted unit cell is located. Furthermore, this procedure is repeated for substituted neighbors up to the third nearest neighbor shell. Subsequently, the total energies, as well as the occurring forces, can be calculated by means of DFT. In order to calculate the interactions with respect to the parent system BT, the same displacements and associated calculations must be carried out for the pure system. In this way, the parameters can be determined in such a way that the interactions already considered in the effective Hamiltonian of pure BT do not occur twice. The calculation of the parameters from Chapter 4.4.3 can be done by two methods. The first method is rather simple, and a linear function is fitted to the total energies determined by DFT. Here, as already mentioned, the reference energy of the pure system must be subtracted first. The second method is a bit more complicated but allows the inclusion of higher orders of the correction term. Such higher orders are not employed in this thesis but could be relevant for future parameterizations. The calculation of the parameters is based on the occurring forces. For this purpose, an effective force is calculated for each unit cell from the individual forces of the atoms. This effective force can be determined analogously to the procedures described above for applying the displacements. Consequently, a fit process can be applied to determine the parameters of the auxiliary spring system from the effective forces. The parameters $Q_{T,R}(\sigma_T)$ thus obtained for the interaction between Zr and Ti unit cells in the context of the auxiliary spring system are listed in Publication 3 and its Supplemental Material. Next, the parameterization of the parameters $S_{T,R}(\sigma_T)$ for the corrections to the dimensionless variables $\boldsymbol{w}$ will be discussed. Basically, the parameterization is quite similar to that of $Q_{T,R}(\sigma_T)$, but certain procedures have to be adapted. Also in this case, in principle, the calculation of supercells substituted with different arrangements would be sufficient for the

determination of the parameters. However, the displacement of the atoms was also taken into account here. Since the dimensionless variables $w$ are defined by an A-centered basis, the displacement must be handled differently. That is, the Ba atom is in the center of the A-centered basis and is therefore displaced with the full amplitude. The B-site here is now shared by eight unit cells, and thus only one-eighth of the amplitude is applied for the Ti atoms. The oxygen atoms, in turn, are shared by four unit cells so that a quarter of the amplitude is used. The eigenvector which is used for the displacement is here a pure translation of the atoms. Analogous to the determination of $Q_{T,R}(\sigma_T)$, different arrangements of substituted atoms are considered and the total energies as well as the forces are calculated by means of DFT. The determination of the parameters $S_{T,R}(\sigma_T)$ can be done by fitting a linear function to the total energies. Furthermore, in this case, after the study of the obtained parameters and to simplify the total energy, only interactions up to the first neighbor shell were considered. The parameters for the correction of the dimensionless variable $w$ can be found in the Supplemental Material of Publication 3.

# 7  Parametrization of Ba($Nb_x$Ti$_{1-x}$)O$_3$

In this chapter, the parameterization for Nb substituted BT (Ba($Nb_x$Ti$_{1-x}$)O$_3$, BNT) shall be discussed. Essentially, Publication 3 and its Supplemental Material cover the basic aspects of the parameterization, but again additional details will be provided here. The basis for the following parameterization is provided by DFT calculations with the settings of Chapters 5 and 6. The valence electronic configurations of the species Ba, Ti, and O are equivalent to those of Chapter 5. For the species Nb, a configuration of $4s^2 4p^6 5s^2 4d^3$ for Nb (13 valence electrons) was used. In principle, the parameterization of Nb substituted BT is similar to that of BZT but differs in some aspects. In this case, the substitution is also carried out at the B-site of BT, but unlike Zr, Nb has a different oxidation state compared to Ti. That is, here, Ti$^{4+}$ is substituted with Nb$^{5+}$ and one can speak of a heterovalent substitution. Furthermore, the different oxidation state demands a suitable charge compensation scheme in order to maintain charge neutrality within the material. In principle, vacancies at the A-site or B-site of the BT structure can be considered for such a charge compensation. In the work of Veerapandiyan et al. [40] it is demonstrated by Raman spectroscopy and DFT calculations that the most probable charge compensation in BNT happens via Ti vacancies (V$_{Ti}$). That is, for the substitution of four Nb ions, one Ti vacancy is generated in turn. Taking these Ti vacancies into account, the chemical formula for BNT can be rewritten as Ba($Nb_x\square_{1/4x}$Ti$_{1-5/4x}$)O$_3$. In this thesis, this finding is built upon, and a third species is introduced for the parameterization of BNT accounting for these Ti vacancies. More on this topic about Ti vacancies in BNT can be found in Publication 1 and its Supplemental Material. The inclusion of Ti vacancies implies that, for the parameterization of the effective Hamiltonian, the corrections for an additional species have to be introduced. First of all, however, the inclusion of the Ti vacancies shall be explained in more detail since some changes in the design of the corrections result from observations. As a first step, DFT calculations were performed on a supercell of size 3x3x3, calculating the phonon band structure for pure BT substituted with one Ti vacancy. From that, it is possible to investigate the coupling between the relevant local modes included in the parent effective Hamiltonian with the induced change in the phonon band structure due to the presence of Ti vacancies. As a result, it can be observed that the relevant modes of the surrounding unit cells couple with a local nonpolar vibration of the oxygen atoms in the vacancy unit cell. This observation can be used to obtain an approximation for the local modes of the Ti vacancy unit cell. Subsequently, the local modes centered on unit cells with Ti vacancies are frozen and thus do not exhibit an active dipole moment. However, this approximation does not mean that the influence of Ti vacancies on the surrounding unit cells is not considered. Rather, it is shown in Publication 1 that such Ti

vacancies exert a significant influence on the surrounding unit cells. To incorporate these effects into the effective Hamiltonian, the auxiliary spring system is used. In summary, the following corrections must be applied for the parameterization of the BNT system. For the species Nb, the parameterization is analogous to the previous chapter on BZT, but the correct charge compensation must be used in the required DFT calculations to ensure the correct oxidation state of $Nb^{5+}$. For the species $V_{Ti}$, only the auxiliary spring system has to be parameterized since the other corrections are omitted due to the approximation made above.

## 7.1 Kinetic Energies

The correction of the kinetic energy for unit cells having Nb instead of Ti on the B-site can be done by adaptation of the effective mass associated with the local mode $u$. The basis for this is Equation 65, where the individual atomic masses are multiplied by the squared entries of the eigenvector associated with $u$. In principle, the choice of the eigenvector, as discussed in detail in Chapter 6.1, is also ambiguous, but since the reference to the parent system BT should be established, the eigenvector associated with the local mode $u$ is used. This eigenvector is discussed in detail in Publication 2. The effective mass associated with the local mode for Nb unit cells obtained by this approach yields $M^*_{dipole}(Nb) = 65.157$ a.m.u. The calculation of the effective mass for the dimensionless variables $w$ can be performed analogously to the procedure described in Chapter 6.1. Here, again, the eigenvector associated with a pure translation is applied for the calculation. As a result, an effective mass of $M^*_{acou}(Nb) = 55.646$ a.m.u. can be determined. A calculation of the effective masses for unit cells that have Ti vacancies is not required since these are considered static in the effective Hamiltonian. An overview of the parameters listed here can be found in the Supplemental Material of Publication 3.

## 7.2 Adapted Local-Mode Self-Energy

As the next step, the correction parameters for the local-mode self-energy for the case of Nb substitution will be discussed. The procedure chosen here is already described in detail in Chapter 6.2, but a suitable charge compensation must be applied here for the required DFT calculations. The starting point for the parameterization is again the 5-atom unit cell of pure BT with the cubic lattice parameters. Subsequently, Ti is replaced by Nb, and different displacements of the atoms in the <001>, <011>, and <111> directions are applied. The displacements of the atoms are also calculated in this instance by the eigenvector associated with the local mode $u$ to establish the reference to the parent system. The constructed structures can subsequently be calculated by DFT to determine the total energies. Here, however, the number of electrons must be adjusted via the NELECT tag in VASP to match the actual

oxidation state of $Nb^{5+}$. That is, for the case of a 5-atom unit cell with Nb at the B-site, the total electron number is set to NELECT=40. Here, one electron was removed from the system to artificially reproduce the assumed charge compensation by the Ti vacancies. The number of total electrons results from the valence electronic configurations as listed at the beginning of Chapters 5 and 7. A disadvantage of this method is that localized charges, which would normally occur due to the presence of Ti vacancies, cannot be considered. Instead, a homogeneous background charge is assumed for the system under consideration. However, for the calculation of the correction parameters, the application of this method is sufficient after a detailed study. This study compared MD simulations to DFT calculations on supercells of size 5x5x5, taking into account the complete defect complex (4 Nb's and 1 Ti vacancy). Therefore, this approach was used to calculate the structures described above by DFT in order to subsequently determine the correction parameters by fitting Equations 67, 68, and 69. The resulting parameters are listed in the Supplemental Material of Publication 3. Complementary to Publication 3, a visualization of the associated DFT data and fits is provided in Figure 10. Compared to BZT, the local-mode self-energy is flatter in the case of BNT, which can also be attributed to the different ionic radii of the two species. Furthermore, a deviation between the individual spatial directions <001>, <011>, and <111> is observed, indicating a preferential displacement direction of the Nb ion in the BT unit cell. Finally, analogous to BZT, the correction parameter $\Delta\kappa_{2,\sigma}$ must be chosen to describe the potential energy surface consistently with respect to the parent system. Consequently, a DFPT calculation, as described in the next chapter, has to be performed, and a corrected parameter has to be extracted.
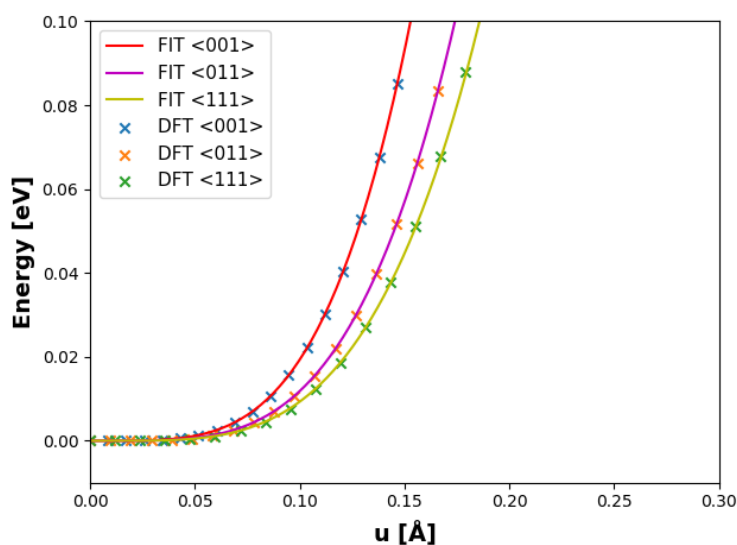


*Figure 10. Visualization of local-mode self-energy when B-site is substituted with Nb. The plot shows the obtained total energies from DFT and the respective fits to estimate the correction parameters.*

## 7.3 Modified long-range interaction

In this chapter, the correction of the long-range interaction for the case of BNT will be discussed. In principle, only the Born effective charge associated with the local mode $\boldsymbol{u}$ has to be calculated for this purpose. However, to provide the necessary Born effective charges, DFPT calculations are required. These were performed using supercells of size 2x2x2, again assuming the underlying structure to be cubic BT. Subsequently, the B-sites in the supercell were replaced by Nb ions, and a DFPT calculation was performed. Here, the charge compensation from the previous chapter was again applied to ensure the correct oxidation state of Nb. The Born effective charges can be read directly from the results of the DFPT calculation. Then, an effective charge associated with the local mode $\boldsymbol{u}$ can be calculated using Equation 74. The choice of the eigenvector corresponding to $\boldsymbol{u}$ has already been discussed in detail in Chapter 6.3. The resulting effective charge can be found in the Supplemental Material of Publication 3. Furthermore, the DFPT calculation was used to calculate the entire phonon band structure along the high-symmetric points in reciprocal space for the supercell substituted by Nb. In the following, the procedure from Chapter 6.3 was applied to solve the linear system of equations from Chapter 4.3.6. Also, in this case, suitable eigenvalues have to be taken from the phonon band structure to be in agreement with the choice of the local basis of the effective Hamiltonian. The choice must be made in such a way as to take into account the modes with the correct symmetries. From this, a new correction parameter $\Delta\kappa_{2,\sigma}$ for the local-mode self-energy can then be extracted.

## 7.4 Auxiliary Spring System

Finally, the auxiliary spring system for BNT must be parameterized. In principle, the interactions between the species Ti, Nb and $V_{Ti}$ must now be taken into account. That means there are interactions between Ti - Nb, Ti - $V_{Ti}$, Nb - $V_{Ti}$, and Nb - Nb. In the context of the effective Hamiltonian, these interactions are naturally to be understood between the individual unit cells through their local modes. The parametrization of this term is already described in detail in Publication 3, as well as its Supplemental Material, but additional details will be explained here. The basis for parameterization here is formed by 3x3x3 supercells with the lattice parameters of pure cubic BT. These supercells are subsequently used to determine the interactions between the local mode $\boldsymbol{u}$ at different arrangements of the substituents. That is, for the calculation of the interaction between Ti and Nb unit cells, an Nb ion is introduced into the supercell. Then, the local unit cell, which is located as a direct neighbor to the substituted atom, is displaced by the application of the eigenvector of the local mode $\boldsymbol{u}$. The approach chosen to calculate the individual atomic displacements is analogous to Chapter 6.4. This procedure is

repeated to account for the various interactions up to the third nearest neighbor shell. Subsequently, the constructed structures are calculated by means of DFT, again paying attention to charge compensation. That is, if only one Nb ion is introduced into the supercell, the total number of electrons must be adapted accordingly since no compensation via Ti vacancies takes place. In the case of one Nb ion in the supercell, one electron must be removed to reach the right oxidation state. Furthermore, the same displacements have to be calculated for pure BT to establish the reference to the parent system. The interaction parameters $Q_{T,R}(\sigma_T)$ can then be determined from the results by fitting the total energy. An alternative way to determine these parameters was elaborated in Chapter 6.4. The determination of the parameters for the interaction between Ti and $V_{Ti}$ can be carried out analogously to the procedure explained above. However, charge compensation must again be applied here in the associated DFT calculations, which can be accomplished by adjusting the total number of electrons. The Ti vacancy would normally compensate for the four surplus electrons of four Nb ions, so for the supercell containing only one Ti vacancy, the number of electrons must be increased by this amount. For the calculation of the interactions between Nb and $V_{Ti}$, two lattice sites of the 3x3x3 supercell have to be substituted, and then the atoms of the Nb unit cell have to be displaced by applying the eigenvector of the local mode $\boldsymbol{u}$. The associated parameters can then be calculated again by fitting the total energy. The correction for the dimensionless variables $\boldsymbol{w}$ is to be carried out analogously to the procedure described in Chapter 6.4. Here, the displacement of the atoms through the A-centered basis has to be performed, and the eigenvector of a pure translation has to be applied. Furthermore, the total energies can be calculated with DFT and the interaction parameters $S_{T,R}(\sigma_T)$ can be determined by fitting the total energy. It should be noted again that appropriate charge compensations for the DFT calculations must be used for the respective supercell calculations. All parameters discussed here are listed in the Supplemental Material of Publication 3.

# 8 Publications

This chapter represents the core of this dissertation, featuring the four publications that were published as a part of it. The publications, along with their supplemental material, have been included in this chapter in the format of their respective journals. Additionally, a brief summary of each publication will be provided, highlighting the contributions made by the author.

- **Publication 1:**

   **Title:** Origin of Relaxor Behavior in Barium-Titanate-Based Lead-Free Perovskites

   **Authors:** Vignaswaran Veerapandiyan, Maxim N. Popov, **Florian Mayer**, Jürgen Spitaler, Sarunas Svirskas, Vidmantas Kalendra, Jonas Lins, Giovanna Canu, Maria Teresa Buscaglia, Marek Pasciak, Juras Banys, Pedro B. Groszewicz, Vincenzo Buscaglia, Jiri Hlinka, Marco Deluca

   **Journal:** Advanced Electronic Materials

   **Status:** Published

   **DOI:** 10.1002/aelm.202100812

   **Personal Contribution:** Elaboration of the DFT study of the atomistic effects in BZT and BNT. This includes the calculation of the local volume change as well as the electrical potential change. Interpretation and preparation of the results to support the experimental data. Reading and feedback on the entire manuscript as well as writing the theoretical chapter on the above results. Preparing the manuscript for publication and helping with revisions.

- **Publication 2:**

   **Title:** Improved description of the potential energy surface in $BaTiO_3$ by anharmonic phonon coupling

   **Authors: Florian Mayer**, Maxim N. Popov, Donald M. Evans, Stephan Krohns, Marco Deluca, Jürgen Spitaler

   **Journal:** Physical Review B

   **Status:** Published

   **DOI:** 10.1103/PhysRevB.106.064108

   **Personal Contribution:** Idea and conceptualization of the revision and modification of the effective Hamiltonian. This included the derivation of the new formalism and all necessary intermediate steps. All DFT calculations for the parameterization of the effective Hamiltonian. The preparation of many scripts for the determination of the parameters. Testing of the developed approach as well as continuous revision. All MD

simulations for testing as well as for the final results in the paper. Preparation of the results and formulation of the final approach. Writing the first draft of the manuscript, including all chapters. Many more calculations after the revision of the paper, such as ab-initio MD simulations.

- **Publication 3:**

  **Title:** Finite-temperature investigation of homovalent and heterovalent substituted $BaTiO_3$ from first principles

  **Authors: Florian Mayer**, Maxim N. Popov, Petr Ondrejkovic, Jiri Hlinka, Jürgen Spitaler, Marco Deluca

  **Journal:** Physical Review B

  **Status:** Published

  **DOI:** 10.1103/PhysRevB.106.224109

  **Personal Contribution:** Idea and conceptualization of the extension of the effective Hamiltonian for substituted systems. This includes the formulation of the theoretical approach as well as the implementation using Fortran. All DFT calculations for the parameterization of the effective Hamiltonian. Preparing all scripts to create the necessary structures for the DFT calculations. Testing of the approach by means of MD simulations and continuous revision. Processing and analysis of the results. Writing the first draft of the manuscript.

- **Publication 4:**

  **Title:** Hidden phases in homovalent and heterovalent substituted $BaTiO_3$

  **Authors: Florian Mayer**, Marco Deluca, Maxim N. Popov

  **Journal:** Physical Review B

  **Status:** Published

  **DOI:** 10.1103/PhysRevB.107.184307

  **Personal Contribution:** Implementation of the necessary functions for the application of the THz pulses. All MD simulations, as well as the corresponding evaluation of the data. Processing of the data and analysis of the results. Writing the first draft of the manuscript. Further simulations after revision of the manuscript.

## 8.1   Publication 1

# Origin of Relaxor Behavior in Barium-Titanate-Based Lead-Free Perovskites

Vignaswaran Veerapandiyan[1], Maxim N. Popov[1], Florian Mayer[1], Jürgen Spitaler[1], Sarunas Svirskas[2], Vidmantas Kalendra[2], Jonas Lins[3], Giovanna Canu[4], Maria Teresa Buscaglia[4], Marek Pasciak[5], Juras Banys[2], Pedro B. Groszewicz[3,6], Vincenzo Buscaglia[4], Jiri Hlinka[5], Marco Deluca[1],

[1]*Materials Center Leoben Forschung GmbH, Roseggerstrasse 12, 8700 Leoben, Austria*
[2]*Faculty of Physics, Vilnius University, Sauletekio al. 9, 2040 Vilnius, Lithuania*
[3]*Institute of Physical Chemistry, Technische Universität Darmstadt, 64287, Darmstadt, Germany*
[4]*CNR-ICMATE, Institute of Condensed Matter Chemistry and Technologies for Energy, National Research Council of Italy, Via de Marini 6, 16149, Genoa, Italy*
[5]*Institute of Physics, Academy of Sciences of the Czech Republic, Na Slovance 2, Praha 8, Czech Republic*
[6]*Department of Radiation Science and Technology, Delft University of Technology, Delft 2629JB, Netherlands.*

Corresponding author: marco.deluca@mcl.at

**Abstract:**

It is well known that disordered relaxor ferroelectrics exhibit local polar correlations. The origin of localized fields that disrupt long range polar order for different substitution types, however, is unclear. Currently, it is known that substituents of the same valence as $Ti^{4+}$ at the B-site of barium titanate lattice produce random disruption of Ti-O-Ti chains that induces relaxor behavior. On the other hand, investigating lattice disruption and relaxor behavior resulting from substituents of different valence at the B-site is more complex due to the simultaneous occurrence of charge imbalances and displacements of the substituent cation. The existence of an effective charge mediated mechanism for relaxor behavior appearing at low (< 10%) substituent contents in heterovalent modified barium titanate ceramics is presented in this work. These results will add credits to the current understanding of relaxor behavior in chemically modified ferroelectric materials and also acknowledge the critical role of defects (such as cation vacancies) in lattice disruption, paving the way for chemistry-based materials design in the field of dielectric and energy storage applications.

# Origin of Relaxor Behavior in Barium-Titanate-Based Lead-Free Perovskites

*Vignaswaran Veerapandiyan, Maxim N. Popov, Florian Mayer, Jürgen Spitaler, Sarunas Svirskas, Vidmantas Kalendra, Jonas Lins, Giovanna Canu, Maria Teresa Buscaglia, Marek Pasciak, Juras Banys, Pedro B. Groszewicz, Vincenzo Buscaglia, Jiri Hlinka, and Marco Deluca\**

It is well known that disordered relaxor ferroelectrics exhibit local polar correlations. The origin of localized fields that disrupt long-range polar order for different substitution types, however, is unclear. Currently, it is known that substituents of the same valence as $Ti^{4+}$ at the B-site of barium titanate lattice produce random disruption of Ti—O—Ti chains that induces relaxor behavior. On the other hand, investigating lattice disruption and relaxor behavior resulting from substituents of different valence at the B-site is more complex due to the simultaneous occurrence of charge imbalances and displacements of the substituent cation. The existence of an effective charge mediated mechanism for relaxor behavior appearing at low (<10%) substituent contents in heterovalent modified barium titanate ceramics is presented in this work. These results will add credits to the current understanding of relaxor behavior in chemically modified ferroelectric materials and also acknowledge the critical role of defects (such as cation vacancies) in lattice disruption, paving the way for chemistry-based materials design in the field of dielectric and energy storage applications.

## 1. Introduction

Recent demands for miniaturized energy storage systems highlight the need for devices combining high power with high recoverable energy density, in order to accommodate rapid energy intake from ambient sources and to provide long-term energy supply.[1,2] Ferroelectric ceramic capacitors have intrinsically high-power density due to fast charge reorientation mechanisms under E-field application. In pure $BaTiO_3$ (BTO)

perovskites, this is provided by the long-range correlation of B-site ($Ti^{4+}$) cation displacements. This correlation encompasses also strains up to the microscale, and is embodied by the appearance of ferroelectric domains.[3] Upon field cycling, as needed for charging–discharging the capacitor, ferroelectric domains switch in the direction of the applied field, thereby dissipating the associated elastic energy as heat. These losses are one of the main origins of the low recoverable energy density in this class of materials.[4]

One often pursued strategy to increase the recoverable energy density of ceramic capacitors is thus to avoid elasticity-driven losses by disembodying electric charge from elastic strain through the disruption of the long-range correlation of $Ti^{4+}$ displacements.[2] When BTO is substituted at the perovskite B-site, in fact, the correlation of Ti—O—Ti chains is broken;[5] consequently, ferroelectric domains cease to permeate the whole lattice and are rather confined to nanoscale polar regions, whose size, correlation and distribution depends on substituent type and concentration.[6] The absence of long-range strain correlation limits the losses associated with elastic energy and slims down the polarization–electric field (P–E) hysteresis loop, thereby increasing the recoverable energy density,[2] provided that the achievable polarization at the maximum

V. Veerapandiyan, M. N. Popov, F. Mayer, J. Spitaler, M. Deluca
Materials Center Leoben Forschung GmbH
Roseggerstrasse 12, Leoben 8700, Austria
E-mail: marco.deluca@mcl.at

S. Svirskas, V. Kalendra, J. Banys
Faculty of Physics
Vilnius University
Sauletekio al. 9, Vilnius 2040, Lithuania

The ORCID identification number(s) for the author(s) of this article can be found under https://doi.org/10.1002/aelm.202100812.

J. Lins, P. B. Groszewicz
Institute of Physical Chemistry
Technische Universität Darmstadt
64287 Darmstadt, Germany

P. B. Groszewicz
Department of Radiation Science and Technology
Delft University of Technology
Delft 2629JB, Netherlands

G. Canu, M. T. Buscaglia, V. Buscaglia
CNR-ICMATE
Institute of Condensed Matter Chemistry and Technologies for Energy
National Research Council of Italy
Via de Marini 6, Genoa 16149, Italy

M. Pasciak, J. Hlinka
Institute of Physics
Academy of Sciences of the Czech Republic
Na Slovance 2, Praha 8 18200, Czech Republic

**ADVANCED
SCIENCE NEWS**
www.advancedsciencenews.com

**ADVANCED
ELECTRONIC
MATERIALS**
www.advelectronicmat.de

applicable electric field remains closer to (or is higher than) that of pure BTO. There is thus a delicate equilibrium between disruption of ferroelectric long-range order and the retention of a high permittivity level that has to be considered when designing new compositions for high energy density ceramic capacitors. Explaining the nature of the polarization disruption for different chemical modifications of BTO is thus of paramount importance for tuning macroscopic material properties such as energy density.

Barium titanate can be substituted at the B-site either with homovalent (4+, as for instance in $BaZr_xTi_{1-x}O_3$—BZT) or heterovalent (5+, like in $BaNb_xTi_{1-x}O_3$—BNbT) substituent ions. By increasing the substituent content, first the temperatures of the phase transitions between the ferroelectric phases increase and merge with the decreasing Curie temperature ($T_c$) in a so-called "triple point" or "tricritical point."[5] For higher substituent contents, a diffuse phase transition (DPT) from rhombohedral ferroelectric to cubic paraelectric phase[7,8] is attained (overlapping of sequential phase transitions). For even higher substitutions, relaxor behavior develops: the material presents Vogel–Fulcher-like frequency dispersion of the permittivity maximum ($T_m$), which—unlike $T_c$—is no longer related to a structural phase transition.[9] Whereas on the macroscopic scale relaxors exhibit a cubic symmetry, which is incompatible with lattice polarization,[10] the structure remains polar at a local scale.[11] The level of substitution for both the DPT and transition to a relaxor state also depends on ionic size and on substituent type (hetero- versus homovalent).[2,7,12]

Relaxors were initially treated with models based on the local compositional fluctuation resulting from different ions spatially distributed in equivalent crystallographic positions.[13] The most widely accepted theory behind the origin of the frequency dispersed dielectric anomaly is the presence of local polarization correlations at the nanoscale (polar nanoregions, PNR), which form from an uncorrelated high-temperature state at the so-called Burns temperature, $T_B$, and then grow with decreasing $T$ until saturation of polar correlations occurs at a freezing temperature, $T_f$, well below ambient conditions.[14] The existence of PNRs in all relaxor systems and their relationship with chemical order/disorder is debated, and there are recent trends to frame evidence behind relaxor behavior with a more fundamental PNR-free argument.[15] Another approach invokes the presence of random electric fields, with different strength and fluctuation dynamics that should originate from chemical substitution.[6] According to Imry and Ma, different ions in the lattice are subjected to different random electric fields as a result of chemical substitution and associated charge-compensating defects, such as vacancies, and the strength of the electric field plays a crucial role in the appearance of relaxor behavior.[16] This model is known for its fundamental approach in addressing the unclear aspects of relaxors, and can be successfully applied to both homo- and heterovalent substituted systems, without necessarily invoking PNRs. One more common theory is based on the striking similarities of highly substituted relaxors to dipolar glasses.[17] The most recent "slush model" demonstrated a universal relaxor behavior on different material classes and claimed that the high density of domain walls and especially low angle domain walls that result in strong local electric fields are the major contributors to relaxor behavior.[18]

Most of the models developed so far target widely studied lead-based relaxor systems, hence they might need adjustments to be applied to lead-free relaxors based on BTO. In BTO, in fact, the polarization is related to the displacement of the $Ti^{4+}$ cation and relaxor behavior is expected to be B-site driven, whereas in the lead-based case the high permittivity comes from displacements of the A-site $Pb^{2+}$ cation.[19] At present, there is no detailed insight on how relaxor behavior emerges in BTO-based systems in response to different types of substitutions.

In this study we demonstrate that the disruption of the long-range spatial correlation of B-site displacements, which is the driving mechanism for the emergence of relaxor behavior in BTO-based perovskites, has a very different origin if homovalent or heterovalent substituents are concerned. We explain here the role of defects and defect-induced disorder in the onset of relaxor behavior in a heterovalent ($Nb^{5+}$-substituted) BTO system (BNbT), and compare it against the well-studied $Zr^{4+}$-substituted BTO-based homovalent relaxor system (BZT). The discussion we provide is supported by local structural methods, such as Raman and nuclear magnetic resonance (NMR) spectroscopy, evidencing the evolution of lattice disorder upon substitution in both systems, and the presence of defect-related phonon modes in the Raman spectra—calculated by the recently developed spherical averaging method[20]—to reveal the effect of substitution type in the local structure. In addition, density functional theory (DFT) simulations of unit cell volume, strain and electrostatic potential landscape showing the effect of defect dipoles in supercells of the substituted BTO lattice are presented. In summary, this work describes the difference between homovalent and heterovalent relaxors from a combined experimental–theoretical viewpoint, and thus unravels the underlying nature of polarization disruption in chemically modified BTO-based materials.

## 2. Results and Discussion

### 2.1. Chemically Modified BTO

As a prime example of how relaxor behavior differs in homovalent- and heterovalent-substituted BTO, we consider systems in which the $Ti^{4+}$ (B-site) cation is substituted by either $Zr^{4+}$ or $Nb^{5+}$. BZT is a homovalent-substituted solid solution where the $Zr^{4+}$ cation has a larger ionic radius than $Ti^{4+}$ (0.72 Å versus 0.605 Å, respectively[21]). BNbT (with formula bruta $BaNb_xTi_{1-5x/4}O_3$, taking into account a B-site charge compensation scheme) presents heterovalent substitution where $Nb^{5+}$ has a similar ionic radius (0.65 Å[21]) to $Ti^{4+}$. These differences (be it the oxidation states and/or ionic radii) define the predominant mechanism by which these substituents disrupt the BTO lattice continuity: $Zr^{4+}$ will introduce strain, likely without strong contributions from charge distribution, whereas in the case of $Nb^{5+}$, a charge mediated mechanism is likely to play a predominant role. This is also suggested by the necessary presence of charge-compensation schemes for $Nb^{5+}$ incorporation: either Ba or Ti vacancies, represented in Kroger–Vink notation as $V''_{Ba}$ and $V''''_{Ti}$, respectively, must be present in BNbT.

The phase evolution presents significant differences in BZT and BNbT. **Figure 1** shows the phase diagram of both systems highlighting the Curie temperature ($T_c$) for FE compositions

**2100812 (2 of 11)**

101

**ADVANCED
SCIENCE NEWS**
www.advancedsciencenews.com

**ADVANCED
ELECTRONIC
MATERIALS**
www.advelectronicmat.de
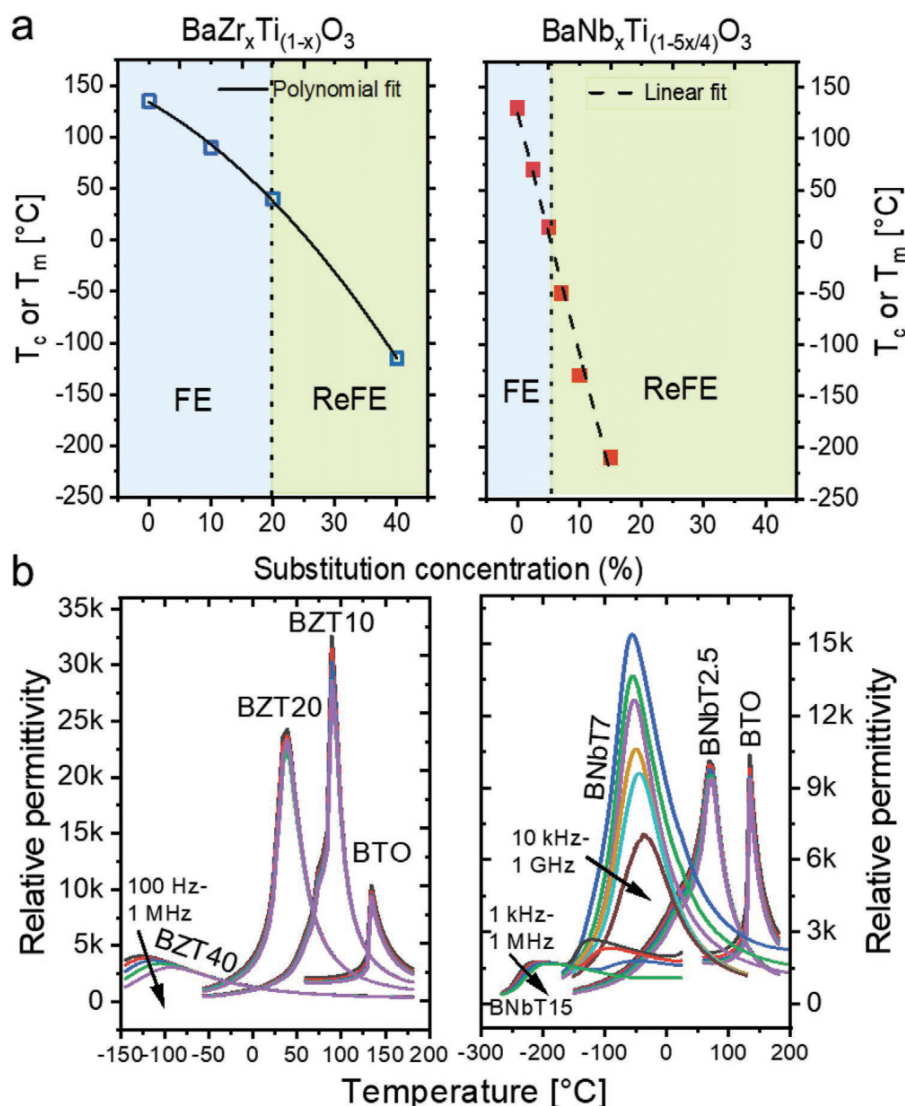
**Figure 1.** a) Curie temperature (FE) or temperature of permittivity maximum (relaxor) of BZT and BNbT samples, clearly depicting the rapid and early onset of relaxor behavior in BNbT compared to BZT. b) Temperature dependent relative permittivity at different frequencies for BZT and BNbT, demonstrating relaxor behavior by the frequency dispersion of permittivity for 40% Zr and 7% Nb substituent concentration, respectively.

and the temperature of relative permittivity maximum ($T_m$) for relaxor compositions, together with dielectric spectroscopy data taken on our samples. The temperature-dependent permittivity at different frequencies is presented to highlight the ferroelectric to relaxor transition, and corresponding results on pure BTO are presented for reference. Our results are in accord with previous findings: Increasing substituent content disrupts ferroelectricity in both systems, as signaled by the shift of the permittivity maximum to lower temperatures and its overall decrease in magnitude. While a diffuse phase transition toward the high-temperature cubic phase is observed for BZT at a substituent content of $x = 0.10$, a lower $Nb^{5+}$ content ($x = 0.025$) is sufficient in case of BNbT. Relaxor behavior, marked by the frequency dispersion of permittivity maximum, is attained for higher substituent contents. Interestingly, the threshold for relaxor

behavior is very different in the heterovalent system compared to the homovalent case, with a substitution concentration of $x = 0.07$ for BNbT and $x \approx 0.25$ in BZT, the latter threshold being observed at similar substituent contents also in other homovalent systems like $BaCe_xTi_{1-x}O_3$ and $BaHf_xTi_{1-x}O_3$.[5,22] This "early" onset of relaxor behavior is a common trait of heterovalent systems,[2] even if substitution is on the A-site like the case of $La^{3+}$ (ref. [23]).

Since the driving force for relaxor behavior is the breaking of the long-range spatial correlation of $Ti^{4+}$ (B-site) cation displacements in the BTO lattice, we can envisage that different substituents will have a different role in inducing disorder at the perovskite B-site. Recent studies on homovalent-substituted systems, for example, with $Ce^{4+}$ (ref. [5]) and $Zr^{4+}$ (ref. [8]), confirmed that large homovalent cations promote a nonpolar (cubic) unit

102

**ADVANCED
SCIENCE NEWS**

www.advancedsciencenews.com

**ADVANCED
ELECTRONIC
MATERIALS**

www.advelectronicmat.de

cell, and thus act as Ti—O—Ti chain breaking centers. Since the off-center displacement of $Ti^{4+}$ is related to the amount and distribution of the substituting homovalent cations,[24] the latter act as ferroelectric domain pinning centers, effectively breaking down larger domains into smaller polar entities. As soon as the substituent content is increased, these domains are expected to shrink in size down to the atomic scale. Previous studies on heavily substituted homovalent relaxor compositions (like $BaZr_{0.50}Ti_{0.50}O_3$[25]) suggested in fact that PNRs are centered on $Ti^{4+}$ clusters of few unit cells. At lower substitution level, non-polar regions coincident with the substituents are embedded into a polar matrix as long as there is sufficient long-range correlation between polar Ti—O—Ti chains. It is somewhat clear that in BTO-based systems, the influence of the substituting cations on $Ti^{4+}$ displacements and on their ability to spatially correlate is thus the determining factor for the appearance of relaxor behavior. While for the homovalent case an ionic-size driven "steric hindrance" or "random strain field" effect is easily envisaged, a different mechanism for polarization disruption must exist in heterovalent substituted systems like BNbT, where the similar ionic size between $Ti^{4+}$ and $Nb^{5+}$ precludes a strong strain-driven effect from appearing. Such alternative mechanism shall also explain in particular why the effect of heterovalent substituents is decisively more effective than homovalent ones in disrupting the long-range FE order, as evidenced in Figure 1 from the viewpoint of dielectric properties.

### 2.2. Dielectric Relaxation in Heterovalent-Substituted BTO

In heterovalent-substituted BNbT, merging of phase transitions without dielectric dispersion is evident already for BNbT2.5, as shown in Figure 1b. For increasing substituent concentration (for 7% and above), two dielectric relaxations appear as a function of temperature: one at $T_m$ (relaxor-like) and a second one at higher temperatures, the latter clearly evident only at 15% $Nb^{5+}$ content. **Figure 2** shows a detailed temperature and frequency dependent analysis of dielectric relaxation for the BNbT15 relaxor composition. The second relaxation (marked as region II) occurs in BNbT15 in the temperature range of −150 °C to RT and hence overlaps with the relaxor-like relaxations in BNbT7 and BNbT10, whose $T_m$ are −50 and −130 °C respectively, at 1 kHz. For this reason, it is clearly visible only in BNbT15 together with the relaxor-like dispersion of $T_m$ (marked as region I) with dispersion that extends at least up to 30 GHz, as shown in Figure 2a.

The progressive increase in the real part of permittivity with decreasing temperature at lower frequencies indicates another competing relaxation process (cf., Figure 2b). As shown in Figure 2c, for almost all temperatures within the region II, the breadth of the imaginary permittivity peak did not change with a decrease in temperature, which is in contrast to a relaxor-like dispersion, in which the relaxation progressively broadens with decreasing temperature.[26] Hence, the relaxation in region II is not related to dynamic polarization fluctuations, but rather to a Debye-type relaxation, which could in principle originate either from charge imbalances located on lattice defects[27] or from interfacial (i.e., Maxwell–Wagner type) free charge carriers.[28] More detailed information about the relaxor-like dispersion in region I and the Debye-like relaxation in region II is given in the Supporting Information.

### 2.3. Lattice Disorder in Heterovalent-Substituted BTO

**Figure 3**a,b reports the Raman spectra of all investigated compositions of BZT and BNbT. The assignment of Raman modes
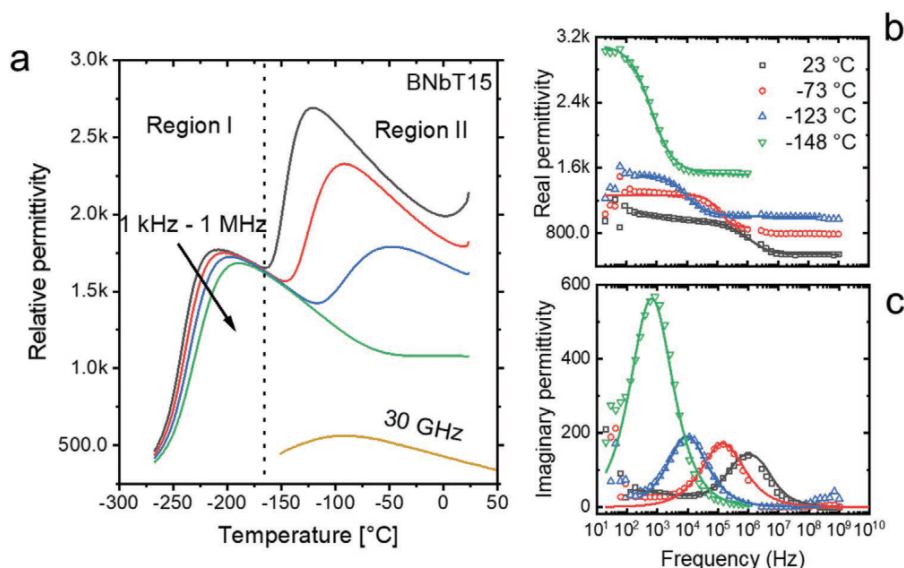


**Figure 2.** a) Dielectric relaxation of $BaNb_{0.15}Ti_{0.81}O_3$ as a function of temperature at different frequencies highlighting two dielectric relaxations differentiated as region I and region II as marked by a vertical dotted line. The partition line shown in the figure is merely a guidance to distinguish the two relaxations. b,c) Complex permittivity of $BaNb_{0.15}Ti_{0.81}O_3$ as a function of frequency at different temperatures in region II, highlighting the fact that the breadth of imaginary permittivity peak is unchanged with decreasing temperature, unlike relaxor-like dispersion.
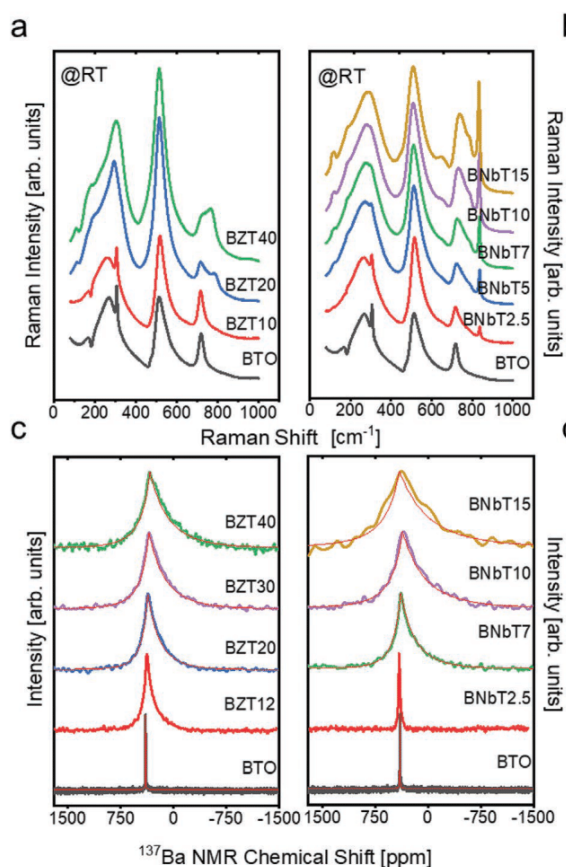
**Figure 3.** Composition dependent Raman spectra of a) $BaZr_xTi_{1-x}O_3$ and b) $BaNb_xTi_{1-5x/4}O_3$ at room temperature. The Raman spectra of BTO at the bottom is added for reference and several substitution-induced Raman bands are evident in both material systems when compared to BTO. The disappearance of the Raman band at ≈300 cm⁻¹ implies a loss of long-range ferroelectric order, that is evident for >20% of $Zr^{4+}$ and >7% $Nb^{5+}$ concentration. $^{137}Ba$ NMR static spectra of c) $BaZr_xTi_{1-x}O_3$ and d) $BaNb_xTi_{1-5x/4}O_3$ samples recorded at 117 and 133 °C, respectively, both above the Curie temperatures of all samples. The presence of broad NMR peaks is related to the existence of disorder in the lattice.

in pure BTO is described in detail in previous work.[20] From the weakening of the ferroelectric-related mode around 300 cm⁻¹ (ref. [29]), it is evident that in BZT ferroelectric long-range order is lost between 20% and 40% of $Zr^{4+}$ content, whereas in BNbT this occurs at a lower concentration of heterovalent B-site cation, namely between 5% and 7% of $Nb^{5+}$ content, in agreement with dielectric measurements.

In addition to the typical first-order Raman bands of BTO, there are several other bands that can be associated with either $Zr^{4+}$ or $Nb^{5+}$ substitution.[8,12,30] Interestingly, the spectral bands of BNbT are broader than those of BZT (cf., the spectra for 10% substituent content). The spectral width of the Raman bands indicates the correlation length of phonon propagation, and sharp bands with well-defined peak maxima imply a greater correlation length, which if seen in the reciprocal lattice corresponds to pure gamma-point phonons. In contrary, a broad spectral signature suggests phonon activation outside the

Brillouin zone center, which in a real lattice is associated with the onset of lattice disorder.

The local structural disorder evidenced by broad Raman bands in BZT and BNbT—stronger in the latter—can be quantified by means of NMR spectroscopy.[31] In Figure 3c,d we report $^{137}Ba$ NMR spectra of BNbT and BZT samples recorded at 133 and 117 °C, respectively. $^{137}Ba$ NMR is a sensitive probe to distortions of the local structure, as the reported line width is directly related to gradients of the electric field (EFG), a local structure parameter at the nuclear site. The local structure distortion responsible for an EFG ≠ 0 can be either caused by nearby defects (i.e., substituents) or by symmetry breaking in a specific polymorph or polar structure. To suppress the influence of the latter, and hence quantify the lattice disorder in an unbiased manner, samples were analyzed above $T_c$, as no polar displacements should be observed in the cubic, paraelectric phase. This fact can be illustrated in BTO, for which the linewidth follows the temperature-dependent macroscopic polarization and exhibits a negligible line width above $T_c$,[32] also shown in Figure S4, Supporting Information. In short, in the paraelectric state—where electrical polarization ($P$) do not prevail—BTO displays a narrow linewidth of 600 Hz (FWHM), as shown in Figure 3c,d, in which dipolar interactions are the sole contributors to the linewidth with an EFG = 0 (i.e., $C_Q = 0$).

For BNbT, the $^{137}Ba$ NMR linewidth increases from 1.5 kHz in BNbT2.5 to 45.0 kHz in BNbT15, as consequence of increasing structural distortion for higher substituent concentration (Figure 3d and Figure S3, Supporting Information). The wider lines observed for BNbT in the paraelectric state indicate that, locally, a significant deviation from cubic symmetry is present. An analogous trend is observed for the BZT samples (Figure 3c), albeit at a higher substituent content compared to BNbT. Here, it is worth mentioning that $^{137}Ba$ NMR spectra of chemically modified samples exhibit a broad asymmetric peak unlike the line shape observed in the ferroelectric phases of BTO.[33] This featureless line shape results from the substitution-induced chemical disorder and the accompanying distribution of EFG components for the local environment of $Ba^{2+}$ across the lattice, which was previously reported for A-site substituted BTO.[34]

Nonzero EFG above $T_c$ can be directly related to contributions from static and dynamic disorder in the lattice. The Czjzek model expresses the distribution of EFG components in terms of the mean quadrupolar coupling constant ($C_Q$),[35] a parameter that reflects the extent of local structural disorder for the $Ba^{2+}$ site in BZT and BNbT. Considering the fact that spectra are recorded in the paraelectric phase, the mean $C_Q$ value can be interpreted as a measure of the local structural disorder caused by the substituents only, an assumption that can be reinforced by the absence of temperature dependent evolution of linewidth for BNbT samples above $T_c$, as reported in Supporting Information (cf., Figure S3, Supporting Information). **Figure 4** reports the mean $C_Q$ for all investigated compositions, and highlights that $Nb^{5+}$ is much more efficient in disrupting lattice order than $Zr^{4+}$ when substituted at the B-site. While a steep increase in mean $C_Q$ values is observed for small $Nb^{5+}$ contents, a much higher amount of $Zr^{4+}$ is required to produce the same effect. For instance, a 7% $Nb^{5+}$ substitution introduces as much disorder as that of 20% $Zr^{4+}$ in the BTO lattice, as

**ADVANCED
SCIENCE NEWS**
www.advancedsciencenews.com

**ADVANCED
ELECTRONIC
MATERIALS**
www.advelectronicmat.de
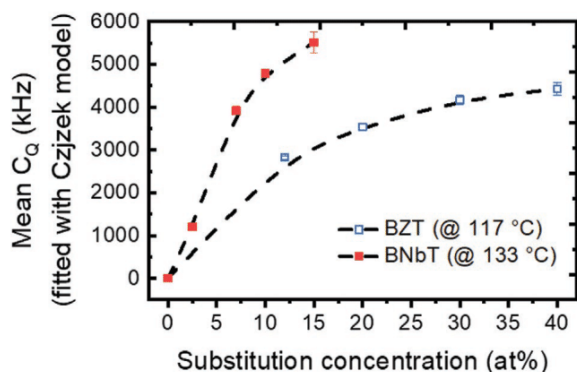
**Figure 4.** The mean $C_Q$ extracted from the [137]Ba NMR for BZT and BNbT samples, depicting a drastic increase in the structural disorder for BNbT (closed symbols) compared to BZT (closed symbols). The mean $C_Q$ values were extracted from spectra recorded at 117 and 133 °C for BZT and BNbT samples, respectively, which is above the Curie temperatures of all samples.



**Figure 5.** Experimental Raman spectra of a) BZT40 and b) BNbT15 relaxor systems recorded at −185 °C along with the calculated Raman spectra. The experimental data show broad spectral signatures specific to locally disordered relaxor systems. The calculated Raman spectra not only replicate all the experimental Raman bands but are also able to reproduce some of the underlying spectral signatures that are difficult to deconvolute in the experimental data.

reflected by the mean $C_Q$ of 3917 kHz for BNbT7 which is close to a value of 3537 kHz for BZT20. It is interesting to note that $C_Q$ values above ≈4000 kHz mark a threshold for occurrence of relaxor behavior, regardless of substituent type. This value lies slightly above the $C_Q$ = 2800 kHz observed for room-temperature BTO in the $P4mm$ polymorph.[33] Moreover, these results show that the amount of local structure disorder induced by $Nb^{5+}$ substitution is larger than that induced by $Zr^{4+}$ addition, and confirm the initial supposition on the basis of the Raman linewidths. This striking difference in ability to induce lattice disorder between homovalent and heterovalent cations hints at a completely different mechanism at play in each substitution type.

## 2.4. Charge-Compensating Defects in Heterovalent Relaxors

From the NMR analysis and the broader Raman modes we evinced that heterovalent substitution induces stronger lattice disorder in BTO compared to the case of homovalent substitution. Furthermore, dielectric spectroscopy data also evidenced the presence of a peculiar dielectric relaxation at temperatures higher than the relaxor-like dispersion, which is ascribed to a Debye-like relaxation compatible with the presence of charge imbalances caused by point defects in the lattice. In this section, we employ a combination of DFT-simulated Raman spectra and DFT calculations of different point defect models to elucidate the nature of these defects. Furthermore, this approach allows us to explore their role in the macroscopic dielectric properties of heterovalent modified BTO by analyzing their effect on the local structure with respect to lattice strain and electric potential and, ultimately, to the disruption of Ti−O−Ti correlations related to electrical polarization.

In **Figure 5**, the Raman spectra of BZT40 and BNbT15, both measured at −185 °C, are presented, with some Raman modes highlighted that are associated with lattice defects in chemically substituted BTO systems.[36] In particular, mode 4 (at ≈750 cm^{−1}) was related previously to the difference in ionic radius of the substituting cation compared to the $Ti^{4+}$ host ion.[37] Following

this reasoning, mode 4 should be closer to mode 3 in BNbT than in BZT, which clearly is not the case.

In addition, we notice in BNbT the presence of two extra modes (2 and 5, at ≈630 cm^{−1} and ≈830 cm^{−1}, respectively), one of which (mode 5) was previously reported in both BNbT[12] and La-substituted $BaTiO_3$.[37] In the BNbT case, mode 5 was associated to a localized $BO_6$ oxygen breathing vibration in the vicinity of $Nb^{5+}$ cations.[12] In the $La^{3+}$ case, on the other hand, this mode was associated with $V_{Ti}''''$ providing charge compensation for the $La^{3+}$ addition.[37] We also recently demonstrated that this mode is absent in dipole-compensated systems (such as $BaGa_xTa_xTi_{1−2x}O_3$ and $BaGa_xNb_xTi_{1−2x}O_3$), where formation of B-site cation vacancies is limited.[36,38] Mode 5 is also clearly composition-dependent and displays no temperature dependence (cf., Figure 3 and Figure S5, Supporting Information), contrary to what would be expected from long-range oxygen sublattice modes. Hence, it is suggested that peak 5 can be attributed to a localized mode originating from charge-compensating B-site defects in heterovalent-substituted BTO. The same suggestion applies to mode 2, which is also present only in heterovalent-substituted BTO. This mode was previously associated to the presence of stress-induced hexagonal BTO phase,[29,39] but this may apply only to nanostructured or thin film BTO, and not to the present bulk case.

To clarify the origin of extra modes 2 and 5, we calculated the full Raman spectral signature of both BZT40 and BNbT15 within 3 × 3 × 3 supercells, following the spherical averaging method we developed recently based on ab initio Raman-active phonon calculations.[20] In BZT, each supercell was constructed with either $Ti^{4+}$ or $Zr^{4+}$ at the B-site in the right proportion to realize 40% $Zr^{4+}$ amount. Whereas, for BNbT the presence of either 1 $V_{Ti}''''$ and 4 $Nb^{5+}$ at the B-site or 1 $V_{Ba}''$ at the A-site and 2 $Nb^{5+}$ at the B-site was considered for the 3 × 3 × 3 supercell. Figure 5 reports the calculated Raman spectra for BZT40 and BNbT15 compared against the respective experimental spectra

105

(at −185 °C). Most of the experimental Raman spectra of polycrystalline materials show asymmetric Raman bands due to the convolution of $A_1/E$ peaks, LO/TO peaks and oblique phonon dispersion[20] and also significant peak broadening in chemically modified systems because of the lattice disorder, as discussed in the previous section. Hence, the calculated spectra here show spectral signatures that are impossible to deconvolute in the measured spectra at −185 °C. This notwithstanding, the spectral signature above 600 cm$^{-1}$—where all the substitution-related Raman modes are present—is clearly replicated in the calculated Raman spectrum. Notably, in BNbT the extra Raman modes 2 and 5 are only seen when supercells were constructed with the $V_{Ti}''''$ charge compensation scheme, which allows to unambiguously attribute their origin to B-site cation vacancies alone. This is in contrast to low donor concentrations and acceptor doping, where results from literature indicate that heterovalent doping is compensated by electrons.[40,41]

Following this, we evaluated the sum of the square atomic displacements for the O atoms around the $V_{Ti}''''$ in BNbT15, to highlight their contributions to the Raman-active phonons, as reported in **Figure 6**. From this analysis it is clear that the contribution is stronger in the region of occurrence of the two defect modes (Mode 2 and mode 5—labeled as "B" and "C" in Figure 6). Actually, the contributions of these oxygens are also pronounced for a mode just below 200 cm$^{-1}$, albeit masked here in experimental spectra by superposition with neighboring peaks. In particular, the sole contributor of mode 5 is the oxygen neighbors of $V_{Ti}''''$ (also evident from Video S1, Supporting Information) and thus can be unambiguously assigned as a localized $BO_6$ oxygen breathing mode in the vicinity of a $V_{Ti}''''$ (not in the vicinity of Nb$^{5+}$ atoms as previously speculated by Farhi et al.[12]). This confirms the previous reports of this mode in La$^{3+}$ substituted BTO (where $V_{Ti}''''$ are the preferred charge compensation scheme and mode 5 is present),[36,37] and provides an explanation for its absence in dipole-compensated BTO,[36,38] where $V_{Ti}''''$ are severely restricted.

On the basis of the evidence for the existence of $V_{Ti}''''$ defects, we note that each vacancy compensates for four Nb$^{5+}$ substituent cations, according to the defect chemical reaction below:

$$2Nb_2O_5 \rightarrow 4Nb_{Ti}^* + V_{Ti}'''' + 10\,O_O^x \tag{1}$$
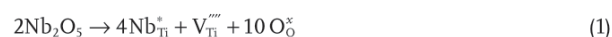
Intuitively, $Nb_{Ti}^{5+}$ shall form clusters around Ti vacancies, due to Coulombic attraction. In an attempt to determine the precise distribution of Nb$^{5+}$ cations in the vicinity of $V_{Ti}''''$, we considered two possible cluster geometries (see Figure S6, Supporting Information) and showed that the formation energy becomes identical for both considered cluster configurations with increasing supercell size (see Figure S7, Supporting Information). This means that the lattice is charge compensated, but locally charge imbalances from lattice defects are present, which may impact on the macroscopic dielectric properties as a function of temperature and applied electric field frequency, irrespective of cluster geometries.

Further arguments supporting the effect of presence of $V_{Ti}''''$ resulting from charge compensation for BNbT are found by the contrasting dielectric relaxation between BZT and BNbT in the highest substituent content studied. Figure 2 and Figure S8, Supporting Information show the temperature dependent permittivity response in relaxor compositions, that is, BNbT15 and BZT40, respectively. The relaxor behavior is evidenced from the low temperature frequency dispersion ($f$ dependent $T_m$) of $\varepsilon_r$ in both compositions. As evident, there are some discrepancies in the dielectric response between BZT40 (which is in accord with previous literature[7]) and BNbT15, most notably the double relaxation we already discussed. There are however further striking differences in BNbT compared to previous literature.[12] **Figure 7** shows the dielectric permittivity response of BNbT15 at 1 MHz with a Ba vacancy ($V_{Ba}''$-Kroger–Vink notation) as charge compensation scheme (dotted line), extracted from Farhi et al.[12] (henceforth ascribed as BNbT15-$V_{Ba}$), whereas the solid line shows the frequency dependent dielectric permittivity response of BNbT15 from the present work, which involves $V_{Ti}''''$ as charge compensation scheme (BNbT15-$V_{Ti}$). First of all, in BNbT15-$V_{Ba}$, the double relaxation is absent. Then, the $T_m$ at 1 kHz is 63 °C lower for BNbT15-$V_{Ti}$ compared to BNbT15-$V_{Ba}$ (cf., Figure 7a,b), the $\varepsilon_r$ value is larger for BNbT15-$V_{Ba}$ compared to BNbT15-$V_{Ti}$ and the diffusivity of the $\varepsilon_r$ response is larger for BNbT15-$V_{Ti}$ compared to BNbT15-$V_{Ba}$ (cf., Figure 7a). Here it is important to note that although Farhi et al. claim $V_{Ba}''$ as a major charge compensation scheme, it is highly unlikely



**Figure 6.** a) Measured Raman intensities for BTO and BNbT15 at −185 °C and b) the calculated Raman spectra of BTO and BNbT. c) Eigenmode analysis for six oxygen atoms around the titanium vacancy, where the sum of the square displacement of the six oxygen atoms is plotted for each mode. This analysis clearly describes the increased contribution of oxygen atoms to Raman-active phonons near the defect related modes that are marked as B and C.

106

**ADVANCED
SCIENCE NEWS**

www.advancedsciencenews.com

**ADVANCED
ELECTRONIC
MATERIALS**

www.advelectronicmat.de

**Figure 7.** a) Temperature dependent dielectric response of BNbT15 at 1 MHz BNbT15-$V_{Ti}$ (solid line) and BNbT15-$V_{Ba}$ (dotted line) demonstrating very different macroscopic dielectric properties depending on the charge compensation scheme. b) The composition-dependent relative permittivity maximum ($T_c$ or $T_m$) for BNbT15-$V_{Ti}$ (solid line) and BNbT15-$V_{Ba}$ (dotted line) (b).

from a processing standpoint to achieve such high substitution concentration without incorporating $V_{Ti}''''$, and we envisage simultaneous occurrence of both $V_{Ti}''''$ and $V_{Ba}''$ in that case. This can be reaffirmed by the presence of mode 5 in Raman spectra reported in that work.[12]

The above results not only prove that defects—especially vacancies—play a crucial role in the local structure, but also that they severely impact the resulting macroscopic dielectric properties. In fact, vacancies either at A or B site can have widely different properties from atomic to macroscopic scale (cf., Figures 5 and 7). The rate at which $T_m$ is lowered as a function of $Nb^{5+}$ concentration in case of BNbT15-$V_{Ti}$ (cf., Figure 7b) suggests that heterovalent substitution is an effective disruptor of long-range order not primarily because of ionic size difference, but rather because $V_{Ti}''''$-$Nb^{5+}$ defect complexes produce strong localized random fields. The difference in the diffusivity and sharp decrease in relative permittivity for BNbT15-$V_{Ti}$ can be related to the increase in the degree of heterogeneity at the B-site, which is the key crystallographic site that contributes to FE order (and its disruption) in BTO-based systems.

### 2.5. Origin of Relaxor Behavior in Ba-Based Perovskites

To further explain the role of $V_{Ti}''''$-$Nb^{5+}$ defect clusters in BTO lattice, and to highlight the difference with relaxor behavior in homovalent substituted BTO systems, here represented by BZT, DFT calculations were carried out studying the effect of $Zr^{4+}$ or $Nb^{5+}$ addition (in the latter case with charge compensation by $V_{Ti}''''$) on the volume and total electric potential of the BTO lattice, as shown in **Figure 8**. $5 \times 5 \times 5$ supercells were considered, in which 4 Ti atoms are replaced by four Zr atoms

and five Ti atoms are replaced by four Nb atoms and one $V_{Ti}''''$, for BZT and BNbT, respectively (i.e., amounting to 3.2% substitution concentration for both BZT and BNbT). Note that Figure 8 is a stacked representation of 5 layers sliced from the $5 \times 5 \times 5$ supercell for clarity.

To analyze the local strain caused by substituents, the local volume was calculated using the eight nearest neighboring Ba ions surrounding the B-site ions of each unit cell within the supercell. A comparison of these values to rhombohedral BTO yields a relative change in local volume (cf., Figure 8a,b for BZT and BNbT, respectively). The change in total electric potential in BZT (c) and BNbT (d) was estimated for planes spanned by B-site ions by computing the difference to the pure BTO system. As can clearly be seen, in BZT there is a large strain difference in the vicinity of Zr atoms, impacting beyond the nearest-neighbor B-site, but the potential difference is confined to the Zr atom. In BNbT, on the other hand, the effect of the defect cluster is very strong both in terms of strain and electrical potential, and its effect is "felt" over a wide range of the supercell. This result again confirms the supposition that only in BNbT a charge-related mechanism is at the basis of the disruption of ferroelectric long-range order, and that these localized random fields can influence the direction of $Ti^{4+}$ and $Nb^{5+}$ cation displacements in several neighboring unit cells, inducing the strong lattice disorder we have detected by NMR and Raman, and the peculiar dielectric response, in BNbT systems. This disorder de facto disrupts the correlation of Ti—O—Ti chains, effectively hindering long-range ferroelectricity. On the other hand, in BZT only strain effects result from the difference in ionic radii and the extent of this effect is drastically smaller than the strain difference observed in BNbT due to the presence of $V_{Ti}''''$-$Nb^{5+}$ defect clusters. Hence, much higher substituent

2100812 (8 of 11)

**ADVANCED**
**SCIENCE NEWS**
www.advancedsciencenews.com

**ADVANCED**
**ELECTRONIC**
**MATERIALS**
www.advelectronicmat.de
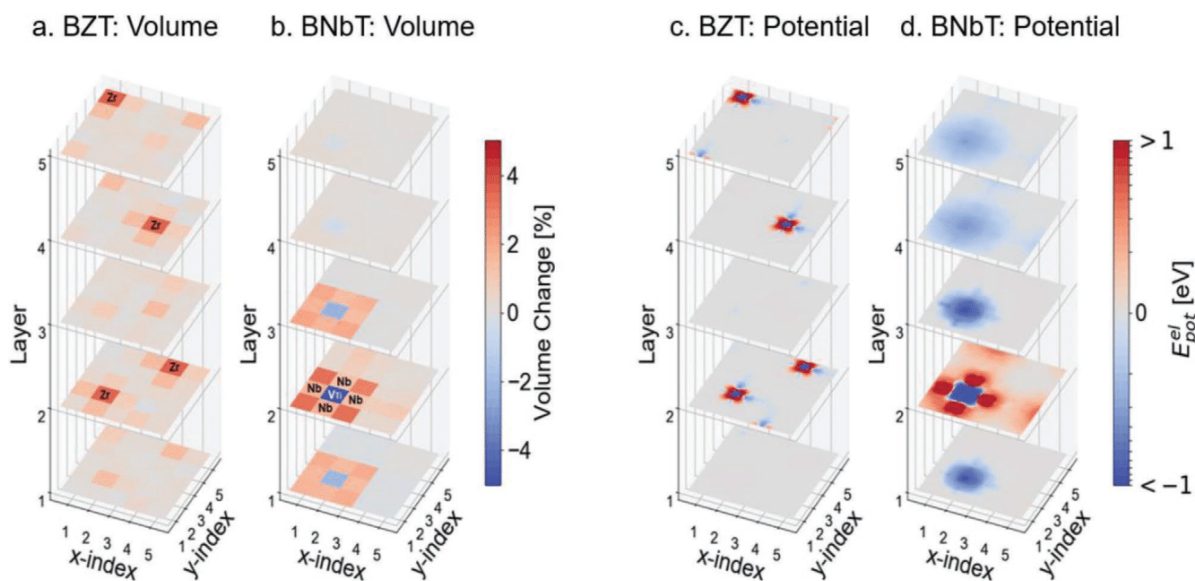
**Figure 8.** a,c) Local 5-atom unit cell volume and total electric potential change in BZT and b,d) BNbT, respectively, as obtained from DFT calculations. Local volume change of each unit cell and the corresponding absolute change of total electric potential with respect to pure BTO is presented, showing the strong impact of $Nb^{5+}$ substitution on the local structure that extends to several unit cells compared to the weak and very localized influence of $Zr^{4+}$ substitution.

content is necessary in homovalent relaxors to effectively disrupt the Ti—O—Ti chain correlation on the long-range, and thus to induce relaxor behavior. A direct analysis of the local dipoles gives additional evidence for the impact of Nb substitution compared to Zr substitution, as shown in Figure S9, Supporting Information and the corresponding discussion. Figure S9, Supporting Information is inspired by the visualization of dipoles in defected supercells presented by Liu et al.,[42] even though it is important to note that we deal only with a static result obtained at 0 K, while Liu et al. investigated the dynamical behavior of dipoles. Nevertheless, the analysis of local dipole changes also shows that Zr defects have a smaller impact on the neighboring dipole moments, and the impact is more isotropic, mostly changing the dipoles along the <100> directions. The Nb-$V_{Ti}$ clusters found in BNbT, in contrast, change the dipole moments of the neighboring cells much more strongly and anisotropically, where the strongest changes are found close to the titanium vacancy, which also determines the direction of the dipole changes.

## 3. Conclusions

This study combines different experimental and theoretical approaches to show that the origin of relaxor behavior in lead-free BTO-based systems is widely different for homovalent and heterovalent substituents. Charge compensation schemes, in fact, can result in different local structures and can impact differently the macroscopic material properties. The role of defects and defect distribution in disrupting the long-range ferroelectric order in heterovalent substitution of BTO is uncovered here through the analysis of $Nb^{5+}$-substituted BTO, demonstrating that the charge-mediated mechanism is more effective

than a purely strain-mediated mechanism (as in homovalent $Zr^{4+}$-substituted BTO) in inducing ferroelectric lattice disruption, thereby resulting in the onset of relaxor behavior at lower substituent content. This understanding is important for the design of new perovskite materials for high energy density capacitors, since the recoverable energy density primarily relies on the reduction of the ferroelectric hysteresis. Judiciously modified BTO ceramics where a high lattice electrical polarizability is combined with the absence of long-range ferroelectric order, as the heterovalent system addressed in this work, may thus deserve attention as high-performance electrostatic energy storage materials.

## 4. Experimental Section

*Sample Preparation*: BaTiO$_3$, BaZr$_x$Ti$_{1-x}$O$_3$ and BaNb$_x$Ti$_{1-5x/4}$O$_3$ ceramics were fabricated by the conventional solid-state mixed oxide route. Based on the required composition, stoichiometric amounts of pure BaCO$_3$ (electronic grade purity, Solvay Bario e Derivati, Italy; SSA = 3.3 m$^2$ g$^{-1}$), TiO$_2$ (electronic grade purity, Toho, Japan; SSA = 6.1 m$^2$ g$^{-1}$), Nb$_2$O$_5$ (99.9% purity, H.C. Starck, SSA = 6.3 m$^2$ g$^{-1}$, ceramic grade), and ZrO$_2$ (grade TZ0, Tosoh, Japan, SSA = 15.3 m$^2$ g$^{-1}$) were weighted and wet mixed with zirconia grinding media using water with ammonium polyacrylate as additive for homogenous mixing. In the case of BNbT, where charge compensation was needed, Ti deficiency was taken into account to avail the formation of Ti vacancies ($V_{Ti}'''$, in Kroger–Vink notation). After calcination, the powders were compacted, pressed, and sintered at different temperatures depending on the composition. Appropriate reoxidation annealing was performed for 48 h at 1000 °C. More details on the procedure can be found in previous work.[8,36]

*Weak Field Permittivity Measurements*: The dielectric permittivity was measured in three different experimental setups based on the measuring frequency range. For 1 mHz to 1 MHz frequency range, the capacitance and loss tangent were measured with Solartron Modulab XM MTS system, which has a low current module. Additional

108

**ADVANCED
SCIENCE NEWS**
www.advancedsciencenews.com

**ADVANCED
ELECTRONIC
MATERIALS**
www.advelectronicmat.de

experiments were carried out with HP4284A LCR meter in 20 Hz–1 MHz frequency range. The dielectric permittivity in 1 MHz–1 GHz frequency range was determined by measuring the complex reflection coefficient from the samples that were placed at the end of the coaxial line. An Agilent 8714ET vector network analyzer was used to measure the complex reflection coefficient. The complex dielectric permittivity was calculated according to the "multi-mode capacitor" model. A detailed description of this experimental setup can be found in the literature.[43] To determine permittivity in the 26–40 GHz frequency range, the sample was placed in a waveguide that supports only TE$_{10}$. A scalar network analyzer ELMIKA R2400 measured the scalar reflection and transmission coefficients simultaneously. The permittivity can be then determined by solving nonlinear equations using the modified Newton method. The details of this experimental setup can be found in the literature.[44,45]

*Temperature Dependent Raman Spectroscopy*: Raman measurements were carried out in a LabRAM 300 spectrometer (Horiba Jobin Yvon, Villeneuve d'Ascq, France) using an excitation wavelength of $\lambda = 532$ nm in a backscattering geometry equipped with an edge filter (cut-off: 80 cm$^{-1}$), 1800 g mm$^{-1}$ grating and charge coupled device (CCD) detector. The laser light was focused on the sample surface by means of a long working distance 100× objective (with NA 0.8, LMPlan FI, Olympus, Tokyo, Japan) with a spot size of 1 μm. The effective power at the sample surface was ≈2 mW. Temperature-dependent Raman measurements were carried out in a Linkam temperature-controlled stage (THMS600, Linkam, Tadworth, UK) placed under the Raman microscope. The spectra were visualized using commercial software environment (Origin 2018b, OriginLab Corp., Northampton MA, USA) after correcting for the Bose–Einstein population factor.

*Nuclear Magnetic Resonance Spectroscopy*: $^{137}$Ba NMR spectra were recorded with a Bruker Avance III spectrometer at a frequency of 66.707 MHz. Ceramic samples were crushed to powders and annealed at 400 °C for 2 h to relieve mechanical stress from grinding. A 3.2 mm magic angle spinning (MAS) probe was used in the variable-temperature, static, NMR experiments. A Hahn-echo pulse sequence was employed with 90° and 180° pulses of 2 and 4 μs, respectively, as well as an echo delay of 100 μs and a recycle delay of 100 ms. $^{137}$Ba NMR spectra were processed with a Gaussian window function no broader than 1/7 of the original linewidth and fitted with the Czjzek model implemented in DMfit.[46] From this procedure, the mean value for the distribution of quadrupolar coupling constants ($C_Q$) can be determined, and its error estimated by a statistical analysis of the fit and of the stability of the model through a Monte Carlo procedure with 100 attempts for each spectrum. Nominal temperatures are reported for the NMR spectra, which were recorded by a thermocouple positioned downstream from the sample.

*DFT Calculations*: The DFT calculations were performed using the VASP code.[47–51] The PBEsol[52] functional was employed to describe the exchange-correlation interactions. The energy cut-off of 520 eV was used for expanding the wave function in the basis of plane-waves. The sampling of the Brillouin zone was performed using the following Γ-centered uniform meshes: 8 × 8 × 8 for bulk, 3 × 3 × 3 for the 3 × 3 × 3 supercell, and 2 × 2 × 2 for both 4 × 4 × 4 and 5 × 5 × 5 supercells. As a preparatory step, the converged structural parameters of the bulk rhombohedral BTO were computed and the lattice parameter of 4.009 Å and the angle $\alpha$ of ≈89.86° were obtained, in good agreement to literature.[53,54] The supercells were then constructed from this optimized bulk r-BTO. After that, the supercells were fully relaxed, that is, the ionic positions as well as the shape and the volume of the supercells were subject to optimization. The simulated Raman spectra were obtained using the spherical averaging method[20] employing 3 × 3 × 3 supercells.

## Supporting Information

Supporting Information is available from the Wiley Online Library or from the author.

## Conflict of Interest

The authors declare no conflict of interest.

## Author Contributions

V.V. performed Raman, dielectric permittivity measurements, treated the respective data, put together, plotted and interpreted the results from other techniques, and wrote the main part of the manuscript. M.N.P. conceived and performed all DFT calculations and computed simulated Raman spectra. F.M. evaluated DFT calculations for the study of local volume and total electric potential changes. J.S. actively contributed to concept, initiation, and evaluation of ab initio calculations, performed the eigenmode analysis, and supported the overall interpretation of results. S.S. performed microwave dielectric spectroscopy experiments and analysis. V.K. and S.S. performed low temperature and low frequency dielectric spectroscopy experiments and analysis. J.B. organized the study of broadband dielectric spectroscopy. J.L. and P.B.G. performed the NMR measurements, along with the data analysis. P.B.G. contributed with the interpretation of NMR spectra, wrote initial passages related to the NMR data, and did the error analysis for spectral fitting. G.C. and M.T.B. prepared the samples and performed their basic characterization. V.B. organized sample preparation. M.P. supported the concept and development of DFT calculations. J.H. provided regular feedback and useful suggestions for modeling of Raman spectra. M.D. conceived, initiated the study and developed the concept, actively contributing to Raman data interpretation, overall results interpretation, and writing the discussion part of the manuscript. All authors corrected manuscript drafts.

## Data Availability Statement

The data that support the findings of this study are openly available in Zenodo at https://doi.org/10.5281/zenodo.5642828.

[1] X. Hao, *J. Adv. Dielectr.* **2013**, *03*, 1330001.

[2] V. Veerapandiyan, F. Benes, T. Gindel, M. Deluca, *Materials* **2020**, *13*, 5742.

[3] J. Li, Z. Shen, X. Chen, S. Yang, W. Zhou, M. Wang, L. Wang, Q. Kou, Y. Liu, Q. Li, Z. Xu, Y. Chang, S. Zhang, F. Li, *Nat. Mater.* **2020**, *19*, 999.

[4] G. Liu, S. Zhang, W. Jiang, W. Cao, *Mater. Sci. Eng., R* **2015**, *89*, 1.

[5] G. Canu, G. Confalonieri, M. Deluca, L. Curecheriu, M. T. Buscaglia, M. Asandulesa, N. Horchidan, M. Dapiaggi, L. Mitoseriu, V. Buscaglia, *Acta Mater.* **2018**, *152*, 258.

[6] W. Kleemann, *J. Adv. Dielectr.* **2012**, *02*, 1241001.

[7] T. Maiti, R. Guo, A. S. Bhalla, *J. Am. Ceram. Soc.* **2008**, *91*, 1769.

[8] V. Buscaglia, S. Tripathi, V. Petkov, M. Dapiaggi, M. Deluca, A. Gajović, Y. Ren, *J. Phys.: Condens. Matter* **2014**, *26*, 065901.

[9] R. Pirc, R. Blinc, *Phys. Rev. B: Condens. Matter Mater. Phys.* **2007**, *76*, 020101.

[10] L. E. Cross, *Ferroelectrics* **1994**, *151*, 305.

[11] P. B. Groszewicz, H. Breitzke, R. Dittmer, E. Sapper, W. Jo, G. Buntkowsky, J. Rödel, *Phys. Rev. B* **2014**, *90*, 220104.

[12] R. Farhi, M. El Marssi, A. Simon, J. Ravez, *Eur. Phys. J. B* **2000**, *18*, 605.

[13] G. Smolensky, *Ferroelectrics* **1984**, *53*, 129.

[14] J. Toulouse, *Ferroelectrics* **2008**, *369*, 203.

[15] J. Hlinka, *J. Adv. Dielectr.* **2012**, *02*, 1241006.

[16] Y. Imry, S. K. Ma, *Phys. Rev. Lett.* **1975**, *35*, 1399.

[17] J. Banys, R. Grigalaitis, A. Mikonis, J. Macutkevic, P. Keburis, *Phys. Status Solidi* **2009**, *6*, 2725.

[18] H. Takenaka, I. Grinberg, S. Liu, A. M. Rappe, *Nature* **2017**, *546*, 391.

[19] Y. Kuroiwa, S. Aoyagi, A. Sawada, J. Harada, E. Nishibori, M. Takata, M. Sakata, *Phys. Rev. Lett.* **2001**, *87*, 217601.

[20] M. N. Popov, J. Spitaler, V. K. Veerapandiyan, E. Bousquet, J. Hlinka, M. Deluca, *NPJ Comput. Mater.* **2020**, *6*, 121.

[21] R. D. Shannon, *Acta Crystallogr., Sect. A: Found. Crystallogr.* **1976**, *32*, 751.

[22] S. Anwar, P. R. Sagdeo, N. P. Lalla, *J. Phys. Condens. Matter* **2006**, *18*, 3455.

[23] F. D. Morrison, D. C. Sinclair, A. R. West, *J. Appl. Phys.* **1999**, *86*, 6355.

[24] C. Laulhé, F. Hippert, J. Kreisel, A. Pasturel, A. Simon, J. L. Hazemann, R. Bellissent, G. J. Cuello, *Phase Transitions* **2011**, *84*, 438.

[25] C. Filipič, Z. Kutnjak, R. Pirc, G. Canu, J. Petzelt, *Phys. Rev. B* **2016**, *93*, 224105.

[26] J. Macutkevic, J. Banys, A. Bussmann-Holder, A. R. Bishop, *Phys. Rev. B* **2011**, *83*, 184301.

[27] C. H. Burton, J. S. Dryden, *J. Phys. C: Solid State Phys.* **1970**, *3*, 523.

[28] *Broadband Dielectric Spectroscopy* (Eds: F. Kremer, A. Schönhals), Springer, Berlin, Heidelberg **2003**.

[29] A. Gajović, J. V. Pleština, K. Žagar, M. Plodinec, S. Šturm, M. Čeh, *J. Raman Spectrosc.* **2013**, *44*, 412.

[30] R. Farhi, M. El Marssi, A. Simon, J. Ravez, *Eur. Phys. J. B* **1999**, *9*, 599.

[31] P. B. Groszewicz, *Open Ceram.* **2021**, *5*, 100083.

[32] O. Kanert, H. Schulz, J. Albers, *Solid State Commun.* **1994**, *91*, 465.

[33] T. J. Bastow, H. J. Whitfield, *Solid State Commun.* **2001**, *117*, 483.

[34] C. Gervais, D. Veautier, M. E. Smith, F. Babonneau, P. Belleville, C. Sanchez, *Solid State Nucl. Magn. Reson.* **2004**, *26*, 147.

[35] G. Czjzek, J. Fink, F. Götz, H. Schmidt, J. M. D. Coey, J.-P. Rebouillat, A. Liénard, *Phys. Rev. B* **1981**, *23*, 2513.

[36] V. K. Veerapandiyan, S. Khosravi H, G. Canu, A. Feteira, V. Buscaglia, K. Reichmann, M. Deluca, *J. Eur. Ceram. Soc.* **2020**, *40*, 4684.

[37] J. Pokorný, U. M. Pasha, L. Ben, O. P. Thakur, D. C. Sinclair, I. M. Reaney, *J. Appl. Phys.* **2011**, *109*, 114110.

[38] V. K. Veerapandiyan, M. Deluca, S. T. Misture, W. A. Schulze, S. M. Pilgrim, S. C. Tidrow, *J. Am. Ceram. Soc.* **2020**, *103*, 287.

[39] S. G. Cao, Y. Li, H. H. Wu, J. Wang, B. Huang, T. Y. Zhang, *Nano Lett.* **2017**, *17*, 5148.

[40] D. M. Smyth, in *The Defect Chemistry of Metal Oxides*, Oxford University Press, New York **2006**, pp. 253–282.

[41] J. Liu, L. Liu, J. Zhang, L. Jin, D. Wang, J. Wei, Z. G. Ye, C. L. Jia, *J. Am. Ceram. Soc.* **2020**, *103*, 5392.

[42] J. Liu, L. Jin, Z. Jiang, L. Liu, L. Himanen, J. Wei, N. Zhang, D. Wang, C.-L. Jia, *J. Chem. Phys.* **2018**, *149*, 244122.

[43] Š. Svirskas, D. Jablonskas, S. Rudys, S. Lapinskas, R. Grigalaitis, J. Banys, *Rev. Sci. Instrum.* **2020**, *91*, 035106.

[44] J. Grigas, A. Brilingas, V. Kalesinskas, *Ferroelectrics* **1990**, *107*, 61.

[45] J. Grigas, *Microwave Dielectric Spectroscopy of Ferroelectrics and Related Materials*, CRC Press, Boca Raton, FL **2019**.

[46] D. Massiot, F. Fayon, M. Capron, I. King, S. Le Calvé, B. Alonso, J.-O. Durand, B. Bujoli, Z. Gan, G. Hoatson, *Magn. Reson. Chem.* **2002**, *40*, 70.

[47] G. Kresse, J. Hafner, *Phys. Rev. B* **1993**, *47*, 558.

[48] G. Kresse, J. Hafner, *Phys. Rev. B* **1994**, *49*, 14251.

[49] G. Kresse, J. Furthmüller, *Comput. Mater. Sci.* **1996**, *6*, 15.

[50] G. Kresse, J. Furthmüller, *Phys. Rev. B* **1996**, *54*, 11169.

[51] G. Kresse, D. Joubert, *Phys. Rev. B* **1999**, *59*, 1758.

[52] G. I. Csonka, J. P. Perdew, A. Ruzsinszky, P. H. T. Philipsen, S. Lebègue, J. Paier, O. A. Vydrov, J. G. Ángyán, *Phys. Rev. B* **2009**, *79*, 155107.

[53] G. H. Kwei, A. C. Lawson, S. J. L. Billinge, S. W. Cheong, *J. Phys. Chem.* **1993**, *97*, 2368.

[54] R. A. Evarestov, A. V. Bandura, *J. Comput. Chem.* **2012**, *33*, 1123.

# ADVANCED ELECTRONIC MATERIALS

## Supporting Information

# Origin of Relaxor Behavior in Barium-Titanate-Based Lead-Free Perovskites

*Vignaswaran Veerapandiyan, Maxim N. Popov, Florian Mayer, Jürgen Spitaler, Sarunas Svirskas, Vidmantas Kalendra, Jonas Lins, Giovanna Canu, Maria Teresa Buscaglia, Marek Pasciak, Juras Banys, Pedro B. Groszewicz, Vincenzo Buscaglia, Jiri Hlinka, and Marco Deluca\**

# Supporting Information

**Origin of Relaxor Behavior in Barium Titanate Based Lead-Free Perovskites**

*Vignaswaran Veerapandiyan, Maxim N. Popov, Florian Mayer, Jürgen Spitaler, Sarunas Svirskas, Vidmantas Kalendra, Jonas Lins, Giovanna Canu, Maria Teresa Buscaglia, Marek Pasciak, Juras Banys, Pedro B. Groszewicz, Vincenzo Buscaglia, Jiri Hlinka, Marco Deluca*[*]

V. Veerapandiyan, M. N. Popov, F. Mayer, J. Spitaler, M. Deluca
Materials Center Leoben Forschung GmbH, Roseggerstrasse 12, 8700 Leoben, Austria
E-Mail: marco.deluca@mcl.at

S. Svirskas, V. Kalendra, J. Banys
Faculty of Physics, Vilnius University, Sauletekio al. 9, 2040 Vilnius, Lithuania

J. Lins, P. B. Groszewicz
Institute of Physical Chemistry, Technische Universität Darmstadt, 64287, Darmstadt, Germany

P. B. Groszewicz
Department of Radiation Science and Technology, Delft University of Technology, Delft 2629JB, Netherlands.

G. Canu, M. T. Buscaglia, V. Buscaglia
CNR-ICMATE, Institute of Condensed Matter Chemistry and Technologies for Energy, National Research Council of Italy, Via de Marini 6, 16149, Genoa, Italy

M. Pasciak, J. Hlinka
Institute of Physics, Academy of Sciences of the Czech Republic, Na Slovance 2, Praha 8, Czech Republic

**Dielectric Relaxation in Heterovalent-Substituted BTO**

Both dielectric relaxations in regions I and II of BNbT15 displayed in Figure 2(a) show a shift in permittivity maximum with increasing frequency. Although initial investigation might suggest the presence of two relaxor-like dispersions, the high temperature relaxation (region II) shows dispersion only in 1 kHz – 10 MHz frequency range. In order to show that the relaxation in Region II is not related to dynamic polarization fluctuations as seen in relaxors below $T_m$, frequency dependent complex permittivity measurements at different temperatures within Region II are shown in Figure 2(b,c). Further, an approximation procedure on the obtained data was performed with a superposition of Cole-Cole equations:

$$\varepsilon^*(f) = \varepsilon_\infty + \sum_{k=1}^{2} \frac{\varepsilon_k(0) - \varepsilon_{k\infty}}{(1 + i2\pi f \tau_k)^{1-\alpha_k}} \tag{1}$$

Where $\varepsilon_\infty$ denotes the highest frequency contributions (i. e. phonons, electronic polarization), $\varepsilon_k(0) - \varepsilon_{k\infty}$ represents the dielectric strength of the k-th process, $\tau_k$ is the mean and most probable relaxation time of the k-th process, $f$ is the probing frequency and $\alpha_k$ is the Cole-Cole breadth parameter of the k-th process.

In case of BNbT7, the relaxor-like frequency dispersion of $T_m$ is becoming evident only at high frequency (at 1 GHz in Figure 1) where the contribution of the second relaxation is suppressed. This is also the reason for the large relative permittivity of BNbT7 at low frequencies that undergoes strong frequency dependent suppression (c.f. Figure 1(b)). In BNbT15, the real part of permittivity increases with the decrease in frequency (note the data in the 20 Hz – 10 kHz frequency range in Figure 2(b)). This indicates the presence of another broad relaxation process at low frequencies which cannot be described by a single function but only by multiple relaxation peaks. In contrary, such single-function relaxation model can very well describe the dielectric response in Region I. Figure S1(a) shows the fitting parameter, $\alpha$, that is directly related to the

2

breadth of the imaginary permittivity peak of Region II. Here, the peak at 23°C can be fitted with $\alpha = 0$, resembling a Debye relaxation, but the fitting is strongly hindered by the lower frequency part. For all other measured temperatures below 23°C, which lie in region II, the breadth of relaxation does not change with decreasing temperature, which is evidenced from a temperature independent fitting parameter and the values being closer to a Debye type relaxation, typical in presence of charged lattice defects or interfacial (Maxwell-Wagner) polarization.

The frequency dependent complex dielectric permittivity is also reported in Figure S1(b) and (c) for several temperatures in Region I for BNbT15. Here the experiments in microwave frequency range were not possible due to the restrictions of the experimental setup. However, experiments performed in the 1 mHz – 1 MHz frequency range provide useful insights when combined with the temperature dependent $\varepsilon_r$ response in the same region. As summarized in Figure S2, the frequency dispersion of $\varepsilon_r$ response of BZT40 and BNbT15 (region I) follows a typical Vogel-Fulcher law that resembles relaxor behavior [1]. In particular, for BNbT15 the dispersion is extended up to 29 GHz with a $T_m$ of -90°C, which indicates that the relaxation in Region I extends to frequencies well above the relaxation frequency range to that of the relaxation in Region II. In addition, from frequency dependent dielectric spectra, it is clear that the relaxation slows down and broadens with the decreasing temperature, in addition to a constant loss regime observed at -268°C, as seen in Figure S1(b). This is a feature that is generally observed in canonical relaxors [2]. Overall, these results confirm that the relaxation shown in Region I can be ascribed to a canonical relaxor behavior (i.e. caused by dynamic polarization fluctuations), whereas Region II is a Debye-like dielectric relaxation.

3

114
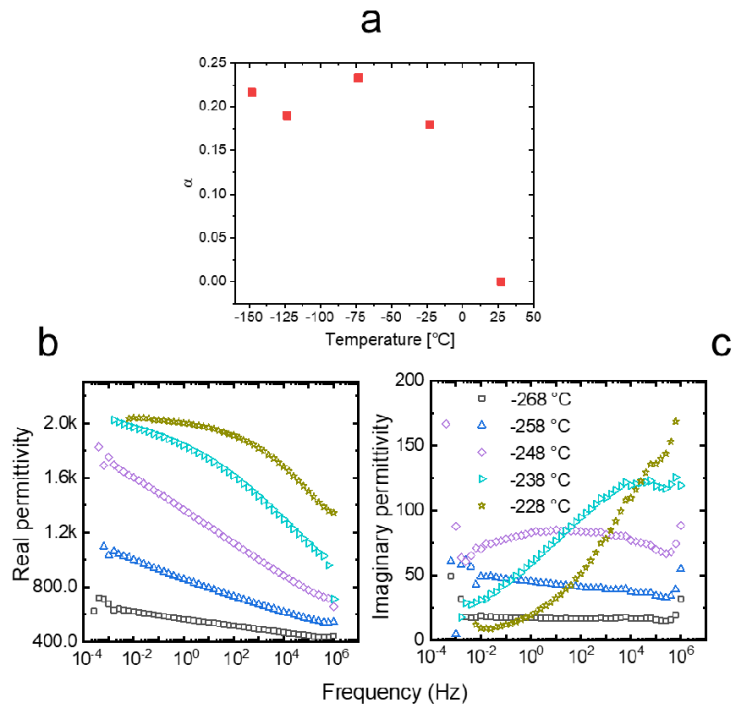
**Figure S1.** Fitting parameter, $\alpha$, obtained from the frequency dependent complex permittivity data of BNbT15 (region II) (a). Complex permittivity of BNbT15 as a function of frequency at different temperatures in region I (b, c).
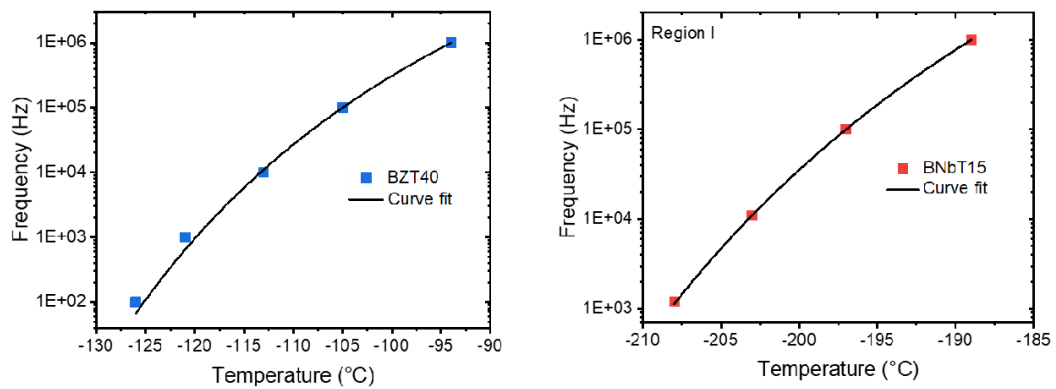


**Figure S2.** The relaxor dispersion following Vogel-Fulcher law for BZT40 and BNbT15.

4

115

**Lattice Disorder in Heterovalent-Substituted BTO.**

Figure S3 shows the FWHM values of the [137]Ba NMR peak for pure BTO and BNbT ceramics. Except for FE BTO and BNbT2.5 that display a drastic drop in FWHM of the NMR peak with decreasing temperature (1500% drop for BTO, not shown in Figure S3), other BNbT compositions demonstrated large and relatively temperature stable FWHM values (i.e. lattice disorder), persistent well above $T_m$. Such temperature stability and large peak width, unlike FE compositions, reassures that the observed NMR peak is resulting from local structural disorder deviating from cubic symmetry.
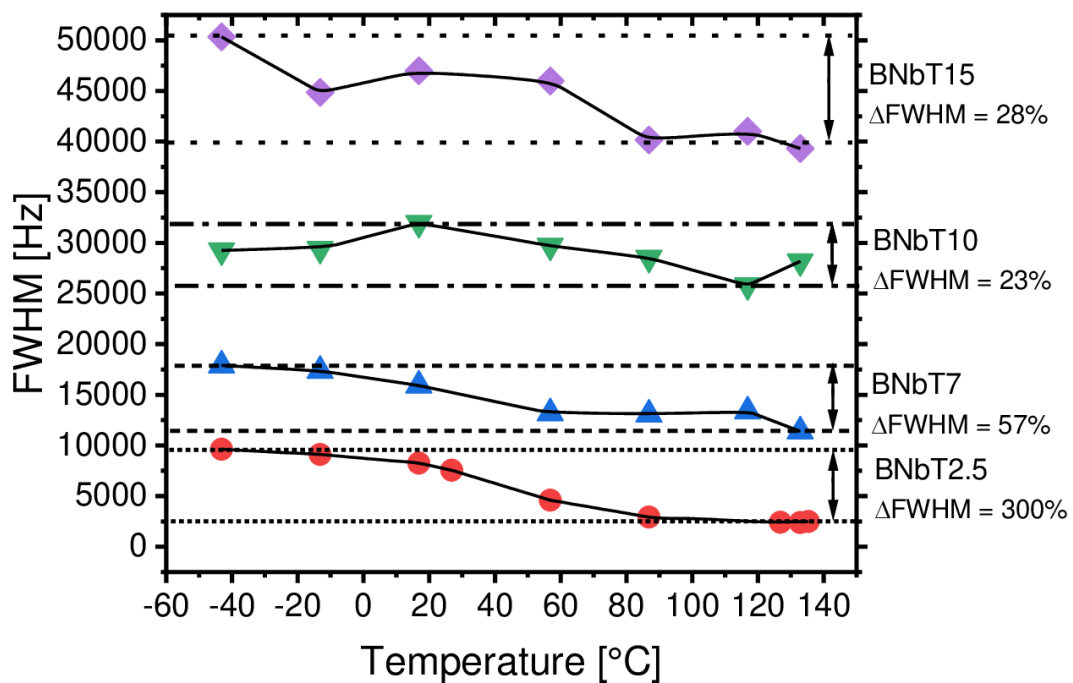


**Figure S3.** [137]Ba NMR static spectra of BNbT samples recorded at different temperatures to demonstrate the temperature insensitivity of the peak width in relaxor compositions (BNbT7 and above) when compared to drastic reduction of peak width for FE systems (BNbT2.5; BTO – not shown – displays 1500% peak width reduction upon temperature decrease).

5
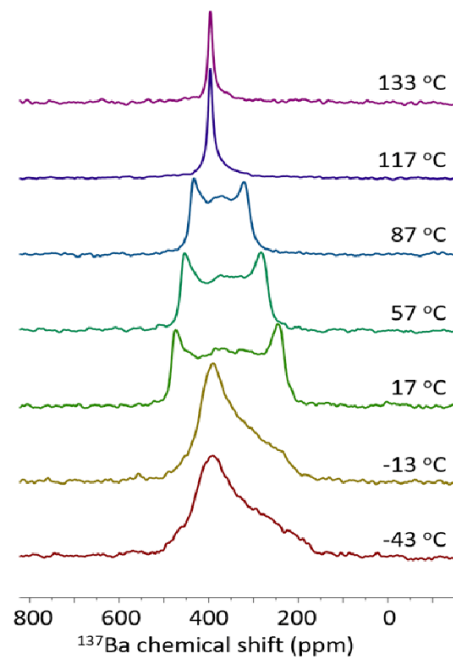
**Figure S4.** [137]Ba NMR static spectra of BTO at different temperatures to show the change in the line width upon phase transition from tetragonal to cubic polymorph.

**Charge-Compensating Defects in Heterovalent Relaxors**

Figure S5 displays the Raman spectrum of BNbT15 measured over a temperature range from -195°C to 155°C. The extra mode at ~830 cm$^{-1}$ (Mode 5 in the main text of the manuscript) shows no appreciable temperature dependence (no changes in position, intensity, or peak width), which highlights its localized character.

6
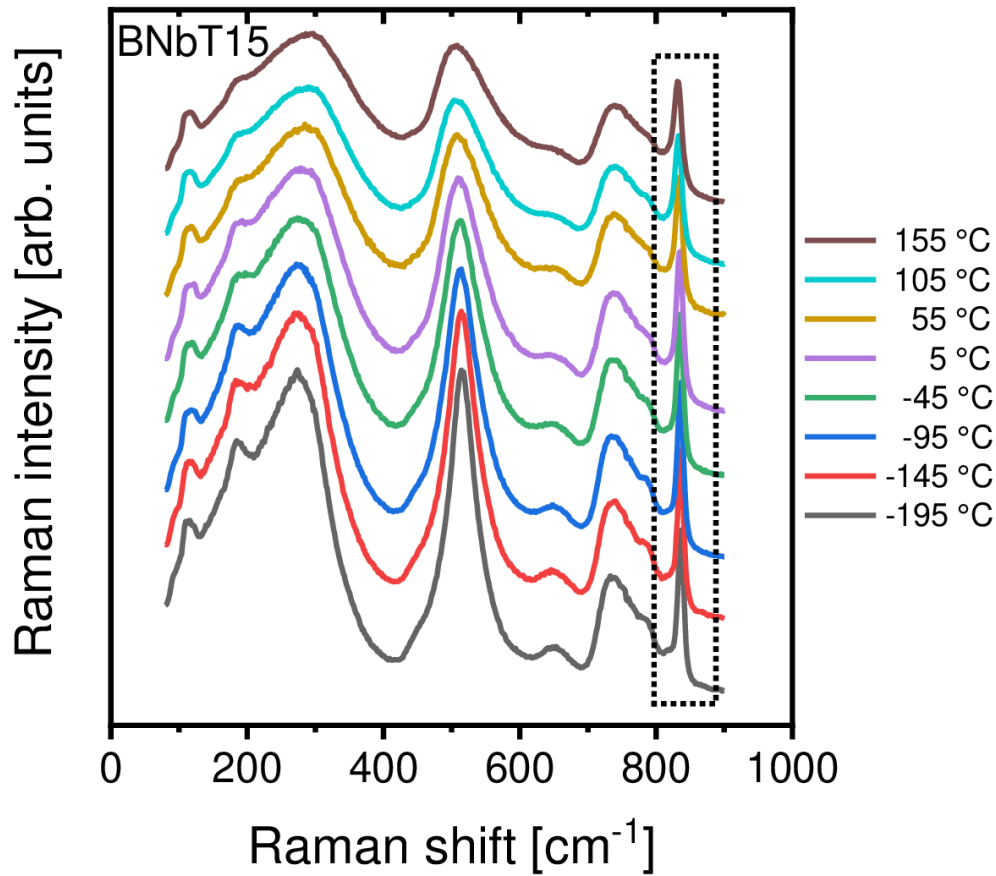
**Figure S5.** Temperature dependent Raman spectra of BNbT15 highlighting the temperature independence of mode 5.

In order to determine the precise distribution of $Nb^{5+}$ cations in the vicinity of $V_{Ti}^{''''}$, we considered two possible cluster geometries as shown in Figure S6: 1) *planar* cross-like cluster with $V_{Ti}^{''''}$ in the center and surrounded by four Nb atoms (c.f. Figure S6-a); 2) *bent* cluster, that is similar to the planar one, but with one Nb atom sticking out of plane (c.f. Figure S6-b). We investigated the energies of these clusters in 3x3x3, 4x4x4, and 5x5x5 supercells using DFT and performing the full relaxation. Interestingly, the bent cluster turned out to be slightly more energetically favorable

7

(~30 meV) in the 3x3x3 supercell as shown in Figure S7. However, this energy difference rapidly decreased as a function of the supercell size, yielding ~5 meV and ~1 meV difference for the 4x4x4 and 5x5x5 supercells, respectively. At the end, there is no decisive difference in the energies of the planar and bent clusters and, thus, both of them can be present in BNbT.
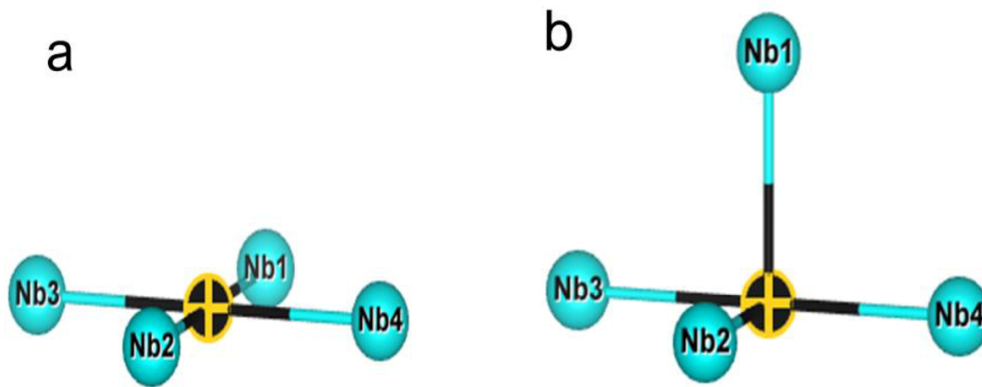


**Figure S6.** Planar (a) and bent (b) cluster. The crossed ball in the center symbolizes the Ti-vacancy.
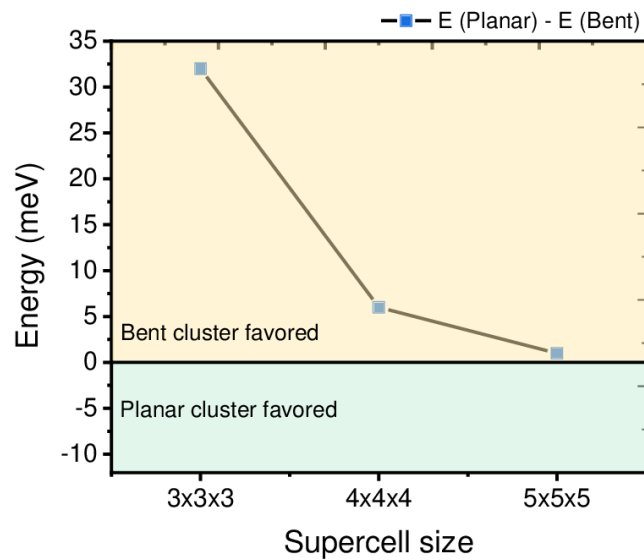


**Figure S7.** Relative energies of the considered clusters as a function of supercell size.

Figure S8 displays the temperature dependent permittivity response in the relaxor composition BZT40. This diagram should be examined together with Figure 2 in the main text of the manuscript. The relaxor behavior of BZT40 is evidenced by the low temperature frequency dispersion. In the BZT40 case there is no additional dielectric relaxation at higher temperatures. The Curie-Weiss law showing large deviation is also reported for BZT40 in Figure S8.
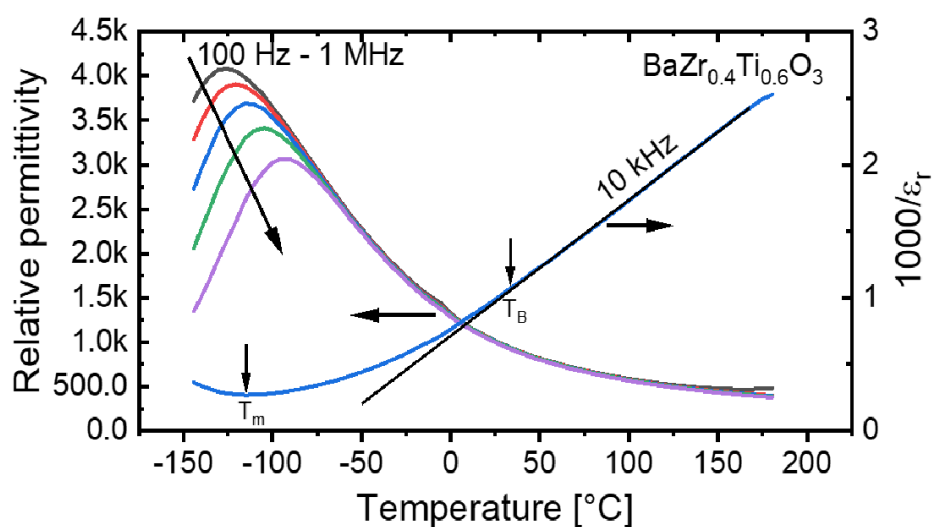


**Figure S8.** Temperature dependent permittivity response of BZT40 demonstrating a typical low temperature frequency dispersion and a large deviation from Curie-Weiss law near $T_m$.

**Impact of defects on polarization vectors**

Figure S9 shows the change in local dipoles induced by doping. To calculate this change, we calculated the difference between local dipoles in the substituted supercells and the pure BT supercell. From that, we get a vector (red arrows in the plot) for each unit cell within the supercell which accounts for the change of dipoles induced by the presence of substituents. The local dipoles

9

are approximated by calculating the shift of B-site atoms with respect to the center of mass of the oxygen octahedra.

In BZT we observe induced changes along the <001>high-symmetry directions, starting from the position of the defect (dark blue balls). The magnitude of the changes is smaller compared to the defect cluster in BNbT. The effect is mostly based on the expansion of the Zr containing unit cells which disrupts the Ti-O-Ti-O chains.

In BNbT, a more anisotropic effect originating from the defect cluster (Nb in light green, $V_{Ti}$ in grey) is observed. The change in dipoles perpendicular to the plane of the cluster is stronger compared to the in-plane changes. This is mostly due to the Ti vacancy, which leads to a strong local charge unbalance and is able to disturb the neighboring unit cells more effectively. Overall, the BNbT supercell shows a more disturbed dipole configuration than the BZT supercells with the same number of substituents.
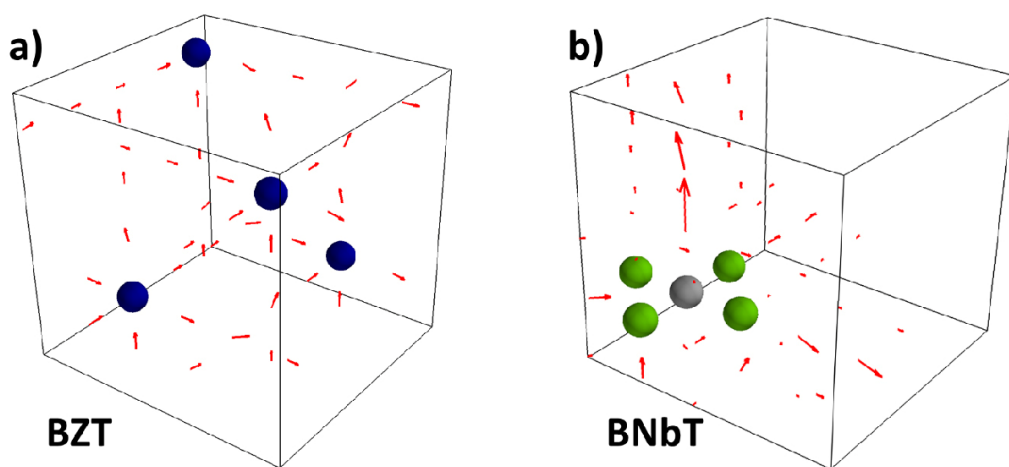


**Figure S9.** Local dipole changes induced by doping BT with a) Zr (dark blue balls) or b) Nb defect cluster (light green balls are Nb, grey balls represents VTi). The plot shows 5x5x5 supercells, where the red arrows are changes in the local dipoles. Local dipole changes were derived from fully relaxed DFT structures and calculating the difference between substituted supercells and pure BT.

10

121

References:

[1]     A. K. Tagantsev, *Phys. Rev. Lett.* **1994**, *72*, 1100.

[2]     J. Macutkevic, J. Banys, A. Bussmann-Holder, A. R. Bishop, *Phys. Rev. B* **2011**, *83*,

184301.

11

## 8.2 Publication 2

# Improved description of the potential energy surface in BaTiO$_3$ by anharmonic phonon coupling

Florian Mayer[1], Maxim N. Popov[1], Donald M. Evans[2], Stephan Krohns[2], Marco Deluca[1],
Jürgen Spitaler[1]

[1]*Materials Center Leoben Forschung GmbH, Roseggerstrasse 12, 8700 Leoben, Austria*
[2]*Experimental Physics V, Center for Electronic Correlations and Magnetism, Institute of Physics,
University of Augsburg, 86135 Augsburg, Germany*

Corresponding author: florian.mayer@mcl.at

**Abstract:**

Barium titanate (BT) based materials are at the forefront of materials searched as possible candidates for the replacement of lead-based compositions in applications ranging from piezoelectrics to energy storage devices. Computational methods are very promising to increase the efficiency of materials discovery, provided that finite temperature properties can be realistically computed using – for example – molecular dynamics (MD). In this work, we present a systematic increase of the quality of MD simulations via an alternative way to calculate anharmonic contributions to the potential energy surface (PES) of barium titanate. A large number of first-principles calculations are performed, which are subsequently used to parameterize an effective Hamiltonian. To test the effects on various physical properties, MD simulations for the determination of transition temperatures, hysteresis and permittivity of BT are shown. Furthermore, measurements were performed on BT single crystals to compare them directly with the MD simulations. It is observed that by incorporating a large number of anharmonic couplings, the description of the local minima in the PES becomes more accurate than in previous simulations. This leads to a better prediction of phase transition temperatures and shows the importance of anharmonic couplings in barium titanate. The presented approach can directly be adapted for other perovskite structures.

# Improved description of the potential energy surface in BaTiO$_3$ by anharmonic phonon coupling

Florian Mayer [ORCID],[1,*] Maxim N. Popov,[1] Donald M. Evans [ORCID],[2] Stephan Krohns,[2] Marco Deluca [ORCID],[1] and Jürgen Spitaler[1]

[1]*Materials Center Leoben Forschung GmbH, Roseggerstrasse 12, 8700 Leoben, Austria*

[2]*Experimental Physics V, Center for Electronic Correlations and Magnetism, Institute of Physics,*
*University of Augsburg, 86135 Augsburg, Germany*

Barium titanate (BT) based materials are at the forefront of materials being searched as possible candidates for the replacement of lead-based compositions in applications ranging from piezoelectrics to energy storage devices. Computational methods are very promising to increase the efficiency of materials discovery, provided that finite temperature properties can be realistically computed using, for example, molecular dynamics (MD). In this work, we present a systematic increase of the quality of MD simulations via an alternative way to calculate anharmonic contributions to the potential energy surface (PES) of barium titanate. A large number of first-principles calculations are performed, which are subsequently used to parametrize an effective Hamiltonian. To test the effects on various physical properties, MD simulations for the determination of transition temperatures, hysteresis, and permittivity of BT are shown. Furthermore, measurements were performed on BT single crystals to compare them directly with the MD simulations. It is observed that by incorporating a large number of anharmonic couplings, the description of the local minima in the PES becomes more accurate than in previous simulations. This leads to a better prediction of phase transition temperatures and shows the importance of anharmonic couplings in barium titanate. The presented approach can be directly adapted for other perovskite structures.

## I. INTRODUCTION

An ever-growing demand for environmentally friendly materials is impacting the microelectronics industry. Many devices where ferroelectric materials are currently used are primarily based on environmentally critical lead-containing materials. In particular, the application of ferroelectrics as piezoelectric actuators [1] and as capacitive energy storage devices [2] has received renewed attention in recent years. Therefore, while it is of great importance to search for new alternative ferroelectric materials, there is also a need to understand the fundamental properties of established materials to provide clear goals for this search. Important parameters that need to be optimized in lead-free ferroelectrics are, for instance, piezoelectric coefficients, piezoelectric coupling factors, dielectric permittivity, and recoverable energy density. The compositional search space for lead-free perovskites is very large [3–5]; hence computational data-driven or even artificial intelligence (AI) methods are needed to improve the efficiency of materials discovery and accelerate experimental procedures [6], which are often based on trial and error. To enable such computational methodologies in the absence, or scarcity, of experimental data, it is necessary to calculate material properties at finite temperatures based on supercells consisting of millions of atoms—in order to reproduce both short-range and long-range order. Such molecular dynamics (MD) simulations rely on approaches derived from density functional theory (DFT) involving, for example, effective Hamiltonians [7–9], which thus need to be developed case by case for different compositions.

In this work, we address the effective Hamiltonian approach taking pure barium titanate [BaTiO$_3$ (BT)] as an example of a lead-free perovskite material. BT is considered as the prototypical ferroelectric material, and many of its chemical modifications have demonstrated excellent performance in piezoelectric [10], energy storage [11], microwave [12], and electrocaloric [13] applications. BT itself is already quite a complex material. It shows four different phases, three of which (rhombohedral, orthorhombic, and tetragonal) are ferroelectric, whereas the high-temperature cubic phase is paraelectric. The corresponding phase transitions make this material and its modifications interesting for many applications since excellent properties such as giant dielectric permittivity and large piezoelectric coefficients, driven by a large spontaneous polarization, can be observed close to these phase transitions [14]. Various methods have been used to explain the origins [15] of ferroelectric behavior in BT. The primary examples of this are first- principles calculations based on density functional theory (DFT) [16–19], semiempirical methods [20], and phase-field approaches [21,22]. Devonshire was one of the first to study the origin of ferroelectricity in BT using Landau-Devonshire theory [23,24]. In the 1990s, Cohen and Krakauer [17] showed the now well-known double well shaped energy surface of BT calculated using DFT. This was followed by the development of semiempirical models, which are still used in the simulation of BT. Of particular note is the work of Zhong *et al.* [18] in developing effective Hamiltonians to simulate properties at finite temperatures. The basic idea was to reduce the complexity and describe the potential energy surface as a function of a small number of variables [25], where first-principles calculations can determine the required parameters. In the early stages, this approach was a mean-field theory which was later adapted to

*florian.mayer@mcl.at

064108-1

a local-mode theory [26] allowing simulations of supercells. Furthermore, this approach has been continuously extended to investigate doped systems as well [7–9]. In 2008, Nishimatsu *et al.* [27] revised this concept by giving a makeover to the formalism, thereby increasing efficiency and accuracy.

In 2017, Paul *et al.* [28] showed that the extension of the self-energy by contributions from anharmonic couplings to higher-energy phonon modes gives an improved description of the potential energy surface. Since the original formalism is parametrized exclusively by the soft mode and its displacement pattern, the extension by including further phonon modes offers an interesting possibility to increase the accuracy of the effective Hamiltonian.

In this paper we introduce a revised effective Hamiltonian which is based on a larger number of anharmonic terms which, therefore, yield a better description of the potential energy surface. Furthermore, we present a systematic way of deriving these anharmonic couplings from first- principles calculations. To test our revised model, we have carried out various measurements on BT single crystals and compared them with predictions from our simulations. The focus of this benchmark is on dielectric properties such as permittivity and hysteresis curves.

This paper is organized as follows: In Sec. II, a revised scheme for including anharmonic couplings for the self-energy in the effective Hamiltonian approach is derived. Building on this, in Sec. III, we show the parametrization by first-principles calculations. Finally, Sec. IV uses our parameter set for MD simulations and compares it to experimental measurements on BT single crystals.

## II. THEORETICAL FRAMEWORK

### A. Definition of local-mode self-energy

In 2008, Nishimatsu *et al.* [27] presented a revised effective Hamiltonian, which has the following form:

$$H^{\text{eff}} = \frac{M^*_{\text{dipole}}}{2} \sum_{\boldsymbol{R},\alpha} \dot{u}_\alpha^2(\boldsymbol{R}) + \frac{M^*_{\text{acoustic}}}{2} \sum_{\boldsymbol{R},\alpha} \dot{w}_\alpha^2(\boldsymbol{R})$$

$$+ V^{\text{self}}(\{\boldsymbol{u}\}) + V^{dpl}(\{\boldsymbol{u}\}) + V^{\text{short}}(\{\boldsymbol{u}\})$$

$$+ V^{\text{elas,homo}}(\eta_1, \ldots, \eta_6) + V^{\text{elas,inho}}(\{\boldsymbol{w}\})$$

$$+ V^{\text{coupl,homo}}(\{\boldsymbol{u}\}, \eta_1, \ldots, \eta_6)$$

$$+ V^{\text{coupl,inho}}(\{\boldsymbol{u}\}, \{\boldsymbol{w}\}) - Z^* \sum_{\boldsymbol{R}} \epsilon \cdot u(\boldsymbol{R}). \quad (1)$$

The Hamiltonian is a function of variables $\{\boldsymbol{u}\}$, the amplitude of the optical soft mode, where the brackets $\{\cdots\}$ represent a set of amplitudes in a supercell. Further variables within the Hamiltonian are dimensionless displacement vectors $\boldsymbol{w}$ for each unit cell and strain variables $\eta_l$ in Voigt notation. $M^*_{\text{dipole}}$ and $M^*_{\text{acoustic}}$ represent effective masses of $\boldsymbol{u}$ and $\boldsymbol{w}$, respectively. $\boldsymbol{R}$ is the position of a unit cell within the supercell. $Z^*$ is the Born effective charge corresponding to the soft mode and $\epsilon$ represents an external field. The time derivatives of the variables are given by $\dot{u}_\alpha$ and $\dot{w}_\alpha$, where $\alpha$ denotes the Cartesian component. The total energy comprises five potential energy contributions: a local-mode self-energy $V^{\text{self}}$, the dipole-dipole interaction $V^{dpl}$, the short-range interaction $V^{\text{short}}$, the homogeneous and inhomogeneous contributions of the elastic energy ($V^{\text{elas,homo}}$ and $V^{\text{elas,inho}}$, respectively), and the homogeneous and inhomogeneous contributions of the strain-phonon coupling ($V^{\text{coupl,homo}}$ and $V^{\text{coupl,inho}}$, respectively). For enabling MD simulations, the kinetic energies of the optical soft mode and the long-wavelength limit of the acoustic branch [first and second terms on the right-hand side of Eq. (1)] are considered. The last term in Eq. (1) allows applying external fields to the supercell. A more detailed description of all terms can be found in Ref. [27].

To derive a scheme for including anharmonic couplings to higher-energy phonons, we first shortly recap the definition of the local-mode self-energy as found in the literature [29]. The original mathematical expression defined by King-Smith *et al.* [25] was given by a fourth-order polynomial of the soft-mode amplitude vector $\boldsymbol{u}$. Nishimatsu *et al.* [29] extended this expression up to the eighth order for a more accurate description of anharmonic contributions originating from $\boldsymbol{u}$. The complete term for the self-energy defined by Nishimatsu *et al.* [29] is presented in Eq. (2), where $\kappa_2, \alpha, \gamma, k_1, k_2, k_3$, and $k_4$ represent parameters. The sum over $\boldsymbol{R}$ accounts for each unit cell in the supercell.

$$V^{\text{self}}(\{u\}) = \sum_{R} \Big\{ \kappa_2 u^2(\boldsymbol{R}) + \alpha u^4(\boldsymbol{R}) + \gamma \big[ u_y^2(\boldsymbol{R}) u_z^2(\boldsymbol{R}) + u_z^2(\boldsymbol{R}) u_x^2(\boldsymbol{R}) + u_x^2(\boldsymbol{R}) u_y^2(\boldsymbol{R}) \big] + k_1 u^6(\boldsymbol{R}) + k_2 \big( u_x^4(\boldsymbol{R}) * \big[ u_y^2(\boldsymbol{R}) + u_z^2(\boldsymbol{R}) \big]$$

$$+ u_y^4(\boldsymbol{R}) * \big[ u_z^2(\boldsymbol{R}) + u_x^2(\boldsymbol{R}) \big] + u_z^4(\boldsymbol{R}) * \big[ u_x^2(\boldsymbol{R}) + u_y^2(\boldsymbol{R}) \big] \big) + k_3 u_x^2(\boldsymbol{R}) u_y^2(\boldsymbol{R}) u_z^2(\boldsymbol{R}) + k_4 u^8(\boldsymbol{R}) \Big\}. \quad (2)$$

In further sequence, we evaluate the above equation for a single unit cell in the high-symmetry directions $\langle 001 \rangle$, $\langle 011 \rangle$, and $\langle 111 \rangle$. We denote the resulting self-energies as $E(u)$, and obtain them by substituting the expressions $\boldsymbol{u} = (0, 0, u)$, $\boldsymbol{u} = (0, u, u)$, and $\boldsymbol{u} = (u, u, u)$, respectively, for the soft-mode amplitude. That results in Eqs. (2a)–(2c) and will also be used for the parametrization in Sec. II C:

$$E_{001}(u) = \kappa u^2 + \alpha u^4 + k_1 u^6 + k_4 u^8, \quad (2a)$$

$$E_{011}(u) = \kappa u^2 + \big( \alpha + \tfrac{1}{4} \gamma \big) u^4 + \big( k_1 + \tfrac{1}{4} k_2 \big) u^6 + k_4 u^8, \quad (2b)$$

$$E_{111}(u) = \kappa u^2 + \big( \alpha + \tfrac{1}{3} \gamma \big) u^4 + \big( k_1 + \tfrac{2}{9} k_2 + \tfrac{1}{27} k_3 \big) u^6 + k_4 u^8. \quad (2c)$$

This energy contribution arises from local displacements according to the displacement pattern of the soft mode. The interaction with neighboring unit cells as well as the energy contribution of associated elastic effects is not included here. The latter are accounted for by strain-phonon coupling and various elastic terms in the Hamiltonian as described above.

### B. Scheme for including anharmonic couplings

In this section, we derive a revised scheme for including anharmonic couplings to higher-energy phonons within the local-mode self-energy. For the construction of the effective Hamiltonian presented in Eq. (1), the choice of a local basis by lattice Wannier functions (LWFs) is required [30,31]. However, this choice is not unambiguous and should be carried out under the following aspects. For cubic BT, the highest symmetry can be obtained by the choice of LWFs centered on the $A$ site or $B$ site. Since it is mainly the $B$ site that is responsible [31] for the ferroelectric distortions, it is advantageous to define it as the center of the LWFs. For the remainder of this paper, we will use this $B$-centered basis for all derivations and calculations including all phonon modes. As a next step, we have to define the phonon modes which are serving as the basis in the conventional effective Hamiltonian of Eq. (1). In cubic BT, there are five eigenmodes with each of them being triply degenerate. Besides the acoustic mode, there are three optical modes with $\Gamma_{15}$ symmetry and one optical mode with $\Gamma_{25}$ symmetry [25,28,30]. Of particular interest are the optical $\Gamma_{15}$ eigenmodes, which are responsible for the ferroelectric transition [25]. We will refer to them as $u$ (soft mode, imaginary frequency of $193i$ cm$^{-1}$), $v_1$ ($178$ cm$^{-1}$), and $v_2$ ($468$ cm$^{-1}$). The corresponding eigenvectors and frequencies can be calculated by means of DFT. For details we refer to the next section. The eigenvector components of the interatomic force constant (IFC) matrix for the soft mode are estimated with values of $\xi_{Ba} = 0.157$, $\xi_{Ti} = 0.774$, $\xi_{O1,O2} = -0.195$ and $\xi_{O3} = -0.547$. Here, we listed barium, titanium, and oxygen values in the five-atom unit cell, whereby $O_1$ and $O_2$ denote the oxygens in plane with the titanium atom. Analogously the patterns for $v_1$ and $v_2$ can be calculated: $\xi_{Ba}^{v_1} = 0.862$, $\xi_{Ti}^{v_1} = -0.311$, $\xi_{O1,O2}^{v_1} = -0.281$, $\xi_{O3}^{v_1} = 0.010$, and $\xi_{Ba}^{v_2} = -0.172$, $\xi_{Ti}^{v_2} = 0.317$, $\xi_{O1,O2}^{v_2} = -0.427$, $\xi_{O3}^{v_2} = 0.709$. To obtain the contributions of these phonons to the ferroelectric distortion between cubic and tetragonal phase, we started with calculating the associated displacement pattern $\vec{f}$. The components of the pattern result in

$f_{Ba} = 0.114$ Å, $f_{Ti} = 0.219$ Å, $f_{O1,O2} = -0.079$ Å, and $f_{O3} = -0.007$ Å. Comparing the ferroelectric distortion with the soft-mode pattern shows a large overlap. Owing to that, the main part of the ferroelectric distortion can be described by the soft mode and, therefore, this mode is chosen as the basis for the effective Hamiltonian in Eq. (1). The acoustic mode is also included by the variables $w$ within the long-wavelength limit. The other phonons have not been considered so far. However, Paul *et al.* [28] showed in their work that not only the soft mode $u$, but also the coupling with the modes $v_1$ and $v_2$ have an influence on the phase transitions. To quantify this contribution, we will apply the same approach as suggested by Paul *et al.* [28]. That is, we use the equation $\vec{S} = \vec{f} - (\vec{f} \cdot \hat{e}_{soft})\hat{e}_{soft}$, where $\vec{S}$ is the fraction of the displacement not yet covered by the soft mode. $\hat{e}_{soft}$ represents the soft-mode eigenvector and $\vec{f}$ the ferroelectric distortion from above. Thus, the overlap of $\vec{S}$ with the phonon modes not yet considered in the effective Hamiltonian can now be calculated. The determined overlap of $v_1$ can be quantified as 0.85 and that of $v_2$ as 0.26. In contrast, the $\Gamma_{25}$ mode shows a negligible overlap. Due to that, for an improved description of the potential energy surface, the inclusion of $v_1$ and $v_2$ is relevant. The next step is to lay the mathematical foundation for this inclusion. To account for the contributions of these high-energy modes, Paul *et al.* [28] developed the self-energy as a Taylor series in eighth order of $u$ and second order of $v_1$ and $v_2$, where mixed terms between $u$ and either $v_1$ or $v_2$ were considered. Since we cannot make *a priori* statements about the importance of individual couplings we decided to take a more general approach. Therefore, we start with the extension of the self-energy by an approximation by means of a multivariate Taylor series as written in Eq. (3). In this paper, we deal exclusively with the $\langle 001 \rangle$ direction. A possible involvement of the other directions will be discussed further below. The variables Taylor series are the amplitudes of the phonon modes $u$, $v_1$, and $v_2$. The evaluation of the series is done around the cubic phase. Therefore, we set $u_0 = 0$, $v_{1,0} = 0$ and $v_{2,0} = 0$. For the soft-mode amplitude $u$, we expand the series up to the eighth order ($n_1 = 0, \ldots, 8$):

$$E_{001}^{anh}(u, v_1, v_2) = \sum_{n_1}^{8} \sum_{n_2}^{6} \sum_{n_3}^{6} \frac{(u - u_0)^{n_1}(v_1 - v_{1,0})^{n_2}(v_2 - v_{2,0})^{n_3}}{n_1! n_2! n_3!} \left( \frac{\partial^{n_1+n_2+n_3} E(u, v_1, v_2)}{\partial u^{n_1} \partial v_1^{n_2} \partial v_2^{n_3}} \right)(u_0, v_{1,0}, v_{2,0}). \tag{3}$$

In contrast to Paul *et al.* [28], the series expansion is also performed for $v_1$ and $v_2$ up to the sixth order ($n_{2,3} = 0, \ldots, 6$). The series expansion in full form can be found in the Supplemental Material [32] in Eq. (S1). Due to the symmetry of the cubic phase, various couplings are zero by definition. These can be determined, for example, by the program ISOTROPY [33,34]. The latter was used to rewrite the full-form function from Eq. (S1) [32]. Thus, the forbidden couplings were removed and the remaining ones were replaced by parameters $a_i$, $b_i$, $c_i$, and $d_i$. The resulting function for the self-energy in the $\langle 001 \rangle$ direction is written in Eq. (4). The parameters $c_i$ are analogous to those used in Eq. (2a). The parameters $a_i$ and $b_i$, which represent couplings between $u$ and either $v_1$ or $v_2$, are introduced. The parameters $d_i$ are mixed couplings of $u$, $v_1$, and $v_2$.

$$E_{001}(u, v_1, v_2) = c_0 + c_1 u^2 + c_2 u^4 + c_3 u^6 + c_4 u^8 + a_1 u v_1 + a_2 v_1^2 + a_3 u^3 v_1 + a_4 u^2 v_1^2 + a_5 u v_1^3 + a_6 v_1^4 + a_7 u^5 v_1 + a_8 u^4 v_1^2$$
$$+ a_9 u^3 v_1^3 + a_{10} u^2 v_1^4 + a_{11} u v_1^5 + a_{12} v_1^6 + b_1 u v_2 + b_2 v_2^2 + b_3 u^3 v_2 + b_4 u^2 v_2^2 + b_5 u v_2^3 + b_6 v_2^4 + b_7 u^5 v_2$$
$$+ b_8 u^4 v_2^2 + b_9 u^3 v_2^3 + b_{10} u^2 v_2^4 + b_{11} u v_2^5 + b_{12} v_2^6 + d_1 v_1 v_2 + d_2 u^2 v_1 v_2 + d_3 u v_1^2 v_2 + d_4 u v_1 v_2^2 + d_5 v_1^3 v_2$$
$$+ d_6 v_1^2 v_2^2 + d_7 v_1 v_2^3 + d_8 u^4 v_1 v_2 + d_9 u^3 v_1^2 v_2 + d_{10} u^3 v_1 v_2^3 + d_{11} u^2 v_1^3 v_2 + d_{12} u^2 v_1^2 v_2^2 + d_{13} u^2 v_1 v_2^3 + d_{14} u v_1^4 v_2$$
$$+ d_{15} u v_1^3 v_2^2 + d_{16} u v_1^2 v_2^3 + d_{17} u v_1 v_2^4 + d_{18} v_1^5 v_2 + d_{19} v_1^4 v_2^2 + d_{20} v_1^3 v_2^3 + d_{21} v_1^2 v_2^4 + d_{22} v_1 v_2^5. \tag{4}$$

126

The derived equation contains many anharmonic couplings, so that a direct determination of the necessary parameters as shown in Paul *et al.* [28] is no longer possible. To determine all couplings as accurately as possible, an alternative approach involving the fitting of anharmonic couplings [35] will be used in Sec. II D. For now, let us assume that we have already determined all the coupling parameters. That means we now have a function for the local-mode self-energy, which depends on $u$, $v_1$, and $v_2$, and is not compatible with the effective Hamiltonian defined in Eq. (1). A solution to this issue would be to extend the whole Hamiltonian by these additional degrees of freedom, but that would be beyond the scope of this paper. In fact, a significant advantage of the effective Hamiltonian lies in its computational speed, and adding more degrees of freedom would change that. To recast our expansion in Eq. (3) to a function of one variable, we can compute the amplitudes $v_1$ and $v_2$ that minimize [28] the self-energy for any value of $u$. Unfortunately, an analytical solution is not feasible in our case due to the complexity of Eq. (3). Therefore, we decided to use a numerical optimization scheme to search for the minimizing $v_{1,\min}(u_i)$ and $v_{2,\min}(u_i)$ amplitudes corresponding to a given discrete value of $u_i$. This allows us to compute the minimum self-energy as a function of $u$ for a chosen discrete range, as shown schematically in this equation:

$$E_{001}(u_i) = E_{001}^{\mathrm{anh}}[u_i, v_{1,\min}(u_i), v_{2,\min}(u_i)]. \quad (5)$$

As the method for the minimization of $v_1$ and $v_2$ we used the Nelder-Mead algorithm [36] for two dimensions.

Finally, for the effective Hamiltonian, we again need an analytic function for the self-energy. The simplest solution is to take Eq. (2a) and fit the data, which now include contributions from anharmonic couplings. This approach is similar to the approximation in Paul *et al.* [28], where they insert their additional anharmonic contribution into the parameters $k_1$ and $k_4$.

An advantage of the above-derived scheme for including anharmonic couplings is that it can be used analogously for the other directions $\langle 011 \rangle$ and $\langle 111 \rangle$. The only difference lies in estimating the coupling parameters via fitting, which will be discussed in detail in the next section.

### C. Parameters of conventional Hamiltonian

In this section we briefly discuss the parametrization of the conventional effective Hamiltonian, i.e., the one defined by Nishimatsu *et al.* [29]. However, we will refrain from a detailed description of all energy terms to be parametrized since this has already been discussed sufficiently in other publications [25,28,29]. Since we use the PBEsol functional [37] in contrast to other parametrizations in the literature, we will nevertheless give an overview of the differences and similarities. A detailed description of the DFT settings and a comparison of the obtained parameters with other exchange-correlation functionals [38,39] are provided in the Supplemental Material [32]. In general, parametrization starts with the relaxation of the cubic phase. In our case, this resulted in a lattice constant of $a_0 = 3.987$ Å, which agrees very well with other PBEsol results from the literature [20,40]. Compared to the value obtained with the Wu-Cohen func-

tional [29,41] of $a_{\mathrm{WC}} = 3.986$ Å, the PBEsol yields an almost identical value. Also the SCAN (Strongly-constrained and appropriately-normed) functional [42] yields a very similar value [28] of $a_{\mathrm{SCAN}} = 3.99$ Å. Altogether, all three functionals yield results close to the experimental value [25] of $a_{\mathrm{expt}} = 4.01$ Å.

The next step is to calculate the eigendisplacements, which are the eigenvectors of the second-order force constant matrix. The latter was calculated using the frozen-phonon method implemented within the VASP package (IBRION 5 tag). To check the obtained results, we also carried out a density functional perturbation theory (DFPT) calculation using the IBRION 7 tag within VASP. Both approaches agree well with each other and yield eigenvector components as listed in the previous section. We now take this soft-mode displacement pattern as the basis for the effective Hamiltonian. To parametrize the local-mode self-energy, we displace the atoms in the different directions, $\langle 001 \rangle$, $\langle 011 \rangle$, and $\langle 111 \rangle$, using the soft-mode pattern. Then Eqs. (2a)–(2c) are used to determine the parameters $\kappa$, $\alpha$, $\gamma$ and $k_1$–$k_4$ by fitting. An overview of the obtained values can be found in Table I. Since these parameters strongly depend on the chosen order of the polynomial and on the chosen exchange-correlation functional, we refrain here from a comparison with values from the literature. Another energy contribution represents the coupling of phonons with the deformation of the unit cell. The parametrization for this case was performed in two different ways. The first method adheres to the literature [25]; i.e., atomic displacements according to the soft mode were frozen in, and the shape of the unit cell was varied. That allows the calculation of the change in the harmonic coefficient $\kappa$ as a function of strain $\eta$, which in turn allows the coupling parameters to be determined. As a second approach, we considered the following. We displaced the atoms analogously to the first approach, but then the internal coordinates were fixed and the unit cell shape and volume were relaxed for each displacement. VASP allows this through the setting ISIF 6. To extract the coupling parameters, we used the scheme Nishimatsu *et al.* used for their valley tracing method (VTM) [29]. The results of the two approaches vary slightly, with values of $B_{1xx} = -230.75$ eV/Å$^2$, $B_{1yy} = -21.76$ eV/Å$^2$, and $B_{4yz} = -15.56$ eV/Å$^2$ determined with the first approach. In contrast, the values of the second method are $B_{1xx} = -235.06$ eV/Å$^2$, $B_{1yy} = -19.34$ eV/Å$^2$, and $B_{4yz} = -15.33$ eV/Å$^2$. Since the second method optimizes each unit cell and allows a larger number of calculated displacements, these parameters are used for the rest of this paper. A more detailed description of each method can be found in the Supplemental Material [32]. Next, we turn to the determination of elastic constants. Since we use the cubic phase as a reference for the description of our system, the number of independent constants is reduced to three. These are given by $B_{11}$, $B_{12}$, and $B_{44}$, whereby these values are obtained from the elastic constants multiplied by the unit cell volume. The calculation was performed by applying different deformations [29] to the unit cell and fitting the equation of state. The corresponding results are listed in Table I.

The determination of short-range interaction parameters $j_1$–$j_7$ was done analogously to the procedure proposed by Nishimatsu *et al.*; that is, a series of phonon calculations at various high-symmetry points in reciprocal space was used

TABLE I. Parameters for the effective Hamiltonian describing pure BT.

| Elastic and coupling | | Self-energy | | Short range and long range | |
|---|---|---|---|---|---|
| $m^*$ (amu) | 38.148 | $\kappa$ (eV/Å$^2$) | −1.965 | $Z^*$ (e) | 10.267 |
| $B_{11}$ (eV) | 126.137 | $\kappa_2$ (eV/Å$^2$) | 8.007 | $\varepsilon_\infty$ | 6.847 |
| $B_{12}$ (eV) | 42.391 | $\alpha$ (eV/Å$^4$) | 123.492 | $j_1$ (eV/Å$^2$) | −2.060 |
| $B_{44}$ (eV) | 50.046 | $\gamma$ (eV/Å$^4$) | −165.344 | $j_2$ (eV/Å$^2$) | −1.173 |
| $B_{1xx}$ (eV/Å$^2$) | −235.064 | $k_1$ (eV/Å$^6$) | −528.388 | $j_3$ (eV/Å$^2$) | 0.680 |
| $B_{1yy}$ (eV/Å$^2$) | −19.341 | $k_2$ (eV/Å$^6$) | 123.688 | $j_4$ (eV/Å$^2$) | −0.610 |
| $B_{4yz}$ (eV/Å$^2$) | −15.333 | $k_3$ (eV/Å$^6$) | 307.317 | $j_5$ (eV/Å$^2$) | 0.000 |
| | | $k_4$ (eV/Å$^8$) | 3370.229 | $j_6$ (eV/Å$^2$) | 0.277 |
| | | | | $j_7$ (eV/Å$^2$) | 0.000 |

to provide the necessary eigenvalues for the linear system of equations (see Eqs. (15a)–(15g) in Ref. [29]). By solving this system of equations, the parameters $j_1$–$j_7$ and $\kappa_2$ could be determined, which are listed in Table I. It should be noted that the $\kappa_2$ value was adapted according to Eq. (17) in Ref. [29]. The remaining parameters in Table I were derived from a DFPT calculation. Table I also includes the Born effective charge of the soft mode as well as the optical dielectric constant, obtained from DFPT. The effective mass $m^*$ was calculated by using the soft-mode eigenvector and the corresponding atomic masses of the ions.

### D. Fitting of anharmonic couplings

In Sec. II B, we discussed a scheme to include additional anharmonic terms, whereas here, the quantitative determination of the corresponding parameters shall be addressed. The chosen approach, i.e., the expansion of the self-energy in three variables $v_1$, $v_2$, and $u$ up to the sixth-, respectively, eighth-order results in a relatively large number of coupling constants. An explicit calculation is possible only for a few of these parameters, an example of which can be found in Paul *et al.* [28]. Nevertheless, to determine all required parameters, we follow a similar approach as Erba *et al.* [35]. That is, we want to determine the anharmonic couplings by fitting Eq. (3) to a correspondingly large set of DFT calculations. The dataset must be built by various displacements according to the displacement patterns of $u$, $v_1$, and $v_2$. These patterns are obtained from the initial phonon calculation of the previous section. We already reported the patterns for the soft mode, $v_1$, and $v_2$ in the previous section. We used these patterns to create structures with different displacements of the atoms by superposition. For the $\langle 001 \rangle$ direction, we generated about 2000 of these structures and calculated the corresponding total energies using DFT. This dataset was then used to fit Eq. (4) to determine all coupling parameters. Since we have a large number of parameters to determine, much emphasis was put on the stability of the fit. For that purpose, different fit algorithms like Levenberg-Marquardt, Nelder-Mead, or Powell were used to cross-check the results. Furthermore, a cross-validation procedure was used to investigate the quality of the fit function. A detailed description of the above-mentioned investigations can be found in the Supplemental Material [32]. Concerning the main task, the determination of the coupling parameters, it could be shown that all algorithms yield the same global minimum. The associated calculated parameters

are listed in Table S2 [32]. A visualization of the derived potential energy as a function of $u_x$, $v_{1x}$, and $v_{2x}$ is provided in Fig. 1(a). It can be observed that the local minima of the potential energy surface are slightly shifted by the inclusion of $v_1$ and $v_2$. That means for each $u > 0$ there are associated nonvanishing amplitudes $v_1$ and $v_2$, which minimize the energy.

A final necessary step is to incorporate these anharmonic couplings into the effective Hamiltonian. As discussed in Sec. II B, we want to take the relatively simple way here and pack the couplings into adapted $k_1$ and $k_4$ parameters. To do this, we evaluate Eq. (4) using the parameters of Table S2 [32] for a discrete range of $u = 0$ to 0.25 Å and simultaneously minimize over the amplitudes $v_1$ and $v_2$ [see Fig. 1(b)]. Equation (2a) is then fitted to the data using $k_1$ and $k_4$ as fit parameters. The resulting fitted parameters $k_1'$ and $k_4'$ are −1443.850 eV/Å$^6$ and 17 216.816 eV/Å$^8$, respectively. A visualization of the self-energy, with and without additional anharmonic couplings, as a function of $u$ in the $\langle 001 \rangle$ direction is presented in Fig. 1(c).

Although in this paper we are mainly concerned with the self-energy in the $\langle 001 \rangle$ direction, the two other directions, $\langle 011 \rangle$ and $\langle 111 \rangle$, should also be briefly discussed here. The calculation of the coupling parameters is analogous to the $\langle 001 \rangle$ direction, whereby the input structures are generated by displacing atoms in two or three dimensions using the displacement patterns, respectively. The Taylor expansion for these directions can be done in two ways; either one uses vectors $\boldsymbol{u}$, $\boldsymbol{v}_1$, and $\boldsymbol{v}_2$, or one treats each direction individually. The latter is somehow analogous to Eqs. (2a)–(2c) and has the advantage that the series expansion from Eq. (3) can be used. We proceeded with the second approach and also calculated the remaining two directions and the corresponding renormalized total energy. The incorporation of these additional directions into the effective Hamiltonian can be done with a refit using the parameters $\gamma$, $k_2$, and $k_3$. However, it became apparent that these parameters are only partially capable of properly incorporating the additional information (see Supplemental Material [32] for more details). A solution to overcome this issue is to extend the self-energy from Eq. (2) with additional parameters. For the remainder of this paper, however, we use the parameter set presented above. It should be noted, nevertheless, that this does not leave the other two directions untouched. The incorporation of anharmonic couplings by adjusting $k_1$ and $k_4$ also impacts the $\langle 011 \rangle$ and $\langle 111 \rangle$ directions as one can see in Eqs. (2b) and (2c).

128
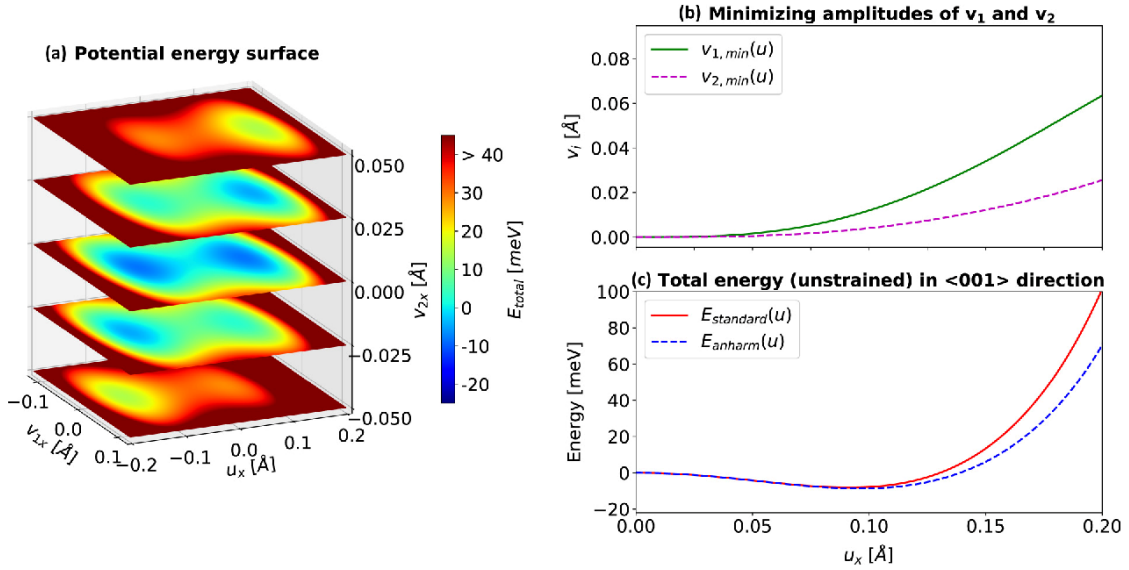
FIG. 1. Visualization of self-energy as a function of the three phonon mode amplitudes $u$, $v_1$, and $v_2$ along the $\langle 001 \rangle$ direction (a). Panel (b) shows the values for $v_1$ and $v_2$ that minimize the self-energy for a given $u$. Panel (c) shows the self-energy back-transformed to a function of one variable $u$ by minimizing the energy with respect to $v_1$ and $v_2$ for a given $u$.

## III. METHODOLOGICAL DETAILS

### A. Experimental setup

A BT single crystal, polished on both sides, was purchased from SurfaceNet GmbH (48432 Rheine, Germany). Prior to measuring, the sample was held at 353 K for a week in air atmosphere. Electrical contacts were made with silver paint on the top and bottom of the sample ($5 \times 2 \times 0.1$ mm) and the wires connected in—typical for dielectric measurements [43]—a pseudo-four-point configuration. The dielectric data in a frequency range from 20 Hz to 1 MHz were collected with an E4980A Precision *LCR* meter (Agilent). The static hysteresis loops were measured using an AixACCT TF2000 Analyzer combined with a high-voltage booster (HVB 1000) and a Krohn-Hite model 7500 amplifier. For both measurements the temperature (300–540 K) was controlled via a nitrogen flow based cryostat (Novocontrol Quatro Cryosystem).

### B. DFT calculations for parametrization of the effective Hamiltonian

For all DFT calculations used for parametrization of the effective Hamiltonian, we applied the projector-augmented [44] DFT package VASP [45–48] and PBEsol [37] as the exchange-correlation functional. All calculations with five-atom unit cells were done using a $k$ grid of size $8 \times 8 \times 8$ and an energy cutoff of 520 eV. The $2 \times 2 \times 2$ supercell calculations were carried out with a $k$ grid of $4 \times 4 \times 4$ and an energy cutoff of 520 eV.

### C. MD setup

All MD simulations in the following section were carried out in the $NVT$ ensemble. The Nosé-Poincaré thermostat [49] was used to maintain a constant temperature. For the simulation of the phase diagram, we decided to use a simulation

box size of $16 \times 16 \times 16$ unit cells. A comparison with other sizes can be found in the Supplemental Material [32]. A time step of 0.002 ps was used for all simulations. The system was thermalized for 360 ps, and then statistical values were recorded over 40 ps. The phase diagram was obtained using a temperature step of 1 K. The simulation of permittivity as a function of temperature was performed as follows: For each temperature step, which was chosen to be 1 K, the system was thermalized for 2 ns, and then over 2 ns the statistical values were recorded. A simulation box of size $16 \times 16 \times 16$ was also chosen here. The permittivity was calculated using the fluctuations of the dipoles, as shown in Eq. (6). Here, $e$ represents the elementary charge and $V$ the volume of the unit cell.

$$\epsilon_r = \frac{e^2 Z^{*2}}{V k_B \epsilon_0 T} (\langle u^2 \rangle - \langle u \rangle^2). \tag{6}$$

The simulations of polarization–electric field hysteresis curves (*P-E* loops) were performed for the quasistatic case. An external electric field was applied from −100 to +100 kV/cm in 0.5 kV/cm steps. For each field strength, the system was thermalized over 360 ps, and then the required values were recorded over 40 ps. Here, we chose a simulation box size of $24 \times 24 \times 24$. A comparison to dynamic loops at high frequencies can be found in the Supplemental Material [32]. All simulations were performed using the open-source code FERAM developed by Nishimatsu *et al.* [27,29].

## IV. RESULTS

This section will now apply the elaborated parametrization and use it to perform molecular dynamics simulations. At the same time, we performed measurements on BT single crystals to provide a basis for comparison of properties such as dielectric permittivity and ferroelectric hysteresis curves.
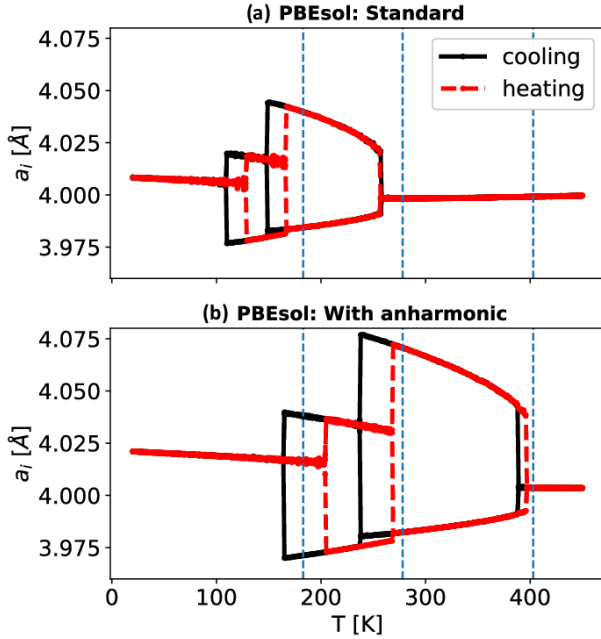
FIG. 2. Phase diagram in terms of the temperature evolution of lattice constants $a_i$ for BT simulated by MD using the two parameter sets (a) without and (b) with additional anharmonic couplings to higher-energy phonons. The black line was obtained by cooling and the red line by heating the system in the MD simulation. The dashed vertical lines represent the experimentally observed transition temperatures.

#### A. Transition temperatures

First, we consider the simulated phase diagram, i.e., the evolution of the lattice constants as a function of temperature, as shown in Fig. 2. To demonstrate the influence of the additional anharmonic couplings, we also present the result of the conventional Hamiltonian. To account for the effect of hysteresis, heating and cooling simulations were performed in each case, and the transition temperature was taken as the average value between the two. It is obvious that the transition

temperatures are significantly closer to the experimental results when additional anharmonic couplings are incorporated. Further, it is observed that the lattice parameters also change accordingly. Thus, an increase of the lattice parameters is observed for all monitored temperatures. The cubic phase shows a lattice constant of 4.00 Å at 405 K in the simulation, which is in excellent agreement with experimental data [50] of 4.00 Å. The lattice parameters of the tetragonal phase, compared with experimental values [50] of $a = 3.99$ Å and $c = 4.04$ Å, are slightly overestimated by the simulation. The same is observed for the lattice parameters [50] of the orthorhombic and rhombohedral phases. For the sake of completeness, thermal expansion should also be briefly discussed here. Although we include a large number of anharmonic terms, the thermal expansion is described qualitatively wrong as shown in Fig. 2. However, these additional couplings are not actively present in our simulation and the original formalism of Nishimatsu *et al.* [29] is used. The latter is known to fail at reproducing the thermal expansion [51]. A solution to this would be to extend the formalism by the degrees of freedom of $v_1$ and $v_2$ and to modify the potential of the acoustic mode. However, this is beyond the scope of this paper and may be addressed in a future publication.

Furthermore, we want to compare our simulations with results from the literature. For this purpose, an overview of parametrizations using different exchange-correlation functionals and the corresponding transition temperatures is presented in Table II. The results of the LDA functional show the largest deviation from the experimental data. The application of a constant pressure on top of LDA yields higher temperatures, but rather large deviations are still observed. The WC-GGA functional expectedly gives results similar to our standard PBEsol simulation. SCAN gives similar results. The WC-GGA functional combined with a temperature-dependent external pressure term yields the transition temperature between the cubic and tetragonal phases close to the experimental value. Nevertheless, the best match to experiments is demonstrated by our PBEsol-based scheme with additional anharmonic couplings as well as another flavor for including anharmonic couplings combined with SCAN [28]. The good agreement between simulation and experiment

TABLE II. Comparison of transition temperatures estimated via molecular dynamics simulations based on effective Hamiltonians. The table shows results for different exchange-correlation functionals used in the parametrization of the Hamiltonian. The first set of results is obtained with the conventional Hamiltonian. The second set of results is obtained with applying pressure. The third set of results includes additional anharmonic couplings. R = rhombohedral, O = orthorhombic, T = tetragonal, C = cubic, and $\Theta$ = Temperature.

| Exchange-correlation functional | Pressure | R↔O | | O↔T | | T↔C | |
|---|---|---|---|---|---|---|---|
| LDA [29] | – | 95 K | –48% | 110 K | –60% | 137 K | –66% |
| WC-GGA [29] | – | 102 K | –44% | 160 K | –42% | 288 K | –29% |
| SCAN [28] | – | 111 K | –39% | 141 K | –49% | 213 K | –47% |
| PBEsol (this work) | – | 119 K | –35% | 158 K | –43% | 257 K | –36% |
| LDA [29] | –5 GPa | 210 K | 15% | 245 K | –12% | 320 K | –21% |
| WC-GGA [29] | –2 GPa | 117 K | –36% | 218 K | –22% | 408 K | 1% |
| WC-GGA [29] | –0.005 $\Theta$ GPa | 103 K | –44% | 187 K | –33% | 411 K | 2% |
| SCAN (anharmonic[a]) [28] | – | 230 K | 26% | 278 K | 0% | 375 K | –7% |
| PBEsol (this work, anharmonic) | – | 186 K | 2% | 255 K | –8% | 395 K | –2% |
| Expt. [28,52] | – | 183 K | 0% | 278 K | 0% | 403 K | 0% |

[a]Different flavor of anharmonic coupling up to second order in $v_1$ and $v_2$.

130
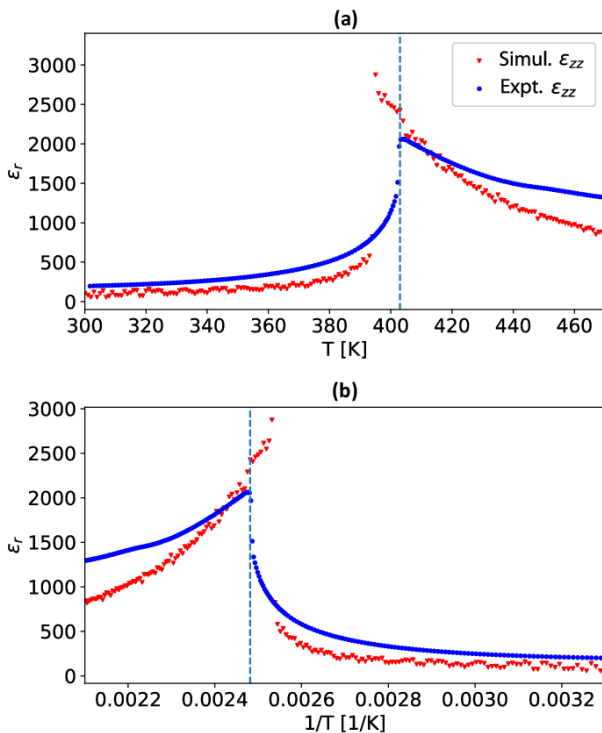
FIG. 3. Permittivity around the cubic to tetragonal phase transition as a function of (a) temperature and (b) inverse temperature, comparing measurements on a BT single crystal (blue) and simulations (red) using the effective Hamiltonian with anharmonic coupling to higher-energy phonons. The dashed line indicates the $T_C$ determined from experiments.

suggests that the local energetic minima are better described by including additional anharmonic couplings. To test this hypothesis, we performed *ab initio* molecular dynamics (AIMD) simulations for different temperatures and compared the potential energy surfaces to those of the effective Hamiltonians. As described in detail in the Supplemental Material [32], the inclusion of anharmonic couplings contributes a significant part to the potential energy surface. Furthermore, the energy differences between AIMD and effective Hamiltonian become smaller when including anharmonic couplings, which indicates that the potential energy surface is better reproduced by the adapted Hamiltonian.

### B. Permittivity

The hallmark features of ferroelectric transitions are temperature-dependent peaks in the dielectric permittivity. In Fig. 3, we present the permittivity as a function of temperature

around the tetragonal to cubic phase transition measured on a BT single crystal and simulated by MD using the adapted effective Hamiltonian. Similar to the experiment, the results for the simulations were obtained by heating the crystal, i.e., by increasing the temperature in the MD run. The simulated trend of the permittivity below the phase transition shows remarkably good agreement with the experiment. The simulation estimates the maximum permittivity value directly at the phase transition to be 25% higher than the measured one. The value of $\epsilon_r$ above $T_C$ is slightly higher in the experiment, whereby even a small peak can be observed at about 450 K. That may be due to an extra relaxation given by impurities present, or slight deviations from perfect stoichiometry, in the single crystal. In summary, the simulation provides good agreement with the measured values. The simulated permittivity for a larger temperature range can be found in the Supplemental Material [32].

### C. *P-E* loops

Another essential property of ferroelectric materials represents the system's response to external electric fields, also known as polarization–electric field hysteresis curves (*P-E* loops). In this work, we focus mainly on the temperature range near the phase transition between the paraelectric and ferroelectric phases (i.e., $T_C$). Already in the 1950s, Merz [53] showed the occurrence of double loops near $T_C$. Therefore, we decided that this temperature range is ideal for testing our Hamiltonian.

As a starting point, we performed experimental measurements of the *P-E* loops using BT single crystals. The results are shown in Fig. 4(a). At 400 K, just below $T_C$, we see the typical single-loop ferroelectric hysteresis curve. Just above it, at 406 K, we observe a double loop, but not as pronounced as in Merz's data [53]—this is likely due to the changes in single-crystal growth techniques over the intervening 70 years. At 410 K, finally, the double loop has almost vanished. An explanation for this behavior across $T_C$ can be found in Refs. [53,54].

In the next step, we simulated the *P-E* loops using our effective Hamiltonians. To take into account the slightly lower phase transition temperature found in our simulations, we used the highest temperature that shows pure ferroelectric behavior as reference; i.e., we compare simulations at 397 K to the experiment at 400 K. Subsequently, the temperature for the simulation was increased by the same steps as in the experiment. The results of these simulations are shown in Fig. 4(b). The experiment and simulation show a very good qualitative match, even though our simulation exhibits more pronounced double loops. This is actually in very good agreement with the measurements by Merz [53]. Regarding the saturated polarization, experiment and simulation agree very well, even quantitatively. The corresponding values of the external field in the simulation, however, are about a factor of 5 larger compared to the experimental data.
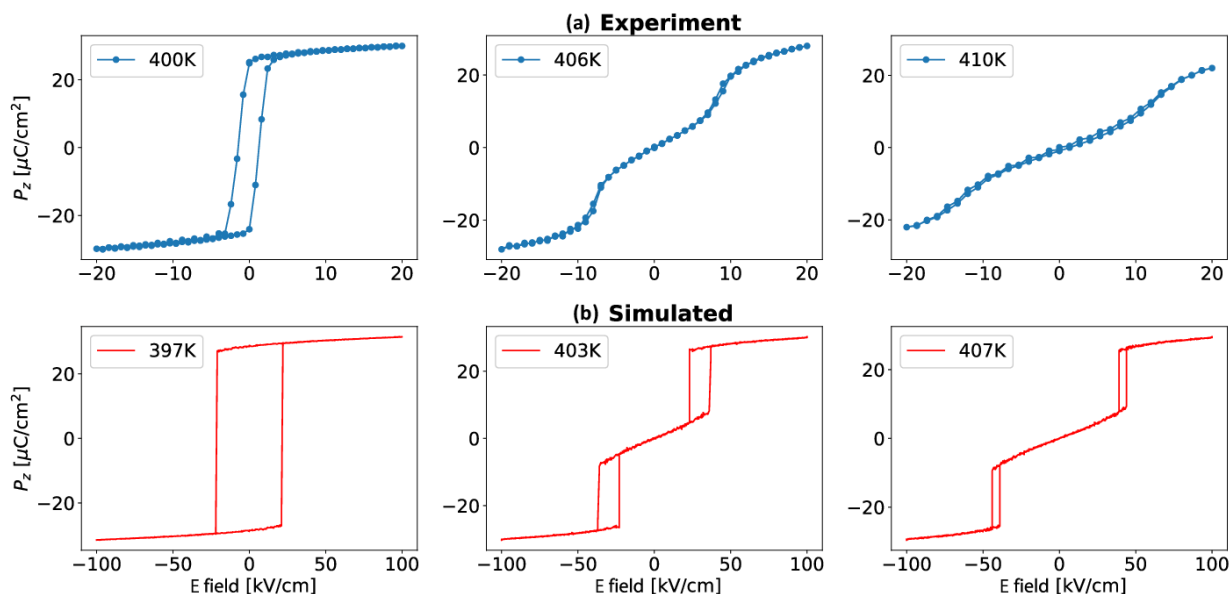
FIG. 4. Comparison between experimental (a) and simulated (b) *P-E* loops of BT near the ferroelectric-paraelectric phase transition. The temperatures for the simulated loops were chosen according to the values of the experiment but shifted to the phase transition temperature observed in the simulation.

## V. CONCLUSION

In this work, an alternative way to incorporate a variety of anharmonic terms to describe the potential energy surface of BT has been shown. The scheme chosen can be easily applied to other systems and provides a systematic extension of the already established formalism of effective Hamiltonians. Instead of relying on individual anharmonic couplings, a larger number of them is included in this work. By this approach a renormalization of the energy surface is observed, which subsequently contributes to an improved description of the transition temperatures. Another advantage of our scheme is the possible extension to all high-symmetry directions. In this work, we focused exclusively on the $\langle 001 \rangle$ direction. Already with this choice the other directions are positively influenced via the chosen parameters and the back-transformation to the original formalism. For further work in this area, the other directions can be taken into account to obtain an even more complete description of the energy surface. Furthermore, the choice of the exchange-correlation functional plays a role. In our case, all calculations were performed with the PBEsol functional. This is obviously a very good choice for the calculation of the required parameters and provides very similar results as the meta-GGA functional SCAN. Comparison with measurements on BT single crystals allowed us to quantify the Hamiltonian as well. The simulated permittivity reflects the

measurements very well. The simulation of the hysteresis was carried out for a quasistatic case in order to create a comparison with low-frequency measurements. Thereby, the absolute values of the saturated polarization between simulation and measurement are in good agreement. Also the occurrence of the double hysteresis in the range of the transition temperature $T_C$ can be confirmed by simulation and measurement. Only regarding the values of the external field is there still room for improvement in order to be able to quantify properties such as the energy stored by the system. Altogether, the parameter set presented here provides an excellent basis for further studies and can be used for possible extensions for substituted systems.

[1] J. Rödel, K. G. Webber, R. Dittmer, W. Jo, M. Kimura, and D. Damjanovic, J. Eur. Ceram. Soc. **35**, 1659 (2015).

[2] V. Veerapandiyan, F. Benes, T. Gindel, and M. Deluca, Materials (Basel). **13**, 5742 (2020).

[3] D. Xue, P. V. Balachandran, R. Yuan, T. Hu, X. Qian, E. R. Dougherty, and T. Lookman, Proc. Natl. Acad. Sci. **113**, 13301 (2016).

[4] P. V. Balachandran, B. Kowalski, A. Sehirlioglu, and T. Lookman, Nat. Commun. **9**, 1668 (2018).

[5] P. V. Balachandran, A. A. Emery, J. E. Gubernatis, T. Lookman, C. Wolverton, and A. Zunger, Phys. Rev. Materials **2**, 043802 (2018).

[6] R. Yuan, Z. Liu, P. V. Balachandran, D. Xue, Y. Zhou, X. Ding, J. Sun, D. Xue, T. Lookman, Adv. Mater. **30**, 1702884 (2018).

132

[7] L. Bellaiche, A. García, and D. Vanderbilt, Ferroelectrics **266**, 41 (2002).

[8] J. Íñiguez and L. Bellaiche, Phys. Rev. Lett. **87**, 095503 (2001).

[9] C. Mentzer, S. Lisenkov, Z. G. Fthenakis, and I. Ponomareva, Phys. Rev. B **99**, 064111 (2019).

[10] M. Acosta, N. Novak, V. Rojas, S. Patel, R. Vaish, J. Koruza, G. A. Rossetti, and J. Rödel, Appl. Phys. Rev. **4**, 041305 (2017).

[11] G. Wang, Z. Lu, Y. Li, L. Li, H. Ji, A. Feteira, D. Zhou, D. Wang, S. Zhang, and I. M. Reaney, Chem. Rev. **121**, 6124 (2021).

[12] T. Maiti, R. Guo, and A. S. Bhalla, Appl. Phys. Lett. **90**, 182901 (2007).

[13] M. Valant, Prog. Mater. Sci. **57**, 980 (2012).

[14] A. J. Moulson and J. M. Herbert, *Electroceramics: Materials, Properties, Applications*, 2nd ed. (John Wiley & Sons Ltd., New York, 2003).

[15] H. D. Megaw, Acta Crystallogr. **5**, 739 (1952).

[16] R. D. King-Smith and D. Vanderbilt, Ferroelectrics **136**, 85 (1992).

[17] R. E. Cohen and H. Krakauer, Phys. Rev. B **42**, 6416 (1990).

[18] W. Zhong, D. Vanderbilt, and K. M. Rabe, Phys. Rev. B **52**, 6301 (1995).

[19] J. C. Wojdeł, P. Hermet, M. P. Ljungberg, P. Ghosez, and J. Íñiguez, J. Phys.: Condens. Matter **25**, 305401 (2013).

[20] J. M. Vielma and G. Schneider, J. Appl. Phys. **114**, 174108 (2013).

[21] R. Pirc and R. Blinc, Phys. Rev. B **60**, 13470 (1999).

[22] L.-Q. Chen, J. Am. Ceram. Soc. **91**, 1835 (2008).

[23] A. F. Devonshire, London, Edinburgh, Dublin Philos. Mag. J. Sci. **40**, 1040 (1949).

[24] A. F. Devonshire, London, Edinburgh, Dublin Philos. Mag. J. Sci. **42**, 1065 (1951).

[25] R. D. King-Smith and D. Vanderbilt, Phys. Rev. B **49**, 5828 (1994).

[26] U. V. Waghmare and K. M. Rabe, Phys. Rev. B **55**, 6161 (1997).

[27] T. Nishimatsu, U. V. Waghmare, Y. Kawazoe, and D. Vanderbilt, Phys. Rev. B **78**, 104104 (2008).

[28] A. Paul, J. Sun, J. P. Perdew, and U. V. Waghmare, Phys. Rev. B **95**, 054111 (2017).

[29] T. Nishimatsu, M. Iwamoto, Y. Kawazoe, and U. V. Waghmare, Phys. Rev. B **82**, 134106 (2010).

[30] K. M. Rabe and U. V. Waghmare, Phys. Rev. B **52**, 13236 (1995).

[31] J. H. Lee, U. V. Waghmare, and J. Yu, J. Appl. Phys. **103**, 124106 (2008).

[32] See Supplemental Material at http://link.aps.org/supplemental/10.1103/PhysRevB.106.064108 for derivation of full fitting function, strain-phonon coupling, and stability of fit.

[33] H. T. Stokes, D. M. Hatch, and B. J. Campbell, INVARIANTS, ISOTROPY Software Suite, iso.byu.edu

[34] D. M. Hatch and H. T. Stokes, J. Appl. Crystallogr. **36**, 951 (2003).

[35] A. Erba, J. Maul, M. Ferrabone, P. Carbonnière, M. Rérat, and R. Dovesi, J. Chem. Theory Comput. **15**, 3755 (2019).

[36] J. A. Nelder and R. Mead, Comput. J. **7**, 308 (1965).

[37] G. I. Csonka, J. P. Perdew, A. Ruzsinszky, P. H. T. Philipsen, S. Lebègue, J. Paier, O. A. Vydrov, and J. G. Ángyán, Phys. Rev. B **79**, 155107 (2009).

[38] S. Piskunov, E. Heifets, R. I. Eglitis, and G. Borstel, Comput. Mater. Sci. **29**, 165 (2004).

[39] R. A. Evarestov, Phys. Rev. B **83**, 014105 (2011).

[40] R. Wahl, D. Vogtenhuber, and G. Kresse, Phys. Rev. B **78**, 104116 (2008).

[41] Z. Wu and R. E. Cohen, Phys. Rev. B **73**, 235116 (2006).

[42] J. Sun, A. Ruzsinszky, and J. P. Perdew, Phys. Rev. Lett. **115**, 036402 (2015).

[43] P. Lunkenheimer, S. Krohns, S. Riegg, S. G. Ebbinghaus, A. Reller, and A. Loidl, Eur. Phys. J.: Spec. Top. **180**, 61 (2009).

[44] P. E. Blöchl, Phys. Rev. B **50**, 17953 (1994).

[45] G. Kresse and D. Joubert, Phys. Rev. B **59**, 1758 (1999).

[46] G. Kresse and J. Furthmüller, Phys. Rev. B **54**, 11169 (1996).

[47] G. Kresse and J. Furthmüller, Comput. Mater. Sci. **6**, 15 (1996).

[48] G. Kresse and J. Hafner, Phys. Rev. B **49**, 14251 (1994).

[49] S. D. Bond, B. J. Leimkuhler, and B. B. Laird, J. Comput. Phys. **151**, 114 (1999).

[50] S. F. Yuk, K. C. Pitike, S. M. Nakhmanson, M. Eisenbach, Y. W. Li, and V. R. Cooper, Sci. Rep. **7**, 43482 (2017).

[51] S. Tinte, J. Íñiguez, K. M. Rabe, and D. Vanderbilt, Phys. Rev. B **67**, 064106 (2003).

[52] C. J. Johnson, Appl. Phys. Lett. **7**, 221 (1965).

[53] W. J. Merz, Phys. Rev. **91**, 513 (1953).

[54] L. E. Cross, J. Phys. Soc. Jpn. **23**, 77 (1967).

133

# Supplemental Material
# Improved description of the potential energy surface in BaTiO$_3$ by anharmonic phonon couplings

Florian Mayer[1,*], Maxim N. Popov[1], Donald M. Evans[2], Stephan Krohns[2], Marco Deluca[1], Jürgen Spitaler[1]

[1]Materials Center Leoben Forschung GmbH, Roseggerstrasse 12, 8700 Leoben, Austria
[2]Experimental Physics V, Center for Electronic Correlations and Magnetism, Institute of Physics, University of Augsburg, 86135 Augsburg, Germany

*e-mail: florian.mayer@mcl.at

# I.    Derivation of the full fitting function

The Taylor series expansion of the self-energy is discussed in the main paper and written in short form in Equation 3. Mathematica [1] was used to derive the expansion in full form as shown in Equation S1. This equation includes a large number of terms, consisting of even and odd terms up to 8$^{th}$ order in $u$ and 6$^{th}$ order in $v_1$ and $v_2$. However, since we choose the highly symmetric cubic phase as the basis for the expansion, we can neglect many terms of the equation due to symmetry reasons. A very useful tool to identify the remaining terms is ISOTROPY [2,3]. This program allows the generation of invariant polynomials of the components of order parameters. In principle, one could also use this program for setting up the series expansion from the beginning. Nevertheless, we used ISOTROPY to identify the terms which occur in the order parameter for cubic (Pm-3m) to tetragonal (P4mm). The final form of the series expansion for the self-energy in <001> direction is given by Equation 4. For the terms only depending on $u$, we decided to use exactly the same expression as presented by Nishimatsu et al. [4], i.e. here described by the parameters $c_0$ - $c_4$. Parameters describing anharmonic couplings just depending on $v_1$ or $v_2$ are labelled with $a_i$ or $b_i$, respectively. Combined couplings consisting of more than one variable $u$, $v_1$ or $v_2$, are represented by $d_i$.

$$\frac{E^{(8,0,0)}(u_0, v_{1,0}, v_{2,0})\,(u-u_0)^8}{40\,320} + \frac{E^{(7,0,0)}(u_0, v_{1,0}, v_{2,0})\,(u-u_0)^7}{5040} + \frac{1}{720}E^{(6,0,0)}(u_0, v_{1,0}, v_{2,0})\,(u-u_0)^6 + \frac{1}{120}E^{(5,0,0)}(u_0, v_{1,0}, v_{2,0})\,(u-u_0)^5 +$$

$$\frac{1}{120}(v_2-v_{2,0})E^{(5,0,1)}(u_0, v_{1,0}, v_{2,0})\,(u-u_0)^5 + \frac{1}{120}(v_1-v_{1,0})E^{(5,1,0)}(u_0, v_{1,0}, v_{2,0})\,(u-u_0)^5 + \frac{1}{24}E^{(4,0,0)}(u_0, v_{1,0}, v_{2,0})\,(u-u_0)^4 +$$

$$\frac{1}{24}(v_2-v_{2,0})E^{(4,0,1)}(u_0, v_{1,0}, v_{2,0})\,(u-u_0)^4 + \frac{1}{48}(v_2-v_{2,0})^2E^{(4,0,2)}(u_0, v_{1,0}, v_{2,0})\,(u-u_0)^4 + \frac{1}{24}(v_1-v_{1,0})E^{(4,1,0)}(u_0, v_{1,0}, v_{2,0})\,(u-u_0)^4 +$$

$$\frac{1}{24}(v_1-v_{1,0})(v_2-v_{2,0})E^{(4,1,1)}(u_0, v_{1,0}, v_{2,0})\,(u-u_0)^4 + \frac{1}{48}(v_1-v_{1,0})^2E^{(4,2,0)}(u_0, v_{1,0}, v_{2,0})\,(u-u_0)^4 +$$

$$\frac{1}{6}E^{(3,0,0)}(u_0, v_{1,0}, v_{2,0})\,(u-u_0)^3 + \frac{1}{6}(v_2-v_{2,0})E^{(3,0,1)}(u_0, v_{1,0}, v_{2,0})\,(u-u_0)^3 + \frac{1}{12}(v_2-v_{2,0})^2E^{(3,0,2)}(u_0, v_{1,0}, v_{2,0})\,(u-u_0)^3 +$$

$$\frac{1}{36}(v_2-v_{2,0})^3E^{(3,0,3)}(u_0, v_{1,0}, v_{2,0})\,(u-u_0)^3 + \frac{1}{6}(v_1-v_{1,0})E^{(3,1,0)}(u_0, v_{1,0}, v_{2,0})\,(u-u_0)^3 + \frac{1}{6}(v_1-v_{1,0})(v_2-v_{2,0})E^{(3,1,1)}(u_0, v_{1,0}, v_{2,0})\,(u-u_0)^3 +$$

$$\frac{1}{12}(v_1-v_{1,0})(v_2-v_{2,0})^2E^{(3,1,2)}(u_0, v_{1,0}, v_{2,0})\,(u-u_0)^3 + \frac{1}{12}(v_1-v_{1,0})^2E^{(3,2,0)}(u_0, v_{1,0}, v_{2,0})\,(u-u_0)^3 +$$

$$\frac{1}{12}(v_1-v_{1,0})^2(v_2-v_{2,0})E^{(3,2,1)}(u_0, v_{1,0}, v_{2,0})\,(u-u_0)^3 + \frac{1}{36}(v_1-v_{1,0})^3E^{(3,3,0)}(u_0, v_{1,0}, v_{2,0})\,(u-u_0)^3 +$$

$$\frac{1}{2}E^{(2,0,0)}(u_0, v_{1,0}, v_{2,0})\,(u-u_0)^2 + \frac{1}{2}(v_2-v_{2,0})E^{(2,0,1)}(u_0, v_{1,0}, v_{2,0})\,(u-u_0)^2 + \frac{1}{4}(v_2-v_{2,0})^2E^{(2,0,2)}(u_0, v_{1,0}, v_{2,0})\,(u-u_0)^2 +$$

$$\frac{1}{12}(v_2-v_{2,0})^3E^{(2,0,3)}(u_0, v_{1,0}, v_{2,0})\,(u-u_0)^2 + \frac{1}{48}(v_2-v_{2,0})^4E^{(2,0,4)}(u_0, v_{1,0}, v_{2,0})\,(u-u_0)^2 + \frac{1}{2}(v_1-v_{1,0})E^{(2,1,0)}(u_0, v_{1,0}, v_{2,0})\,(u-u_0)^2 +$$

$$\frac{1}{2}(v_1-v_{1,0})(v_2-v_{2,0})E^{(2,1,1)}(u_0, v_{1,0}, v_{2,0})\,(u-u_0)^2 + \frac{1}{4}(v_1-v_{1,0})(v_2-v_{2,0})^2E^{(2,1,2)}(u_0, v_{1,0}, v_{2,0})\,(u-u_0)^2 +$$

$$\frac{1}{12}(v_1-v_{1,0})(v_2-v_{2,0})^3E^{(2,1,3)}(u_0, v_{1,0}, v_{2,0})\,(u-u_0)^2 + \frac{1}{4}(v_1-v_{1,0})^2E^{(2,2,0)}(u_0, v_{1,0}, v_{2,0})\,(u-u_0)^2 +$$

$$\frac{1}{4}(v_1-v_{1,0})^2(v_2-v_{2,0})E^{(2,2,1)}(u_0, v_{1,0}, v_{2,0})\,(u-u_0)^2 + \frac{1}{8}(v_1-v_{1,0})^2(v_2-v_{2,0})^2E^{(2,2,2)}(u_0, v_{1,0}, v_{2,0})\,(u-u_0)^2 +$$

$$\frac{1}{12}(v_1-v_{1,0})^3E^{(2,3,0)}(u_0, v_{1,0}, v_{2,0})\,(u-u_0)^2 + \frac{1}{12}(v_1-v_{1,0})^3(v_2-v_{2,0})E^{(2,3,1)}(u_0, v_{1,0}, v_{2,0})\,(u-u_0)^2 +$$

$$\frac{1}{48}(v_1-v_{1,0})^4E^{(2,4,0)}(u_0, v_{1,0}, v_{2,0})\,(u-u_0)^2 + E^{(1,0,0)}(u_0, v_{1,0}, v_{2,0})\,(u-u_0) + (v_2-v_{2,0})E^{(1,0,1)}(u_0, v_{1,0}, v_{2,0})\,(u-u_0) +$$

$$\frac{1}{2}(v_2-v_{2,0})^2E^{(1,0,2)}(u_0, v_{1,0}, v_{2,0})\,(u-u_0) + \frac{1}{6}(v_2-v_{2,0})^3E^{(1,0,3)}(u_0, v_{1,0}, v_{2,0})\,(u-u_0) + \frac{1}{24}(v_2-v_{2,0})^4E^{(1,0,4)}(u_0, v_{1,0}, v_{2,0})\,(u-u_0) +$$

$$\frac{1}{120}(v_2-v_{2,0})^5E^{(1,0,5)}(u_0, v_{1,0}, v_{2,0})\,(u-u_0) + (v_1-v_{1,0})E^{(1,1,0)}(u_0, v_{1,0}, v_{2,0})\,(u-u_0) + (v_1-v_{1,0})(v_2-v_{2,0})E^{(1,1,1)}(u_0, v_{1,0}, v_{2,0})\,(u-u_0) +$$

$$\frac{1}{2}(v_1-v_{1,0})(v_2-v_{2,0})^2E^{(1,1,2)}(u_0, v_{1,0}, v_{2,0})\,(u-u_0) + \frac{1}{6}(v_1-v_{1,0})(v_2-v_{2,0})^3E^{(1,1,3)}(u_0, v_{1,0}, v_{2,0})\,(u-u_0) +$$

$$\frac{1}{24}(v_1-v_{1,0})(v_2-v_{2,0})^4E^{(1,1,4)}(u_0, v_{1,0}, v_{2,0})\,(u-u_0) + \frac{1}{2}(v_1-v_{1,0})^2E^{(1,2,0)}(u_0, v_{1,0}, v_{2,0})\,(u-u_0) +$$

$$\frac{1}{2}(v_1-v_{1,0})^2(v_2-v_{2,0})E^{(1,2,1)}(u_0, v_{1,0}, v_{2,0})\,(u-u_0) + \frac{1}{4}(v_1-v_{1,0})^2(v_2-v_{2,0})^2E^{(1,2,2)}(u_0, v_{1,0}, v_{2,0})\,(u-u_0) +$$

$$\frac{1}{12}(v_1-v_{1,0})^2(v_2-v_{2,0})^3E^{(1,2,3)}(u_0, v_{1,0}, v_{2,0})\,(u-u_0) + \frac{1}{6}(v_1-v_{1,0})^3E^{(1,3,0)}(u_0, v_{1,0}, v_{2,0})\,(u-u_0) +$$

$$\frac{1}{6}(v_1-v_{1,0})^3(v_2-v_{2,0})E^{(1,3,1)}(u_0, v_{1,0}, v_{2,0})\,(u-u_0) + \frac{1}{12}(v_1-v_{1,0})^3(v_2-v_{2,0})^2E^{(1,3,2)}(u_0, v_{1,0}, v_{2,0})\,(u-u_0) +$$

$$\frac{1}{24}(v_1-v_{1,0})^4E^{(1,4,0)}(u_0, v_{1,0}, v_{2,0})\,(u-u_0) + \frac{1}{24}(v_1-v_{1,0})^4(v_2-v_{2,0})E^{(1,4,1)}(u_0, v_{1,0}, v_{2,0})\,(u-u_0) + \frac{1}{120}(v_1-v_{1,0})^5E^{(1,5,0)}(u_0, v_{1,0}, v_{2,0})\,(u-u_0) +$$

$$E(u_0, v_{1,0}, v_{2,0}) + (v_2-v_{2,0})E^{(0,0,1)}(u_0, v_{1,0}, v_{2,0}) + \frac{1}{2}(v_2-v_{2,0})^2E^{(0,0,2)}(u_0, v_{1,0}, v_{2,0}) + \frac{1}{6}(v_2-v_{2,0})^3E^{(0,0,3)}(u_0, v_{1,0}, v_{2,0}) +$$

$$\frac{1}{24}(v_2-v_{2,0})^4E^{(0,0,4)}(u_0, v_{1,0}, v_{2,0}) + \frac{1}{120}(v_2-v_{2,0})^5E^{(0,0,5)}(u_0, v_{1,0}, v_{2,0}) + \frac{1}{720}(v_2-v_{2,0})^6E^{(0,0,6)}(u_0, v_{1,0}, v_{2,0}) +$$

$$(v_1-v_{1,0})E^{(0,1,0)}(u_0, v_{1,0}, v_{2,0}) + (v_1-v_{1,0})(v_2-v_{2,0})E^{(0,1,1)}(u_0, v_{1,0}, v_{2,0}) + \frac{1}{2}(v_1-v_{1,0})(v_2-v_{2,0})^2E^{(0,1,2)}(u_0, v_{1,0}, v_{2,0}) +$$

$$\frac{1}{6}(v_1-v_{1,0})(v_2-v_{2,0})^3E^{(0,1,3)}(u_0, v_{1,0}, v_{2,0}) + \frac{1}{24}(v_1-v_{1,0})(v_2-v_{2,0})^4E^{(0,1,4)}(u_0, v_{1,0}, v_{2,0}) + \frac{1}{120}(v_1-v_{1,0})(v_2-v_{2,0})^5E^{(0,1,5)}(u_0, v_{1,0}, v_{2,0}) +$$

$$\frac{1}{2}(v_1-v_{1,0})^2E^{(0,2,0)}(u_0, v_{1,0}, v_{2,0}) + \frac{1}{2}(v_1-v_{1,0})^2(v_2-v_{2,0})E^{(0,2,1)}(u_0, v_{1,0}, v_{2,0}) + \frac{1}{4}(v_1-v_{1,0})^2(v_2-v_{2,0})^2E^{(0,2,2)}(u_0, v_{1,0}, v_{2,0}) +$$

$$\frac{1}{12}(v_1-v_{1,0})^2(v_2-v_{2,0})^3E^{(0,2,3)}(u_0, v_{1,0}, v_{2,0}) + \frac{1}{48}(v_1-v_{1,0})^2(v_2-v_{2,0})^4E^{(0,2,4)}(u_0, v_{1,0}, v_{2,0}) + \frac{1}{6}(v_1-v_{1,0})^3E^{(0,3,0)}(u_0, v_{1,0}, v_{2,0}) +$$

$$\frac{1}{6}(v_1-v_{1,0})^3(v_2-v_{2,0})E^{(0,3,1)}(u_0, v_{1,0}, v_{2,0}) + \frac{1}{12}(v_1-v_{1,0})^3(v_2-v_{2,0})^2E^{(0,3,2)}(u_0, v_{1,0}, v_{2,0}) + \frac{1}{36}(v_1-v_{1,0})^3(v_2-v_{2,0})^3E^{(0,3,3)}(u_0, v_{1,0}, v_{2,0}) +$$

$$\frac{1}{24}(v_1-v_{1,0})^4E^{(0,4,0)}(u_0, v_{1,0}, v_{2,0}) + \frac{1}{24}(v_1-v_{1,0})^4(v_2-v_{2,0})E^{(0,4,1)}(u_0, v_{1,0}, v_{2,0}) + \frac{1}{48}(v_1-v_{1,0})^4(v_2-v_{2,0})^2E^{(0,4,2)}(u_0, v_{1,0}, v_{2,0}) +$$

$$\frac{1}{120}(v_1-v_{1,0})^5E^{(0,5,0)}(u_0, v_{1,0}, v_{2,0}) + \frac{1}{120}(v_1-v_{1,0})^5(v_2-v_{2,0})E^{(0,5,1)}(u_0, v_{1,0}, v_{2,0}) + \frac{1}{720}(v_1-v_{1,0})^6E^{(0,6,0)}(u_0, v_{1,0}, v_{2,0})$$

(S1)

2

# II.     Parametrization of the Strain-Phonon coupling

Here, we will go into more detail about our approach for determining strain-phonon coupling. This approach is based on the valley tracing method (VTM), but we do not re-define the soft-mode amplitude and stick with the conventional displacement pattern. That is, we shift the atoms based on the soft-mode shift pattern along directions <001> and <011>. We chose a maximum amplitude of 0.25 Å calculated on 25 grid points. This is where the important difference in DFT comes into account. For each frozen displacement pattern, VASP was used with the tag ISIF 6 to optimize the unit cell as well as the volume. The internal coordinates remain fixed. From this, the strain can be calculated as a function of soft-mode amplitude, as illustrated in Figure S1. To calculate the strain-phonon couplings $B_{1xx}$, $B_{1yy}$, and $B_{4yz}$ from this data, we follow the approach of Nishimatsu et al. [4]. That is, we fit a quadratic function to the data of Figure S1 and then use Equation 13a-13c of Ref. [4] to determine the couplings.
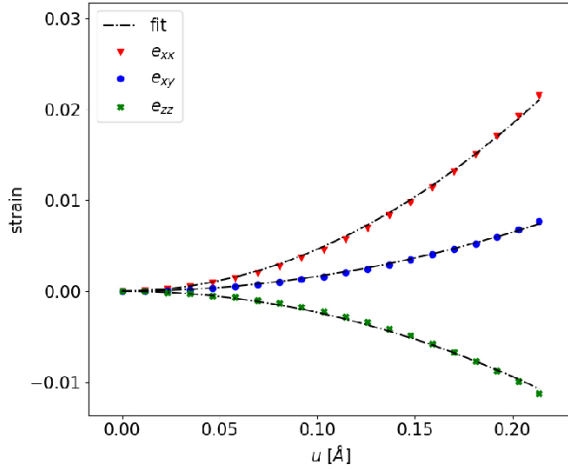


*Figure S1. Strain as a function of soft-mode amplitude obtained via DFT calculations and used for the estimation of strain-phonon coupling parameters*

Furthermore, the same parameters, as already described in the main paper were also determined with the method known from literature. A good description of this method can be found in the doctoral thesis [5] of R. C. Herchig. A comparison of the parameters calculated in this work and values from the literature is given in Table S1. Our values agree well with those of Ref. [6], although we used PBEsol instead of the SCAN functional. The results of our alternative method show a slightly higher value for the $B_{1xx}$ coupling. However, we decided to use this value and the corresponding parameters because a larger number of values were used for the calculation. Another point in favor of this value is that we determined the deformation of the unit cell directly by DFT for each amplitude of the soft mode.

3

*Table S1. Comparison of strain-phonon coupling parameters obtained with different approaches and XC-functionals for BT. The method called standard refers to one explained in R.C. Herchig's PhD thesis. VTM is the so-called valley tracing method.*

|  | **this work** | **this work** | **Ref.** [6] | **Ref.** [7] | **Ref.** [4] |
|---|---|---|---|---|---|
| **method** | see text | standard | standard | standard | VTM |
| **XC-functional** | PBEsol | PBEsol | SCAN | LDA | W&C |
| $\mathbf{B_{1xx}}$ **[eV/Å²]** | -235.06 | -230.75 | -225.76 | -211.00 | -185.35 |
| $\mathbf{B_{1yy}}$ **[eV/Å²]** | -19.34 | -21.76 | -18.04 | -19.30 | -3.28 |
| $\mathbf{B_{4yz}}$ **[eV/Å²]** | -15.33 | -15.56 | -20.93 | -7.75 | -14.55 |

# III.     Stability of fitting the anharmonic couplings

Here, we want to describe in detail the fitting of the self-energy given by Equation 4. As already mentioned in the main paper, about 2000 DFT calculations with different displacements in $u$, $v_1$, and $v_2$ (by superposing the displacements) have been carried out. This results in a data set of structure $E(u_i, v_{1i}, v_{2i})$, which can now be used to determine all parameters in Equation 4. We started by creating a Python script for this task. For the fitting part, the package LMFIT [8] was used. LMFIT includes a variety of different algorithms like Levenberg-Marquardt, Nelder-Mead, Powell and many more. Due to the robustness of the least squares algorithm we decided to use it mainly. However, to exclude possible errors, the parameters were also determined with Nelder-Mead, Powell and L-BFGS-B. An overview of all fitted parameters can be found in Table S2. Furthermore, statistical values that characterize the quality of the fit are also listed. All algorithms used show a very good agreement. Only small, not relevant, deviations in the individual parameters can be observed.

More important than the values of the individual parameters are the results of the re-fit (see main paper for a detailed explanation). The function from Equation 4 is transformed back into a function depending only on $u$. For this purpose, the amplitudes of $v_1$ and $v_2$ for a given $u$ are minimized. This data set is then used to fit the self-energy from Equation 2a (in the main paper) varying $k_1$ and $k_4$. The remaining parameters are fixed with the values of the accompanying parameterization. The adapted anharmonic parameters $k'_1$ and $k'_4$ are listed at the bottom of Table S2. These were also calculated for each fit algorithm. All values agree excellently and thus confirm the stability of the fit.

*Table S2. Fitted parameters corresponding to Equation S1. The table shows a comparison of different fitting algorithms. At the bottom, the final parameters for the effective Hamiltonian are presented, which were obtained by refitting the self-energy.*

|  | **LeastSQ** | **Nelder** | **Powell** | **L-BFGS-B** |
|---|---|---|---|---|
| **Fit statistics** | | | | |
| $\chi^2$ | 2.42E-08 | 2.42E-08 | 2.42E-08 | 2.42E-08 |
| **reduced** $\chi^2$ | 1.59E-11 | 1.59E-11 | 1.59E-11 | 1.59E-11 |
|  | | | | |
| **Fitted parameters** | | | | |
| $\mathbf{a_1}$ | 0.01 | 0.01 | 0.01 | 0.01 |

| | | | | |
|---|---|---|---|---|
| $a_2$ | 4.20 | 4.20 | 4.20 | 4.20 |
| $a_3$ | -115.50 | -115.50 | -115.50 | -115.50 |
| $a_4$ | 35.09 | 35.09 | 35.09 | 35.09 |
| $a_5$ | 1.54 | 1.54 | 1.54 | 1.54 |
| $a_6$ | 3.64 | 3.65 | 3.64 | 3.64 |
| $a_7$ | 590.09 | 590.13 | 590.09 | 590.09 |
| $a_8$ | -233.02 | -233.01 | -233.02 | -233.02 |
| $a_9$ | 66.06 | 66.05 | 66.06 | 66.06 |
| $a_{10}$ | -64.77 | -64.97 | -64.77 | -64.77 |
| $a_{11}$ | -44.34 | -44.38 | -44.34 | -44.34 |
| $a_{12}$ | -80.18 | -80.59 | -80.19 | -80.18 |
| $b_1$ | 0.01 | 0.01 | 0.01 | 0.01 |
| $b_2$ | 6.81 | 6.81 | 6.81 | 6.81 |
| $b_3$ | -62.65 | -62.65 | -62.65 | -62.65 |
| $b_4$ | 25.57 | 25.58 | 25.57 | 25.57 |
| $b_5$ | -5.15 | -5.15 | -5.15 | -5.15 |
| $b_6$ | -0.05 | -0.04 | -0.05 | -0.05 |
| $b_7$ | -114.56 | -114.53 | -114.56 | -114.56 |
| $b_8$ | 33.03 | 33.04 | 33.02 | 33.03 |
| $b_9$ | -0.27 | -0.30 | -0.28 | -0.27 |
| $b_{10}$ | 16.35 | 16.27 | 16.35 | 16.35 |
| $b_{11}$ | 12.43 | 12.80 | 12.43 | 12.43 |
| $b_{12}$ | 22.53 | 21.57 | 22.52 | 22.53 |
| $c_0$ | -39.72 | -39.72 | -39.72 | -39.72 |
| $c_1$ | -1.98 | -1.98 | -1.98 | -1.98 |
| $c_2$ | 127.76 | 127.76 | 127.76 | 127.76 |
| $c_3$ | -858.02 | -857.97 | -858.02 | -858.02 |
| $c_4$ | 12100.28 | 12098.36 | 12100.27 | 12100.28 |
| $d_1$ | 0.00 | 0.00 | 0.00 | 0.00 |
| $d_2$ | 52.25 | 52.25 | 52.25 | 52.25 |
| $d_3$ | -7.54 | -7.54 | -7.54 | -7.54 |
| $d_4$ | -10.69 | -10.69 | -10.69 | -10.69 |
| $d_5$ | 4.41 | 4.40 | 4.41 | 4.41 |
| $d_6$ | 0.35 | 0.35 | 0.35 | 0.35 |
| $d_7$ | 1.43 | 1.43 | 1.43 | 1.43 |
| $d_8$ | 72.40 | 72.40 | 72.40 | 72.40 |
| $d_9$ | -35.20 | -35.24 | -35.20 | -35.20 |
| $d_{10}$ | -1.84 | -1.90 | -1.89 | -1.84 |
| $d_{11}$ | 75.44 | 75.39 | 75.45 | 75.44 |
| $d_{12}$ | 35.62 | 35.63 | 35.62 | 35.62 |
| $d_{13}$ | 0.62 | 0.48 | 0.62 | 0.62 |
| $d_{14}$ | -34.18 | -33.99 | -34.17 | -34.18 |
| $d_{15}$ | -21.86 | -21.73 | -21.86 | -21.86 |
| $d_{16}$ | 13.17 | 13.33 | 13.17 | 13.17 |
| $d_{17}$ | -38.81 | -39.11 | -38.82 | -38.81 |

5

| | | | | |
|---|---|---|---|---|
| $d_{18}$ | -125.72 | -125.82 | -125.71 | -125.72 |
| $d_{19}$ | -59.40 | -59.06 | -59.40 | -59.40 |
| $d_{20}$ | -58.40 | -57.89 | -58.39 | -58.40 |
| $d_{21}$ | 17.37 | 17.28 | 17.37 | 17.37 |
| $d_{22}$ | 64.49 | 64.41 | 64.48 | 64.49 |
| | | | | |
| **Refitting of $k_1$ and $k_4$** | | | | |
| $k_1'$ | -1443.85 | -1443.82 | -1443.88 | -1443.85 |
| $k_4'$ | 17216.82 | 17215.61 | 17218.02 | 17216.83 |

What we have not yet investigated is the stability or quality of the fit function when the number of fit parameters is changed. To quantify this, we used a cross-validation procedure. More precisely, we used a k-fold cross-validation scheme to determine the mean squared error (chosen as cross validation score) on the data points to be predicted. The procedure was as follows: First, the DFT data were shuffled. These were then divided into 24 patches. Following that, 23 patches were used to fit the objective function. The fitted function was then used to predict the data from the 24th patch. The error between DFT data and prediction was determined using MSE. This procedure was repeated so that each of the 24 patches was used at least once for prediction. Figure S2 shows the results of cross-validation for a different number of fit parameters. Here, the number was changed as follows: Region I consists of all parameters which are dependent on $u$ only. Region II includes parameters which are dependent on $v_1$ and/or $u$. Region III are parameters which depend on $v_2$ and/or $u$. Region IV is all remaining parameters which depend on $u$ and/or $v_1$ and/or $v_2$. In principle, exactly the order of the parameters from Equation 4, with these added in that order. The quality of the fit function increases gradually with the number of parameters. Thus, jumps between the individual regions are observed, which is of course also due to the approach of adding parameters. To avoid this, one could of course use different combinations of parameters, but this is not possible with the given number of parameters. Anyway, the plot explicitly shows the importance of additional parameters for the description of the energy surface. For example, by adding region IV, a much better result is achieved than with only regions I, II and II. Furthermore, this plot also shows that the chosen approach of Paul et al. [6] with a strongly reduced number of parameters can work but important additional couplings could be overlooked.

6

139
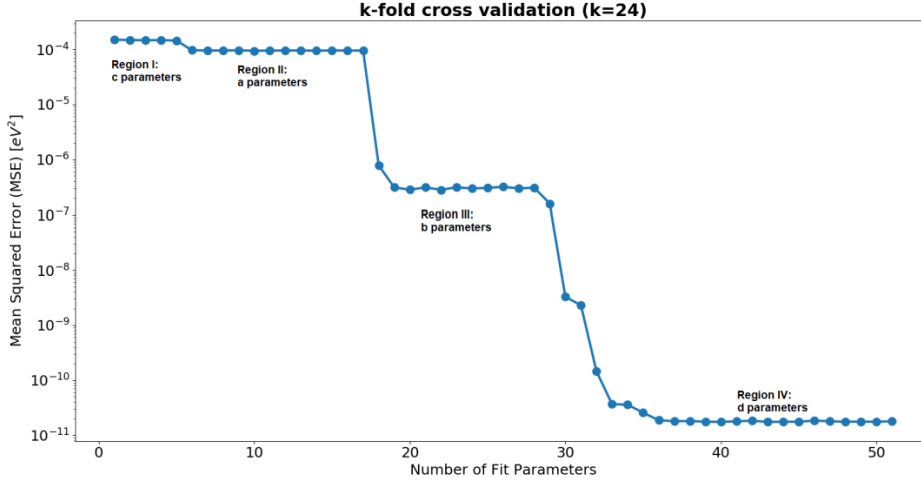
*Figure S2. Cross validation results for fit functions with different numbers of fitting parameters. The plot shows the mean squared error of predicted values as a function of fitting parameters. The data was split into k=24 equal patches for the calculation.*

## IV.    Strain-Phonon coupling for the higher-energy phonon modes $v_1$ and $v_2$

As it is discussed in the main paper, the adapted version of the effective Hamiltonian yields an improved description of transition temperatures, thus the local minima of $H_{eff}^{anh}$ fit better to experiment. On the other hand, we observe that these minima are lower than the fully relaxed DFT structures. That mismatch was also reported by Paul et al. [6], although they observed this overestimation for $PbTiO_3$ using the SCAN functional and their flavor of anharmonic coupling. To explain this mismatch, we start with a look at the self-energy shown in Figure 1c. We can clearly see that the anharmonic contributions lower the self-energy, especially for larger amplitudes of u. This still does not explain the much more significant difference when looking at the total energy. For this, we have to consider that for the total energy, contributions from elastic effects and their corresponding energy are included as well. Important to note is that these terms are independent of $v_1$ and $v_2$ and, therefore, strain effects originating from displacements of these phonons are not included. That implies, for both Hamiltonians $H_{eff}^{anh}$ and $H_{eff}$ (with and without anharmonic couplings), the amount of strain energy and strain-phonon coupling is identical. To check if this approximation is valid or falsely overestimates the local minima, we carried out an in-depth study of strain-phonon coupling parameters for the phonon modes $v_1$ and $v_2$:

An important contribution to the total energy is the so-called strain-phonon coupling. In the previous chapter we already dealt with the parameterization of the necessary parameters. However, only the coupling between soft mode and strain was treated, which obviously leaves out additional contributions from other phonon modes. Here, we want to examine these contributions by parametrizing the strain-phonon coupling for the higher-energy phonon modes $v_1$ and $v_2$. For the parametrization, we use the scheme with the VASP parameter ISIF=6, as described in the previous chapter, whereby the

7

corresponding displacement patterns are presented in the main paper. The obtained coupling parameters for $u$, $v_1$ and $v_2$ are listed in Table S3. The values of the $v_1$ and $v_2$ modes are significantly lower than the parameters corresponding to $u$. Figure S3 shows the strain-phonon coupling as a function of the mode amplitudes.

*Table S3. Strain-phonon couplings for the soft mode u and the two higher-energy optical modes $v_1$ and $v_2$.*

| Mode | u | $v_1$ | $v_2$ |
|---|---|---|---|
| $B_{1xx}$ [eV/Å$^2$] | -235.06 | -44.63 | -2.31 |
| $B_{1yy}$ [eV/Å$^2$] | -19.34 | -44.79 | -11.08 |
| $B_{4yz}$ [eV/Å$^2$] | -15.33 | -34.84 | 10.23 |
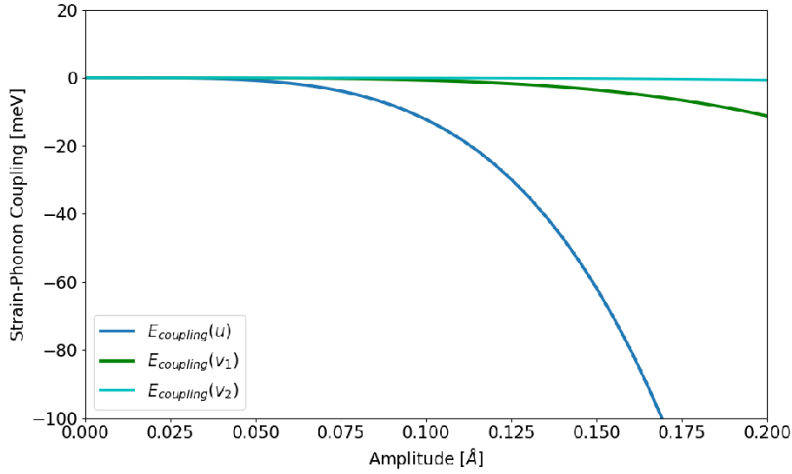


*Figure S3. Strain-phonon coupling energy as a function of the corresponding amplitude of the optical phonon modes u, $v_1$ and $v_2$.*

Furthermore, to investigate the contributions to the total energy we have to use the amplitudes of $v_1$ and $v_2$ which are incorporated in the adapted self-energy, see Figure S4a. These values were obtained by minimizing the self-energy with respect to the higher-energy modes $v_1$ and $v_2$ (see Figure 1b in the main paper). In Figure S4b, we use these amplitudes and plot the corresponding strain-phonon coupling energy. From that, we can estimate the energy contribution originating from $v_1$ or $v_2$ for a given soft-mode amplitude. For example, a soft-mode amplitude of $u = 0.25$ Å includes an amplitude of $v_1 = 0.09$ Å. The latter gives a strain-phonon coupling energy of about -0.4 meV. One can observe that these contributions are negligibly small compared to the strain-phonon coupling originating from the soft-mode itself (blue line in Figure S3). Therefore, the observed overestimation of the fully relaxed DFT result is not due to a possible wrong treatment of strain but directly related to the approach of minimizing the self-energy in terms of $v_1$ and $v_2$.
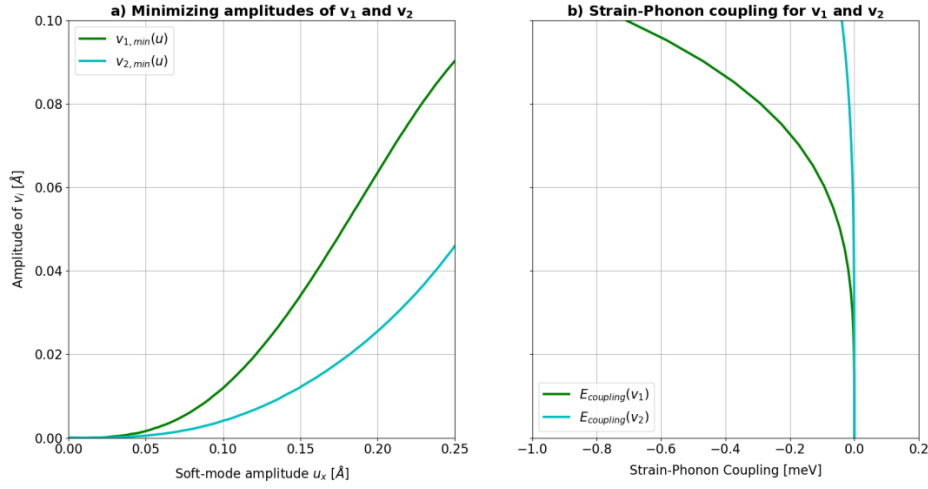
*Figure S4. Quantitative values for the strain-phonon coupling contribution to the total energy originating from the higher-energy phonon modes $v_1$ and $v_2$. Panel a) shows the amplitudes of $v_1$ and $v_2$ which minimize the total energy as a function of u. In panel b), the corresponding strain-phonon coupling is plotted.*

# V.    Influence of simulation box size on temperature hysteresis

In order to test the influence of the simulation box size, heating-up as well as cooling-down simulations with sizes of L=14,16,18, and 20 were performed. The results are illustrated in Figure S5. The same settings for the MD simulation as described in the main paper were used. These were also kept for each size of the box. An increase of the temperature hysteresis can be observed when the simulation box size is increased. However, the exact transition temperature may vary slightly and therefore, if this property is of particular interest, multiple heating and cooling runs should be performed. In addition, the total simulation time may contribute to the increased temperature hysteresis.
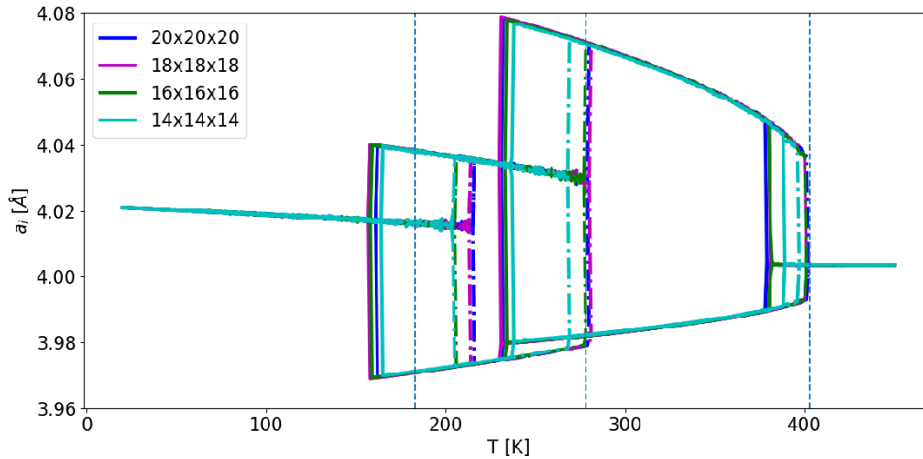


*Figure S5. Comparison of different simulation box sizes*

# VI.    Permittivity simulation
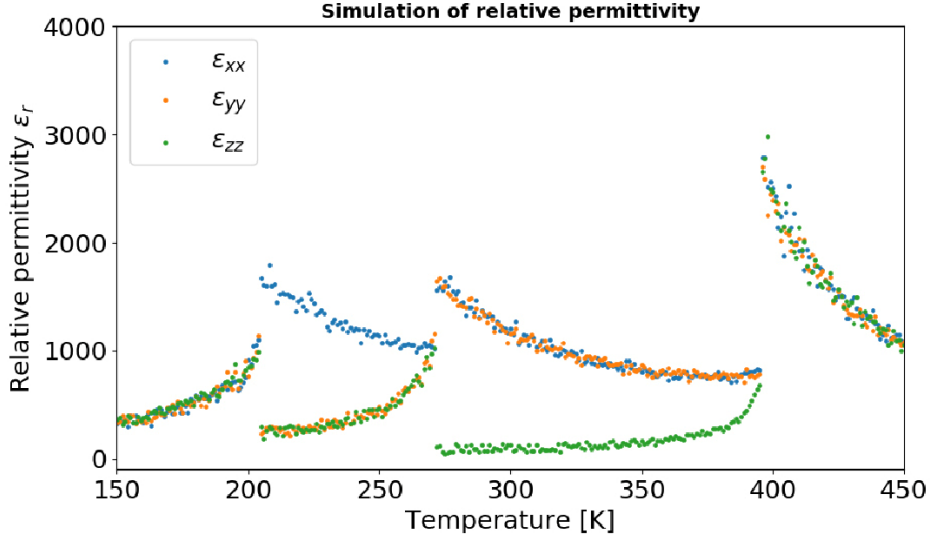


*Figure S6. Simulation of relative permittivity obtained via cooling the system for a temperature range capturing all three phase transitions.*

# VII.    Dynamic PE loops
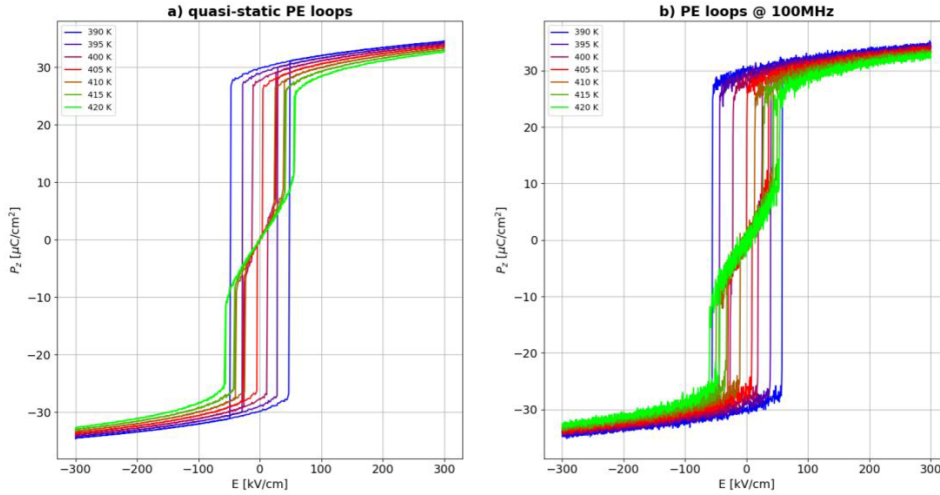


*Figure S7. Comparison between PE loop simulations in the quasi-static case and at 100MHz.*

# VIII.    Comparison of DFT obtained properties

In this section we want to compare a selection of material properties with other results from the literature calculated via DFT. In our case, all calculations were performed using the XC-functional (exchange-correlation functional) PBEsol and the DFT package VASP. The following settings were used in our calculations. Projector-augmented wave potentials [9] with valence electronic configurations of $5s^2\,5p^6\,6s^2$ for Ba (10 valence electrons),  $3s^2\,3p^6\,4s^2\,3d^2$ for Ti (12 valence electrons), and $2s^2\,2p^4$ for O (6

10

valence electrons) were used. For all 5-atom unit cell calculations, a k-grid of size 8x8x8 was used. The cut-off energy was set to 520 eV throughout all calculations. Both parameters, k-grid and energy cut-off, were checked for convergence. The convergence criterion for the SCF cycle was set by EDIFF to a value of 1E-8 eV. For the relaxation we used the tags IBRION=2 (ionic relaxation, conjugate-gradient algorithm) and ISIF=3 (full relaxation). The convergence criterion for the atomic relaxations in terms of the maximal residual forces was set to 1E-4 eV/Å. The stress tensor was converged to a value below 1E-2 MPa.

First, let us look at the elastic constants as listed in Table SIV. All the listed functionals overestimate the elastic constant $C_{11}$. The BLYP and the hybrid functional B3LYP give the best values here. In the case of $C_{12}$, all functionals underestimate the experimental value. Here, LDA and SCAN provide the slightly better values. PBEsol as well as PBE and BLYP perform worst here. For $C_{44}$, all functionals are close to the experimental value, with PBEsol performing best.

*Table SIV. Comparison of elastic constants of cubic BT obtained with different exchange-correlation functionals.*

|  | PBEsol (this work) | SCAN (Ref. [6]) | LDA (Ref. [7]) | PBE (Ref. [10]) | BLYP (Ref. [10]) | B3LYP (Ref. [10]) | Expt. (Ref. [10]) |
|---|---|---|---|---|---|---|---|
| $C_{11}$ [GPa] | 318 | 328 | 329 | 310 | 282 | 298 | 206 |
| $C_{12}$ [GPa] | 107 | 118 | 117 | 107 | 108 | 116 | 140 |
| $C_{44}$ [GPa] | 126 | 131 | 130 | 140 | 122 | 146 | 126 |

Next, we compare the lattice parameters obtained by DFT relaxation for cubic BT. Table SV lists the lattice parameter for different XC-functionals. The best results are obtained for the functionals PBEsol, SCAN and the hybrid functional HSE. The first two slightly underestimate the lattice parameter, with the hybrid functional slightly overestimating it. The PBE and BLYP functionals perform worst in this comparison.

*Table SV. Comparison of lattice parameters for cubic BT obtained with different exchange-correlation functionals.*

| XC-functional | $a_0$ [Å] |
|---|---|
| PBEsol (this work) | 3.99 |
| SCAN (Ref. [6]) | 3.99 |
| LDA (Ref. [10]) | 3.96 |
| PBE (Ref. [10]) | 4.03 |
| BLYP (Ref. [10]) | 4.08 |
| B3LYP (Ref. [10]) | 4.04 |
| HF (Ref. [10]) | 4.01 |
| vdW-DF-C09 (Ref. [11]) | 3.98 |
| Expt. (Ref. [10]) | 4.00 |

To get an insight into the lattice dynamics, the phonon frequencies for the cubic phase of BT at the $\Gamma$-point are listed in Table SVI. Significant differences can be identified for the frequency of the soft mode depending on the selected XC functional. That frequency plays an important role for the parameterization of the effective Hamiltonian, since it defines the harmonic potential of the Hamiltonian. Considering that no experimental reference value can be determined for this imaginary frequency, it is difficult to make a statement on the accuracy here. Since both SCAN and PBEsol give very good results with respect to the transition temperatures and PBE overestimates the transition temperatures, it can be assumed that the values for SCAN and PBEsol are approximately in the correct range. For the other phonon frequencies, SCAN gives the best result, followed by PBEsol and the hybrid functional PBE0.

Table SVI. Comparison of phonon frequencies at the $\Gamma$-point for cubic BT obtained with different exchange-correlation functionals. All values are in units of $cm^{-1}$.

|  | LDA (Ref. [6]) | WC-GGA (Ref. [6]) | B1-WC (Ref. [6]) | SCAN (Ref. [6]) | PBE0 (Ref. [12]) | PBEsol (this work) | Expt. (Ref. [6]) |
|---|---|---|---|---|---|---|---|
| $\Gamma_{15}$ (TO1) | 75i | 128i | 145i | 196i | 281i | 193i |  |
| $\Gamma_{15}$ (TO2) | 193 | 186 | 195 | 182 | 196 | 178 | 182 |
| $\Gamma_{15}$ (TO3) | 480 | 469 | 482 | 478 | 478 | 468 | 482 |
| $\Gamma_{25}$ (TO4) | 286 | 282 | 299 | 297 | 314 | 285 | 306 |

Since the eigenvector belonging to the soft mode is of special importance for the parameterization of the effective Hamiltonian, we have prepared a comparison in Table SVII. Here it can be clearly seen that PBEsol and WC provide approximately the same eigenvector. This is to be expected since the functionals are quite similar. Also the eigenvector calculated by SCAN is in good agreement with that of PBEsol. The eigenvector of LDA differs slightly from the above.

Table SVII. Comparison of the soft-mode eigenvector of cubic BT obtained with different exchange-correlation functionals

| XC-functional | $\xi_z^A$ | $\xi_z^B$ | $\xi_z^{O_1}$ | $\xi_z^{O_2}$ | $\xi_z^{O_3}$ |
|---|---|---|---|---|---|
| PBEsol (this work) | 0.16 | 0.77 | -0.20 | -0.20 | -0.55 |
| SCAN (Ref. [6]) | 0.15 | 0.77 | -0.18 | -0.18 | -0.56 |
| WC (Ref. [4]) | 0.17 | 0.77 | -0.20 | -0.20 | -0.55 |
| LDA (Ref. [6]) | 0.20 | 0.76 | -0.21 | -0.21 | -0.53 |

Finally, we want to discuss the spontaneous polarization calculated by a Berry phase analysis. The relaxed structures served as the basis for this calculation. In order to be able to calculate the occurring polarization of the unit cells, the structures for all phases were aligned at the A-site. Through this reference point it is subsequently possible to determine the ionic and electronic polarization by using VASP and the LCALCPOL tag. A comparison of our data with the literature is given in Table SVIII. This analysis shows that the spontaneous polarization is overestimated by PBEsol. The best agreement is given by the vdW-DF-C09 and the LDA functional.

*Table SVIII. Comparison of spontaneous polarization in BT obtained via Berry phase analysis and different exchange-correlation functionals. All values are in units of C/m².*

| | PBEsol (this work) | LDA (Ref. [11]) | PBE (Ref. [11]) | PBEsol (Ref. [11]) | vdW-DF-C09 (Ref. [11]) | Expt. (Ref. [11]) |
|---|---|---|---|---|---|---|
| **Tetragonal** | 0.34 | 0.26 | 0.48 | 0.35 | 0.30 | 0.27 |
| **Orthorhombic** | 0.31 | 0.31 | 0.61 | 0.31 | 0.30 | 0.30 |
| **Rhombohedral** | 0.39 | 0.31 | 0.50 | 0.39 | 0.35 | 0.33 |

# IX.    Importance of anharmonic couplings

Since our parameterization is based on a large number of anharmonic terms, it is difficult to make a statement about the importance of the individual couplings. Therefore, the whole parameterization was repeated including only harmonic contributions between u, $v_1$ and $v_2$. The resulting parameters $k_1'$ and $k_4'$ yield $-700.037$ eV/Å$^6$ and $7075.418$ eV/Å$^8$, respectively. Subsequently, a cooling and heating run were performed again using MD simulations. The settings for the MD simulations here are analogous to those described in the main paper in section III.C. Table SIX shows the results of the transition temperatures for the different parameterizations. The first row is the parameterization which is based on the already established approach of Nishimatsu et al. As explained in the main paper, this approach underestimates the transition temperatures by about 40%. The second row shows the results for the inclusion of harmonic couplings between the individual phonons. Here it must be pointed out that for u, anharmonic contributions were also included. The determined transition temperatures about 4% closer to the experimental data compared to the previous case. The third row shows the results for the inclusion of a large number of anharmonic terms. The simulated transition temperatures are now in very good agreement with the experimental data. This fact indicates that anharmonic couplings in the BT system make a significant contribution to the potential energy surface and should definitely be included for a more accurate description.

*Table SIX. Comparison of transition temperatures different (harmonic and anharmonic) couplings are included in the parametrization of the effective Hamiltonian. R = rhombohedral, O = orthorhombic, T = tetragonal, C = cubic.*

| Exchange-correlation functional | R↔O | | O↔T | | T↔C | |
|---|---|---|---|---|---|---|
| PBEsol (standard) | 120 K | -34% | 159 K | -43% | 258 K | -36% |
| PBEsol (harmonic coupling) | 124 K | -32% | 171 K | -38% | 272 K | -33% |
| PBEsol (anharmonic coupling) | 186 K | 2% | 255 K | -8% | 395 K | -2% |
| Expt. (Ref. [6,13]) | 183 K | 0% | 278 K | 0% | 403 K | 0% |

# X.    Influence of $v_1$ and $v_2$ on polarization

In our simulation, the polarization is calculated using the amplitude of the soft mode and the associated Born effective charge. However, the other polar phonon modes can also contribute to the total polarization. These modes were designated $v_1$ and $v_2$ in the main paper. These modes were considered

13

146

for the parameterization of the potential energy surface but by back transforming to the original formalism, these degrees of freedom are not actively included in the MD simulation. Therefore, we will discuss here the contribution of these modes to total polarization. For this purpose, we first calculated the Born effective charge to these phonons. Using the displacement patterns and the effective charges of the individual ions obtained from DFT, the values $Z_{v1}^* = 1.206$ e and $Z_{v2}^* = -0.455$ e are obtained. In comparison, the Born effective charge of the soft mode is $Z_u^* = 10.267$ e. It can be clearly seen that modes $v_1$ and $v_2$ have much lower effective charges. To estimate the contribution to the overall polarization, we proceeded as follows. In our calculation, we computed the amplitudes of $v_1$ and $v_2$ which minimize the total energy to a given amplitude of u. That is, for each amplitude of u we have an admixture of $v_1$ and $v_2$. This admixture is shown in Figure S4a and can be used to calculate the polarization of $v_1$ and $v_2$. The result can be seen in Figure S8. It can be clearly seen that $v_1$ and $v_2$ give only a minimal change in the total polarization. To note, the relevant range is from 0 to 0.11 Å, since these are the occurring amplitudes during the MD simulation. This justifies our approximation that treats the total polarization as a function of only u.
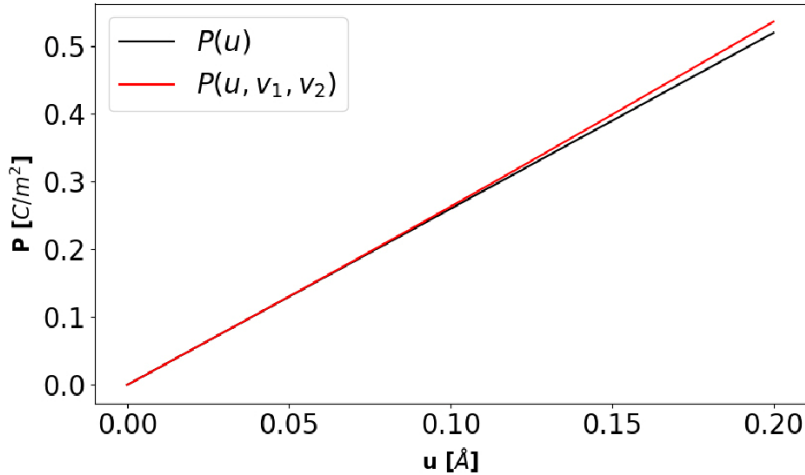


*Figure S8. Contributions of u, v₁, and v₂ to the total polarization.*

# XI.    Ab-initio molecular dynamics

The formalism for including anharmonic couplings to higher energy phonons into the effective Hamiltonian leads to the renormalization of the potential energy surface. To assess the effect of this renormalization, we performed ab-initio molecular dynamics (AIMD) for a selection of temperatures. We limit this analysis to smaller supercells of size 3x3x3 due to computational cost of AIMD. Though this choice is not ideal for a ferroelectric system where long-range interactions play a major role, with these simulations we want to study solely the local minima of the potential energy surface at different temperatures and compare them with the results obtained from the effective Hamiltonians. To perform the AIMD simulations, VASP was used again. The settings for the simulations were chosen as follows.

14

The simulation was to be performed under an NpT ensemble. This was implemented by choosing MDALGO=3 (Langevin thermostat) and ISIF=3. The necessary friction parameters for the Langevin thermostat were chosen to be 10 ps$^{-1}$. The time step was set as 0.5 fs. Subsequently, AIMD simulations were performed for temperatures of 50 K, 300 K, 450 K, and 600 K. Initially, 2000 steps with Γ-only were used to thermalize the systems. Then the k-grid was set to 2x2x2 and the systems were thermalized for another 2000 steps. The criterion for thermalization was chosen with the temperature and energies levelling off. For the final simulation, another 4000 steps were used and the energies were averaged over this time window.

The MD simulations with the effective Hamiltonian ($H_{eff}$) and the effective Hamiltonian with the anharmonic coupling ($H_{eff,anh}$) were performed with the FERAM code. In this case, we simulated in the canonical ensemble using a Nosé-Poincaré thermostat. For the comparison between AIMD and MD, we shifted the potential energies by the energy of the cubic phase at 0 K. The result is shown in Figure S9. It is clear that the AIMD simulation shows the largest differences, since it contains all couplings. The results of the effective Hamiltonians are systematically smaller. However, it can be clearly shown that by including additional anharmonic terms, the difference with the AIMD simulation becomes smaller. That is, the effective Hamiltonian with additional anharmonic terms improves the description of the system. The deviations still occurring can be attributed to various terms still missing in the Hamiltonian. For example, an inclusion of anharmonic terms in the short-range parameters was omitted. Furthermore, the <011> and <111> directions were not fully extended either, since the back transformation to the original formalism does not allow this. However, these two extensions are beyond the scope of this paper and may be addressed in a future publication.
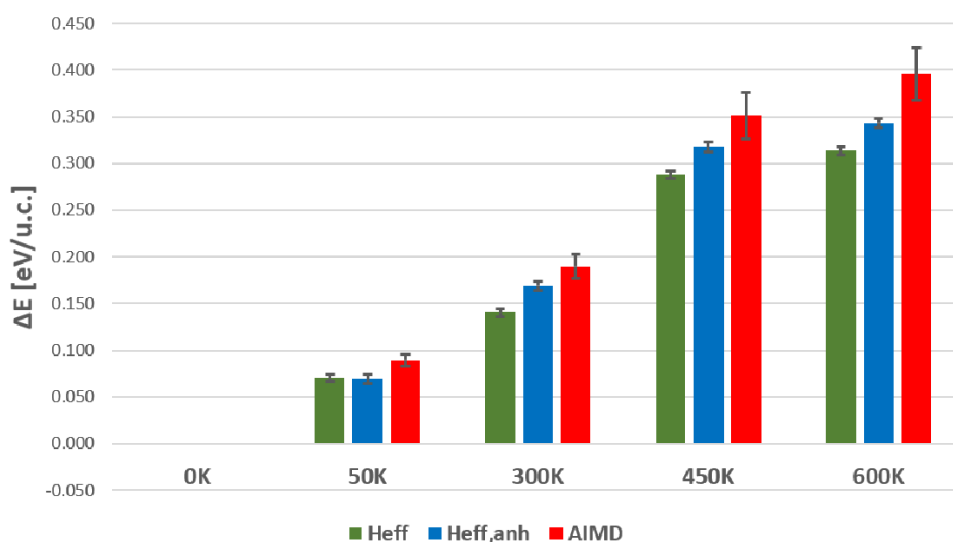


Figure S9. Comparison of potential energies differences at certain temperatures obtained with effective Hamiltonians and ab-initio molecular dynamics (AIMD). The Heff represents the effective Hamiltonian without additional anharmonic couplings, whereas Heff,anh is the adapted effective Hamiltonian. The energy differences refer to the 0 K reference state. The energy difference is given in units of eV per unit cell (u.c.).

15

# XII.    Inclusion of <011> and <111> direction
## A. DFT calculations

In this subsection, the required DFT calculations for estimating the anharmonic self-energy in directions <011> and <111> should be briefly discussed. Similar to the procedure already performed for the direction <001>, DFT calculations were also carried out for directions <011> and <111> in order to provide a large data set for subsequent fitting. The construction of the input structures was again based on the eigenvectors. That is, for the <011> direction, $u$, $v_1$, and $v_2$ were superimposed and used to displace the ions with in two cartesian directions simultaneously. The maximal amplitude in these calculations for each direction was set to 0.2 Å. In sum, about 1500 structures were created, which were subsequently calculated using DFT. For the <111> direction, a similar procedure was followed. For the <111> direction, approximately 1300 different structures were calculated. The settings of the DFT calculations can be found in section III.B from the main paper. All these calculations are based on a 5-atom unit cell.

## B.  Inclusion of anharmonicity in <011> and <111> directions

Next, let's examine the fitting of the self-energy and possible issues that arise. The equations needed for the fitting process are 2a-2c in the main paper. These equations are basically fitted to a data set of DFT calculations to determine the parameters $\kappa_2$, $\alpha$, $\gamma$ and $k_1$ to $k_4$. First, we want to fit these equations to the raw DFT data prepared without explicit coupling to higher energy phonons. The result can be seen in Figure S10a. This process determines the polynomial coefficients of the conventional effective Hamiltonian. As can be seen, the fitted curves reproduce the DFT data very well. The fit range was chosen far above the local minimum to account for the anharmonic part.

For the inclusion of anharmonic couplings to higher energy phonons, other data must now be used for fitting. These data result from DFT calculations where a superposition of the three included phonon modes was applied and then fitted by the Taylor expansion described in the main paper. This analytical function is subsequently transformed back to a function of $u$. The latter is done by minimizing the total energy for a given $u$ with respect to $v_1$ and $v_2$. As described in detail in the main paper, this results in a new data set which we can now use to fit the polynomial coefficients again. In the main paper, we focused exclusively on the <001> direction. There, the refit was performed only with the two coefficients $k_1'$ and $k_4'$. However, in this section we also want to consider the <011> and <111> directions. Furthermore, all parameters with orders higher than 2 are to be refitted.

The new data were fitted with the exact same settings as for the DFT data without explicit coupling to the higher-energy phonons. That is, all available fit parameters were used and the same fit ranges were selected. It became apparent that the new data could only be fit in a partially useful way with the existing fit functions. Nevertheless, to include the two directions <011> and <111> we tried to change the fit

ranges to allow a better refit of the data. The corresponding results are illustrated in Figure S10b. Parameters $\alpha'$, $k_1'$ and $k_4'$ were obtained by fitting the <001> direction. A maximum amplitude of 0.25 Å was used for the fit. The parameters determined from this fit ($\alpha' = 123.302$ eV/Å$^4$, $k_1' = -1464.540$ eV/Å$^6$ and $k_4' = 17768.012$ eV/Å$^8$) agree very well with those listed in the main paper. It is also clear here that $\alpha'$ changes only minimally when this parameter is considered variable in the fitting process (i.e. in the main paper, this parameter was kept fixed during the refit process). Next, the <011> direction was fitted. Here we tried to find a suitable fit range to cover the local minimum and the anharmonic range as well as possible. The parameters determined from this are $\gamma' = -169.639$ eV/Å$^4$ and $k_2' = 290.017$ eV/Å$^6$. Finally, the <111> direction was also fitted to extract remaining parameters. Again, the fit range was adjusted to obtain the best possible result. The parameter determined from it amounts to $k_3 = 679.924$ eV/Å$^6$. In summary, the following conclusions can be drawn. The refit process is very stable for the <001> direction. For this direction, the anharmonic data over a range up to 0.25 Å can be fitted very well. For the other two directions, the fit ranges had to be adjusted to get a fit describing low-energy region reasonably well. Even though adjusting the range looks like a common practice [4] for improving the fit, we are not satisfied with this result. Especially the fact that we lose valuable information at the anharmonic region by reducing the fit range must be mentioned here. Therefore, we are currently working on an extension of the self-energy in the Hamiltonian formulated by Nishimatsu et al. [4] to achieve more flexibility for the refit. The results on this topic will be addressed in a future publication.
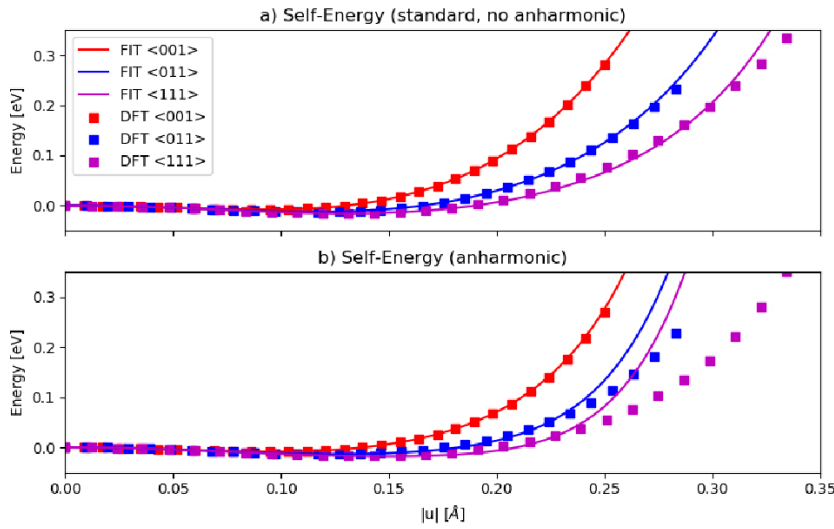


*Figure S10. Estimation of polynomial coefficients of the self-energy term. a) represents the case of the conventional self-energy without further couplings to higher-energy phonons. b) shows the re-fit of the parameters using the energy including anharmonic contributions from explicit coupling to higher-energy phonons.*

## C. MD simulation with parameters including <011> and <111> directions

In this subsection we want to test the parameters determined by the re-fit including all directions by MD simulations. An overview of the parameters is given in Table SX. The settings of the MD simulations are analogous to the main paper. However, a temperature step of 5K was set here. The phase diagram resulting from the simulation can be seen in Figure S11. The transition temperature from paraelectric to ferroelectric phase is in good agreement with the results from the main paper. This also reflects the stability of the fit in the <001> direction. The transitions from tetragonal to orthorhombic phase and from orthorhombic to rhombohedral phase are slightly different compared to the main paper. However, in order to verify these results, we must first improve the refit in the <011> and <111> directions. Overall, the results from the main paper can also be confirmed by this parameter set.

*Table SX. Self-energy parameters for pure BT obtained from refit including all directions.*

| | |
|---|---|
| $\kappa_2'$ [eV/Å$^2$] | 8.007 |
| $\alpha'$ [eV/Å$^4$] | 123.302 |
| $\gamma'$ [eV/Å$^4$] | -169.639 |
| $k_1'$ [eV/Å$^6$] | -1464.54 |
| $k_2'$ [eV/Å$^6$] | 290.017 |
| $k_3'$ [eV/Å$^6$] | 679.924 |
| $k_4'$ [eV/Å$^8$] | 17768.012 |
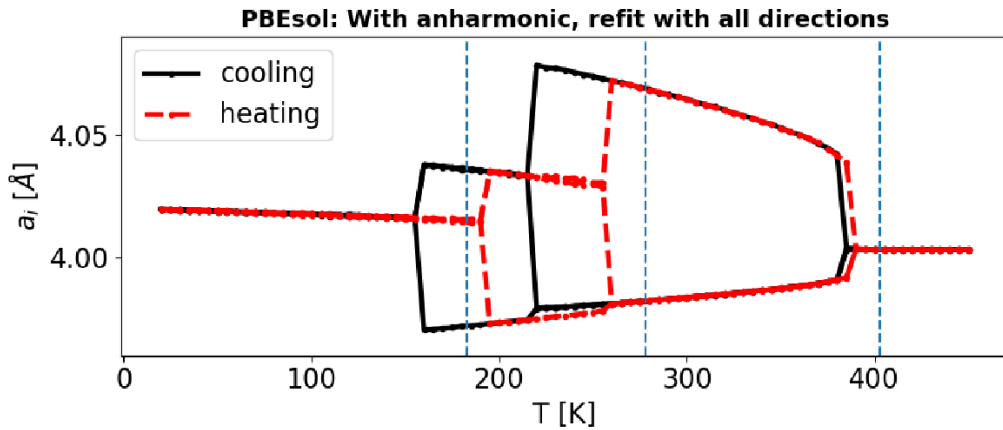


*Figure S11. Phase diagram of BT from MD simulations using the parameter set including all directions in the refit process. The plot shows the lattice constant versus the temperature. Blue vertical lines are the experimental values from Ref. [6,13].*

# References

[1]     Wolfram Research, Inc., Mathematica, Version 12.2, Champaign, IL (2020).

[2]     H. T. Stokes, D. M. Hatch, and B. J. Campbell, INVARIANTS, ISOTROPY Software Suite, iso.byu.edu.

[3]     D. M. Hatch and H. T. Stokes, J. Appl. Crystallogr. **36**, 951 (2003).

[4]     T. Nishimatsu, M. Iwamoto, Y. Kawazoe, and U. V Waghmare, Phys. Rev. B **82**, 134106 (2010).

[5]     R. C. Herchig, Ph.D. Thesis: Complex Electric-Field Induced Phenomena in Ferroelectric / Antiferroelectric Nanowires, https://digitalcommons.usf.edu/etd/6710/, 2017.

[6]     A. Paul, J. Sun, J. P. Perdew, and U. V. Waghmare, Phys. Rev. B **95**, 054111 (2017).

[7]     R. D. King-Smith and D. Vanderbilt, Phys. Rev. B **49**, 5828 (1994).

[8]     Python Package: LMFIT, https://lmfit.github.io/lmfit-py/.

[9]     P. E. Blöchl, Phys. Rev. B **50**, 17953 (1994).

[10]    S. Piskunov, E. Heifets, R. I. Eglitis, and G. Borstel, Comput. Mater. Sci. **29**, 165 (2004).

[11]    S. F. Yuk, K. C. Pitike, S. M. Nakhmanson, M. Eisenbach, Y. W. Li, and V. R. Cooper, Sci. Rep. **7**, 43482 (2017).

[12]    R. A. Evarestov, Phys. Rev. B **83**, 014105 (2011).

[13]    C. J. Johnson, Appl. Phys. Lett. **7**, 221 (1965).

19

### 8.3 Publication 3

# Finite-temperature investigation of homovalent and heterovalent substituted BaTiO$_3$ from first principles

Florian Mayer[1], Maxim N. Popov[1], Petr Ondrejkovic[2], Jiri Hlinka[2], Jürgen Spitaler[1], Marco Deluca[1]

[1]*Materials Center Leoben Forschung GmbH, Roseggerstrasse 12, 8700 Leoben, Austria*
[2]*Institute of Physics of the Czech Academy of Sciences, 182 00, Praha 8, Czech Republic*

Corresponding author: florian.mayer@mcl.at

**Abstract:**

Barium titanate (BT) solid solutions are used in a wide range of applications such as piezoelectric actuators and high-performance energy storage devices. The key to achieve and tune desired macroscopic properties is the chemical modification, which is done by substituting Ba or Ti with other homovalent or heterovalent cations. This work uses large-scale molecular dynamics simulations based on an effective Hamiltonian approach to calculate the macroscopic properties of BT solid solutions from first principles, thereby offering a framework for the prediction of properties prior to materials synthesis. To this end, we elaborate on the theoretical description of substitution in effective Hamiltonians as well as their parametrization by density functional theory (DFT) calculations for two model systems: homovalent substituted BaZr$_x$Ti$_{1-x}$O$_3$ (BZT) and heterovalent substituted BaNb$_x$Ti$_{1-x}$O$_3$ (BNT). The effective Hamiltonian for BZT obtained in this work is first used for benchmarking against other models and experimental data on the phase diagrams and dielectric properties. Subsequently, the effective Hamiltonian is further extended and used to parametrize BNT and compare the model's predictions to the available experimental data. The parameter sets obtained in this work can be used for future studies and provide deep insight into the subject of relaxor ferroelectrics.

# Finite-temperature investigation of homovalent and heterovalent substituted BaTiO$_3$ from first principles

Florian Mayer [1,*] Maxim N. Popov [1] Petr Ondrejkovic [2] Jiri Hlinka [2] Jürgen Spitaler [1] and Marco Deluca [1]

$^1$*Materials Center Leoben Forschung GmbH, Roseggerstrasse 12, 8700 Leoben, Austria*
$^2$*Institute of Physics of the Czech Academy of Sciences, 182 00, Praha 8, Czech Republic*

Barium titanate (BT) solid solutions are used in a wide range of applications such as piezoelectric actuators and high-performance energy storage devices. The key to achieve and tune desired macroscopic properties is the chemical modification, which is done by substituting Ba or Ti with other homovalent or heterovalent cations. This work uses large-scale molecular dynamics simulations based on an effective Hamiltonian approach to calculate the macroscopic properties of BT solid solutions from first principles, thereby offering a framework for the prediction of properties prior to materials synthesis. To this end, we elaborate on the theoretical description of substitution in effective Hamiltonians as well as their parametrization by density functional theory calculations for two model systems: homovalent substituted BaZr$_x$Ti$_{1-x}$O$_3$ (BZT) and heterovalent substituted BaNb$_x$Ti$_{1-x}$O$_3$ (BNT). The effective Hamiltonian for BZT obtained in this work is first used for benchmarking against other models and experimental data on the phase diagrams and dielectric properties. Subsequently, the effective Hamiltonian is further extended and used to parametrize BNT and compare the model's predictions to the available experimental data. The parameter sets obtained in this work can be used for future studies and provide deep insight into the subject of relaxor ferroelectrics.

## I. INTRODUCTION

Relaxor ferroelectrics (RFs) have recently been the subject of intensive investigations as possible energy storage materials with both high power and energy density [1–3]. RFs, in essence, are ferroelectrics where the long-range polarization correlation is disrupted [1] due to chemical substitution. On the macroscopic scale, this results in a reduction of the hysteretic losses originating from the reorientation of polar domains, which increases the recoverable energy density. Other parameters play a role in achieving high energy density, for instance, a high saturated polarization, small leakage currents, and a high breakdown voltage. As permittivity (and thus saturation polarization) decreases with the loss of ferroelectric character, one issue is how to stabilize a high permittivity in a RF. These aspects are intimately related with how the chemical substitution affects the local lattice structure, its polar order, and how the material interacts with external applied electric fields at atomic scale and on the mesoscale. It is thus very important to be able to predict macroscopic electrical properties in such systems at finite temperatures and external fields, starting from simulated atomic scale structures. In other words, realistic molecular dynamics (MD) simulations need to be performed to investigate substitution effects at the atomic level and their impact on the material's properties.

In this work, we provide an improved model of the potential energy surface for the application in MD simulations. Our approach is based on so-called effective Hamiltonians [4,5],

first introduced in the early 1990s for perovskites. The required parameters for the effective Hamiltonians can entirely be determined by first-principles calculations. Furthermore, a significant advantage of this approach is the computational efficiency due to the reduced number of degrees of freedom. In the beginning, this model was a mean-field theory [5], which was later adapted to a local-mode framework [6]. In 2010, Nishimatsu *et al.* [7] revised this model, improving its accuracy. Paul *et al.* [8] showed that including anharmonic couplings further enhances the quality of such simulations. In our previous work [9], we established a more general approach for including these couplings, which improved the description of both phase transitions and dielectric properties. Here we build upon our previous findings and use the parameter set for pure barium titanate (BT) as the basis for the parametrization of effective Hamiltonians for substituted systems. In literature, such effective Hamiltonians for substituted systems are found with different approaches for incorporating the substituted ions. This includes the parametrization by the virtual crystal approximation [10,11], by adding additional terms to the Hamiltonian [12–14], or simply treating the system by averaging [15] parameters of two constitutive systems. The present work introduces an alternative approach based on the following principles. First, the used Hamiltonian of the parent system BT builds on a revised parametrization [9] including a large number of anharmonic couplings to higher energy phonons. That increases the accuracy of the potential energy surface as well as the quantitative description of the transition temperatures [9]. Second, the substituted ions are incorporated as perturbation to the pure BT system using a revised treatment of interactions. Thus, special consideration

*florian.mayer@mcl.at

154

is given to the local description of the occurring substitution effects. In addition, the presented effective Hamiltonian is independent of concentration and hence the parametrization procedure is more flexible and has to be performed only once.

To test our approach, we parametrize two fundamentally different RF systems: one homovalent and one heterovalent substituted BT. In the former case, $Ti^{4+}$ ions on the B-site are substituted by $Zr^{4+}$ ions, leading to the $BaZr_xTi_{1-x}O_3$ (BZT) solid solution. For the heterovalent case, $Ti^{4+}$ are substituted by $Nb^{5+}$, which yields $BaNb_x\square_{1/4x}Ti_{1-5/4x}O_3$ (BNT). Here, it is essential to consider the presence of Ti vacancies for charge compensation as discussed in detail in a former publication [16]. The BZT Hamiltonian serves as the basis for a benchmark to test our model and its assumptions. For BZT, the effective Hamiltonians are already available, however, they lack the incorporation of additional anharmonic couplings. These references offer the possibility to test our approach. Furthermore, a cross check between simulations and experimental data is presented. In the case of BNT, we are not aware of any existing parametrizations, and therefore we rely on experimental data to carry out a comparison with the simulations.

The cornerstone of this investigation is the alternative parametrization of our models from density functional theory (DFT) calculations. DFT was already used in one of our previous publications [16] to study the effects of the above-mentioned substituents in a static picture in terms of local volume change and impact on electrical potential. The present paper continues our previous work by expanding the effective Hamiltonian towards substituted systems, as presented in Sec. II. Subsequently, we discuss the parametrization of BZT by DFT calculations, followed by a benchmark of this Hamiltonian with other models and experimental data. Building on this, the parametrization of BNT is presented, followed by application of the model for simulating the phase diagram and dielectric properties, and the comparison with the experiments.

## II. THEORETICAL FRAMEWORK

### A. Effective Hamiltonian of pure BT

The basis of our simulations is the effective Hamiltonian defined by Nishimatsu *et al.* [7,17], as stated in Eq. (1). This Hamiltonian is used to describe the pure BT system. The required parameters can be obtained by DFT calculations and are discussed in the next section. In general, this Hamiltonian consists of the following energy contributions: Kinetic energies of the optical soft-mode $\boldsymbol{u}$ and the acoustic mode $\boldsymbol{w}$, local-mode self-energy $V^{self}$, dipole-dipole interaction $V^{dpl}$, short-range interaction $V^{short}$, elastic energies $V^{elas}$, strain-phonon interactions $V^{coupl}$, and interaction with an external field. The time derivatives of the variables are represented by $\dot{u}_\alpha$ and $\dot{w}_\alpha$, where $\alpha$ denotes the Cartesian component. $\boldsymbol{R}$ represents a translation vector indicating the position of the unit cells within the supercell. $\eta_i$ are strain variables in Voigt notation. $Z^*$ is the Born effective charge associated with the soft mode $\boldsymbol{u}$. The brackets {} indicate a set of amplitudes $u$ within a supercell. $M^*_{dipole}$ and $M^*_{acoustic}$ are the effective masses of the soft mode and the acoustic mode in the long

wavelength limit, respectively. The parameter $\epsilon$ allows applying an external field. It should be mentioned here that for the soft mode a local basis by lattice Wannier functions (LWFs) [18,19] centered on the B cation was chosen. This also applies to all further calculations in which the soft mode and its displacement pattern are used.

$$
\begin{aligned}
H_{BTO}^{eff} = {} & \frac{M^*_{dipole}}{2} \sum_{R,\alpha} \dot{u}_\alpha^2(\boldsymbol{R}) + \frac{M^*_{acoustic}}{2} \sum_{R,\alpha} \dot{w}_\alpha^2(\boldsymbol{R}) \\
& + V^{self}(\{u\}) + V^{dpl}(\{u\}) + V^{short}(\{u\}) \\
& + V^{elas,homo}(\eta_1, \dots, \eta_6) + V^{elas,inho}(\{w\}) \\
& + V^{coupl,homo}(\{u\}, \eta_1, \dots, \eta_6) + V^{coupl,inho}(\{u\}, \{w\}) \\
& - Z^* \sum_R \epsilon \cdot u(\boldsymbol{R}).
\end{aligned}
\tag{1}
$$

### B. Substitution via perturbation of BT

To extend the formalism for substituted systems, we add an additional term to the effective Hamiltonian of Eq. (1). This term accounts for effects induced by the presence of substituents. Compared to some previous work in this area, we are not using an averaged system as basis and, therefore, treat the substituents in terms of a perturbation to the Hamiltonian of the pure system [14]. A general form of the extended Hamiltonian is stated in Eqs. (2) and (3). The new symbolic variable $\sigma$ is used to differentiate between unit cells with different B-site ions (e.g. $\sigma = Ti, Zr, Nb, V_{Ti}$).

$$
\begin{aligned}
& H_{total}^{eff}(\{u\}, \{w\}, \eta_i, \{\sigma\}) \\
& \quad = H_{BTO}^{eff}(\{u\}, \{w\}, \eta_i) + H^{perturb.}(\{u\}, \{w\}, \{\sigma\}),
\end{aligned}
\tag{2}
$$

$$
\begin{aligned}
H^{perturb.} = {} & \Delta T(\{u\}, \{w\}, \{\sigma\}) + \Delta V^{self}(\{u\}, \{\sigma\}) \\
& + \Delta V^{dpl}(\{u\}, \{\sigma\}) + V^{aux}(\{u\}, \{w\}, \{\sigma\}).
\end{aligned}
\tag{3}
$$

The perturbation term is inspired by former works of Bellaiche *et al.* [10,12,13] as well as Mentzer *et al.* [14] and consists of four different adaptations to the total energy as written in Eq. (3). The first term $\Delta T$ accounts for different effective masses and, therefore, the influence on the kinetic energies of the optical soft-mode and the acoustic branch.

The second term $\Delta V^{self}$ adapts the local-mode self-energy by introducing the new parameters $\Delta\kappa_{2,\sigma}$, $\Delta\alpha_\sigma$, $\Delta\gamma_\sigma$ and $\Delta k_{1,\sigma}$ to $\Delta k_{4,\sigma}$. These parameters account for the change in local-mode self-energy when the B site is substituted with different ions compared to Ti. The complete form of this energy contribution is written below:

$$
\begin{aligned}
& \Delta V^{self}(\{u\}, \{\sigma\}) \\
& = \sum_R \Big\{ \Delta\kappa_{2,\sigma} u^2(\boldsymbol{R}) + \Delta\alpha_\sigma u^4(\boldsymbol{R}) \\
& \quad + \Delta\gamma_\sigma \big[ u_y^2(\boldsymbol{R}) u_z^2(\boldsymbol{R}) + u_z^2(\boldsymbol{R}) u_x^2(\boldsymbol{R}) + u_x^2(\boldsymbol{R}) u_y^2(\boldsymbol{R}) \big] \\
& \quad + \Delta k_{1,\sigma} u^6(\boldsymbol{R}) + \Delta k_{2,\sigma} \big( u_x^4(\boldsymbol{R}) * \big[ u_y^2(\boldsymbol{R}) + u_z^2(\boldsymbol{R}) \big] \\
& \quad + u_y^4(\boldsymbol{R}) * \big[ u_z^2(\boldsymbol{R}) + u_x^2(\boldsymbol{R}) \big] + u_z^4(\boldsymbol{R}) * \big[ u_x^2(\boldsymbol{R}) + u_y^2(\boldsymbol{R}) \big] \big) \\
& \quad + \Delta k_{3,\sigma} u_x^2(\boldsymbol{R}) u_y^2(\boldsymbol{R}) u_z^2(\boldsymbol{R}) + \Delta k_{4,\sigma} u^8(\boldsymbol{R}) \Big\}.
\end{aligned}
\tag{4}
$$

155

A further correction is made for the long-range interaction $\Delta V^{\mathrm{dpl}}$ between dipoles. Since different B-site ions exhibit different Born effective charges, the $Z^*$ must be adjusted accordingly. As a further correction, we introduce a term according to Refs. [10,12]. For the remainder of this paper, we call this term an auxiliary spring system. That is applied to compensate for the interaction of neighboring unit cells with different B-site ions:

$$V^{\mathrm{aux}}(\{u\}, \{w\}, \sigma) = \sum_R \sum_T Q_{T,R}(\sigma_T) e_{T,R} \cdot u(R)$$
$$+ \sum_R \sum_T S_{T,R}(\sigma_T) f_{T,R} \cdot w(R). \quad (5)$$

In detail, the term in Eq. (5) is used to calculate the influences of adjacent unit cells on the dynamics of the local mode $u(R)$ and the acoustic displacement variables $w(R)$. Here, the parameters $Q_{T,R}(\sigma_T)$ and $S_{T,R}(\sigma_T)$ account for differences between the substituted system's interactions compared to the pure system's interactions. $T$ denotes the translation to unit cells up to the third nearest neighbor shell (3NN). $e_{T,R}$ represents a unit vector joining the site $T$ to the center of $u(R)$. Analogously, the unit vector $f_{T,R}$ is joining the site $T$ with the center of $w(R)$. At present, we restrict the auxiliary spring system to the first order [10] in $u(R)$ and $w(R)$, but it can be systematically expanded to higher orders, if required. As a final correction, we want to include the effects of lattice expansion or contraction in terms of homogenous strain induced by impurity ions. To compensate for these volume changes in the extended Hamiltonian, we apply a hydrostatic pressure [14,15] as a function of concentration. It should be noted, that this volume change directly affects the correction parameters $S_{T,R}(\sigma_T)$. In principle, these parameters would have to be determined individually for each concentration, but we decided to keep them constant in order not to lose the flexibility of the approach. This assumption is a good choice for small concentrations, but for higher concentrations an overestimation of local distortions can occur.

The parameterization of the extended Hamiltonian by first-principles calculations is detailed in the next section. For using the adapted Hamiltonian for MD simulations, we customized the *feram* code developed by Nishimatsu *et al.* [7,17,20].

### C. Computational details

For all first-principles calculations, we used the projector-augmented [21] DFT package VASP [22–25] and the PBEsol [26] as exchange-correlation functional. An energy cutoff of 520 eV was used throughout all calculations. More details on DFT calculations and the following parametrization can be found in the Supplemental Material [27]. To increase the accuracy of the potential energy surface of pure BT, a large number of anharmonic couplings to higher energy phonons were considered, as described in detail in our previous publication [9]. These couplings were determined by an elaborate fitting procedure, as described in Ref. [9].

#### 1. Parametrization of BZT

The parametrization of the extended Hamiltonian for BZT by means of DFT calculations is discussed here. First, we

calculated the parameters for the adapted local-mode self-energy using a 5-atom unit cell. The lattice constant of this unit cell was set to that of pure BT ($a_i = 3.987$ Å) [9]. Subsequently, the B-site was replaced by Zr. The unit cell served as the basis for the calculation of displaced structures given by the displacement pattern of the soft-mode found in cubic BT (see Ref. [9] for the pattern). These displacements were constructed for directions $\langle 001 \rangle$, $\langle 011 \rangle$, and $\langle 111 \rangle$, respectively, whereby DFT was used to calculate the total energy. For the 5-atom unit cell calculations, a k grid size of $8 \times 8 \times 8$ was chosen. The results were then used to fit the Eqs. (14a)–(14c) from Ref. [7]. The resulting parameters are listed in the Supplemental Material [27] in Table SI. The calculation of the parameter $\Delta \kappa_2$ was performed as follows. $2 \times 2 \times 2$ supercells were constructed from the 5-atom unit cells. These were used to perform linear-response calculations (DFPT). The k grid was set to $4 \times 4 \times 4$. The phonon band structure was calculated for the respective systems from these calculations. Subsequently, the procedure as in Ref. [7] was used to determine short-range parameters. From this, the parameters $\Delta \kappa_2$ for BZT were determined (see Table SI in the Supplemental Material [27]). The DFPT calculations just mentioned were also used to calculate $Z^*$ for a Zr unit cell, obtained from the Born effective charges.

For the calculation of the parameters for the auxiliary spring system, as a first step, a $3 \times 3 \times 3$ supercell of pure BT was constructed. Subsequently, one B site in this supercell was substituted with Zr. The atoms of the local unit cell containing the substituted atom were then displaced in discrete steps using the displacement pattern of the soft mode of pure BT. DFT was then used to calculate the total energy of the system and the forces acting on the atoms. Here, a k grid of size $2 \times 2 \times 2$ was chosen. From these data, the parameters $Q_{T,R}(\sigma_T)$ were determined using the total energies and fitting a linear function. To avoid double-counting, contributions were already taken into account by the Hamiltonian of pure BT, a reference system was calculated, and the corresponding total energies were subtracted from the substituted supercells. That procedure was repeated by displacing local unit cells up to the 3NN shells with respect to the substituted Zr ion. For the interaction between two Zr unit cells, two Zr ions were substituted as nearest neighbors. The calculation of the parameters is analogous to the above-mentioned procedure. The correction parameters $S_{T,R}(\sigma_T)$ were calculated using a A-centered basis and displacing the ions according to a translational eigenvector. Here, also the lattice constant was adapted to get the correction parameters in accordance with the lattice change already captured by the applied pressure correction. The estimation of the parameters using the total energy is analogous to the procedure described for $Q_{T,R}(\sigma_T)$. All results of the parameters discussed here are listed in Table SII in the Supplemental Material [27].

Next, a pressure correction was calculated to describe the Zr induced expansion or contraction of the lattice. For this purpose, the dependence of the BT lattice constant on an external pressure was first calculated using DFT. Then, a supercell of size $2 \times 2 \times 2$ was constructed and substituted with different concentrations of Zr. The full range of concentrations was used. These structures were relaxed using DFT and thus a dependence of a pseudocubic lattice parameter on

156

concentration was calculated. Using both results, a linear pressure correction of the magnitude $P(x) = -19.5x$ GPa could be calculated, where $x$ denotes the concentration of Zr. From this result, it is clear that Zr exerts a negative pressure on the lattice, causing it to expand. This pressure correction is in good agreement with results of Mentzer *et al.* [14]; the small deviations can be explained by the different choice of the exchange-correlation functional. The corresponding plots of the pressure and concentration dependence of the lattice parameter can be found in the Supplemental Material [27], Figs. S1–S3.

### *2. Parametrization of BNT*

As a next step, we parameterized an effective Hamiltonian for BNT. The main difference to BZT stems here from the heterovalency of Nb. This leads to charge compensation by Ti vacancies ($V_{Ti}$), as discussed in Ref. [16]. Thus, we simultaneously introduced Nb and $V_{Ti}$ into the effective Hamiltonian, rather than Nb alone. To probe the effect caused by the introduction of these species, DFT calculations were performed on $5 \times 5 \times 5$ supercells; the results of which are shown in our previous work [16]. It turns out that the titanium vacancy has a considerable influence [16] on the surrounding unit cells. The unit cell containing $V_{Ti}$, on the other hand, contributes with its local dipole moment only to a limited extend to the polar order of the system. This is based on the observation from phonon calculations where the unit cells with Ti vacancies couple to the relevant polar modes of the surrounding unit cells only by a nonpolar oxygen oscillation. Owing to that, these unit cells are henceforth considered static with a zero net dipole. Consequently, the effective Hamiltonian was extended by another species $\sigma$ and its associated parameters. The interactions of Ti vacancies with surrounding unit cells were considered by the parameters $Q_{T,R}(\sigma_T)$. The parameters for the adapted self-energy are not needed for the Ti vacancy since these unit cells are fixed with respect to the variable $u$ for the simulation. What remains are the parameters of the auxiliary spring system for the interactions between the unit cells Ti-Nb, Ti-$V_{Ti}$, Nb-$V_{Ti}$, and Nb-Nb, as well as the adapted self-energy, effective mass, and Born effective charge for Nb unit cells. The parameterization of the latter is analogous to that for the case of BZT, but a suitable charge compensation has to be applied in the DFT calculations. The calculation of the parameters $Q_{T,R}(\sigma_T)$ was thus carried out as follows: A $3 \times 3 \times 3$ supercell was first prepared from pure cubic BT, then, for the calculation of Ti-Nb interactions, one B site was substituted with Nb. For Nb-Nb interaction, two Nb ions were introduced. The interaction between Ti or Nb unit cells with Ti vacancies was calculated by removing one Ti ion from the first coordination shell within the supercell. Subsequently, all supercells were calculated with DFT, and the resulting total energies were used to determine the parameters. The rest of the procedure is analogous to BZT. The estimation of the correction parameters $S_{T,R}(\sigma_T)$ for the acoustic displacement variables was carried out analogously to the procedure explained for BZT. All parameters derived for BNT are listed in the Supplemental Material [27]. The pressure correction must be computed also for BNT to account for any changes in the lattice due to substitution, and we can use the pressure

dependence of the BT lattice parameter, analogous to BZT. The following calculations were then performed to estimate the dependence of the lattice parameter on the Nb concentration. Supercells of size $2 \times 2 \times 2$ and $3 \times 3 \times 3$ were used to substitute one or more sets of four Nb ions and one Ti vacancy. Subsequently, these structures were relaxed using DFT and a pseudocubic lattice constant was calculated. This results in a pressure correction of magnitude $P(x) = -8x$ GPa, where $x$ is the concentration of Nb ions. This outcome reveals that Nb also induces an expansion of the lattice, which is, however, smaller as compared to BZT.

### *3. MD simulations*

For the supercells used for MD simulations, the question of the distribution of substituted atoms arises. In the case of BZT, a random distribution [28] as well as a slight clustering [29–31] of Zr ions have been reported experimentally. In our case, we also tested different distributions, but finally convened on a randomly distributed arrangement of Zr ions. First of all, we determined effective cluster interactions from VASP supercell calculations, which were then used to perform Monte Carlo (MC) simulations to determine chemical ordering as a function of temperature [32]. The MC simulations showed that for experimentally relevant temperatures no ordering is found. In order to generate the disordered supercells, a random generator was used to create input structures for MD simulations. A simulation box of size $30 \times 30 \times 30$ was chosen. Subsequently, a series of structures with different concentrations of Zr were prepared. An MD run with the following settings was performed for each of these structures. A velocity-scaling algorithm was used to cool the system from 800 K to 20 K in steps of 5 K. At each temperature, the system was thermalized for 200 ps and averaged over 600 ps with a discrete-time step of 2 fs. The output configuration of dipoles was used as the initial condition for the following temperature. All simulations were carried out in the canonical ensemble. The obtained results made it possible to derive the phase diagrams. The transition temperatures were determined using the following procedures. For concentrations below the tricritical point, the results of polarization vs temperature and the change in shape of the simulation cell as a function of temperature were used. For concentrations beyond the tricritical point, the permittivity as a function of temperature was used to estimate $T_m$. The random distribution as determined by the MC simulation yields the best agreement of the phase diagram with experiments.

## III. RESULTS

### A. Simulations for BZT

#### *1. Phase diagram*

As the first step, we use our obtained model to simulate the phase diagram of BZT as a function of temperature and concentration. The simulation results of the phase diagram for BZT are presented in Fig. 1(a). It can be seen that the transition temperature between the paraelectric and ferroelectric phase initially decreases almost linearly with Zr concentration. At about 35% Zr content, this transition begins to flatten out. The transition boundaries between the

157
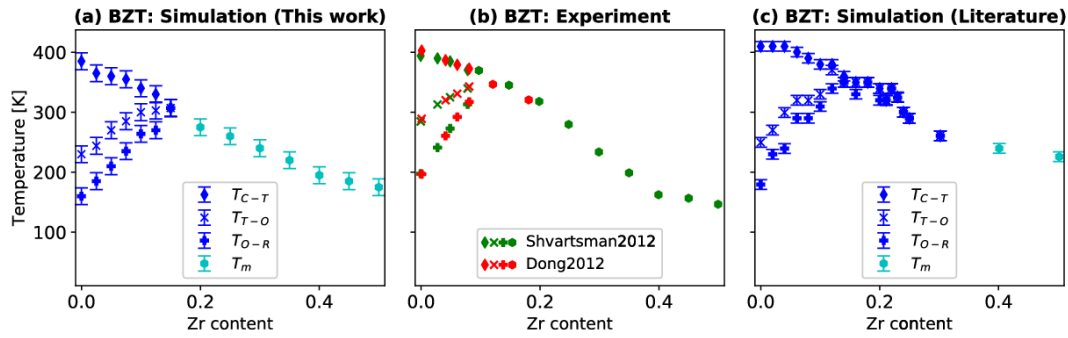
FIG. 1. Phase diagram of BZT simulated with effective Hamiltonians (a),(c) and experimentally observed values (b). The experimental values are from Refs. [1,33]. The simulated data from literature were taken from Ref. [14]. $T_{C-T}$, $T_{T-O}$, $T_{O-R}$ transitions between cubic (C), tetragonal (T), orthorhombic (O), and rhombohedral (R) phases, respectively. $T_m$ temperature of maximum in dielectric permittivity.

tetragonal and orthorhombic phase, and between the rhombohedral and orthorhombic phase increase significantly with Zr content until they merge at the tricritical point, which is located at about 12.5% Zr content. Compared to the experiment [1,33] [see Fig. 1(b)], our simulations yield slightly lower transition temperatures for concentrations between 0 and 30% of Zr. For higher concentrations, the simulated transition temperatures slightly overestimate the experimental data. This indicates that the pressure correction for this region of concentrations might be too strong. Furthermore, it should be noted that the transition temperatures depend relatively strongly on the distribution of Zr ions. Overall, the shape of the phase diagram is reproduced very well. Figure 1(c) shows simulation results from the literature [14], which were calculated using a different effective Hamiltonian. The difference lies on the one hand in the procedure of parameterization of the Hamiltonian for pure BT and on the other hand in the inclusion of substituted unit cells. For the latter, the application of a concentration-dependent pressure and the use of a restoring force was chosen in the work of Mentzer *et al.* [14]. The first term is equivalent to the pressure correction used in this work with the applied pressures agreeing well with our values (see Sec. II C 1 for details). The restoring force approach is similar to our correction of the local mode self-energy. Another difference is the auxiliary spring system for the correction of effects originating from the substituted unit cells, which is not included in the work of Mentzer *et al.* [14]. The reference simulation shows good agreement with our results as well as with the experimental data. For higher concentrations, our simulation yields slightly better comparison with the experimental data (i.e., lower transition temperatures), which can mainly be attributed to the marginally different pressure correction. However, a direct comparison should be made with caution since the distribution of Zr cations used in the reference simulation is not available.

#### *2. Dielectric properties*

Here, we use our MD simulations to calculate dielectric properties for the concentrations of 5% Zr (BZT05) and 50% Zr (BZT50). A simulation box size of $30 \times 30 \times 30$ was used for this purpose. The remaining settings for the MD simulations can be found in the previous section. Again, a

cooling series was simulated for both systems, with the output configurations serving as input for the following temperature. The results for polarization as a function of temperature can be seen in Figs. 2(a) and 2(b). Ferroelectric behavior is observed for BZT05, with all three phase transitions of BT still clearly visible, albeit the spacing between transitions is closer than in pure BT case. The absolute values of the spontaneous polarization are in good agreement with experimentally observed values [34] and other simulations [14] from the literature. For the case of BZT50, no macroscopic polarization is detected, which means that the system remains in a nonpolar state for any simulated temperature. Furthermore, the strain tensor was examined, indicating that the system possesses cubic structure throughout all temperatures.

To calculate the susceptibility, we employed the scheme of Akbarzadeh *et al.* [13]. On the one hand, the susceptibility was determined by a direct method. For this purpose, an external field was applied during cooling MD runs in $\langle 111 \rangle$ direction with a maximum magnitude of 50 kV/cm. From this, the response of the system can be used to calculate the susceptibility in the respective directions. A reference simulation was performed for systems with spontaneous polarization to calculate the response induced purely by the applied external field. The corresponding formula reads

$$\chi_{\alpha\beta}^{\text{direct}} = \frac{NZ^*(\langle u_\alpha \rangle_{\text{ext}} - \langle u_\alpha \rangle_{\text{ref}})}{V \epsilon_0 E_{\text{ext},\beta}}. \quad (6)$$

Here, $\langle u_\alpha \rangle_{\text{ext}}$ is the average amplitude of the local mode when applying an external field $E_{\text{ext}}$. $\langle u_\alpha \rangle_{\text{ref}}$ represents the average amplitude of the reference simulation. $\alpha$ and $\beta$ denote the Cartesian components of the local mode vector and the electric field vector. $\epsilon_0$ is the vacuum permittivity. $Z^*$ is the Born effective charge and $V$ the volume of the supercell. $N$ is the number of unit cells within the supercell. This susceptibility corresponds to the static limit. On the other hand, we use the dipole fluctuations as described by the correlation function (CF) to calculate the susceptibility:

$$\chi_{\alpha\beta}^{\text{CF}} = \frac{(NZ^*)^2}{V \epsilon_0 k_B T} (\langle u_\alpha u_\beta \rangle - \langle u_\alpha \rangle \langle u_\beta \rangle). \quad (7)$$

In this equation, $u_i$ represents the Cartesian component of the local mode vector. $T$ denotes the temperature and $k_B$ is the Boltzmann constant. The obtained susceptibility can be

158
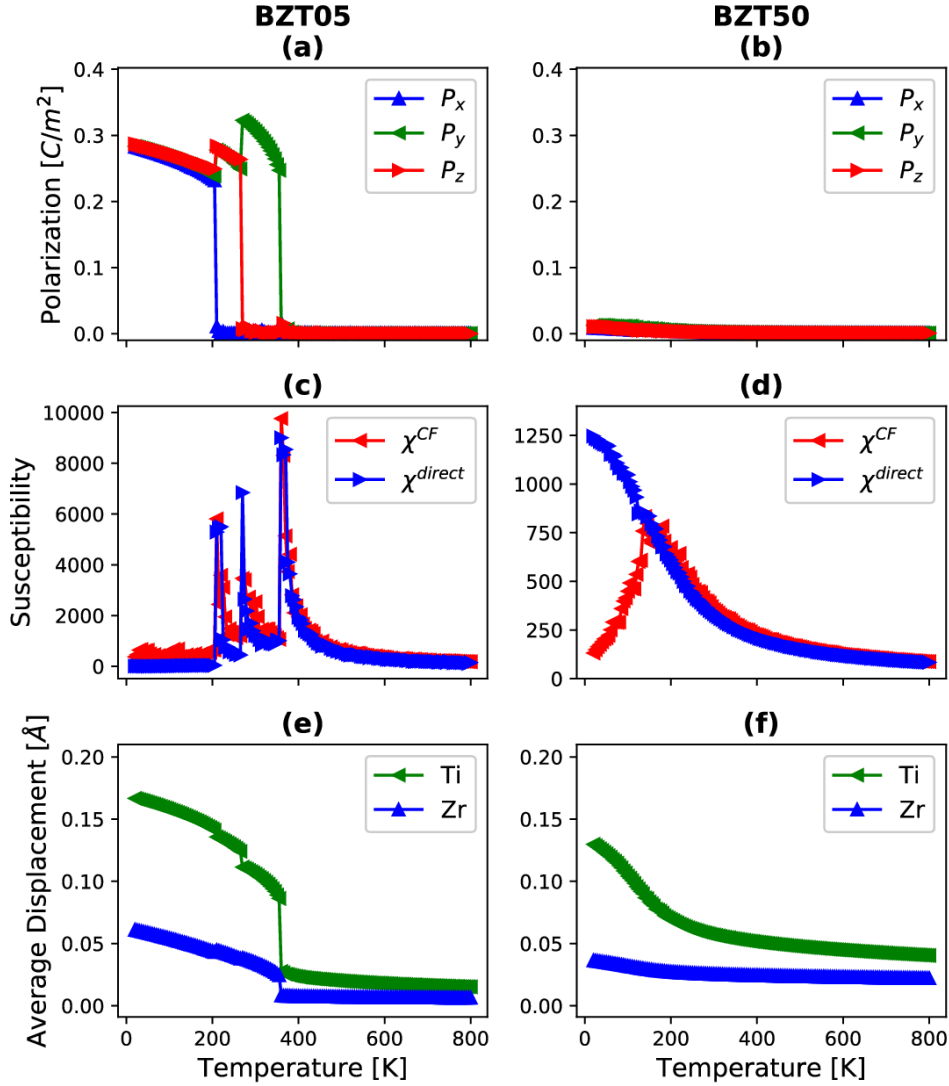
FIG. 2. Comparison of BZT05 (5% Zr) and BZT50 (50% Zr) in terms of the polarization (a),(b), the susceptibility (c),(d), and the average displacement of the two B-site species (e),(f). The susceptibility was calculated using a direct method and the correlation function (CF) describing fluctuations of the dipoles, respectively. The average displacement is calculated using the average absolute values.

referred to as the low-frequency dielectric response of the system [13].

The corresponding results are illustrated in Figs. 2(c) and 2(d). Here, we averaged the three diagonal components of the susceptibility tensor. In the case of BZT05, we observe good agreement between the two methods for determining susceptibility. The plot shows three peaks that can be assigned to the phase transitions of the parent system. It can already be seen that the individual transitions get closer to one other and lead to a possible diffuse transition between the paraelectric and ferroelectric phases. Furthermore, a Curie-Weiss (CW) behavior is found above $T_c$ for both curves. For BZT50, a broad peak in $\chi^{\mathrm{CF}}$ with a $T_m$ of 180 K is observed, which is in good agreement with experimental data [35,36]. The static susceptibility shows a steady increase with decreasing temperature, with a tendency to flatten as low temperatures are approached. This behavior is consistent with experimentally measured patterns [37] in relaxor ferroelectrics. Furthermore, the results of BZT50 are in qualitatively good agreement with the simulations of Akbarzadeh *et al.* [13]. Nonetheless, we observe that the behavior of the static susceptibility in the low temperature region differs both in terms of shape, as well as in the absolute value as compared to Akbarzadeh *et al.* [13], if we apply moderate field strengths up to 50 kV/cm. Since the shape obtained in our work is more consistent with the experiment [37], we ascribe this difference to a more suitable choice of the applied external field strength. Hence, a comparison of the static susceptibility at the lowest temperature to Akbarzadeh is not necessary. Akbarzadeh *et al.* [13] provided an interesting analysis in the medium and high temperature regions. They reported that at temperatures above the Burns temperature $T_b$, both approaches (direct and CF) obey the

159

CW law, which we also observe (see more details in the Supplemental Material [27]). In our case, the fit of the CW law yields a $T_0$ of 140 K which is in reasonable agreement with an experimental value [35] of 114 K. They further reported that in the region below $T_b$ down to $\sim$ 240 K the direct approach still follows the CW law, while CF starts to deviate. Finally, according to Ref. [13], both methods exhibit deviations from the CW law below 240 K. We can only partially confirm this peculiar behavior in the regions below $T_b$ – in our case, a slight deviation between both methods is observed for this temperature range, but both methods start to deviate from the CW law for temperatures below $\sim$340 K. Unfortunately, it is not possible to trace down the origin of the discrepancy, however, we suspect it might be related to the parametrization of the model itself or the choice of the applied external field strength, which is consistent with the odd behavior of static susceptibility in the low temperature region.

To quantify the contribution to polarization by the different unit cells, the shifts of the B-site cations was calculated with respect to the center of mass of the oxygen octahedra. The basis for these calculations is MD simulations with the same settings described in detail in the previous section. The properties discussed further have been averaged over 600 ps. The relative displacement of the B-site cations can be seen in Figs. 2(e) and 2(f). In BZT05, it is clear that Ti atoms determine most of the polarization in BZT, while Zr atoms show only a slight off-centering. In our simulation of BZT25 (25% Zr content), at low temperatures, Ti ions are found to have an average displacement of 0.16 Å and Zr ions of 0.04 Å. That is in excellent agreement with values from a DFT study of $BaTi_{0.74}Zr_{0.26}O_3$ [38], which predicts a shift of 0.17 Å for Ti ions and 0.03 Å for Zr ions. In the case of BZT50, a slight off-centering of the B-site cations is observed throughout all simulated temperatures, increasing with decreasing temperature. In contrast to the work of Akbarzadeh *et al.* [13] we observe this increase not only for Ti but also for Zr ions. Although macroscopically there is no polarization of the system, the B-site ions shift to an energetically preferred position outside the center of the unit cell [28,38,39]. The increased off-centering at higher temperatures compared to BZT05 can be attributed to the expansion of the lattice, leading to increased activity of the local modes.

### 3. Hysteresis loops

Here, we present simulated hysteresis loops of BZT05 (5% Zr), BZT15 (15% Zr), BZT20 (20% Zr), and BZT30 (30% Zr). For that purpose, a simulation box size of $30 \times 30 \times 30$ was chosen. The frequency of the oscillating field was set to 1 GHz, whereby the maximum field strength was 100 kV/cm, always applied along the $\langle 111 \rangle$ direction. For each composition and temperature several cycles were recorded. Figure 3 shows the hysteresis loops computed at the temperatures of 250, 300, and 350 K. In this figure, the net polarization is plotted. For BZT05, a classic ferroelectric behavior is observed at room temperature. Lowering the temperature leads to an increase in the saturated polarization and an increase in the remanent polarization. Increasing the temperature reduces the remanent polarization and the saturation
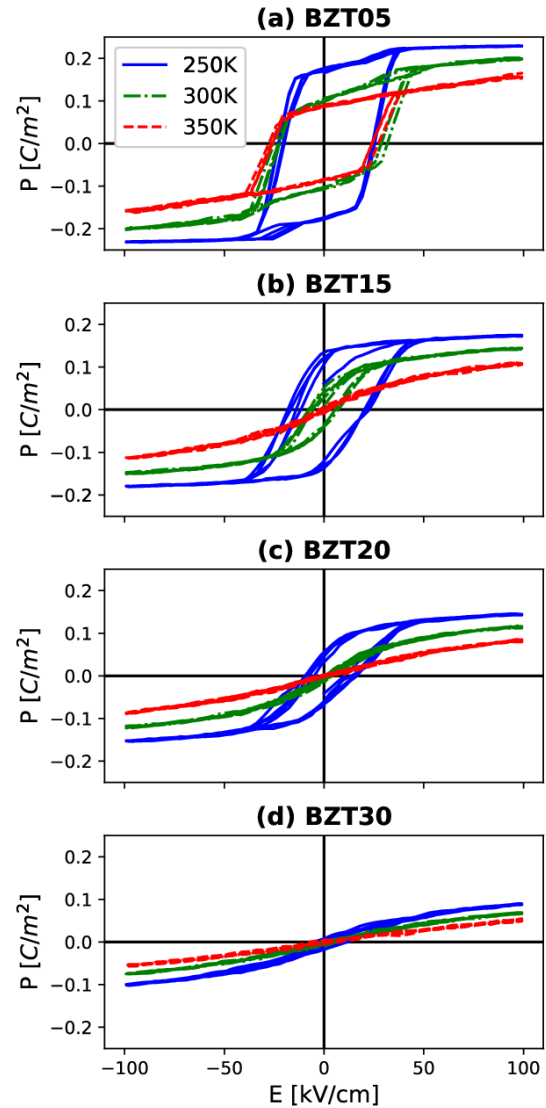


FIG. 3. Hysteresis loops of BZT05 (5% Zr), BZT15 (15% Zr), BZT20 (20% Zr) and BZT30 (30% Zr) at temperatures of 250, 300, and 350 K obtained from MD simulations.

polarization. In the case of BZT15, slightly above $T_c$ a nonlinear trend of the hysteresis loop with zero remanent polarization is observed, which changes to a linear behavior when the temperature is increased further. We observe lower saturation polarization for a higher Zr content at the given temperature. Furthermore, hysteresis progressively dwindles and disappears entirely in the case of BZT30, leading to a linear dielectric behavior, as is expected by the increasing suppression of long-range ferroelectric order in BT by adding Zr. A comparison with experimental loops [40,41] from the literature shows that our simulated loops reproduce the general behavior of the BZT system, with absolute values of the saturation polarization in good agreement with the measured values. However, the associated field strengths are slightly overestimated in the simulated curves. This might be due to

160

the fact that the simulation assumes a perfect system where neither leakage currents nor other defects can occur.

Interestingly, the individual components of polarization (not shown) reveal that for concentrations between 10% and 20% of Zr, each of the three ferroelectric phases can be stabilized by applying external fields in certain directions. Indeed, it confirms that the three phases near the tricritical point are energetically very close to each other. This phenomenon has already been shown and discussed in detail by Mentzer *et al.* [14].

### B. Simulations for BNT

#### 1. Phase diagram

First, we use our parameterization for BNT to simulate the phase diagram. The settings of the MD simulations required for this are analogous to the phase diagram of BZT. Due to lack of experimental evidence on the distribution of Nb and $V_{Ti}$ in BNT, we considered a spectrum of possible distributions and chose the one leading to the best match to experimental phase diagram. The choice of the final configuration was also motivated by previous DFT calculations of $5 \times 5 \times 5$ supercells performed applying complete structural relaxation, which indicated that (i) Nb cations tend to cluster randomly around Ti vacancies (four Nb atoms for one Ti vacancy) and that (ii) dissociated clusters (i.e., where Nb atoms are at least one nearest neighbor away from the Ti vacancy) are energetically slightly favorable [16]. For more details we refer readers to the Supplemental Material [27]. The results in Fig. 4(a) were obtained for a randomly distributed arrangement of Nb ions and Ti vacancies, which corresponds to the aforementioned dissociated clusters. Compared to BZT, a faster decrease in the transition temperature between the paraelectric and ferroelectric phases is observed here. Furthermore, the transition between the tetragonal and orthorhombic phases is flatter and almost constant up to the tricritical point. On the other hand, the transition between the orthorhombic and rhombohedral phases increases slightly. The tricritical point is found between 7.5% and 10% Nb content.

For comparison with experimental data, values from the literature as determined from dielectric measurements [42] are listed in Fig. 4(b). However, since these results do not show transition temperatures for all three phases, we also performed Raman measurements on BNT samples. These samples were prepared via the solid-state route and analyzed using a commercial Raman spectrometer. Details of both sample preparation and experimental parameters are reported elsewhere [43]. Raman spectra were collected as a function of temperature from $-196\,^{\circ}\text{C}$ to $300\,^{\circ}\text{C}$ using $25\,^{\circ}\text{C}$ intervals. The phase diagram in Fig. 4(b) represents the resulting data. Compared to values from Ref. [42], a slightly higher transition temperature is observed for lower concentrations. However, a good agreement between the two experimental data is observed for higher concentrations. Comparison of the experimental data with the simulation data shows that the simulated transition temperatures agree very well for concentrations <10%. For higher concentrations (≥15%), the simulation slightly overestimates the experimental data. This can again be attributed to the applied pressure correction, which appears to be overestimated for higher concentrations.
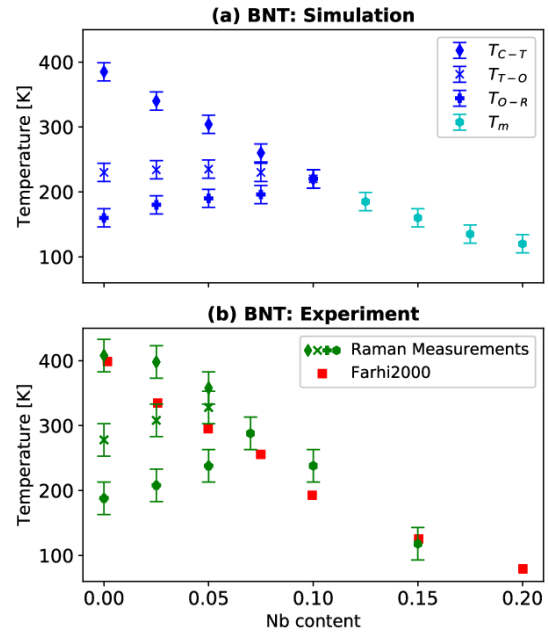


FIG. 4. Phase diagram of BNT as a function of concentration and temperature. (a) shows the simulated data. (b) experimental data obtained by Raman measurements (green symbols) and from dielectric measurements presented in literature [42] (red symbols). $T_{C-T}$, $T_{T-O}$, $T_{O-R}$ transitions between cubic (C), tetragonal (T), orthorhombic (O), and rhombohedral (R) phases, respectively. $T_m$ temperature of maximum in dielectric permittivity.

Overall, the simulation reproduces the phase diagram quite well.

#### 2. Dielectric and structural properties

To further test the parametrization, dielectric properties and structural properties were calculated using MD on $30 \times 30 \times 30$ supercells for BNT05 and BNT15 (5% and 15% Nb content, respectively). Only lattice parameters for BNT15 were calculated using a larger ($96 \times 96 \times 96$) supercell size, as early tests showed that smaller supercell sizes (e.g. $30 \times 30 \times 30$) might lead to difficulties in the determination of lattice type in BNT15 due to the presence of local distortions. Large supercell sizes, in fact, statistically average local distortions and yield a cubic structure for temperatures between 20 and 800 K (for BNT15). That agrees well with experimental data [44] for Nb-substituted systems above a concentration of 12.5% Nb. For BNT05, a cubic phase is found at temperatures above 300 K. Furthermore, this system undergoes three phase transitions analogous to the parent system [see Fig. 5(a)]. The ground state at very low temperatures is a rhombohedral structure. The calculation of the static $\chi^{\text{direct}}$ as well as low-frequency susceptibility $\chi^{\text{CF}}$ is plotted in Figs. 5(c) and 5(d). For the calculation of the static susceptibility, an external field with a maximum amplitude of 50 kV/cm was applied in the $\langle 111 \rangle$ direction. Similar behavior can be seen for BNT05 as for BZT05. However, the transition temperatures are significantly lower than those of BZT05. For BNT15, $\chi^{\text{direct}}$ shows
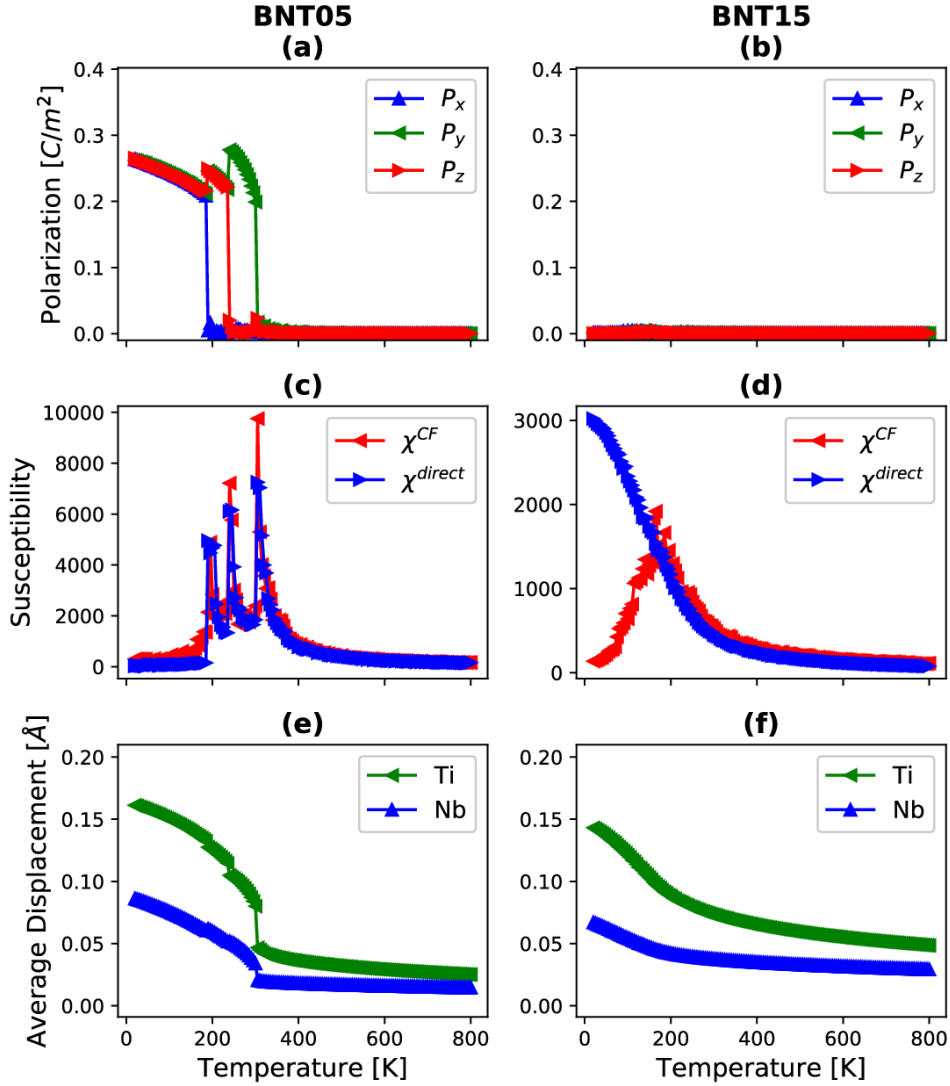
FIG. 5. Comparison of dielectric properties for BNT05 (5% Nb) and BNT15 (15% Nb). (a) and (b) show the polarization of the system. (c) and (d) show the susceptibility obtained from the direct method and the correlation function (CF) describing fluctuations of the dipoles, respectively. (e) and (f) show the average displacement of the individual B-site cations calculated using the average absolute values.

a typical relaxor behavior [37]. The corresponding $\chi^{CF}$ shows a broad peak with a $T_m$ of 175 K. Such behavior was found earlier in BZT50 and suggests that in BNT the onset for relaxor behavior happens at less than 15% of Nb, as also confirmed experimentally [16,42]. Furthermore, a CW behavior for higher temperatures is observed for both systems above $T_c$ and $T_m$, respectively.

Next, we focus on the averaged displacements of the B-site cations in BNT. The calculation of these displacements was carried out as described for BZT. Figures 5(e) and 5(f) show the shift for Ti and Nb ions in BNT05 and BNT15. Compared to BZT, Nb ions experience a significantly larger displacement than Zr ions. This local cation off-centering has already been confirmed by experiments [44]. It should be mentioned that a spontaneous polarization below 300 K is observed for BNT05

whereas BNT15 shows a nonpolar behavior [see Figs. 5(a) and 5(b), respectively). However, an averaged nonzero displacement is found in BNT15 at all temperatures simulated. That can be attributed to the lattice expansion through the applied pressure correction, similar to BZT50 and discussed in detail in Sec. III A 2. Furthermore, the fact that Nb shows a relatively large displacement also suggests that unit cells containing Nb at the B site may contribute substantially to the polarization. Hence, Nb unit cells may be considered only as a weak disruptor of the long-range ferroelectric correlation. In BNT, however, we need to consider also the presence of Ti vacancies, which indeed seem to affect the polar order in BNT significantly. Ti vacancies were considered as polar inactive in our parametrization, since DFT calculations found no significant contribution originating from the local mode,
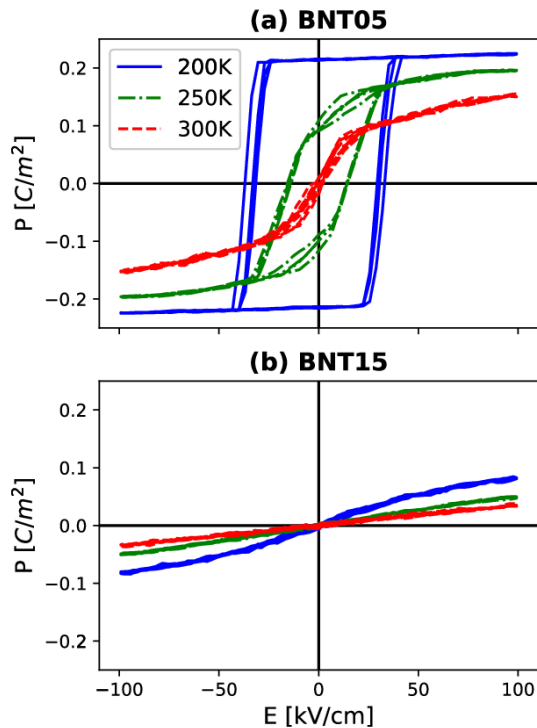
FIG. 6. Hysteresis loops of (a) BNT05 (5% Nb) and (b) BNT15 (15% Nb) at temperatures of 200, 250, and 300 K obtained from MD simulations.

i.e. nonpolar oxygen oscillation. However, these vacancies are considerably coupled to the surrounding unit cells, as described by the auxiliary spring system. That results in a constellation of $V_{Ti}$ unit cells surrounded by unit cells with polarization biased in specific directions. These ensembles of unit cells can act as pinning centers for the surrounding ferroelectric matrix and thus can be considered as potential disruptors of the long-range ferroelectric order. In fact, increasing Nb concentration will increase the concentration of ferroelectrically inactive nanodomains centered on Ti vacancies, leading to overall disruption of the long-range correlation of B-site displacements.

In summary, the interplay between Ti vacancies and Nb unit cells as well as Ti unit cells appears to be responsible for the more effective disruption of long-range correlation within BNT compared to BZT.

### 3. Hysteresis loops

Finally, we consider hysteresis loops for BNT. Again, unit cells of size $30 \times 30 \times 30$ were used. The settings for the MD simulations are analogous to those of BZT. Figures 6(a) and 6(b) show the simulated hysteresis curves for BNT05 and BNT15 at different temperatures. For BNT05, a temperature of 200 K results in a saturated ferroelectric loop. When the temperature is increased, the remanent and the saturation polarization are reduced. A temperature close to the transition temperature (300 K) gives a nonlinear trend without showing a ferroelectric behavior anymore. Analogously to BZT, the

application of an external field can also stabilize the ferroelectric phases of the parent system in the case of BNT. This indicates that also for the case of BNT the different phases close to the tricritical point are energetically very close to one other. For BNT15, a linear dielectric response is observed for temperatures above 250 K. At 200 K the loop shows a nonlinear behavior but without remanent polarization. Furthermore, in BNT15, no ferroelectric behavior can be induced by applying an external field.

## IV. CONCLUSION

In this work, we carried out a parameterization of effective Hamiltonian models to describe the potential energy surface of BT-based substituted systems, which allowed the calculation of structural and electrical properties of the considered materials. The theoretical framework was based on the extension of our effective Hamiltonian approach for BT, considering substituting cations as perturbations of the parent system. First, we parametrized the homovalently substituted BZT system and presented a benchmark comparison with theoretical and experimental results from literature. Our model demonstrated good agreement with previous results on phase transitions, susceptibilities, and atomic displacement patterns. Only a slight overestimation of transition temperatures was found for high substituent contents, which was ascribed to the applied pressure correction and the Zr cation distribution. Following, the model was applied to the parametrization of the heterovalently substituted BNT system. The simulated phase diagram of BNT is in good agreement with our Raman measurements and experimental data from the literature. Furthermore, simulations have shown the onset of relaxor behavior at concentrations of about 15%, in good agreement to experiments. The associated structure remains macroscopically cubic and nonpolar for BNT15, and the dielectric behavior is in accord with experimental data for all simulated BNT compositions.

In summary, two parameter sets were presented which can be used for further studies on the investigated BZT and BNT systems, and can be adapted to represent other BT-based solid solutions. Since this approach requires only a small amount of computational effort, even very large supercells can be simulated in the future, leading to a realistic description and prediction of structural and electrical properties in BT solid solutions. The large-scale implementation of such simulations could become a decisive step towards the design of compositions with unprecedented properties.

[1] V. V. Shvartsman and D. C. Lupascu, J. Am. Ceram. Soc. **95**, 1 (2012).

[2] L. E. Cross, Ferroelectrics **151**, 305 (1994).

[3] V. Veerapandiyan, F. Benes, T. Gindel, and M. Deluca, Materials (Basel) **13**, 5742 (2020).

[4] R. D. King-Smith and D. Vanderbilt, Phys. Rev. B **49**, 5828 (1994).

[5] W. Zhong, D. Vanderbilt, and K. M. Rabe, Phys. Rev. B **52**, 6301 (1995).

[6] U. V. Waghmare and K. M. Rabe, Phys. Rev. B **55**, 6161 (1997).

[7] T. Nishimatsu, M. Iwamoto, Y. Kawazoe, and U. V. Waghmare, Phys. Rev. B **82**, 134106 (2010).

[8] A. Paul, J. Sun, J. P. Perdew, and U. V. Waghmare, Phys. Rev. B **95**, 054111 (2017).

[9] F. Mayer, M. N. Popov, D. M. Evans, S. Krohns, M. Deluca, and J. Spitaler, Phys. Rev. B **106**, 064108 (2022).

[10] L. Bellaiche, A. García, and D. Vanderbilt, Phys. Rev. Lett. **84**, 5427 (2000).

[11] L. Bellaiche and D. Vanderbilt, Phys. Rev. B **61**, 7877 (2000).

[12] L. Bellaiche, A. García, and D. Vanderbilt, Ferroelectrics **266**, 41 (2002).

[13] A. R. Akbarzadeh, S. Prosandeev, E. J. Walter, A. Al-Barakaty, and L. Bellaiche, Phys. Rev. Lett. **108**, 257601 (2012).

[14] C. Mentzer, S. Lisenkov, Z. G. Fthenakis, and I. Ponomareva, Phys. Rev. B **99**, 064111 (2019).

[15] T. Nishimatsu, A. Grünebohm, U. V. Waghmare, and M. Kubo, J. Phys. Soc. Jpn. **85**, 114714 (2016).

[16] V. Veerapandiyan, M. N. Popov, F. Mayer, J. Spitaler, S. Svirskas, V. Kalendra, J. Lins, G. Canu, M. T. Buscaglia, M. Pasciak, J. Banys, P. B. Groszewicz, V. Buscaglia, J. Hlinka, and M. Deluca, Adv. Electron. Mater. **8**, 2100812 (2022).

[17] T. Nishimatsu, U. V. Waghmare, Y. Kawazoe, and D. Vanderbilt, Phys. Rev. B **78**, 104104 (2008).

[18] K. M. Rabe and U. V. Waghmare, Phys. Rev. B **52**, 13236 (1995).

[19] J. H. Lee, U. V. Waghmare, and J. Yu, J. Appl. Phys. **103**, 124106 (2008).

[20] J. Paul, T. Nishimatsu, Y. Kawazoe, and U. V. Waghmare, Phys. Rev. Lett. **99**, 077601 (2007).

[21] P. E. Blöchl, Phys. Rev. B **50**, 17953 (1994).

[22] G. Kresse and J. Hafner, Phys. Rev. B **49**, 14251 (1994).

[23] G. Kresse and J. Furthmüller, Comput. Mater. Sci. **6**, 15 (1996).

[24] G. Kresse and J. Furthmüller, Phys. Rev. B **54**, 11169 (1996).

[25] G. Kresse and D. Joubert, Phys. Rev. B **59**, 1758 (1999).

[26] G. I. Csonka, J. P. Perdew, A. Ruzsinszky, P. H. T. Philipsen, S. Lebègue, J. Paier, O. A. Vydrov, and J. G. Ángyán, Phys. Rev. B **79**, 155107 (2009).

[27] See Supplemental Material at http://link.aps.org/supplemental/10.1103/PhysRevB.106.224109 for tables of parameters, additional MD simulations, and analysis of susceptibilities.

[28] I. Levin, E. Cockayne, V. Krayzman, J. C. Woicik, S. Lee, and C. A. Randall, Phys. Rev. B **83**, 094122 (2011).

[29] J. Kreisel, P. Bouvier, M. Maglione, B. Dkhil, and A. Simon, Phys. Rev. B **69**, 092104 (2004).

[30] A. A. Bokov, M. Maglione, and Z.-G. Ye, J. Phys.: Condens. Matter **19**, 092001 (2007).

[31] C. Laulhé, F. Hippert, J. Kreisel, M. Maglione, A. Simon, J. L. Hazemann, and V. Nassif, Phys. Rev. B **74**, 014106 (2006).

[32] Andrei Ruban (private communication, 27 January 2022).

[33] L. Dong, D. S. Stone, and R. S. Lakes, J. Appl. Phys. **111**, 084107 (2012).

[34] H. H. Wieder, Phys. Rev. **99**, 1161 (1955).

[35] T. Maiti, R. Guo, and A. S. Bhalla, J. Am. Ceram. Soc. **91**, 1769 (2008).

[36] J. Petzelt, V. Bovtun, D. Nuzhnyy, M. Kempa, M. Savinov, M. Paściak, S. Kamba, G. Canu, and V. Buscaglia, Phys. Status Solidi B **258**, 2100259 (2021).

[37] A. Levstik, Z. Kutnjak, C. Filipič, and R. Pirc, Phys. Rev. B **57**, 11204 (1998).

[38] C. Laulhé, A. Pasturel, F. Hippert, and J. Kreisel, Phys. Rev. B **82**, 132102 (2010).

[39] A. Bootchanont, J. Jutimoosik, S. Chandarak, M. Unruan, S. Rujirawat, R. Yimnirun, R. Guo, and A. Bhalla, Ceram. Int. **39**, 579 (2013).

[40] Z. Yu, R. Guo, and A. S. Bhalla, J. Appl. Phys. **88**, 410 (2000).

[41] Q. Xu and Z. Li, Process. Appl. Ceram. **14**, 188 (2020).

[42] R. Farhi, M. El Marssi, A. Simon, and J. Ravez, Eur. Phys. J. B **18**, 605 (2000).

[43] V. K. Veerapandiyan, S. Khosravi H, G. Canu, A. Feteira, V. Buscaglia, K. Reichmann, and M. Deluca, J. Eur. Ceram. Soc. **40**, 4684 (2020).

[44] K. Page, T. Kolodiazhnyi, T. Proffen, A. K. Cheetham, and R. Seshadri, Phys. Rev. Lett. **101**, 205502 (2008).

164

# Supplemental Material

Finite-temperature investigation of homovalent and heterovalent substituted BaTiO$_3$ from first principles

Florian Mayer[1,*], Maxim N. Popov[1], Petr Ondrejkovic[2], Jiri Hlinka[2], Jürgen Spitaler[1], Marco Deluca[1]

[1]Materials Center Leoben Forschung GmbH, Roseggerstrasse 12, 8700 Leoben, Austria
[2]Institute of Physics of the Czech Academy of Sciences, 182 00, Praha 8, Czech Republic

*e-mail: florian.mayer@mcl.at

## I.  EXTENSION PARAMETERS FOR EFFECTIVE HAMILTONIAN

In this chapter the parameters obtained via DFT calculations of the extended Hamiltonian are listed. In our case, all calculations were performed using the XC-functional (exchange-correlation functional) PBEsol [1] and the DFT package VASP [2–5]. The following settings were used in our calculations: Projector-augmented wave potentials [6] with valence electronic configurations of $5s^2\,5p^6\,6s^2$ for Ba (10 valence electrons), $3s^2\,3p^6\,4s^2\,3d^2$ for Ti (12 valence electrons), $4s^2\,4p^6\,5s^2\,4d^2$ for Zr (12 valence electrons), $4s^2\,4p^6\,5s^2\,4d^3$ for Nb (13 valence electrons), and $2s^2\,2p^4$ for O (6 valence electrons) were used. Table SI lists the values for the corrections to the effective mass, the local self-energy, and the correction for the long-range interaction. Table SII shows the parameters for the auxiliary spring system for BZT. Analogously, the values for BNT are listed in Table SIII. A comparison of the obtained parameters for the auxiliary spring system with values from the literature is not appropriate, since our values refer to the parent system BT and not to the average structure calculated by virtual crystal approximation (VCA). The calculation of the correction parameters will also be discussed in more detail here. The basis is a supercell of size 3x3x3 with the structure of pure BT. From this supercell, structures containing the various substituents were constructed. In principle, one could already calculate the parameters $Q_{T,R}(\sigma_T)$, which are related to the occurring forces, by DFT calculations of these structures. However, in order to obtain a larger data set for the estimation of the parameters the following approach was chosen. The displacement pattern of the soft mode of pure BT was used to locally displace unit cells within the substituted supercells. That is, each of the 27 unit cells in the supercell can be displaced in different directions to calculate the resulting forces and the total energy using DFT calculations. For symmetry reasons, not each of the 27 cells had to be displaced, but only one in each of the three next nearest neighbor shells. The parameters were determined using the total energy from the DFT data by

1

fitting a linear function. In order to make sure that doping represented by a (small) supercell does not lead to artifacts in terms of electronic properties (e.g. metallic character), we analyzed the electronic density of states (DOS) for a 3x3x3 supercell with one Ti vacancy and 4 Nb ions. It exhibited a band gap of 1.924 eV (compared to 2.174 eV in pure rhombohedral BT), i.e. doping had only minor impact on the DOS and no spurious metallic character was introduced.

The calculation of the correction parameters $S_{T,R}(\sigma_T)$ for the acoustic displacement variables was done by using a similar procedure. However, a A-centered basis was chosen and a different eigenvector was used. That means, a pure translation was applied to the local unit cells containing the substituted ions and DFT was used to calculate the corresponding total energies. Here, also the lattice constant was adapted to get the correction parameters in accordance with the lattice change already captured by the applied pressure correction. From that, it was possible to estimate the parameters $S_{T,R}(\sigma_T)$ by fitting a linear function. Furthermore, after investigating the obtained parameters, we decided to use interactions up the first nearest neighbor shell. The corresponding parameters for BZT and BNT are listed in Table SIV.

*Table SI. Correction parameters for unit cells containing either Zr (BZT) or Nb (BNT). The parameters for pure BT from the literature are also given. It should be noted that the values listed for BZT and BNT are absolute values and do not represent the difference to the BT system.*

|  | **BT (Ref. [7] )** | **BZT** | **BNT** |
|---|---|---|---|
| $m^*$ [amu] | 38.148 | 64.148 | 65.157 |
| $m^*_{acou}$ [amu] | 46.638 | 55.309 | 55.646 |
| $\kappa_2$ [eV/Å$^2$] | 8.007 | 17.390 | 15.080 |
| $\alpha$ [eV/Å$^4$] | 123.492 | 150.107 | 210.682 |
| $\gamma$ [eV/Å$^4$] | -165.344 | -282.685 | -311.402 |
| $k_1$ [eV/Å$^6$] | -1443.850 | -250.913 | -1286.742 |
| $k_2$ [eV/Å$^6$] | 123.688 | -196.287 | 1165.514 |
| $k_3$ [eV/Å$^6$] | 307.317 | -95.201 | 2897.463 |
| $k_4$ [eV/Å$^8$] | 17216.816 | 2369.902 | 8791.560 |
| $Z^*$ [e] | 10.267 | 8.816 | 12.253 |

*Table SII. Parameters of the auxiliary spring system for BZT. 1NN, 2NN and 3NN represent the nearest neighbor shells.*

| **Parameter** | **Value [eV/Å]** |
|---|---|
| $Q_{1NN,R}(Ti-Zr)$ | -0.791 |
| $Q_{2NN,R}(Ti-Zr)$ | - 0.026 |
| $Q_{3NN,R}(Ti-Zr)$ | -0.017 |
| $Q_{1NN,R}(Zr-Zr)$ | -0.821 |

2

166

*Table SIII. Parameters of the auxiliary spring system for BNT. 1NN, 2NN and 3NN represent the nearest neighbor shells.*

| Parameter | Value [eV/Å] |
|---|---|
| $Q_{1NN,R}(Ti - Nb)$ | -1.020 |
| $Q_{2NN,R}(Ti - Nb)$ | -0.074 |
| $Q_{3NN,R}(Ti - Nb)$ | -0.033 |
| $Q_{1NN,R}(Ti - V_{Ti})$ | 1.778 |
| $Q_{2NN,R}(Ti - V_{Ti})$ | 0.213 |
| $Q_{3NN,R}(Ti - V_{Ti})$ | 0.026 |
| $Q_{1NN,R}(Nb - V_{Ti})$ | 3.008 |
| $Q_{2NN,R}(Nb - V_{Ti})$ | 0.257 |
| $Q_{3NN,R}(Nb - V_{Ti})$ | -0.064 |
| $Q_{1NN,R}(Nb - Nb)$ | -0.875 |

*Table SIV. Parameters for the auxiliary spring system for BZT and BNT listing the correction parameters for the acoustic displacement variables.*

| Parameter | Value [eV/Å] |
|---|---|
| $S_{1NN,R}(Zr)$ | 0.364 |
| $S_{1NN,R}(Nb)$ | 0.118 |
| $S_{1NN,R}(V_{Ti})$ | -0.161 |

# II.  PRESSURE CORRECTION

In this section we want to address the calculation of a so-called pressure correction. The idea behind this is the inclusion of lattice expansion or contraction induced by the introduction of impurity atoms. On the one hand, these effects could be accounted for directly using a term as in Equation 5 in the main paper. The adapted term provides corrections in terms of forces acting on the local variable $w$. Thus, the deformation of the unit cell can be influenced locally. In our work we constructed such a term with the corresponding parameters. However, we found that this term gives wrong results at higher concentrations of impurity atoms. The reason for this is the mutual cancellation of forces when two impurity atoms are positioned in close proximity to each other. Furthermore, deviations of the local deformation compared to DFT reference values were also observed. Nevertheless, we believe that such an adaptation of the local variables $w$ is feasible and are currently working on a refinement of it. However, the results on this will be addressed in a later publication. In this work, we decided to consider the lattice effects in a different way. That is, we apply a pressure correction to our system that corresponds to the deviation of pure barium titanate (BT). To do this, we first calculate the pressure dependence of the lattice constant of pure BT using DFT. The settings for the pressure dependent DFT relaxations are a k-grid of 8x8x8 and an energy cutoff of 620 eV. To obtain the pressure dependence as illustrated in Figure S1, an external pressure via the Tag PSTRESS was applied in VASP. It can be seen that the lattice constant behaves slightly nonlinearly under pressure. However, since we want to provide as simple a formula as possible for our pressure correction, a linear change is assumed in the remainder of this section. Next, the dependence of the lattice parameter on the concentration of Zr and Nb was

3

calculated. For Zr, a supercell of 2x2x2 was constructed from pure BT. Subsequently, starting with one Zr ion, the supercell was substituted and relaxed using DFT. This process was repeated with increasing number of Zr until the complete range of possible concentrations was covered. This subsequently allows a pseudo-cubic lattice constant to be determined. The result can be seen in Figure S2. Here we see a strongly linear behavior of the lattice constant as a function of concentration. Using Figures S1 and S2, a linear pressure correction for BZT could be calculated. This amounts to $-19.5 \cdot x$ GPa, where x represents the concentration of Zr ions. For the case of BNT, the calculation of the pressure correction turned out to be somewhat more complicated. First, the correct oxidation state must be ensured for $Nb^{5+}$ in the DFT calculation. This can be done by adjusting the number of electrons. However, DFT relaxations with adjusting the number of electrons have to be done with caution. Alternatively, the charge compensation can also be ensured by introducing Ti vacancies. That is, for 4 Nb ions, one Ti vacancy must be introduced into the system. In our case, we decided to use the second method and constructed supercells of size 2x2x2 and 3x3x3. For the 2x2x2 supercell, four Nb ions and one vacancy were introduced, corresponding to a concentration of 50% Nb. For the supercells of size 3x3x3, four Nb's and one vacancy were substituted one time and eight Nb's and two vacancies were substituted one time, corresponding to a concentration of 14.8% and 29.6%, respectively. Then, all supercells were relaxed by DFT and a pseudo cubic lattice constant was determined. The result can be seen in Figure S3. In this case, also a roughly linear behavior is observed. Next, Figures S1 and S3 were used to determine the pressure correction for BNT. This amounts to $-8 \cdot x$ GPa, where x denotes the concentration of Nb ions in the system.
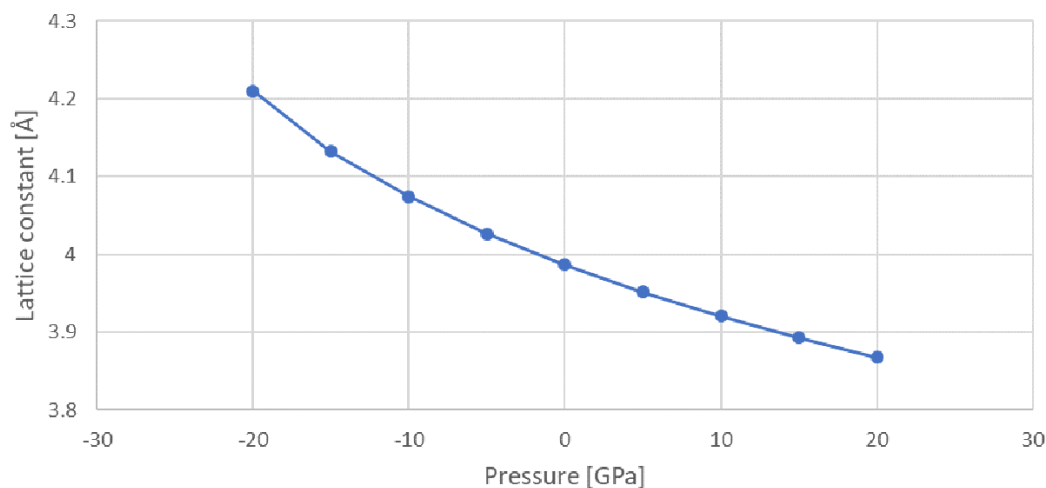


*Figure S1. Lattice constant of pure BT as a function of external pressure obtained from DFT relaxations.*
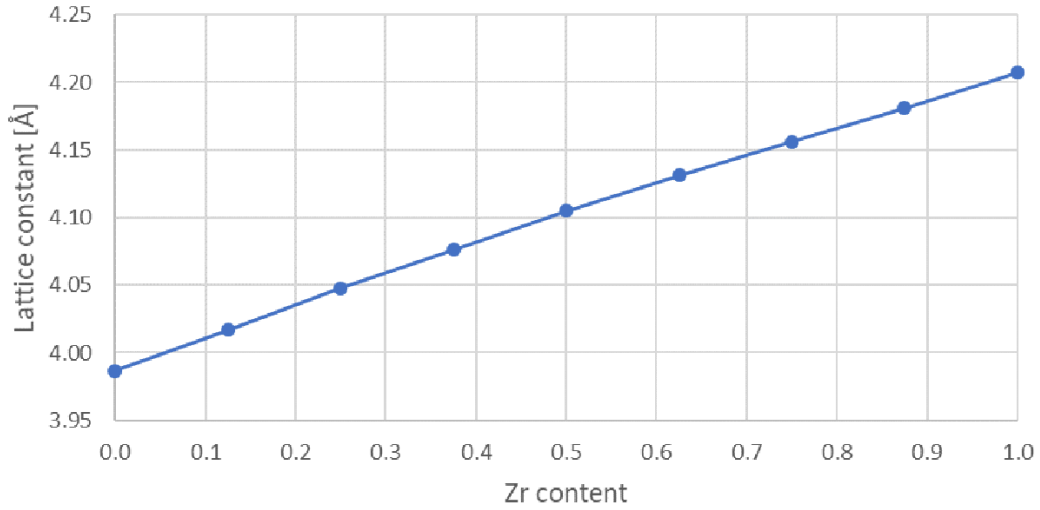
*Figure S2. Pseudo cubic lattice constant of BZT as a function of concentration obtained from DFT relaxations using 2x2x2 supercells and substituting different amounts of Zr ions.*
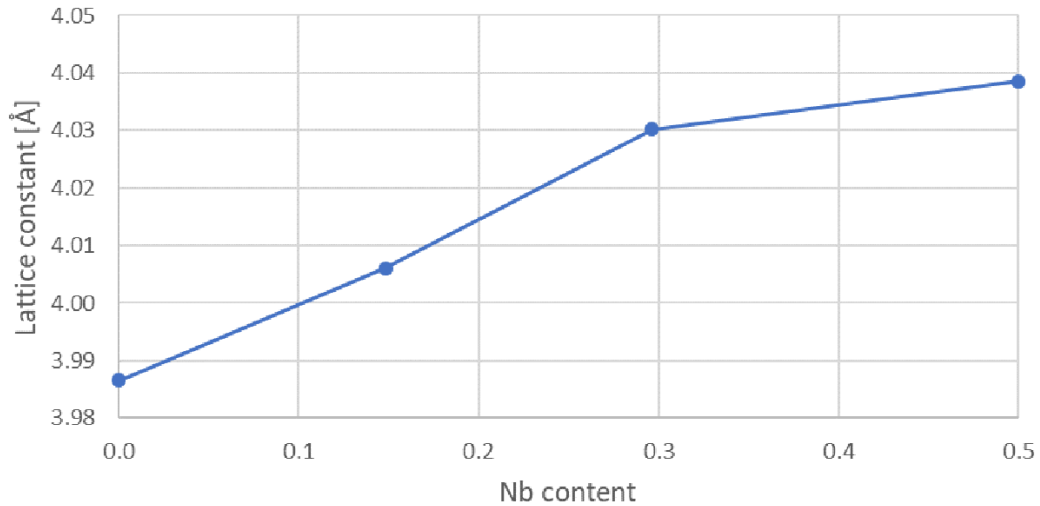


*Figure S3. Pseudo cubic lattice constant of BNT as a function of concentration obtained from DFT relaxations using 2x2x2 and 3x3x3 supercells with different amounts of Nb. Charge compensation was applied via including the right amount of Ti vacancies.*

# III.   PHASE DIAGRAM OF BNT USING DIFFERENT DISTRIBUTIONS OF SUBSTITUENTS

Here we want to discuss the influence of the distribution of Nb ions on the simulated phase diagram. For this purpose, two different approaches were chosen to distribute the Nb ions, which are based on the results of previous calculations we performed [8]. The first approach is a clustering of four Nb ions surrounding a Ti vacancy. These clusters are randomly distributed in the supercell. The second approach is a completely random distribution of Nb ions and Ti vacancies (dissociated clusters). Figure S4 shows the corresponding phase diagrams. The settings of the MD simulations can be found in the main paper.

5

It is clear that both phase diagrams are quite different from each other. The associated clustering shows significantly higher transition temperatures which can be explained by the following argument. If one places the Nb ions close to the Ti vacancies, they screen the quite strong interaction with neighboring unit cells emanating from the Ti vacancies. This in turn leads to an increased transition temperature since the long-range correlation is not as strongly suppressed. In the case of the completely randomly distributed arrangement, which corresponds to dissociated clusters, the interactions have a much stronger effect and, at the same concentration, interrupt the long-range correlation more strongly. As seen, the dissociated arrangement gives a better agreement with experiment. Moreover, preliminary DFT calculations of 5x5x5 supercells, applying complete structural relaxation, also indicated that dissociated clusters are energetically slightly favorable [8]. Thus, a random distribution is assumed for all simulations in the main paper.
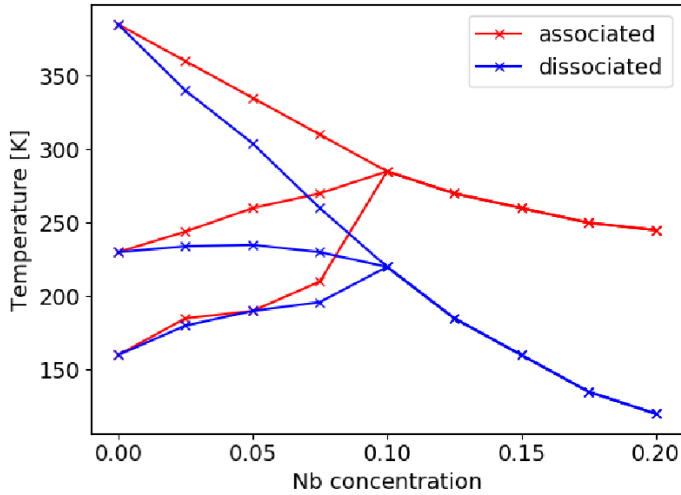


*Figure S4. Comparison of the phase diagram of BNT using different distributions of Nb ions. Associated are defect clusters consisting of four Nb's and one Ti vacancy which are randomly distributed. Dissociated are completely randomly distributed defects.*

# IV.   POLAR ORDER OF BZT50

In this section, we deal with the local polar order of BZT50. To simulate a meaningful structure, and for consistency with the BNT simulations, we decided to increase the system size to 96x96x96. The distribution of the 50% Zr ions was done using a script that randomly distributes the Zr ions. The structure was then simulated using the effective Hamiltonian model we developed. The setting for this can be found in the main paper. To study the polar order, we decided to run the simulation at 20 K and average the relevant quantities over 80 ps. A slice through the supercell can be seen in Figure S5, where the arrows describe the local dipole moments. It is clear that the polar order of BZT50 is mostly uncorrelated. Only sporadically can smaller correlated regions be perceived, which is due to an accumulation of Ti unit cells. It is also clear here that Ti unit cells have a much larger off-centering compared to Zr-based unit cells. This is consistent with the results presented in the main paper.

6

170
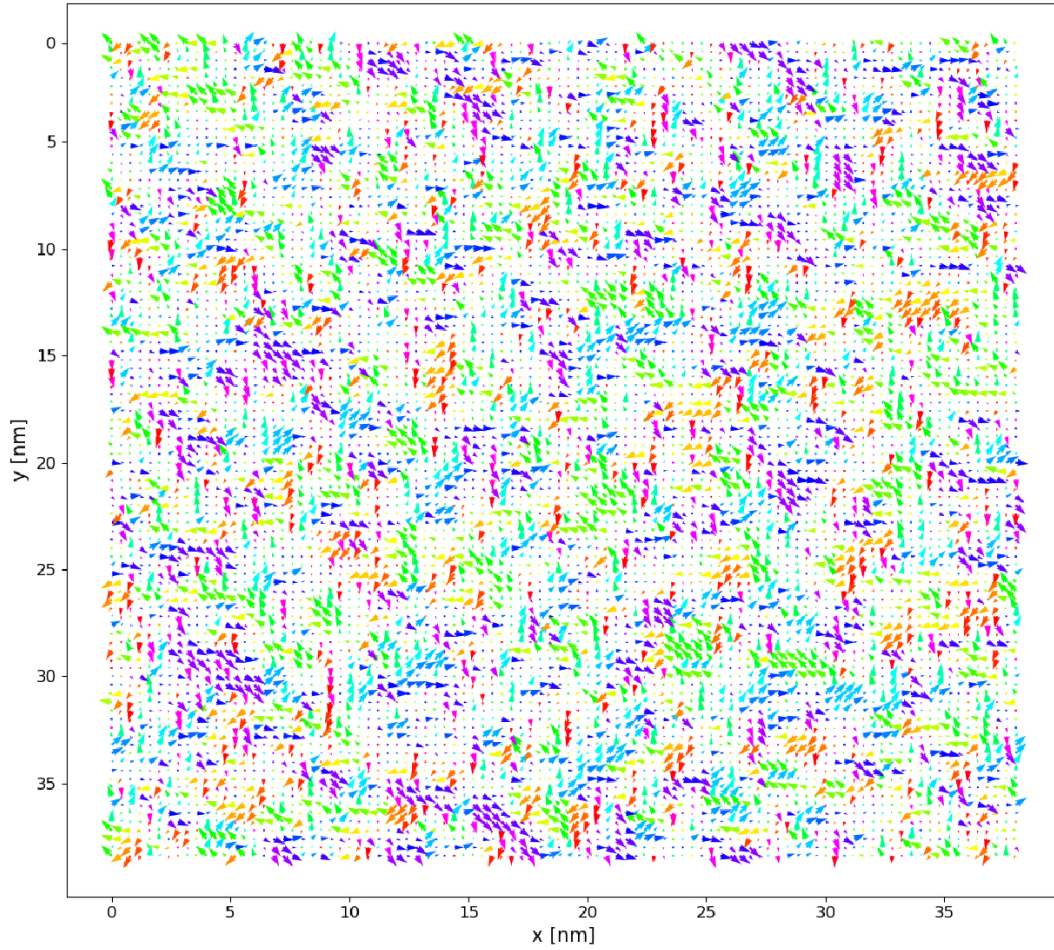
*Figure S5. Polar order of BZT50 illustrated via a slice through a 96x96x96 supercell. Arrows describe the local dipole moments. Color represents the direction of the arrows.*

# V.    HYSTERESIS LOOPS

In this section we examine the composition of the hysteresis loops by the individual components of the polarization. As an example, we will take the BZT05 (5% Zr) system at a temperature of 250K. Figure S6 shows the corresponding hysteresis curve with an oscillating field (1 GHz) applied in the <111> direction. It is observed that, for fields above the coercivity, the system follows the external field in the <111> direction. This displacement corresponds to the rhombohedral phase. Below the coercivity, two polarization directions follow a ferroelectric response. Interestingly, however, the third direction shows a paraelectric behavior. In principle, this behavior corresponds to the orthorhombic phase. That is, by applying a field it is possible to switch between two phases. The corresponding overall response of the system can be seen in the main paper. The phase diagram reveals that the temperature of 250 K is very

7

171

close to the phase transition between orthorhombic and rhombohedral phase and thus explains why such a response can be obtained.
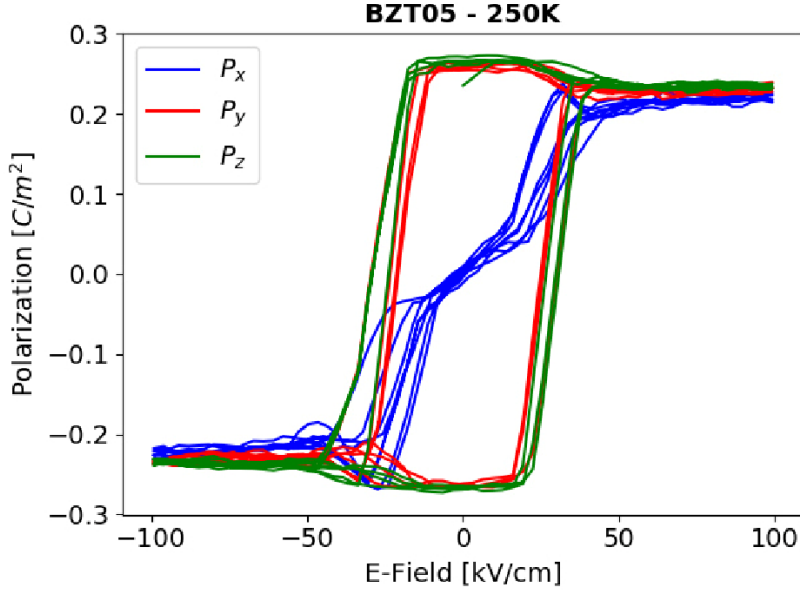


*Figure S6. Hysteresis loop of BZT05 (5% Zr content) obtained from MD simulations at a temperature of 250 K. The plot shows the three components of the polarization vector.*

# VI.   SUSCEPTIBILITY ANALYSIS

In this section, investigated the simulated susceptibility of BZT50 in more detail. As discussed in the main paper, we use two methods to calculate the susceptibility. The first method (CF) uses the fluctuations of the dipoles as described by the correlation function for the calculation, which represents the low-frequency susceptibility. The second method (direct) calculates the static susceptibility by applying an external field. Figure S7 shows the results of both methods for the case of BZT50. To better analyze the results, we divide the curves into three regions. In region I, the susceptibility of both methods follows a Curie-Weiss behavior, which is illustrated by the two fits. The temperature $T_0$ obtained by the fit amounts to approximately 140 K. This is in good agreement with experimental data [9] from the literature. In region II, both curves start to deviate from the Curie-Weiss behavior. In region II, both curves start to deviate slightly from each other, that is in good agreement with data from Akbarzadeh et al. [10]. However, in contrast to [10], we observe that both methods start to deviate from the Curie-Weiss behavior almost simultaneously. Finally, in region III, the direct method continues to increase, whereas the CF method decreases. This behavior is also in excellent agreement with experimental data [11] measured on relaxor ferroelectrics.
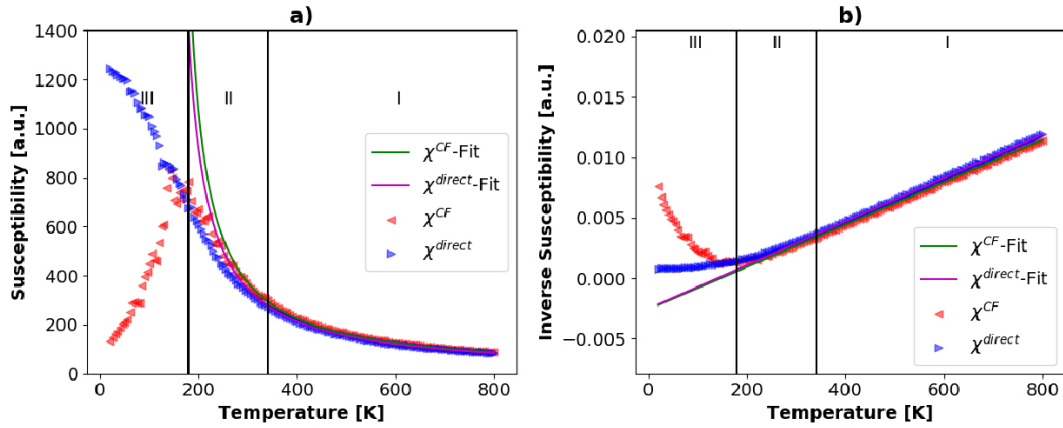
*Figure S7. Comparison of the static (direct) and low-frequency (CF) susceptibilities. a) Temperature dependence of direct and CF and their CW trend lines. b) Inverse susceptibilities vs temperature and the linear fits according to the CW law.*

# References

[1]     G. I. Csonka, J. P. Perdew, A. Ruzsinszky, P. H. T. Philipsen, S. Lebègue, J. Paier, O. A. Vydrov, and J. G. Ángyán, Phys. Rev. B **79**, 155107 (2009).

[2]     G. Kresse and J. Hafner, Phys. Rev. B **49**, 14251 (1994).

[3]     G. Kresse and J. Furthmüller, Comput. Mater. Sci. **6**, 15 (1996).

[4]     G. Kresse and J. Furthmüller, Phys. Rev. B **54**, 11169 (1996).

[5]     G. Kresse and D. Joubert, Phys. Rev. B **59**, 1758 (1999).

[6]     P. E. Blöchl, Phys. Rev. B **50**, 17953 (1994).

[7]     F. Mayer, M. N. Popov, D. M. Evans, S. Krohns, M. Deluca, and J. Spitaler, Phys. Rev. B **106**, 064108 (2022).

[8]     V. Veerapandiyan, M. N. Popov, F. Mayer, J. Spitaler, S. Svirskas, V. Kalendra, J. Lins, G. Canu, M. T. Buscaglia, M. Pasciak, J. Banys, P. B. Groszewicz, V. Buscaglia, J. Hlinka, and M. Deluca, Adv. Electron. Mater. **8**, 2100812 (2022).

[9]     T. Maiti, R. Guo, and A. S. Bhalla, J. Am. Ceram. Soc. **91**, 1769 (2008).

[10]    A. R. Akbarzadeh, S. Prosandeev, E. J. Walter, A. Al-Barakaty, and L. Bellaiche, Phys. Rev. Lett. **108**, 257601 (2012).

[11]    A. Levstik, Z. Kutnjak, C. Filipič, and R. Pirc, Phys. Rev. B **57**, 11204 (1998).

9

173

## 8.4   Publication 4

# Hidden phases in homovalent and heterovalent substituted BaTiO$_3$

Florian Mayer[1], Marco Deluca[1], Maxim N. Popov[1]

[1]*Materials Center Leoben Forschung GmbH, Roseggerstrasse 12, 8700 Leoben, Austria*

Corresponding author: florian.mayer@mcl.at

**Abstract:**

Ferroelectric materials can exhibit metastable phases when exposed to THz pulses, characterized by a polarization integration capability related to the amplitude and frequency of the pulses. These so-called "hidden" phases enable gradual switching of polarization that can be utilized in artificial synapses for non-conventional (neuromorphic) computing machines. In this work, we employ large-scale molecular dynamics simulation based on an effective Hamiltonian approach and report on the discovery of hidden phases in Zr- and Nb-doped barium titanate (BaTiO$_3$). We investigate the formation and the stability of those phases at different stimuli and temperatures (20 K and 200 K). Our results shed light on the compositional dependence of the properties of these phases, demonstrating the potential of lead-free relaxor ferroelectrics for near-room-temperature neuromorphic computing.

# Hidden phases in homovalent and heterovalent substituted BaTiO$_3$

Florian Mayer ◉,* Marco Deluca ◉, and Maxim N. Popov ◉†

*Materials Center Leoben Forschung GmbH, Roseggerstrasse 12, 8700 Leoben, Austria*

Ferroelectric materials can exhibit metastable phases when exposed to THz pulses, characterized by a polarization integration capability related to the amplitude and frequency of the pulses. These so-called "hidden" phases enable gradual switching of polarization that can be utilized in artificial synapses for nonconventional (neuromorphic) computing machines. In this work, we employ large-scale molecular-dynamics simulation based on an effective Hamiltonian approach, and we report on the discovery of hidden phases in Zr- and Nb-doped barium titanate (BaTiO$_3$). We investigate the formation and the stability of those phases at different stimuli and temperatures (20 and 200 K). Our results shed light on the compositional dependence of the properties of these phases, demonstrating the potential of lead-free relaxor ferroelectrics for near-room-temperature neuromorphic computing.

## I. INTRODUCTON

Artificial intelligence is almost indispensable today, and a great deal of effort is being put into developing new and better computing techniques compared to the traditional Von Neumann architecture. A subarea of this research is the so-called neuromorphic computing, which is a rapidly growing interdisciplinary research field [1]. Within this concept, an attempt is made to mimic the characteristics and functionalities of neurons and their networks, such as memory, learning, and massive parallelism, via software and novel hardware. For the latter, the development and discovery of new materials or the tuning of properties of existing materials is inevitable. A class of materials showing promising properties for this purpose are ferroelectric materials and substituted versions thereof [2]. In this context, the out-of-equilibrium long-lived phases of matter appearing upon THz-irradiation recently reported in relaxor ferroelectrics Pb(Mg$_{1/3}$Nb$_{2/3}$)O$_3$ (PMN) [3] and Pb(Zr, Ti)O$_3$ (PZT) [4], as well as in anti-ferroelectric NaNbO$_3$ [5], offer intriguing prospects. These phases are often referred to as "hidden phases", due to their metastable nature and inaccessibility under equilibrium conditions. The presence of hidden phases results in a gradual switching of the electric polarization when the THz pulses are applied with a high repetition rate. Moreover, the polarization states persist even after removal of the external stimuli. Both of these properties—gradual (analog) switching and nonvolatility—are sought after for mimicking synaptic behavior in artificial synapses. Gradual switching of the remanent polarization in ferroelectrics has also been experimentally demonstrated in, e.g., PZT [6], however it happens at a much slower pace. Also, applying strain *nanosecond* pulses has been shown to result in a gradual switching in PZT [7]. Hence, quasianalog switching between hidden phases

happening at a picosecond timescale combined with their persistence offers an attractive playground for applications in ultrafast neuromorphic, i.e., brain-inspired, computing. Such materials can be potentially used in ferroelectric tunnel junctions (FTJ) to modulate tunneling currents via the tunneling electroresistance (TER) effect [8], i.e., in resistors with memory (memristors). Alternatively, one can also create capacitors with memory (memcapacitors), which can result in even more energy-efficient neuromorphic devices [9]. In previous works [3–5], either pure substances (NaNbO$_3$) or solid solutions with a fixed composition (PMN and PZT) were considered. That is, the effect of varying the composition of such a solid solution has so far remained unexplored. In this work, we present *ab initio*–based simulations leading to the discovery of hidden phases in lead-free relaxor Zr- and Nb-doped BaTiO$_3$ (BT) solid solutions [BaZr$_x$Ti$_{1-x}$O$_3$ (BZT) and BaNb$_x$Ti$_{1-x}$O$_3$ (BNT)], we characterize their behavior under applied THz pulses, explore compositional tuning of the gradual polarization switching, and discuss possible implications for designing synaptic devices based on the hidden phases.

The paper is organized as follows: In Sec. II, the theoretical foundations of the simulations used are explained by means of so-called effective Hamiltonians. This is followed by a detailed analysis of the results in Sec. III, where several important quantities are discussed. This includes a study of hidden phases in the respective systems as well as the gradual switching of the electric polarization. Subsequently, the stability and reversibility of the induced phases are also examined. Finally, a study at higher temperatures is discussed, and stability problems are explained.

## II. METHODOLOGICAL DETAILS

### A. Effective Hamiltonian

All simulations in this work are based on the concept of effective Hamiltonians [10–14], which are used to describe the potential energy surface of the considered systems. The main difference from other potentials used in molecular-dynamics

---

*florian.mayer@mcl.at
†maxim.popov@mcl.at

(MD) simulations is the choice of the parametrization basis. Instead of considering the atoms individually, in an effective Hamiltonian the description of the energy is based on a basis of phonon modes [10]. Therefore, the amplitudes [11] of selected phonon modes serve as central variables, with amplitude vectors defined for each unit cell in a given supercell. Additionally, a dimensionless displacement vector [11] is defined for each unit cell to account for inhomogeneous strains. The homogeneous strain is taken into account via using the deformation of the whole supercell [11,12]. A detailed description of the formalism can be found in Refs. [11–13]. In general, the effective Hamiltonian consists of the following energy contributions: Local-mode self-energy, homogeneous and inhomogeneous contributions to the elastic energy, dipole-dipole interaction, short-range interactions, strain-phonon coupling, and interactions with an external field. The parametrization of the required parameters can be done entirely by using first-principles calculations [15]. The effective Hamiltonian formalism, originally derived only for pure systems, has been recently extended in order to be able to describe substituted systems [16–19]. The incorporation of substituted atoms can be done in different ways. For the parametrization of the base system, either (i) the virtual crystal approximation [16,20] (VCA) can be used, (ii) the two systems can be simply averaged [21], or (iii) one of the two systems can be defined as the parent system [18]. The effects caused by substitution are further taken into account by additional terms in the Hamiltonian. This allows us to account for different local-mode self-energies, different long-range interactions, and the influence of substitution atoms on neighboring unit cells. In this work, we use the approach from Ref. [22], which considers the substituted atoms as a perturbation of the pure system. The associated Hamiltonian for pure BT was parametrized using a significant number of anharmonic couplings to higher-energy phonons, leading to an improved description of the transition temperatures of pure BT [13]. Furthermore, the inclusion of $Zr^{4+}$ and $Nb^{5+}$ was performed by using additional terms to the Hamiltonian, showing excellent agreement of the simulated phase diagrams with experimental data [22]. It should be noted that the effective Hamiltonian for BNT includes the treatment of Ti vacancies as the main charge compensation scheme in this material [23]. All required parameters for the extended effective Hamiltonian are listed in the Supplemental Material of Ref. [22].

### B. Molecular dynamics

To simulate properties at finite temperatures, we use MD simulations. The fundamental basis of these simulations is the potential energy surfaces in the form of effective Hamiltonians as described in the previous section. To make use of the effective Hamiltonian formalism in terms of MD simulations, we use the FERAM code developed by Nishimatsu and co-workers [11,12,21]. This code was adapted in order to take into account the additional terms from Ref. [22]. In addition, a function was added to be able to apply customized external fields during our simulations. Since we want to compare our materials of interest with simulations from the literature, we decided to apply the same external stimuli as in Refs. [3,5].

The corresponding formula of the applied external field is defined in Eq. (1). Here, $E_0$ denotes the amplitude of the pulse, $t_0$ is the position of the maximum, $t$ is the time variable, $w$ represents the angular frequency, and $\Delta$ is the width of the Gaussian function. The parameters are also taken from Ref. [3] and read $E_0 = 4\sqrt{3} \times 10^7$ V/m, $\Delta = 0.2$ ps, and $\omega/2\pi = 1.5$ THz. For all simulations, the field was applied along the $\langle 111 \rangle$ direction,

$$\boldsymbol{E}_{\text{ext}}(t) = \boldsymbol{E}_0 e^{-\frac{(t-t_0)^2}{\Delta^2}} \cos\left(\omega(t - t_0)\right). \tag{1}$$

The choice of parameters by Prosandeev *et al.* [3] was considered to mimic experimentally observed THz pulses [24,25]. Due to the low computational costs of effective Hamiltonian simulations, we decided to use supercells of size $96 \times 96 \times 96$ for all our investigations. Moreover, such large supercells allow better statistical quantities to be taken from the simulations. All simulations were performed using the canonical ensemble. Furthermore, a discrete time step of 2 fs was used. A velocity scaling algorithm was applied to keep the temperature constant during the simulation. To start with systems in equilibrium, each supercell was thermalized for 200 ps before applying external fields.

### III. RESULTS AND DISCUSSION

#### A. Integration and hidden phases

Hidden phases exhibit gradual switching of polarization when a train of THz pulses is applied, referred to as "integration." In this section, we aim to study the presence of hidden phases and the integration over time for different concentrations of Zr and Nb substituted BT (i.e., BZT and BNT, respectively) by applying trains of THz pulses. The shape of the pulses and its parameters have already been described in Sec. II B. As a starting point for these simulations, supercells of size $96 \times 96 \times 96$ were constructed using random distributions of substituents for both systems. It should be noted that for BNT also the right amount of Ti vacancies was included to achieve charge neutrality of the system, due to substitution with a donor cation, $Nb^{5+}$, occupying the atomic site of $Ti^{4+}$. For BZT this is not necessary since $Zr^{4+}$ is a homovalent substituent for $Ti^{4+}$. Following, these supercells were used to perform MD simulations at a temperature of 20 K. Later in this work, the simulation of higher temperatures is also addressed. Another important aspect for the upcoming MD simulations is the initial position of the local dipoles. Here, we decided to use two different approaches. First, we employed a starting configuration with randomly oriented dipoles, which led to a multidomain structure after thermalization for BT. For higher concentrations of substituents, states with nearly zero net polarization were observed, which are to be anticipated in such systems [22]. In the second approach, we used a ferroelectric single-domain distribution of dipoles as a starting point. This approach led for small concentrations to a preservation of this state, whereas for higher concentrations the thermalization was not sufficient to move from this state to a state of vanishing polarization typically observed in that concentration range [22]. As we are primarily interested in identifying the compositions with the best properties for integration, stability, and reversibility, results for both starting
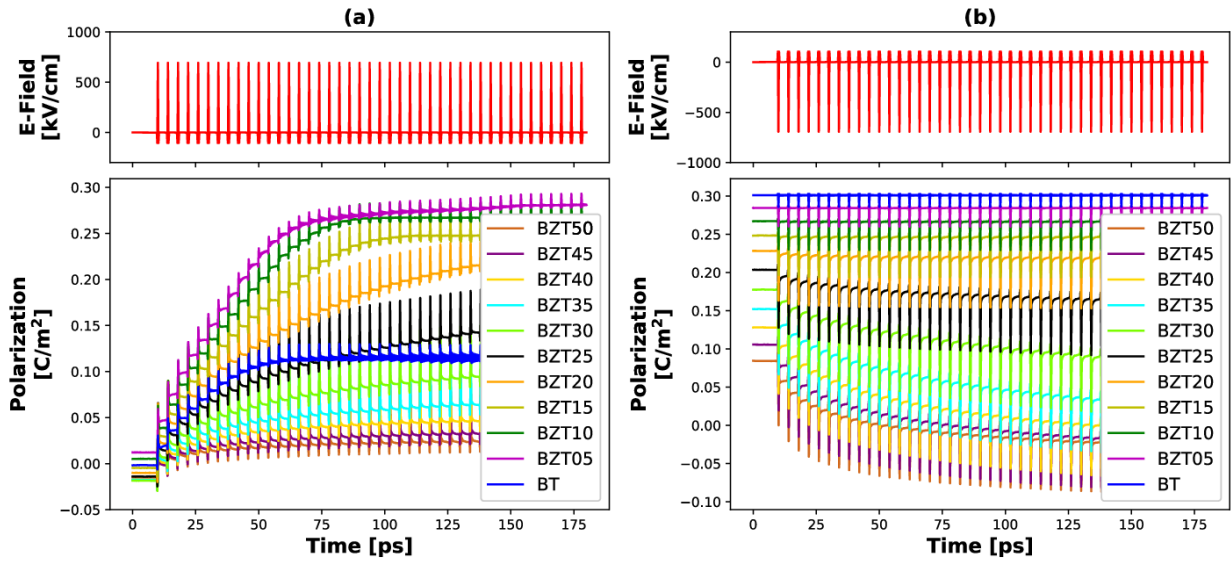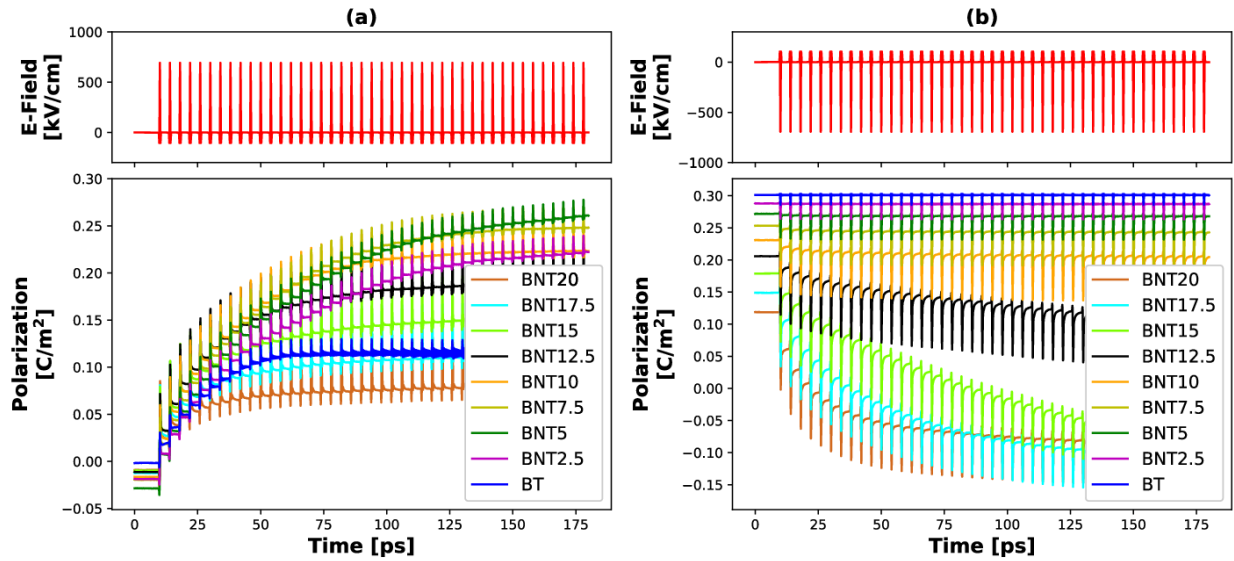
FIG. 1. Evolution of polarization in BZT (from 0% to 50% Zr content) due to an applied train of THz pulses (at 20 K). The polarization refers to the $z$-component of the averaged supercell polarization. Part (a) shows the results starting from a random configuration, and (b) illustrates the results starting from a single-domain configuration. The system was equilibrated for 200 ps before the first trends were plotted.

conditions are shown in the course of this section. This allows us to better understand the occurrence of hidden phases and to investigate their basic mechanisms.

To start with our investigation, we first want to focus on the case of BZT where the corresponding results are presented in Fig. 1. Figure 1(a) illustrates the results for a starting configuration of randomly distributed dipoles, where a train of pulses with positive polarity was applied after thermalization. In Fig. 1(b), a single-domain configuration was chosen as the starting configuration, with a negative-polarity pulse train applied after thermalization. The results of Fig. 1(a) shall be discussed first. Here, after thermalization, a nearly vanishing polarization is observed for all compositions studied. For the case of small concentrations, a multidomain configuration of the dipoles is observed. This is confirmed by the illustration of the dipole pattern for the case of pure BT and BZT05 (i.e., 5% of Zr) in Fig. 2. In this figure, snapshots for different compositions are presented at three different times during the simulations. The first snapshot was taken right after thermalization, the second one at 40 ps, and the third one at 180 ps after thermalization. For higher concentrations, a nearly vanishing net polarization is found in Fig. 1(a), which is to be expected for these systems [22]. Applying a positive train of pulses now has the following effects on the polarization states: For BT, an integration (i.e., a gradual increase of polarization induced by the train of pulses) of the polarization is observed, with the saturation polarization lying in the middle range compared to the other compositions. The reason that BT does not exhibit the largest net polarization of all compositions can again be found in Fig. 2. Here, it is clear that the train of pulses can change the orientation of parts of the multidomain configuration but not reach a pure single-domain state. That is, the applied pulses are simply not strong enough, and a larger amplitude has to be applied to reach the single-domain state. Furthermore, in Fig. 1(a), a small amount of 5% Zr

already changes the observed integration of the polarization significantly. In contrast to pure BT, the saturation polarization is almost twice as large. This can be explained by the partial disruption of the long-range correlation of the dipoles induced by the impurity ions, leading to higher fragmentation of the polar order. This facilitates reaching a near-perfect single-domain state as demonstrated by the case of BZT05 in Fig. 2 at 180 ps. If the concentration is increased further, the saturation polarization decreases, which is to be expected in such a system. This is caused by the nonpolar nature of the unit cells centered on Zr impurity cations, which reduces the overall polarization. Furthermore, for higher concentrations, the long-range correlation of the dipoles is further and further disrupted until the systems are in a state where only a mixture of equally sized polar and nonpolar nanodomains is present. The occurrence and behavior of such nanodomains is confirmed in Fig. 2 with the example of BZT35. The appearance of nanodomains is consistent with the concentration range where relaxor behavior is also observed. Based on the results from Fig. 1(a), two main differences can be identified for the integration of polarization as well as the intermediate states. For low concentrations and BT, starting from a multidomain configuration, the ferroelectric domains are changed in size and orientation by applying the train of pulses. The intermediate states obtained are merely a different arrangement of ferroelectric domains. For larger concentrations, the disorder of the system results in an arrangement of nanodomains that are uncorrelated in the initial state. By applying the train of pulses, these nanodomains can be aligned and thus result in the measured integration of the polarization. The intermediate states are now an ensemble of correlated and uncorrelated polarization states and are further referred to as hidden phases.

As a next step, we want to discuss the results from Fig. 1(b) where the thermalization was started with a single-domain configuration. Here, it is clear that all systems show larger
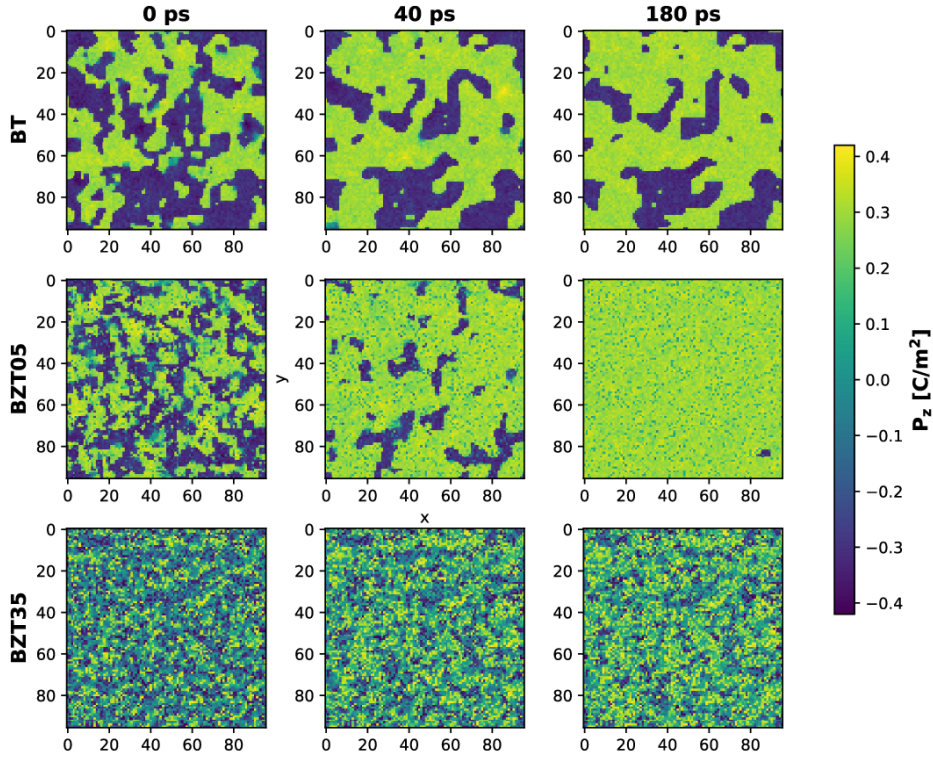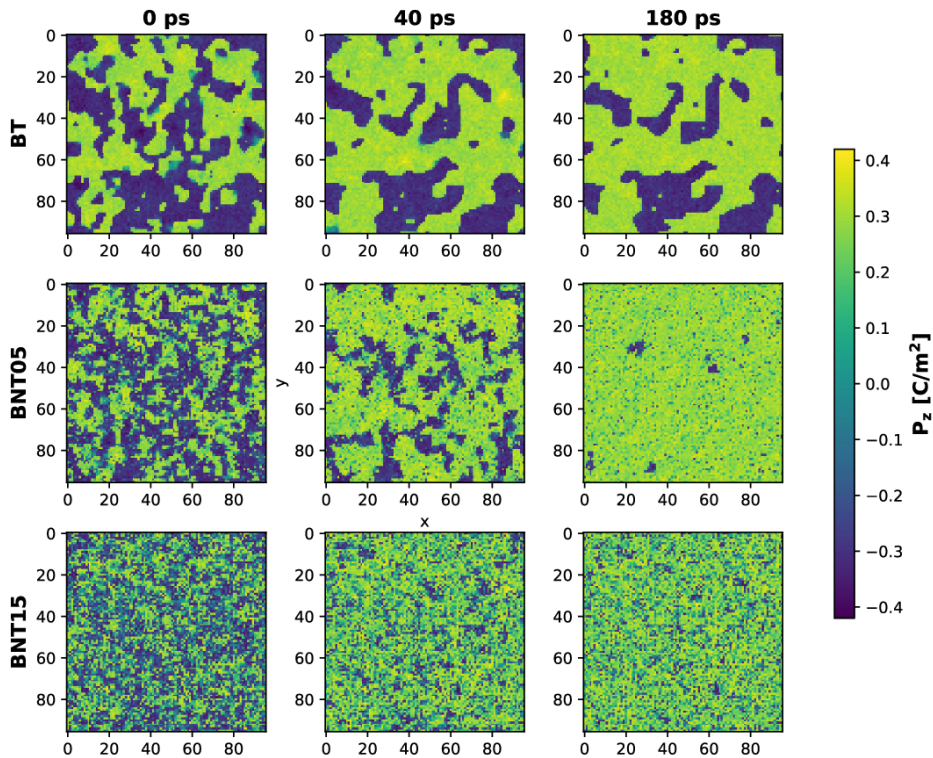
FIG. 2. Snapshots of the compositions BT, BZT05 (5% Zr), and BZT35 (35% Zr) at different times of the simulation (at 20 K). The color represents the $z$-component of the polarization in an $x-y$ plane of the $96 \times 96 \times 96$ supercells. The 0 ps snapshot was taken right after thermalizing the system for 200 ps.

net polarization after thermalization compared to Fig. 1(a). That is, for BT and small concentrations, the systems are in a pure single-domain state. For higher concentrations, the nanodomains are correlated and no vanishing polarization state is established. For all compositions, therefore, it can be seen that such an induced state is certainly stable in the simulation, and that thermalization has not caused any major relaxations either. Furthermore, it can be observed how the net polarization decreases with increasing Zr content. For more details on this decrease of polarization, we refer to the Supplemental Material [26]. In the following, we will investigate how the individual systems behave when the same train of pulses from before is applied but only inverted. For BT and concentrations lower than 25%, no significant change of the polarization can be achieved by applying the train of pulses. This shows that once the system is in such a single-domain configuration, the selected pulse shape can no longer break it up. In this case, the pulses would have to be significantly higher in order to achieve changes. We shall stress that switching behavior is dependent on the parameters of the external stimulus. For instance, domain-wall motion has been reported for a similar magnitude of the E-field, but a longer pulse width (up to ns) in BaTiO$_3$ [27]. If the concentration is now increased, the ferroelectric domains become smaller and smaller down to nanodomains. These nanodomains are also in this case initially aligned and correlated similar to a single domain, but the pulses gradually manage to align them differently and thus to change the overall polarization. In principle, such negative

integration starting from a saturated state is the reversibility of the induced polarization, which is discussed in detail in Sec. III C. In summary, the following statements can be drawn for integration in BZT: If a multidomain configuration is taken as the starting point, integration to the highest saturated polarizations is seen at rather low concentrations of Zr. For BT, on the other hand, the selected pulse is not sufficient to align all ferroelectric domains. However, for both cases, no negative integration is observed at unchanged pulses, which can be attributed to the strong correlation between the individual local dipoles. At higher concentrations, the reached saturated polarization becomes lower, but integration is also possible in the other direction. This is caused by the diversity of hidden phases and the rather simple alignment of the nanodomains by the selected train of pulses. In general, compositions with concentrations above 25% Zr provide a better basis for application to mimic synapses when considering the chosen shape of the applied train of pulses and the respective integration in both directions.

As a further step, we will conduct an analogous study for the case of BNT, with the results of the simulations displayed in Fig. 3. The two different starting conditions were also included in this study, with the results in Fig. 3(a) obtained from the random input configuration discussed first. The results for pure BT have already been discussed in detail and will therefore not be discussed again. Concerning the substituted systems, the trend for BNT is quite similar to that of BZT, but there are differences in the concentration range as well

FIG. 3. Evolution of polarization in BNT (from 0% to 20% Nb content) due to an applied train of THz pulses (at 20 K). The polarization refers to the $z$-component of the averaged supercell polarization. Part (a) shows the results starting from a random configuration, and (b) illustrates the results starting from a single-domain configuration. The system was equilibrated for 200 ps before the first trends were plotted.

as the achieved saturated polarizations. As in the case of BZT, an increase in saturated polarization is found for small concentrations compared to pure BT. This is again due to the partial disruption of the long-range interaction by substituents, thereby facilitating the alignment of the ferroelectric domains by the train of pulses. Furthermore, this behavior can be illustrated also in BNT by plotting snapshots from the simulations as shown in Fig. 4. Here, significantly smaller ferroelectric domains are observed for BNT05 compared to BT right after thermalization. In addition, also the integration up to a nearly single-domain state at 180 ps is evident. If the concentration is increased further, the saturated polarization decreases again. This behavior is again comparable with BZT, but here the saturation polarization decreases faster at the same concentration, which is compatible with the evolution of relaxor behavior in heterovalent substituted BaTiO$_3$ systems [23]. For the case of BNT15, after thermalization, noncorrelated nanodomains result. The corresponding polar structure can be found in Fig. 4. If the train of pulses is applied for this system, the nanodomains can align and result in a variety of different possible intermediate states, which again can be referred to as hidden phases. In this case, a distinction must also be made between small and larger concentrations. For smaller concentrations, the intermediate states are merely a variety of different ferroelectric domains with different sizes and orientations. For larger concentrations from about 10% of Nb, the ferroelectric order is destroyed to such an extent that one can only speak of nanodomains (i.e., similar to what happened in BZT with 25% of Zr and above). The occurrence of such nanodomains coincides with the concentration range where relaxor behavior is also observed.

In the following, we will now investigate how the compositions behave when a single-domain state is used as starting configuration. The corresponding results are shown in Fig. 3(b). Here, again, an increased polarization state is

obtained for all systems after thermalization. For smaller concentrations, the induced single-domain state remains. But even for larger concentrations, no major relaxations to a vanishing polarization are observed. That means that, in this case, nanodomains remain also correlated after thermalization and provide a polarization state that differs from the single-domain state by the reduced net polarization. If the inverted pulse train is now applied, the following observations can be made: For concentrations lower than 7.5%, there is no significant change in the net polarization, and the systems remain in their initial state. The correlation between the local dipoles is so strong here that no repolarization of the system can be induced by the selected shape of the train of pulses. However, at concentrations higher than 7.5%, the sizes of the ferroelectric domains already become so small that other polarization states can be introduced by applying a negative train of pulses. The higher the concentration becomes, the easier it is for the selected pulse to break the correlation and align the nanodomains differently. This behavior is analogous to BZT, but the concentration range for the occurrence of negative integration is much smaller here starting at about 10% of Nb, whereas in BZT more than 25% of Zr was necessary to induce the same effect. This is again in accord with the evolution of relaxor behavior in heterovalent substituted BT [23]. Considering the selected pulse, the interesting concentration range is also specified here with concentrations above 10% for the application to mimic synapses. However, it should be emphasized that these results depend on the selected shape of the pulse and that the concentration ranges listed are only indicative values for the upcoming further analyses.

### B. Stability

Here, we examine the stability of the hidden phases over a certain period of time. This is done by means of the MD

FIG. 4. Snapshots of the compositions BT, BNT05 (5% Nb), and BNT15 (15% Nb) at different times of the simulation (at 20 K). The color represents the $z$-component of the polarization in an $x-y$ plane of the $96 \times 96 \times 96$ supercells. The 0 ps snapshot was taken right after thermalizing the system for 200 ps.

simulations, where a different number of pulses are applied to induce the individual states. Furthermore, the simulations for the individual states are continued without external stimuli, and their evolution is monitored. It should be mentioned that the simulations can only run for a limited time due to resource constraints and thus the stability can only be ascertained for this time range. We thermalized the individual simulations first for 200 ps and then ran them for another 180 ps. To reduce computational load, we tested stability only for selected compositions of BZT and BNT, based on the insight from the previous sections. Specifically, we decided to use the BZT35 (35% Zr) and BNT15 (15% Nb) compositions due to the favorable integration properties and both systems being in the concentration range where relaxor behavior is observed. First, the BZT35 composition is investigated in more detail, with the associated results presented in Fig. 5(a). Here, the system was thermalized and subsequently the excitation of the system was started by applying 1–15 pulses. After applying each group of pulses, the simulation was continued over several decades of picoseconds. It can clearly be seen that various intermediate polarization states are reached. The spacing between these states varies and becomes smaller with each next pulse, as illustrated in the inset of Fig. 5(a). For the temperature of 20 K, the obtained states appear rather stable over the simulated time period, similar to PMN [3]. However, if the polarization curves are examined more closely, a tendency to creep towards lower polarizations becomes apparent, which can be clearly

seen in Fig. 6(a). This creep indicates that BZT35 strives for an equilibrium state with significantly lower polarization. This tendency is consistent with the expected zero net polarization state in a relaxor ferroelectric [22]. All in all, the induced states can be considered to be metastable over a time range of several decades of picoseconds. To study stability on longer timescales, the simulations would have to be extended considerably, but this is not feasible even with the low-cost effective Hamiltonians. The number of states that can still be distinguished from each other also plays an important role for the application. In the case of BZT35, multiple states can be clearly separated. However, if the polarization approaches saturated polarization, the states become blurred and can only be hardly distinguished.

An analogous study is now presented for the BNT15 composition. The protocol for the MD simulations is the same as that already explained in detail for BZT35. The corresponding results can be seen in Fig. 5(b). At first glance, a significant number of induced states can also be seen here, whereby these states also appear stable over the simulated time span. A more detailed analysis also shows a creep of the individual states. It is observed that after excitation the individual states slowly creep to lower polarizations, as evident in Fig. 6(b). This creep is again expected for the BNT15 system, since the ground state of this relaxor ferroelectric is associated with vanishing polarization. However, this creep is barely noticeable over the simulated time period. The number of clearly distinguishable

180
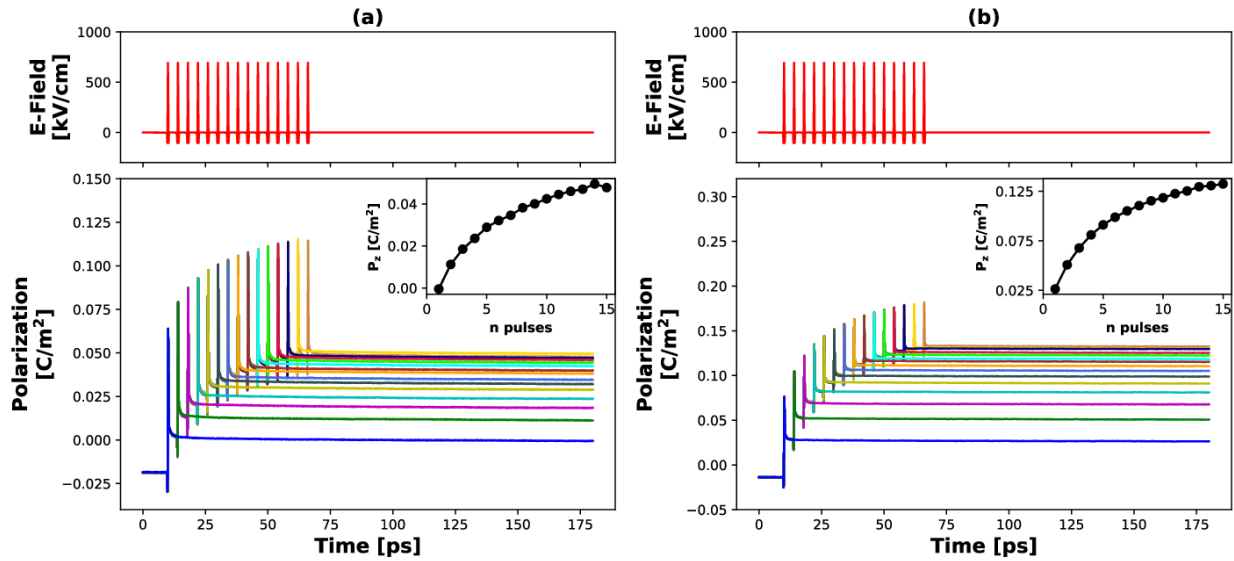
FIG. 5. Stability of hidden phases at 20 K obtained from MD simulations. Part (a) shows the stability for BZT35 (35% Zr), and (b) illustrates the stability for BNT15 (15% Nb). Colors denote different number of pulses applied (blue = 1 pulse, gold = 15 pulses). The insets show the induced polarization as a function of the number of applied pulses.

states in this case is similar to BZT35, and multiple well-defined intermediate polarization states are visible. In comparison, the saturated polarization reached is more than twice as high as in BZT35. Near the saturated polarization, these states again become increasingly blurred, as is evident in



FIG. 6. Illustration of the observed creep behavior of intermediate states at 20 K. Part (a) shows the creep of the lowest induced state in BZT35 (35% Zr), and (b) demonstrates the creep of the lowest induced state in BNT15 (15% Nb).

the inset of Fig. 5(b), and it is difficult to differentiate between them.

Altogether, the stability of hidden phases can be confirmed for both systems for the simulated time span and for the selected low temperature. The number of achievable polarization states is strongly dependent on the considered composition [see Figs. 1(a) and 3(a)] and becomes smaller with increasing concentration.

### C. Reversibility

Another property that is important in the possible application of such materials in neuromorphic computing devices is the possibility of reversing the induced states. To test this property, MD simulations were again employed. First, the systems were thermalized and then the application of the pulses was started. A train of pulses with positive amplitudes was first applied until integration near saturated polarization was achieved. Then, a train of pulses with negative polarity was applied to check if the integration also occurs starting from such an induced state, and brings the system to opposite polarization states. To be consistent with the previous sections, the two systems BZT35 and BNT15 are also examined here. The reversibility results for BZT35 can be found in Fig. 7(a). Here, the integration of the polarization over time is observed initially. The polarization saturates gradually up to the maximum value from Fig. 1(b). Since this saturation is rather slow, the application of positive pulses was stopped after a certain time and continued with the application of negative pulses. The negative pulses lead to a gradual decrease of the polarization, followed by the inversion of the polarization and further integration. The progression of integration after switching polarity of the pulses is slightly different compared to the integration before switching and implies that different states can be accessed here. Through this simulation, we confirm
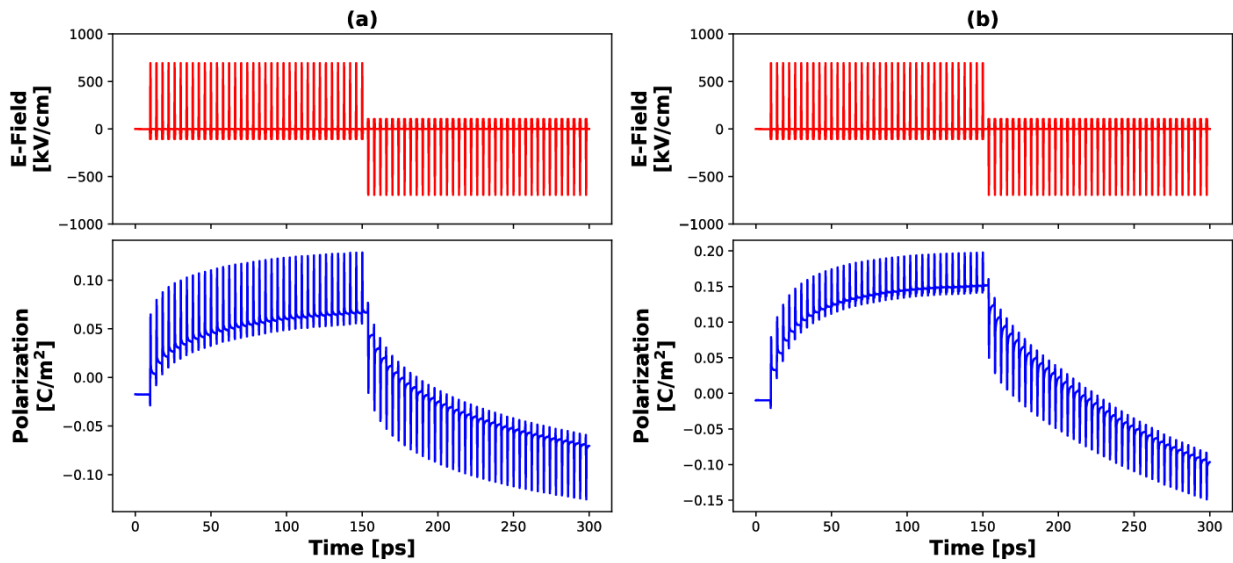
FIG. 7. Reversibility at 20 K obtained by applying a train of pulses and then inverting the amplitude. Part (a) shows the reversibility of BZT35 (35% Zr), and (b) illustrates the reversibility of BNT15 (15% Nb).

the feasibility of gradual polarization reversal in BZT35 by applying a negative train of pulses. The polarization reversal allows us to attain negative polarization values well below the initial state prior to pulse application.

The same method is used next to investigate reversibility for BNT15. The corresponding results can be seen in Fig. 7(b). Again, after thermalization of the system the simulation was started with a positive train of pulses. This results in an integration of the polarization that appears to start saturating with increasing time to a maximum polarization level as presented in Fig. 1(b). Afterwards the train of pulses was inverted and a negative integration of the polarization can be observed. The progression of this negative integration is different from the positive integration, which means that different states can be accessed. Compared to BZT35, the negative integration in BNT15 is nearly linear, showing the variety of different hidden phases and the different response to the train of THz pulses in these systems. Altogether, also for the case of BNT15, it can be confirmed by this kind of simulation that the induced polarization can be inverted using a negative train of pulses.

Further possibilities of reversibility and problems that can occur at lower concentrations of substituents will also be discussed here. As an alternative method for returning to the initial state after excitation of the system, an increase in temperature can be used [3]. Increasing the temperature results in a strong increase of the mobility of the local dipoles, and thus the induced polarization state decays. However, the required temperature increase for reversibility again depends on the considered concentrations of the respective systems. Another problem we observed at lower concentrations is that the induced polarization state is so stable that it cannot be inverted with the pulses used for excitation. This observation was also made in the work of Prosandeev *et al.* [3], although the systems considered are different. A solution to overcome this problem is again to apply a temperature increase or to

choose a larger amplitude of the negative pulse. More details on these issues and simulations of reversibility for lower concentrations can be found in the Supplemental Material [26].

### D. Higher temperatures

In the previous sections, a temperature of 20 K was used to study the properties of hidden phases and their behavior. Here, we will increase the temperature to 200 K and investigate if we can observe similar results. Only results for BZT are presented here. The reason for this is that for BNT the ferroelectric phases as well as the transitions to the relaxor ferroelectric state are found at lower temperatures compared to BZT. Thus, no intermediate states can be induced at 200 K by the train of pulses because a large part of the concentration range finds itself already in the paraelectric phase at this temperature [22]. First, the integration property and the presence of hidden phases are investigated. MD simulations were performed with the same settings from Sec. III A, but the temperature was increased to 200 K. The corresponding result can be seen in Fig. 8(a). The results for pure BT and BZT05 were removed since no integration was found for these systems at 200 K. Instead of integration, these systems hopped from a multidomain configuration directly to a single-domain configuration when a single pulse was applied. For higher concentrations, integration of the polarization stimulated by the train of pulses can be observed similar to the 20 K case. Again, the integration to higher saturation polarization is found at low concentrations. The saturated polarization decreases with increasing concentration, which is consistent with the results observed in Sec. III A. However, the achievable saturated polarization for higher concentrations is much lower than previously observed. This can be attributed to the increased activity of the local dipoles, whereby the dipoles can no longer be easily stabilized into a correlated configuration. Furthermore, it is found that the peak following the excitation
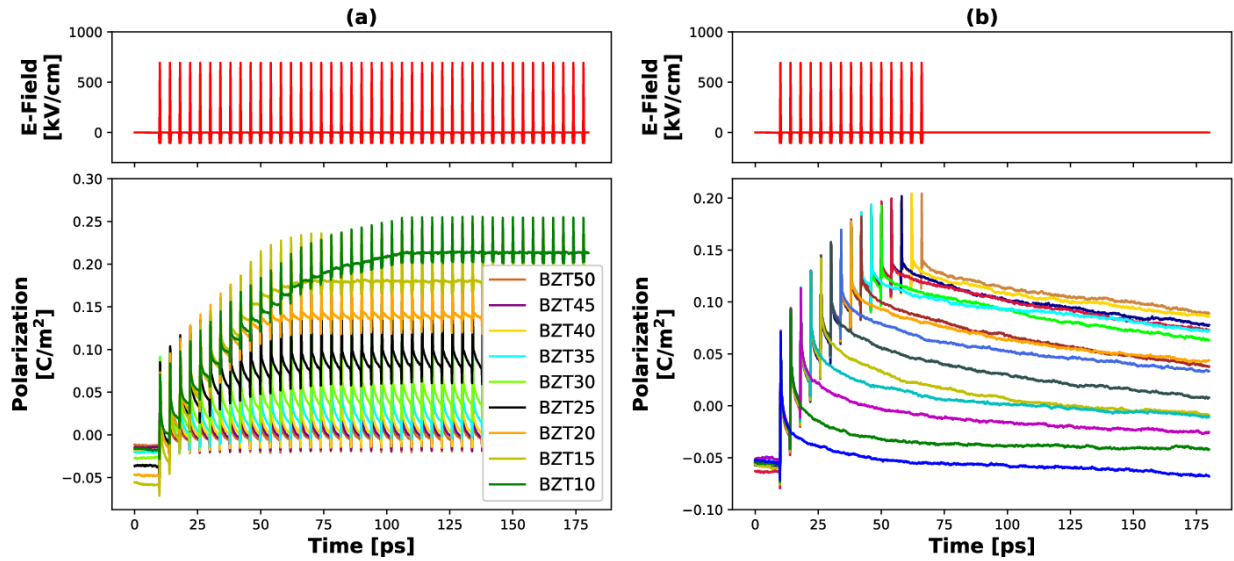
FIG. 8. Integration and stability of hidden phases in BZT at 200 K. Part (a) shows the integration of polarization when applying a train of pulses. Part (b) illustrates the stability of BZT20 (20% Zr) of hidden phases at 200 K.

is enhanced compared to the results at low temperatures. In general, an integration property is observed for BZT at a temperature of 200 K for a wide range (10–30 % Zr) of concentrations, and it can be associated with the presence of hidden phases.

The composition with 20% Zr (BZT20) was chosen here to examine the stability of the intermediate states. This concentration is slightly below the limit of relaxor behavior and shows a still reasonable number of intermediate states. The MD simulations were carried out as described in detail in Sec. III B. The corresponding results for BZT20 at a temperature of 200 K can be seen in Fig. 8(b). It can be clearly observed that different intermediate states can be achieved



FIG. 9. Reversibility of BZT20 (20% Zr) at 200 K obtained by applying a train of pulses and then inverting the amplitude.

by applying a different number of pulses. However, at this elevated temperature, the stability of the individual states is greatly reduced compared to the results for low temperatures. A strong relaxation to lower polarization states is observed for all intermediate states. This occurrence is expected as the system approaches a paraelectric phase with uncorrelated states at this temperature [22]. Furthermore, the increased mobility of the local dipoles counteracts the induced correlated states and aims to drive the system to an energetically lower state with lower polarization. All in all, the stability of the individual states at elevated temperature can only be confirmed for a range of several decades of picoseconds. Beyond that, the system relaxes back to a state with equilibrium polarization at a given temperature and concentration.

As a final property, the reversibility of the induced states in BZT20 is investigated. MD simulations were performed with positive and negative pulse trains, the details of which can be found in Sec. III C. The results for BZT20 at a temperature of 200 K can be seen in Fig. 9. When a positive pulse train is applied, integration of polarization is initially observed. Compared to results at lower temperature, saturated polarization is achieved faster here. Subsequently, the pulse polarity was inverted and the response of the system was investigated. The negative pulses are able to reverse the induced polarization state. Furthermore, it is found that negative integration travels through different states compared with positive integration. This shows the diversity of hidden phases in such a material.

## IV. CONCLUSION

In this work, molecular-dynamics simulations based on effective Hamiltonians were used to screen Zr and Nb substituted BT (i.e., BZT and BNT, respectively) for various properties relevant to neuromorphic computing systems. The basic idea was to investigate the response of different compositions to an applied train of electric THz pulses to study the

183

material's polarization integration properties, including the stability and reversibility of the achieved polarization states. For both systems, a wide range of compositions showed integration of polarization. Furthermore, the application of the external pulses revealed the presence of hidden phases, akin to those reported for PMN [3] and PZT [4]. Here, however, it must be distinguished for the respective concentration how these intermediate states appear. For small concentrations of substituent (either Zr or Nb), these intermediate states are merely differently oriented ferroelectric domains. The latter become more and more disrupted with increasing concentration of substituents (due to substituent-driven disruption of long-range ferroelectricity), leading to the appearance of polar nanodomains. The occurrence of such nanodomains was confirmed for both systems in the region corresponding to the onset of relaxor behavior. The stability of the individual intermediate states could be demonstrated for the low temperature of 20 K using the examples of BZT35 and BNT15. Here, a slight creep to lower polarization states was detected for both cases. Consequently, reversibility was also demonstrated for the examples of BZT35 and BNT15, where the induced polarization state could be reversed by applying a negative pulse train. Overall, the following conclusions can be drawn from the results at 20 K for the application in neuromorphic devices: The materials with composition close to the onset of the relaxor transition appear to offer the best tradeoff between (i) the range of the attainable polarizations, and (ii) the field strength required for switching/resetting the material. The former defines the number of polarization levels that can be used to encode information, i.e., the number of bits, whereas the latter determines the operation power. That means that for BZT a Zr content above 30% and for BNT an Nb content above 10% are promising for neuromorphic applications. In this range of relaxor behavior, on the one hand, an integra-

tion to reasonably saturated polarizations can be found, and on the other hand, the induced polarization can be inverted with the same shape of the pulses. Moreover, there is also stability of the intermediate states over at least several decades of picoseconds. The study at higher temperatures showed integration for concentrations above 10% of Zr, whereas for lower concentrations a direct transition to a single-domain configuration was found. The study of the stability of the intermediate states is given for the example of BZT20 only for a few decades of picoseconds. In contrast, reversibility of the induced polarization state is possible with the same pulse and was confirmed by the simulations. These results appear promising for the applications of these material in artificial synapses active near room temperature. In summary, this study demonstrates that both homovalent and heterovalent substituted $BaTiO_3$ show promising properties for use in neuromorphic computing systems if a compositional range in proximity to relaxor behavior is chosen. Such materials would be interesting for building artificial synaptic devices without the need of complex circuit design and processing, provided that sufficient maturity of the THz-technology is reached to allow the *in situ* application of pulses enabling the generation of hidden phases in those materials.

[1] D. V. Christensen, R. Dittmann, B. Linares-Barranco, A. Sebastian, M. Le Gallo, A. Redaelli, S. Slesazeck, T. Mikolajick, S. Spiga, S. Menzel *et al.*, Neuromorph. Comput. Eng. **2**, 022501 (2022).

[2] E. Covi, H. Mulaosmanovic, B. Max, S. Slesazeck, and T. Mikolajick, Neuromorph. Comput. Eng. **2**, 012002 (2022).

[3] S. Prosandeev, J. Grollier, D. Talbayev, B. Dkhil, and L. Bellaiche, Phys. Rev. Lett. **126**, 027602 (2021).

[4] S. Prosandeev, S. Prokhorenko, Y. Nahas, J. Grollier, D. Talbayev, B. Dkhil, and L. Bellaiche, Adv. Electron. Mater. **8**, 2200808 (2022).

[5] S. Prosandeev, S. Prokhorenko, Y. Nahas, Y. Yang, C. Xu, J. Grollier, D. Talbayev, B. Dkhil, and L. Bellaiche, Phys. Rev. B **105**, L100101 (2022).

[6] M. F. Sarott, M. D. Rossell, M. Fiebig, and M. Trassin, Nat. Commun. **13**, 3159 (2022).

[7] X. Shi, J. Wang, X. Cheng, and H. Huang, Adv. Theor. Simul. **5**, 2100345 (2022).

[8] A. Gruverman, D. Wu, H. Lu, Y. Wang, H. W. Jang, C. M. Folkman, M. Y. Zhuravlev, D. Felker, M. Rzchowski, C. B. Eom, and E. Y. Tsymbal, Nano Lett. **9**, 3539 (2009).

[9] K. U. Demasius, A. Kirschen, and S. Parkin, Nat. Electron. **4**, 748 (2021).

[10] W. Zhong, D. Vanderbilt, and K. M. Rabe, Phys. Rev. B **52**, 6301 (1995).

[11] T. Nishimatsu, U. V. Waghmare, Y. Kawazoe, and D. Vanderbilt, Phys. Rev. B **78**, 104104 (2008).

[12] T. Nishimatsu, M. Iwamoto, Y. Kawazoe, and U. V. Waghmare, Phys. Rev. B **82**, 134106 (2010).

[13] F. Mayer, M. N. Popov, D. M. Evans, S. Krohns, M. Deluca, and J. Spitaler, Phys. Rev. B **106**, 064108 (2022).

[14] A. Paul, J. Sun, J. P. Perdew, and U. V. Waghmare, Phys. Rev. B **95**, 054111 (2017).

[15] R. D. King-Smith and D. Vanderbilt, Phys. Rev. B **49**, 5828 (1994).

[16] L. Bellaiche, A. García, and D. Vanderbilt, Phys. Rev. Lett. **84**, 5427 (2000).

[17] L. Bellaiche, A. García, and D. Vanderbilt, Ferroelectrics **266**, 41 (2002).

[18] C. Mentzer, S. Lisenkov, Z. G. Fthenakis, and I. Ponomareva, Phys. Rev. B **99**, 064111 (2019).

[19] A. R. Akbarzadeh, S. Prosandeev, E. J. Walter, A. Al-Barakaty, and L. Bellaiche, Phys. Rev. Lett. **108**, 257601 (2012).

184

[20] L. Bellaiche and D. Vanderbilt, Phys. Rev. B **61**, 7877 (2000).

[21] T. Nishimatsu, A. Grünebohm, U. V. Waghmare, and M. Kubo, J. Phys. Soc. Jpn. **85**, 114714 (2016).

[22] F. Mayer, M. N. Popov, P. Ondrejkovic, J. Hlinka, J. Spitaler, and M. Deluca, Phys. Rev. B **106**, 224109 (2022).

[23] V. Veerapandiyan, M. N. Popov, F. Mayer, J. Spitaler, S. Svirskas, V. Kalendra, J. Lins, G. Canu, M. T. Buscaglia, M. Pasciak, J. Banys, P. B. Groszewicz, V. Buscaglia, J. Hlinka, and M. Deluca, Adv. Electron. Mater. **8**, 2100812 (2022).

[24] S. Lin, S. Yu, and D. Talbayev, Phys. Rev. Appl. **10**, 044007 (2018).

[25] H. Hirori, A. Doi, F. Blanchard, and K. Tanaka, Appl. Phys. Lett. **98**, 091106 (2011).

[26] See Supplemental Material at http://link.aps.org/supplemental/10.1103/PhysRevB.107.184307 for further simulations on stability, reversibility, and saturated polarization.

[27] R. Khachaturyan, A. Dimou, and A. Grünebohm, Phys. Status Solidi—Rapid Res. Lett. **16**, 2200038 (2022).

# Supplemental Material

## Hidden phases in homovalent and heterovalent substituted BaTiO$_3$

Florian Mayer[1,*], Marco Deluca[1], Maxim N. Popov[1]

[1]Materials Center Leoben Forschung GmbH, Roseggerstrasse 12, 8700 Leoben, Austria

*e-mail: florian.mayer@mcl.at

## I.     ADDITIONAL STABILITY TESTS

In this section, additional stability simulations for lower concentrations of Zr and Nb will be discussed. The first example is the composition BZT05 with 5% of Zr. The temperature used in the simulations was again set to 20 K. The corresponding results can be seen in Figure S1. Compared to the results for BZT35 (35% Zr) from the main paper, increased integration to a higher saturated polarization over time and a greater number of distinguishable intermediate states can be discerned. Stability over several hundred picoseconds is observed for the intermediate states considered. Furthermore, it is also observed here that the spacing between the states decrease with increasing polarization. This is due to the fact that as the saturated polarization is approached, simply only small subregions of the local dipoles are aligned anymore, since most of the dipoles are already aligned.
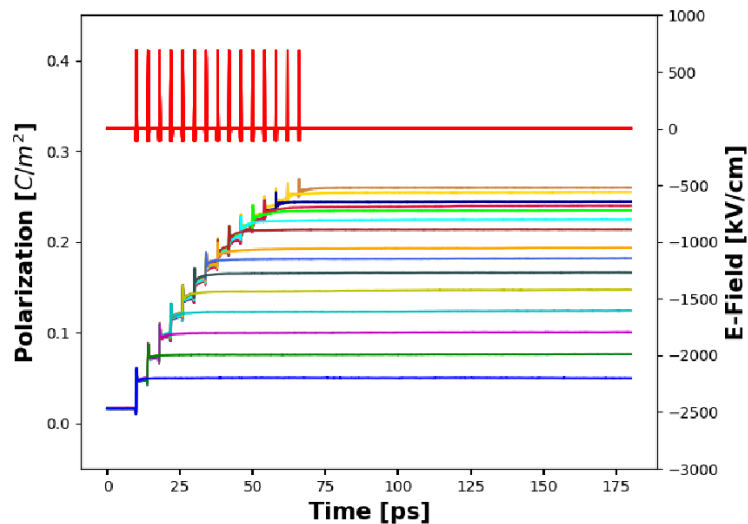


*Figure S1. Stability of intermediate states in BZT05 (5% Zr) at 20 K obtained from MD simulations.*

1

An analogous study was performed for the composition BNT05 (5% Nb), with the associated results shown in Figure S2. Again, an integration to a higher saturated polarization is observed compared to BNT15 (15% Nb) from the main paper. Furthermore, the number of distinguishable intermediate states is also increased compared to BNT15. The stability of the intermediate states at the chosen temperature of 20 K is present over several hundred picoseconds. However, we have to speak of metastable states here as well, since the simulations can only run for a certain time due to existing limitations by computational resources. Furthermore, a creep of the polarization is also observed for the concentrations presented here, although this creep is smaller than for larger concentrations.
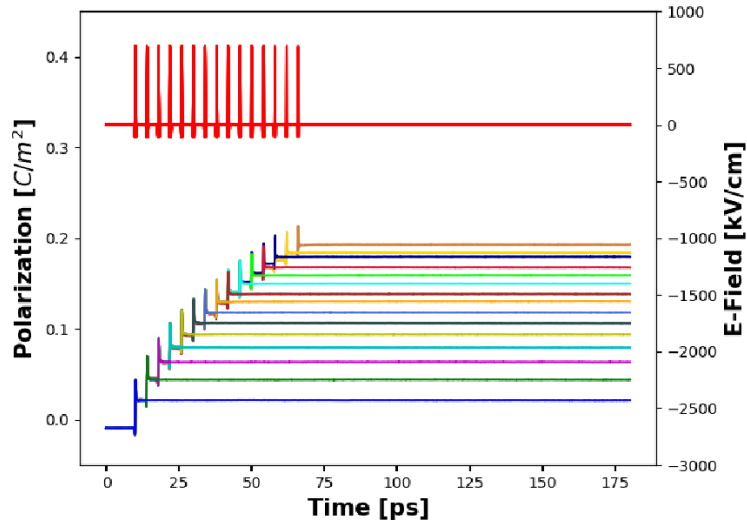


*Figure S2. Stability of intermediate states in BNT05 (5% Nb) at 20 K obtained from MD simulations.*

# II.    ADDITIONAL REVERSIBILITY TESTS

In this section, the reversibility of the induced polarization states for lower concentrations of Zr in BZT will be investigated. For this purpose, the composition BZT05 (5% Zr) was chosen as an example. This system shows an integration to higher saturated polarization compared to the lower achievable saturated polarizations in higher concentrations. The simulations were again performed at a temperature of 20 K. The procedure was as described in the main paper. That is, first the system was thermalized for a duration of 200 ps. Then, a train of pulses with positive amplitudes was applied. Subsequently, the amplitude of the train of pulses was inverted and the response of the system was monitored. The results for BZT05 when the identical pulses are used for the positive and negative train can be seen in Figure S3. Here, integration of the polarization is first observed until it approaches saturated polarization. Since the approach to this saturated polarization is rather slow, the train of pulses was inverted ahead of time. The result shows that the same only inverted pulse is not able to permanently change the induced polarization state again. Only small negative peaks are observed and these immediately relax back to the saturated polarization state. The latter represents an almost single-domain state for the considered system and,

2

therefore, it can be explained why the pulse train is incapable of changing this state. A multi-domain state offers enough flexibility for the train of pulses to change individual domains in size and orientation. In a single-domain state, however, the generation of differently poled subdomains is made much more difficult due to the strong correlation between the dipoles. If, for example, higher concentrations are used, these interrupt the correlation and the reversal of polarity of individual dipoles becomes much easier.
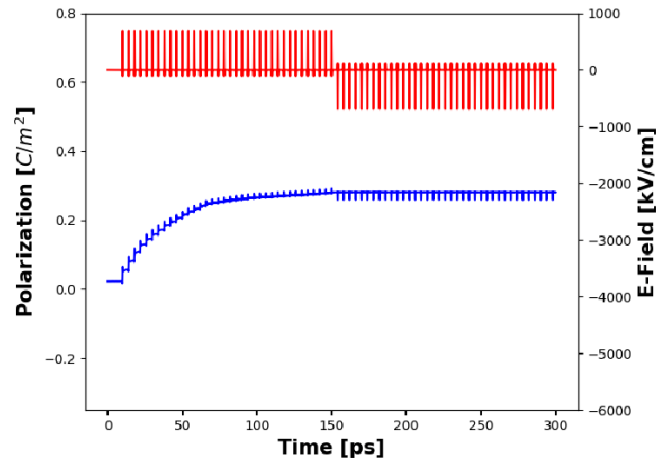


*Figure S3. Reversibility in BZT05 (5% Zr) at 20 K. Trying to invert the induced polarization state by the same pulses with opposite direction.*

A possibility to still escape the induced single-domain state can be found in increasing the amplitude of the pulse chain. For the case of BZT05, different amplitudes were tried and it turned out that the negative pulse has to be about three times stronger to achieve a change. The corresponding results for reversibility due to a tripled pulse with negative sign can be seen in Figure S4. Other methods for reversibility of induced polarization states are discussed in the main paper.
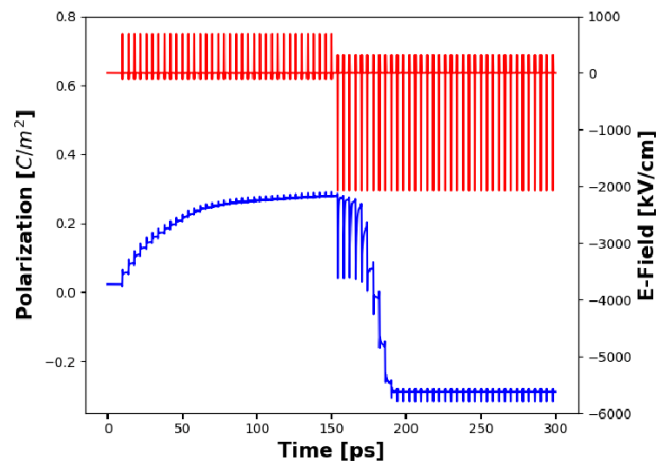


*Figure S4. Reversibility in BZT05 (5% Zr) at 20 K. Trying to invert the induced state by tripling the pulses with opposite direction.*

3

# III.   SATURATED POLARIZATION

Another property that can be revealed by the MD simulations is the maximum saturated polarization that can be achieved as a function of concentration. Basically, this information can be taken from Figures 1 and 3 from the main paper. Here the simulation was started with random as well as with completely aligned dipoles i.e. a kind of single-domain configuration. The results for BZT can be seen in Figure S5. For the random initial configuration, three regions with distinct behavior can be observed in Figure S5a: 1) 0-5%; 2) 5-20%; 3) >20%. In region 1, there is an almost linear increase of polarization as a function of Zr content. Here, adding Zr appears to facilitate breaking the long-range order in the domains by fragmenting them and, hence, aiding the reorientation in response to the THz pulses.  However, at about 5% this effect reaches its limits and another phenomenon becomes dominant – the unit cells containing Zr atoms exhibit negligible dipole moment and do not partake in responding to the external E-field. As a consequence, further increase of Zr content leads to lowering polarization in region 2. In region 3, interactions between Zr atoms and the dielectric response of polar nanoregions lead to a significantly non-linear behavior. The evolution of polarization of the single-domain configuration as a function of Zr content is shown in Figure S5b. Here, an approximately linear decrease in saturated polarization is observed when the concentration increases, with a change in slope at about 20%. This is to be expected due to the almost non-polar behavior of Zr unit cells.
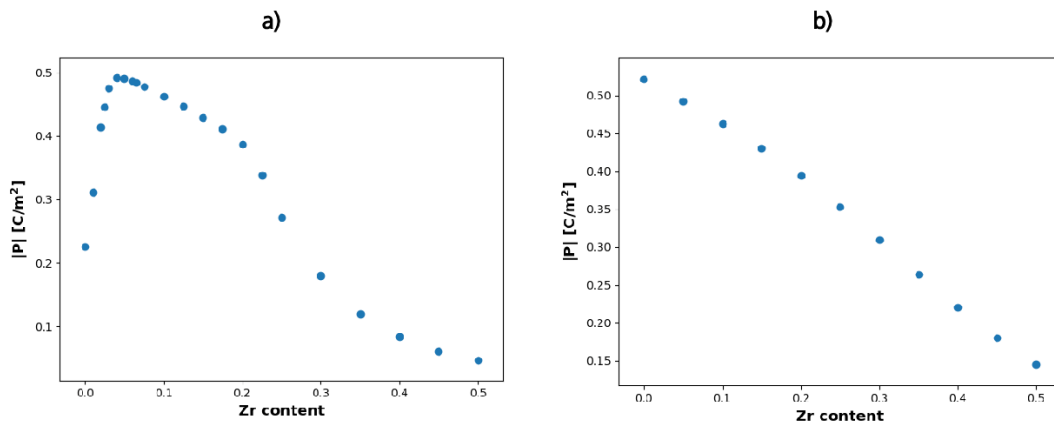


*Figure S5. Total saturated polarization of BZT as a function of concentration obtained from MD simulations starting with: a) random distribution; b) an induced single-domain state. The polarization shown was obtained after thermalizing the system for 200 ps.*

The saturated polarization can be extracted analogously for BNT as shown in Figure S6. Here, the trends are similar to those of BZT, however, the regions 1 to 3 are less pronounced and one can observe slight deviations from linearity in regions 1 and 2. Furthermore, the decrease in BNT is stronger per unit of Nb content as compared to BZT.

4
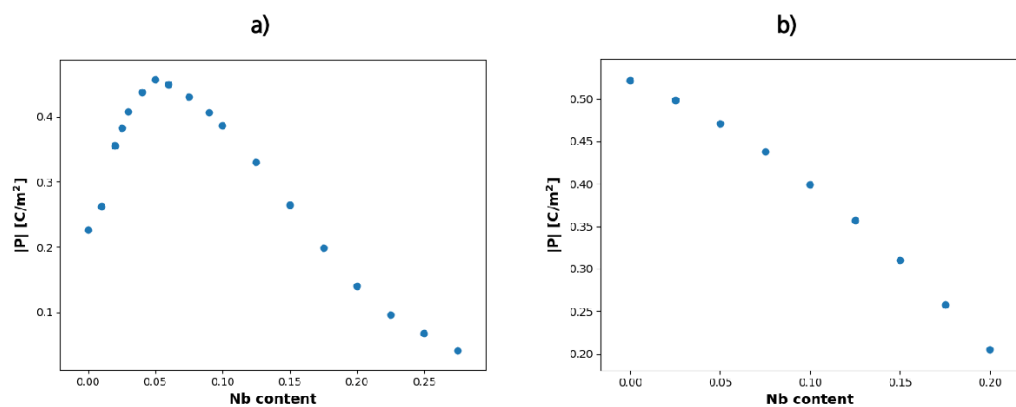
*Figure S6. Total saturated polarization of BNT as a function of concentration obtained from MD simulations starting with: a) random configuration; b) an induced single-domain state. The polarization shown was obtained after thermalizing the system for 200 ps.*

5

# 9 Continuative Studies

In this chapter, additional results of this thesis will be discussed, which are not yet part of a publication. These include the determination of the recoverable energy from simulations of the P-E hysteresis loop, the computation of the frequency-dependent permittivity, or the application of the effective Hamiltonian for the investigation of nanoscale topological objects in ferroelectrics.

## 9.1 Recoverable Energy Density

In the context of Publication 3, several simulations have been presented that include the ability to simulate hysteresis curves at different concentrations and temperatures. The rationale behind the development of the methods in this work is based on the ability to predict properties that are important for the practical implementation of said materials. Therefore, in this chapter, the possibility of determining the recoverable energy shall be demonstrated, which is important for the application of materials in dielectric capacitors. Such a workflow could indeed become a predictive tool to design compositions with excellent properties in light of energy storage applications, provided that the methodology is automated and embedded into materials accelerator loops. The basis for such a calculation has already been prepared in detail in the introductory Chapter 2.3, where Equations 9 and 10 are employed here. These integrals are to be applied to the hysteresis curves obtained by MD simulations. However, the actual implementation required numerical methods and was performed using Python scripts. Here, the data were first averaged over the different cycles, and then the recoverable energy, as well as the total energy, were determined using a numerical integration procedure. The study shown here is limited to the Zr-substituted BT (BZT) but can be performed analogously for the case of Nb substitution (BNT). The results for the recoverable energy as a function of temperature and concentration in BZT can be found in Figure 11. It must be stated here that the calculated energies should only be compared relative to each other. The absolute values are difficult to compare due to the differences in the applied field strengths between the simulation and experiment (i.e. dependence on voltage level, material thickness, and so on). See Publications 2 and 3 for more details on that topic. The maximum field strength applied in the hysteresis simulations associated with the results shown in Figure 11 was 100 kV/cm. The concentration trend in Figure 11 indicates a peak at a specific temperature, beyond which the recoverable energy decreases. BZT05 (5% Zr) exhibits the highest value at 400 K, just above the paraelectric to the ferroelectric phase transition. Figure 11b shows the associated losses, revealing that high temperatures produce a nearly loss-free hysteresis curve attributed to

paraelectric behavior. As the temperature decreases, the losses gradually increase, with smaller concentrations showing higher losses due to ferroelectric behavior. At higher concentrations, the substitution disrupts long-range interaction, narrowing the hysteresis curve. This results in fewer losses but at the expense of the saturated polarization.
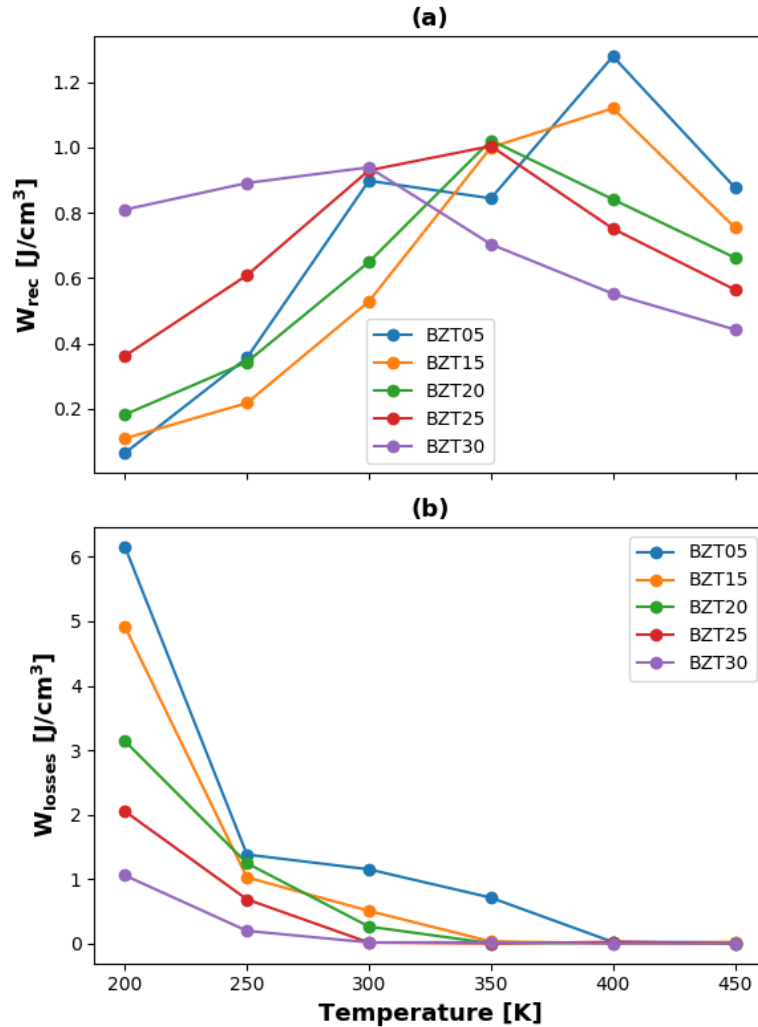


*Figure 11. Recoverable energy density from MD simulations for different concentrations of Zr in BZT obtained at different temperatures. (a) shows the recoverable energy density as a function of temperature and concentration. (b) illustrates the associated losses as a function of temperature and concentration. The associated hysteresis loops were obtained using a maximum field of 100 kV/cm and a frequency of 1 GHz.*

For practical applications, temperatures close to room temperature are more relevant. Therefore, in Figure 12, the energy densities have been plotted against Zr content at 300 K. It is observed that losses are minimal at higher concentrations, which is expected because long-range interaction is suppressed, allowing nanoscale dipoles to align to the external field more efficiently. Additionally, the maximum recoverable energies are observed at higher concentrations, where a balance between maximum saturated polarization and low losses is

necessary for high recoverable energy. The maximum energy stored is found at BZT05, being in a ferroelectric state at 300 K. At this concentration, however, there are still large losses due to the ferroelectric long-range order. Thus, for energy storage applications, compositions with concentrations 20%-25% should be considered. At these Zr contents, the ferroelectric long-range order is disrupted to an extent that losses are minimized (i.e. slim hysteresis loop), but the saturated polarization is still very high. Above 25%, the polarization decreases (i.e. due to further size reduction of polar nanoregions), and this is associated with a decrease in the recoverable energy density. It should be taken into account, of course, that the results were calculated for an oscillating field with a frequency of 1 GHz. For lower frequencies, the results might be slightly different. These, however, require very long MD calculations (cf. details in the next chapter) and were not carried out here.
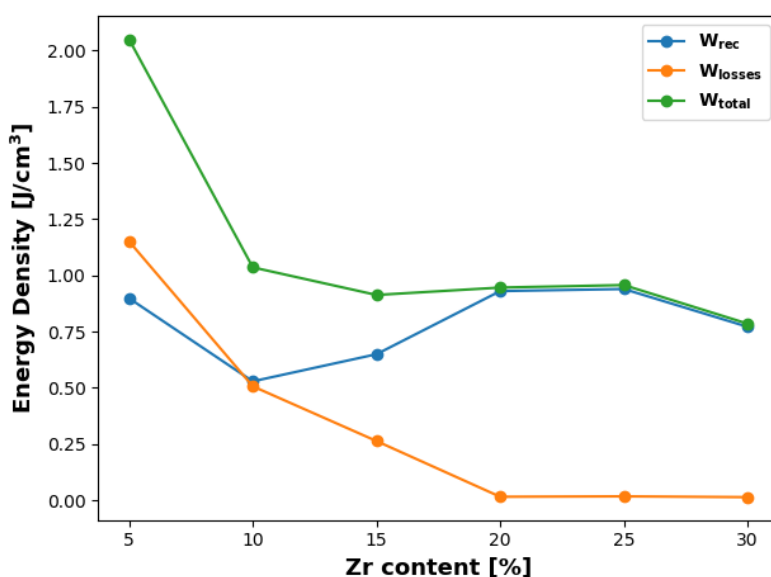


*Figure 12. Illustration of recoverable energy density, losses, and total energy as a function of concentration in BZT obtained from MD simulations. The results are obtained at a temperature of 300 K.*

Overall, the purpose of this chapter is to illustrate that simulations can be used to scan a wide range of concentrations and temperatures for practical properties for energy storage. The required simulations can be performed efficiently, and any promising materials can be identified. However, a comparison of absolute values is only partially possible due to the deviations in electric field strengths mentioned in Publications 2 and 3.

## 9.2   Frequency-Dependent Susceptibility

In the timeframe of this thesis, the frequency-dependent susceptibility of a considerable number of BZT and BNT compositions at different temperatures has also been simulated. In this chapter, however, only a part of them will be presented to showcase what these calculations can

deliver. The focus is on the compositions BZT50 (50% Zr) and BNT15 (15% Nb), which both display relaxor behavior. The basis for the calculation has already been laid in Chapter 4.2.3, and Equation 43 is to be applied here. In principle, this equation consists of two parts. The first part describes the static part of the susceptibility, whereas the second part gives the frequency-dependent contribution. The calculation of the first part is straightforward and has already been discussed in detail in Publication 3. For the second part, the autocorrelation function for the trajectory of the polarization values must be calculated from the MD simulations. This can be done quite efficiently using Fast Fourier transformation (FFT) algorithms. The MD simulations required for these calculations differ somewhat from those shown so far because the frequency range that can be calculated depends on the length of the trajectory. That is, the longer the MD simulation, the larger the frequency range becomes toward smaller frequencies. For the following calculations, MD simulations with a total simulation time of 1.2 ns were employed. Furthermore, a supercell of size 20x20x20 was applied, and the simulations were carried out at temperatures between 450 K and 10 K in steps of 5 K. The remaining settings are analogous to the simulations presented in Publication 3. The results of the MD simulations shall now be used to investigate the dispersion of susceptibility as a function of temperature and frequency. For this purpose, the frequency-dependent susceptibility must first be calculated for each temperature and then plotted over the different temperatures. The result for BZT50 can be seen in Figure 13, where the real and imaginary parts of the susceptibility were plotted versus temperature and frequency. The result shows a dispersion of the susceptibility, which can be recognized by the shift of the susceptibility peaks to higher temperatures when the frequency is increased. Furthermore, a decrease in the absolute values is observed when the frequency increases. A comparison with Figure 4 from Chapter 2.2 shows that this behavior is a main feature of relaxor ferroelectrics [13]. This finding is crucial because it indicates that the parameterization of BZT is capable of replicating the distinctive behavior observed in the relaxor region. In addition, Publication 1 provides a means for conducting a comparison with experimental data.

194
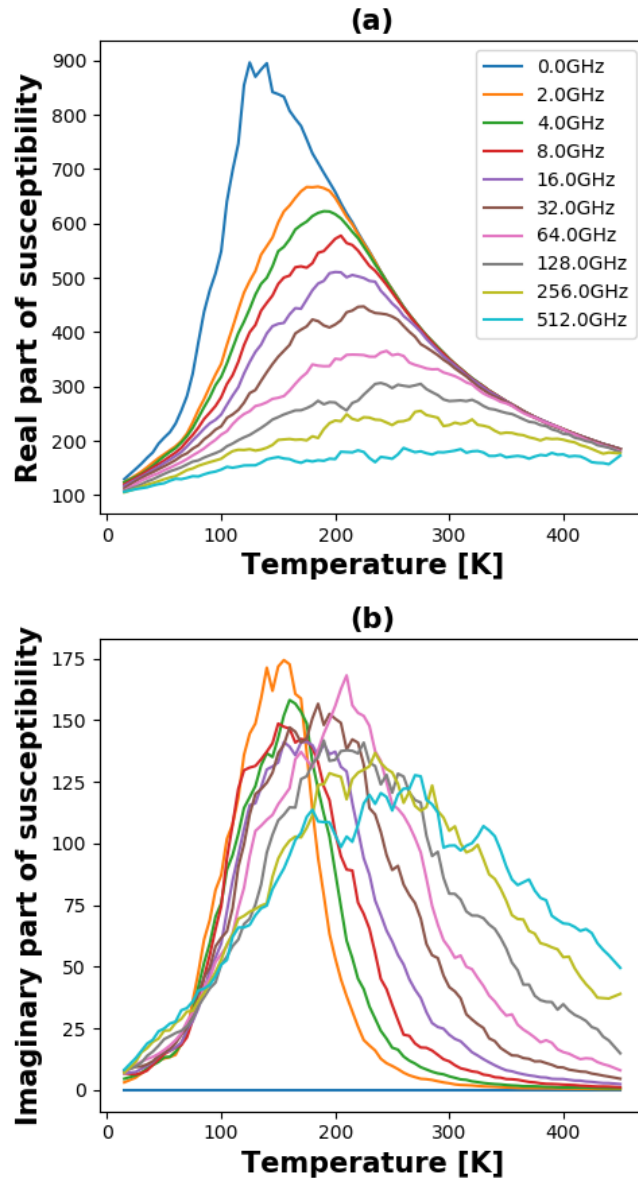
*Figure 13. Susceptibility of BZT50 (50% Zr) as a function of temperature and frequency. (a) shows the real part of the susceptibility. (b) shows the imaginary part of the susceptibility.*

An analogous study is now to be carried out for BNT15. The MD simulations required for this composition were carried out analogously with the above settings. The results for the susceptibility as a function of temperature and frequency can be found in Figure 14. Again, the real and imaginary parts of the susceptibility were plotted. Dispersion can be seen in the real part, characterized by the shift of the peaks to higher temperatures when the frequency is increased. This behavior is again characteristic of relaxor ferroelectrics [13] and shows that the parameterization of BNT15 is able to reproduce this behavior. Furthermore, Publication 1 can be used for comparison with experimental data.
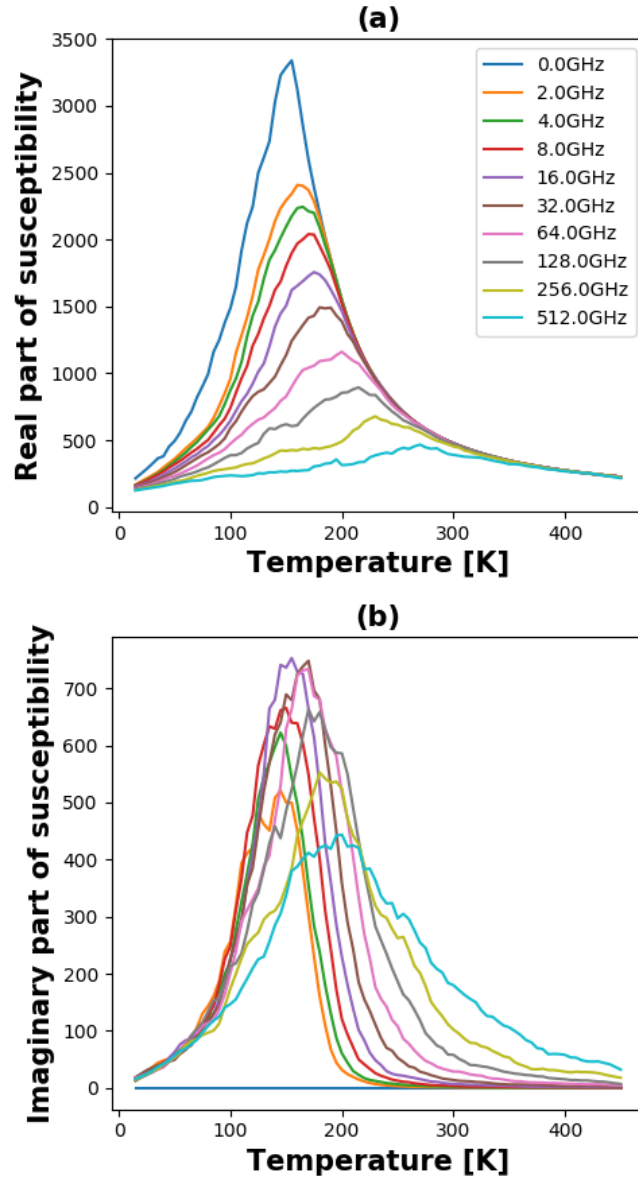
*Figure 14. Susceptibility of BNT15 (15% Zr) as a function of temperature and frequency. (a) shows the real part of the susceptibility. (b) shows the imaginary part of the susceptibility.*

All in all, this short chapter shall show the possibility of such calculations by using effective Hamiltonians. The calculation of the frequency-dependent susceptibility for the compositions BZT50 and BNT15 shows, for both cases, a dispersion that is to be expected in this concentration range (see Publication 1 for experimental data) and is distinctive of relaxor behavior. A more detailed study of frequency-dependent susceptibility by the developed models is planned for the future.

## 9.3 Antiskyrmions in BaTiO₃

Skyrmions are topological solitons that can occur in certain magnetic materials, such as thin films or multilayers, where the interactions between electron spin lead to a complex order parameter [106,107]. These solitons are characterized by a localized region of magnetic order

with a topological charge [108,109], meaning that they cannot transition to the uniform background state without creating a singularity. Even though skyrmions are usually associated with magnetic materials, recent research [110–115] has shown that they can also be found in nonmagnetic ferroelectrics, i.e., materials that exhibit spontaneous electric polarization. In nonmagnetic ferroelectrics, the electric polarization can couple with other degrees of freedom, such as strain or lattice distortions, which can lead to a complex order parameter. This coupling can lead to the formation of skyrmions in these materials, where the skyrmion has a topological charge [108,109] due to the localized order region. Examples of the occurrence of skyrmions in ferroelectric materials were found in superlattices [115] of lead titanate ($PbTiO_3$) and strontium titanate ($SrTiO_3$), but also pure $PbTiO_3$ can theoretically exhibit skyrmions [114] under certain conditions.

In this chapter, it will be demonstrated that such topological objects can also be theoretically observed in pure $BaTiO_3$ (BT). The inspiration for this study came from a recently published article on arXiv about topological objects in rhombohedral BT by Goncalves et al. [116]. Although this work is still under review at the time of this thesis, the findings of their work shall be reproduced, and additional investigations will be carried out in this chapter. To better comprehend the following concept, a brief overview of the work of Goncalves et al. [114] must be provided. Their research demonstrated the potential to stabilize skyrmions in pure $PbTiO_3$ by introducing a nanodomain into the ferroelectric phase. The ferroelectric phase of $PbTiO_3$ is tetragonal, which means that polarization takes place in the <001> direction, also referred to as the z-axis. To begin with, a system in a single-domain state is assumed in which the polarization direction is aligned in the +z direction, i.e., all local dipoles are uniformly oriented. When a nanodomain is now introduced along the polarization direction but with opposite polarization, a skyrmion with a topological charge of $Q = 1$ forms around this nanodomain [114].

The idea from Ref. [116] is based on observations of $PbTiO_3$, specifically, what happens when a nanodomain is introduced into rhombohedral BT along the polarization direction. It should be noted that the polarization in rhombohedral BT is found along the <111> direction. Figure 15 shows a visualization of such a nanodomain, which was created by constructing a supercell of size 40x40x40 and aligning all dipoles along the <111> direction. A script was then created to induce a nanodomain along this direction with opposite polarization, with a diameter of approximately 18 unit cells for this case.
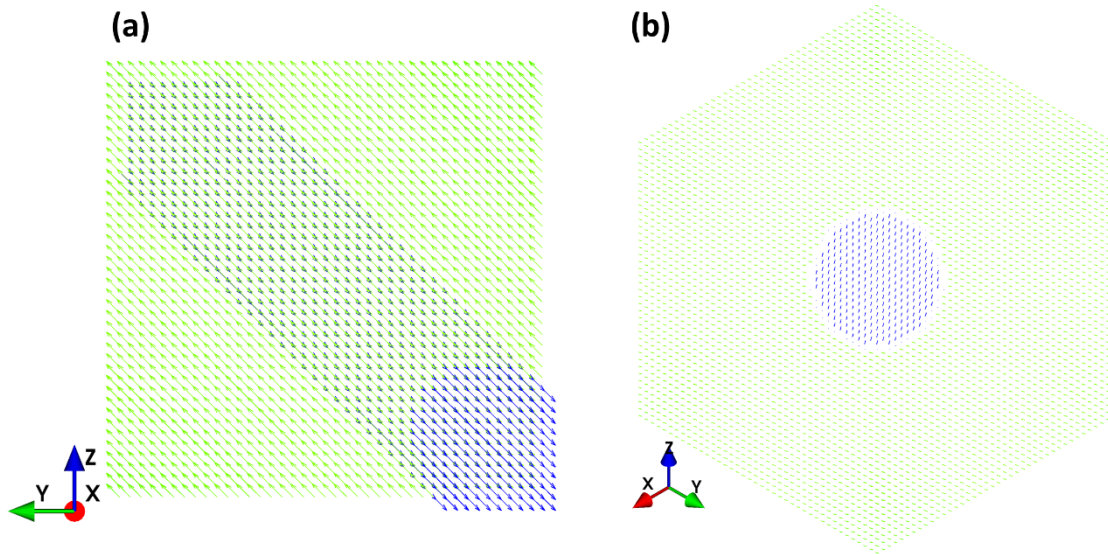
*Figure 15. Illustration of a 40x40x40 supercell of rhombohedral $BaTiO_3$ including a nanodomain along the <111> direction with opposite polarization. (a) shows the side view of the supercell as a projection along the <001> direction. (b) shows the projection along the <111> direction. The blue color represents the z-component of the polarization.*

In the following, MD simulations based on the models developed in Publication 2 are shown. It should be noted that the methodology used in this study involves effective Hamiltonians, which differs from the simulations conducted by Goncalves et al. [116], who used core-shell potentials. Additionally, the study presented here employs much larger unit cells, which minimizes any influences of boundary conditions. First, a low temperature of 1 K shall be considered to exclude temperature-induced fluctuations as far as possible. Furthermore, the Nose-Poincare thermostat was chosen here to keep the temperature constant. The simulations of the 40x40x40 supercell were performed over a period of 200 ps choosing the starting configuration of the dipoles from Figure 15. Furthermore, a dead layer was introduced at the boundaries of the nanodomain. To study the evolution over time, snapshots were written out at different time steps. The results of the MD simulations can be observed in Figure 16. Here, the snapshots were plotted as a projection along the <111> direction. The color mapping, in this case, is different from Figure 15 and represents the absolute length of the dipoles. At the starting point of the simulation at 0 ps, the configuration from Figure 15 is evident, with the nanodomain in the center having an inverted polarization compared to the surrounding matrix. If the simulation is now started, the local dipoles can relax. It is observed that already after 1 ps, a pattern emerges which shows vortices of local dipoles. This pattern remains until the end of the simulation at 200 ps.
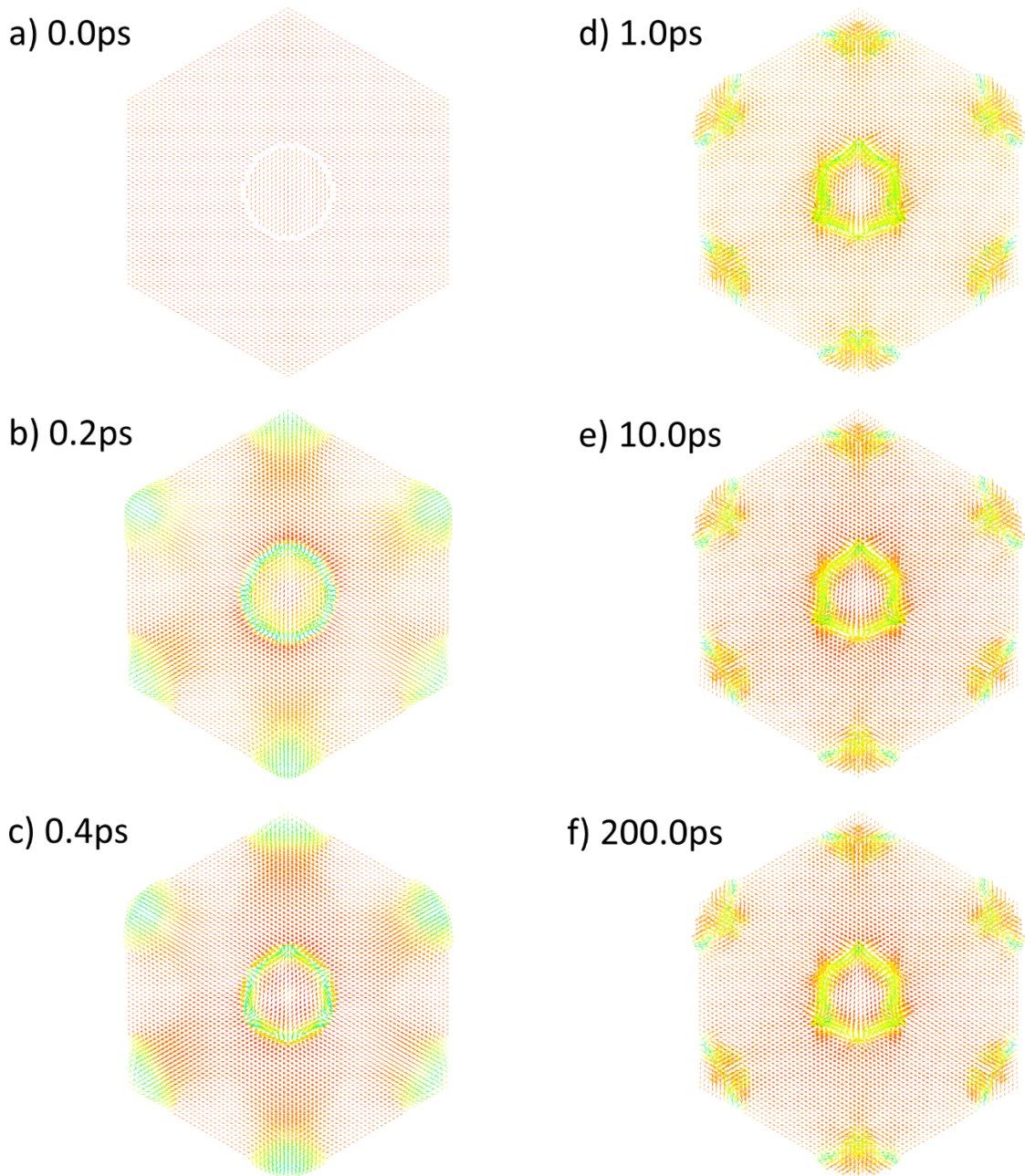
*Figure 16. Time evolution of MD simulation of the 40x40x40 supercell of rhombohedral $BaTiO_3$ with induced nanodomain along the <111> direction at a temperature of 1 K. The plots show a projection of the supercell along the <111> direction at different time steps. The color represents the total length of the polarization. (a) shows the starting configuration where a nanodomain with opposite polarization along the <111> direction was induced.*

The above results show that there are vortices of local dipoles around the introduced nanodomain, which are stable over a considerable period of time. To better understand these results, this pattern needs to be studied in more detail. For this purpose, a script was first written which can write out cross sections of the supercell perpendicular to the <111> direction. Such a cross-section is shown in Figure 17 for the time step at 200 ps from the above simulation. In

this figure, it is clear that a highly symmetric arrangement of different vortices of the dipoles results here. The local vortices show opposite rotations and produce a symmetric arrangement around the nanodomain. Whether such a pattern is a topological object can be investigated in more detail by calculating the topological charge. This can be calculated for a 2D grid of dipoles using the definition of Berg and Lüscher [117], as evident in the work of Heo et al. [108]. Since no electron spins are used here, the local dipoles must be included in the equations. Furthermore, the elementary triangles must be chosen to be consistent with the definition. To obtain the correct topological charge, the normalized vectors of the local dipole moments must be used. In this work, a script has been prepared which can perform such a calculation and therefore determine the topological charge for the cross sections considered. Remarkably, for the cross section from Figure 17, using this approach, a topological charge of $Q = -2$ is obtained. The numerical value resulting directly from the calculation is $Q = -1.998$. Such a negative topological charge is assigned to the topological object of an antiskyrmion. This result is in excellent agreement with the observations of Goncalves et al. [116].
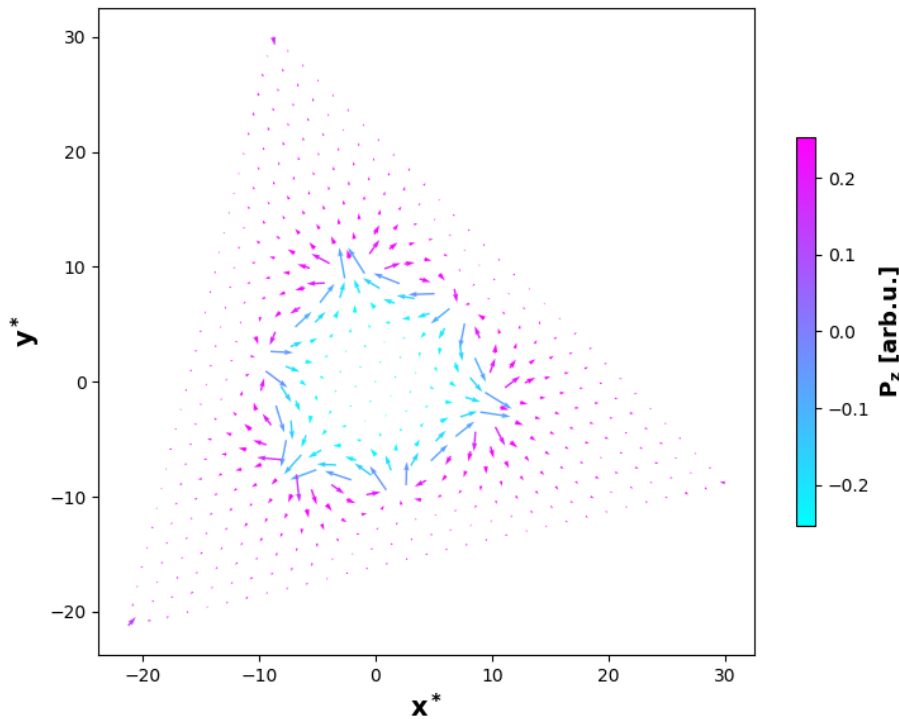


*Figure 17. Cross section through the 40x40x40 supercell from a snapshot at 200 ps. The cross-section represents a plane perpendicular to the <111> axis of the supercell. The arrows visualize the in-plane local dipole moments. The color represents the out-of-plane polarization.*

The advantage of the approach chosen here by effective Hamiltonians is that many different simulations can be performed quite inexpensively. It is interesting to carry out such simulations also at higher temperatures, which are more easily accessible by experiments. For this purpose,

again, the 40x40x40 supercell was taken, and the simulation was started at a temperature of 1 K. Subsequently, the temperature was steadily increased with steps of 5 K, and snapshots were written out repeatedly. The simulation duration per temperature step was chosen to be 200 ps. The corresponding snapshots at different temperatures can be found in Figure 18. At low temperatures, the already-known dipole pattern from the above results appears. If the temperature is now steadily increased, the fluctuations of the dipoles become stronger. However, the antiskyrmion manages to remain stable over a large temperature range. Only at a temperature above 101K does the surrounding matrix swallow the antiskyrmion, and a single-domain state is established.
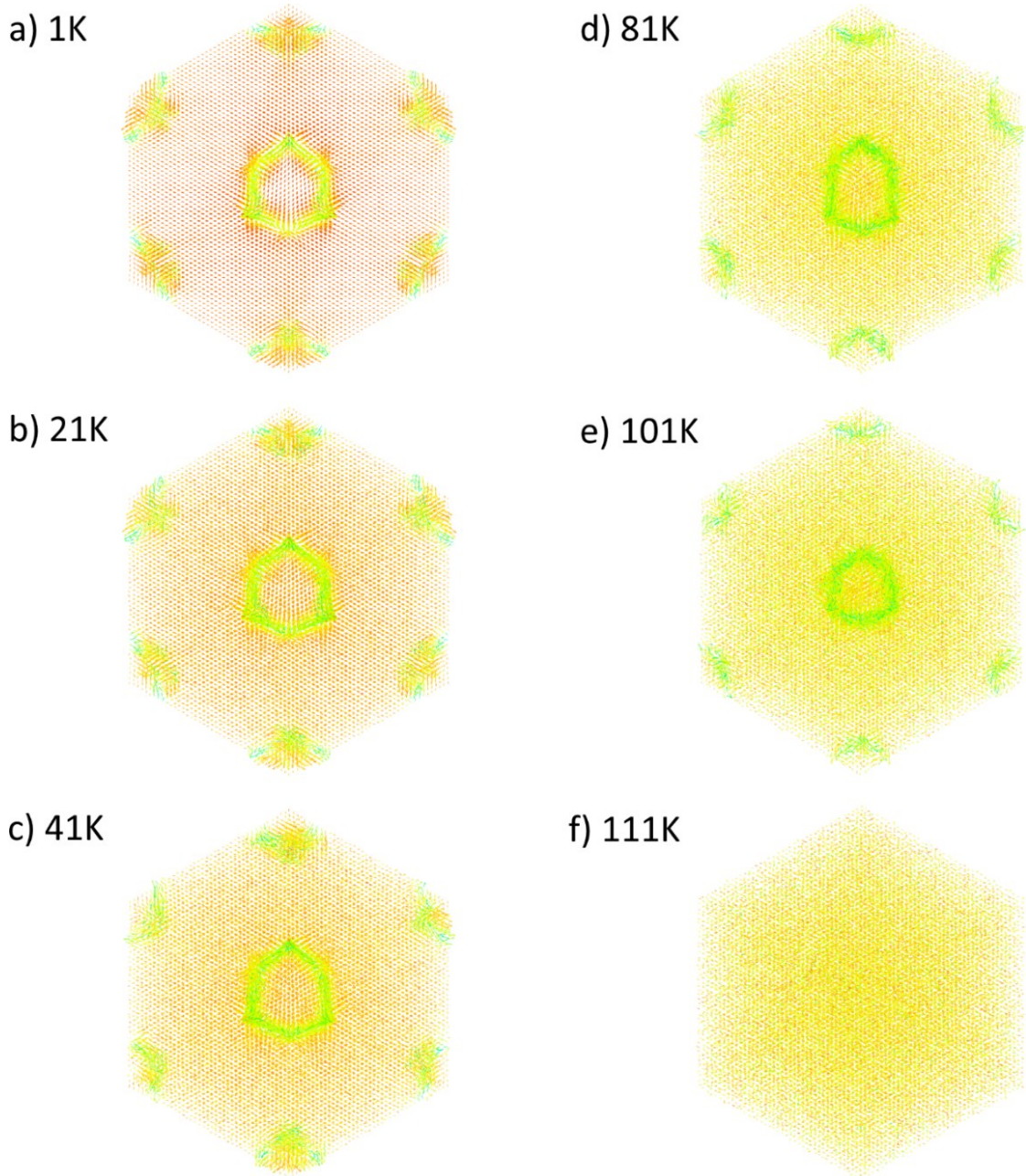
*Figure 18. Temperature evolution of antiskyrmion in rhombohedral $BaTiO_3$ using MD simulations and a 40x40x40 supercell. The temperature was steadily increased by steps of 5 K. The plots show a projection of the supercell along the <111> direction at different temperature steps.*

As a final step, the influence of nanodomain diameters will be examined. To do so, the supercell size was increased to 100x100x100, allowing for the efficient use of the effective Hamiltonian. MD simulations were conducted on the rhombohedral phase of BT at a temperature of 1 K over 200 ps, introducing nanodomains of different diameters (9, 18, 24, and 36 unit cells) and observing their behavior. The nanodomain with a diameter of 9 unit cells disappeared after a few picoseconds and was swallowed by the surrounding matrix without producing an antiskyrmion. In contrast, a nanodomain with a diameter of 18 unit cells resulted in the formation of an antiskyrmion, as shown in Figure 19. The corresponding topological charge of

this antiskyrmion was found to be $Q = -2$ (obtained numerical value $Q = -2.00006$). For a diameter of 24 unit cells, a cross-section at 200 ps is illustrated in Figure 20. Also, in this case, an antiskyrmion results in the vicinity of the nanodomain. The topological charge also gives a value of $Q = -2$ (obtained numerical value $Q = -2.0001$). The occurrence of an antiskyrmion is also observed in the case of a diameter of 36 unit cells. The corresponding cross-section can be seen in Figure 21. The topological charge is again $Q = -2$ (obtained numerical value $Q = -2.0002$).
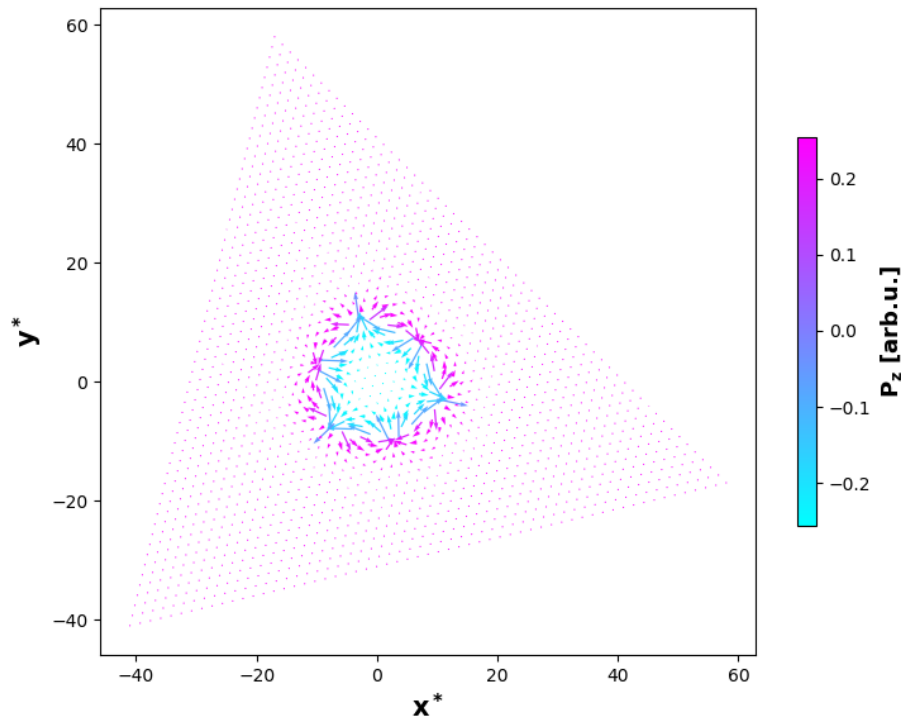


*Figure 19. Cross section of a 100x100x100 supercell containing a nanodomain with a diameter of 18 unit cells. The snapshot was taken after 200 ps. The simulation was carried out at 1 K. The cross-section represents a plane perpendicular to the <111> axis of the supercell. The arrows visualize the in-plane local dipole moments. The color represents the out-of-plane polarization.*
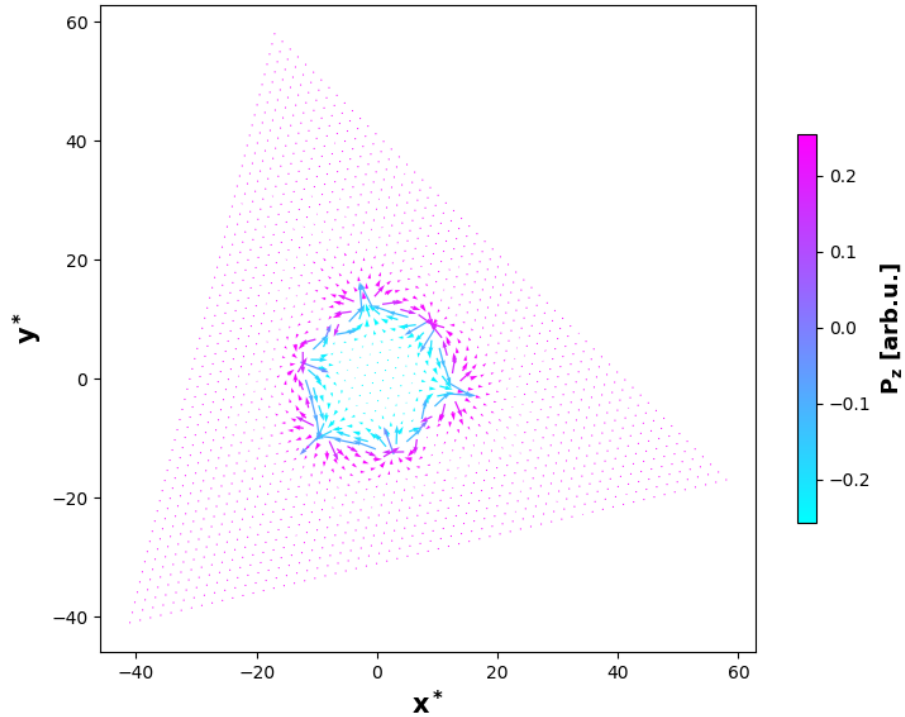
*Figure 20. Cross section of a 100x100x100 supercell containing a nanodomain with a diameter of 24 unit cells. The snapshot was taken after 200 ps. The simulation was carried out at 1 K. The cross-section represents a plane perpendicular to the <111> axis of the supercell. The arrows visualize the in-plane local dipole moments. The color represents the out-of-plane polarization.*
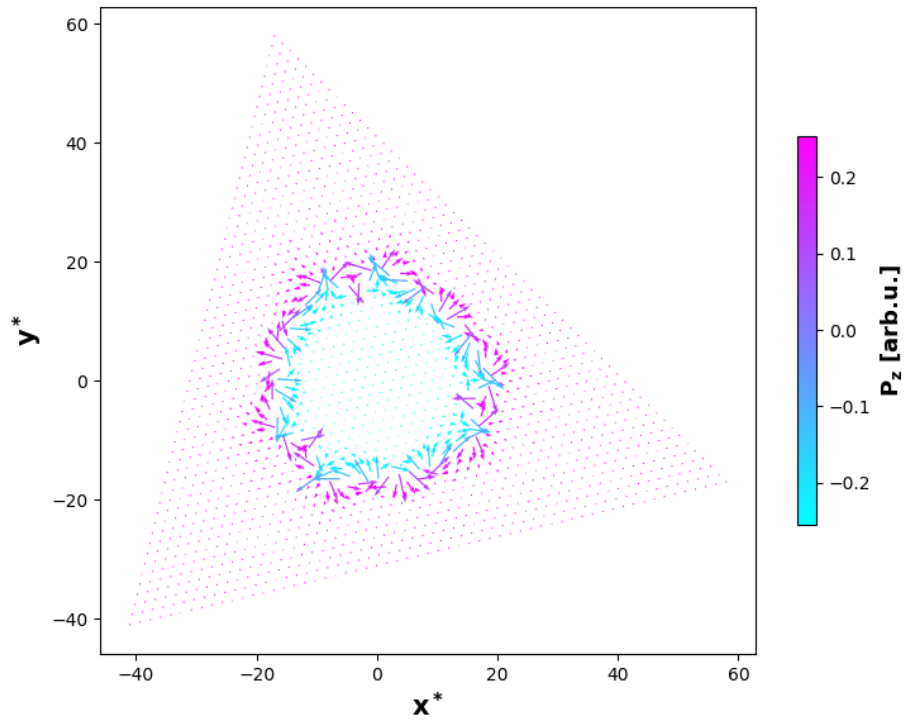


*Figure 21. Cross section of a 100x100x100 supercell containing a nanodomain with a diameter of 36 unit cells. The snapshot was taken after 200 ps. The simulation was carried out at 1 K. The cross-section represents a plane perpendicular to the <111> axis of the supercell. The arrows visualize the in-plane local dipole moments. The color represents the out-of-plane polarization.*

204

In summary, the following statements can be drawn about topological objects in BT: The introduction of nanodomains into the rhombohedral phase along the polarization direction of BT generates topological objects with a topological charge of $Q = -2$. These objects can be referred to as antiskyrmions due to the associated negative topological charge. The study tested the stability of an antiskyrmion using a 40x40x40 supercell at a low temperature of 1 K and observed its formation and stability over the simulated time period. Simulations were also conducted at different temperatures, revealing that antiskyrmions formed at low temperatures remain stable over a range of almost 100 K before transitioning to a single-domain state. The study also examined the effect of nanodomain diameter on antiskyrmion occurrence with supercells of size 100x100x100 and found that a minimum diameter is required for stabilization. The study confirms earlier findings of Goncalves et al. [116] but suggests the need for additional simulations to further explore the phenomenon, including the effect of supercell size, temperature, and nanodomain size. Future work may address these questions in subsequent publications.

# 10 Summary and Conclusion

In this final chapter, the main findings of this thesis and the resulting conclusions will be explained and summarized. The primary objective of this dissertation is to provide a theoretical description of ferroelectric materials, including solid solutions, which can further be used to predict application-relevant properties of substituted systems in order to enable a computationally based design of ferroelectric materials. The theoretical framework is based on density functional theory (DFT) and molecular dynamics (MD) simulations that rely on effective Hamiltonians. Publication 1 discussed the origin of relaxor (RF) behavior in homovalently and heterovalently substituted BT. Along with various experimental measurements, DFT calculations were performed to study these systems at the atomic level. The prime examples of such substituted variants of BT, which are shown in this publication as well as throughout the dissertation, are BZT and BNT. The difference between the two systems lies in the oxidation state of the substituents. In the case of BZT, $Zr^{4+}$ is substituted on the B-site of BT, while in BNT, $Nb^{5+}$ is substituted on the B-site. Publication 1 initially discussed general differences such as ionic radii, defect formation, or the different onset of RF behavior. BNT is of particular interest, where Raman spectroscopy and DFT calculations were utilized to prove the occurrence of Ti vacancies. This information was used to conduct more advanced DFT studies. The local deformation of BZT and BNT was studied, and in both cases, a local change in the lattice induced by the substituents was detected. Subsequently, the change in the total electric potential was investigated, and a strong effect of the substituents on the surrounding unit cells was found only for BNT. For BZT, in contrast, only a localized change in the potential was observed compared to the parent system BT. In summary, Publication 1 provides a detailed comparison of BZT and BNT and discusses both macroscopic and atomistic effects. The disruption of long-range correlation in BZT can be attributed to the non-polar Zr unit cells and their induced deformations of the lattice in the surrounding unit cells. In contrast, substitution by Nb is much more effective in disrupting ferroelectric long-range order due to the induced Ti vacancies and the associated disturbance of the total electric potential in addition to the induced strains.

In order to provide a comprehensive theoretical description of materials at finite temperatures, MD simulations were applied with the potential energy surface (PES) modeled through the use of effective Hamiltonians, which parameterize the PES on a local basis specified by phonon modes. In Publication 2, this approach was employed to parameterize the PES of the ferroelectric BT. Significant efforts were made to improve the accuracy of the PES description, including a complete revision of the local-mode self-energy and an extension of this approach

to incorporate additional phonon modes. Subsequently, a large set of DFT calculations was used to parameterize a significant number of parameters. In order not to lose the efficiency of the effective Hamiltonian, the formalism was constructed in a way that preserves the original form. The effects of the revised approach were studied using MD simulations. The phase diagram of BT was simulated, and a significant improvement in the phase transition temperatures was observed compared to experimental data. Furthermore, the simulations were used to also compare the permittivity as well as the P-E hysteresis curves with experiments. Again, good agreement was found, with the occurrence of a double-hysteresis loop also observed in BT near the transition between paraelectric and ferroelectric. All in all, an alternative scheme for the parameterization of effective Hamiltonians could be developed within the framework of this thesis, whereby improvements in the description of the PES could be achieved.

The effective Hamiltonian, which was developed and described in Publication 2, was used as a foundation for the development of a substituent integration concept. Similarly, a model was parameterized for two primary examples, BZT and BNT, to enable the calculation of properties at finite temperatures through MD simulations. As a result, Publication 3 focused on an alternative concept that extended the effective Hamiltonian, and corrections were implemented to attain the most precise description of the substituents concerning the parent system, BT. Several corrections were implemented, including the correction of kinetic energies, local-mode self-energy, long-range interaction, hydrostatic pressure, and an auxiliary spring system. While drawing inspiration from existing approaches in the literature, these corrections were extended with own ideas. The parameterization of these models was accomplished using DFT calculations and supercells up to sizes of 5x5x5. Following this, MD simulations were carried out using the developed models to calculate phase diagrams, P-E hysteresis loops, and other relevant properties. The simulated results for both BZT and BNT systems demonstrated good agreement with experimental data. Overall, this thesis successfully parameterized two precise models for BZT and BNT, offering deep insights into the dynamics of these systems.

In Publication 4, the previously developed models were utilized to conduct additional studies on BZT and BNT systems, with the objective of assessing their suitability for use in neuromorphic computing. Specifically, MD simulations were employed to investigate the systems' response to ultrafast terahertz (THz) pulses. The use of THz pulses facilitated the induction of states in the materials that are not present in thermodynamic equilibrium, commonly referred to as hidden phases. Publication 4 investigated various compositions exposed to THz pulses to determine the occurrence of hidden phases. In addition, properties

such as polarization integration through pulse train application were examined. Stability runs were conducted on selected concentrations to assess the stability of these hidden phases for potential use in neuromorphic computing systems. The study revealed that different compositions responded uniquely to THz pulses, but those within the concentration range of RF behavior demonstrated promising potential for neuromorphic computing applications.

## 10.1 Conclusive Remarks

Finally, the results obtained in this thesis as well as the related publications will be discussed, and final conclusions will be drawn. The discussion is divided into the four attached publications, which were published in the framework of this dissertation.

1. Publication 1 explored the underlying causes of RF behavior in BZT and BNT through a combination of experimental and theoretical approaches, yielding new insights into the phenomena. It was discovered that the long-range ferroelectric correlation in homovalent- or heterovalent-substituted systems is disrupted by fundamentally different effects. In the case of BZT, the disruption is caused by the local deformation of unit cells induced by the larger Zr cation being substituted on the B-site. In contrast, BNT requires the consideration of charge compensation via Ti vacancies, leading to complex defect structures, as well as local lattice deformation. Additionally, a significant change in electric potential beyond the substituted unit cells was observed in BNT, which more effectively breaks the long-range correlation of B-site displacements and thus explains the differences in the onset of RF behavior. However, further studies are needed to fully explain the onset of RF behavior, including the study of the dynamics and interaction of local dipoles and the role of polar and non-polar nanoregions.

2. In Publication 2, an alternative approach for the parameterization of effective Hamiltonians was presented, which enables the incorporation of additional phonon modes. The proposed concept involved adapting the local-mode self-energy and introducing a significant number of new parameters. However, the emphasis was placed on achieving an accurate description of the total energy rather than depending on individual parameters. The parameterization required a large set of DFT calculations but could be performed at a low cost due to the small unit cell. The approach also aimed to preserve the original form of the effective Hamiltonian to maintain its performance. MD simulations demonstrated a significant improvement in phase transition temperatures compared to reference simulations. Although this approach is not definitive and can be adapted in the future, it provides an accurate description of

ferroelectric materials with perovskite structure and can be built upon for further developments. These developments could include the expansion of the local-mode self-energy by further orders and the extension of other relevant energy terms.

3. Publication 3 presents the extension of the effective Hamiltonian for substituted versions and introduces an alternative scheme for the corrections. This approach is based on the findings of Publication 2 and accurately predicts phase transition temperatures for the studied systems. The development of the corrections is supported by comparing MD simulations with DFT calculations, emphasizing a precise description on a local basis. The resulting MD simulation results agree well with experimental data and provide valuable insights into the dynamics of the local dipoles. The developed models are available for free and can be used for further investigations, including the exploration of polar and non-polar nanoregions to address the remaining open questions from Publication 1. Additionally, the models permit the study of various compositions over a broad concentration range. In the future, the models can be expanded further, and the corrections for substitution effects can be refined. For instance, it is possible to increase the orders considered in the auxiliary spring system or reparametrize for other material systems.

4. Publication 4 employs all the methods developed in this thesis to explore the BZT and BNT compositions for their potential use in neuromorphic computing systems. The investigation of the systems' responses to ultrafast THz pulses represents a novel and fascinating area, providing profound insight into the dynamics of local dipoles. However, it should be noted that experimental investigation using ultrafast THz pulses is not currently feasible, and the potential properties demonstrated here should be regarded as a starting point for future research. Additionally, a more thorough understanding of the dynamics of local dipoles and the impact of concentration on relevant properties is necessary. As the most favorable properties are observed in the RF behavior range, such research is also complementary to the open questions posed in Publication 1.

The present thesis has conducted numerous DFT studies to enhance the understanding of the considered materials. Three effective Hamiltonians (i.e. for three different material systems) have been formulated and parametrized within this framework to enable the description of the materials at finite temperatures by implementing MD simulations. These models are now

available for free and can be utilized in future research endeavors to explore the fascinating properties of ferroelectric and relaxor ferroelectric materials. Moreover, this thesis demonstrated the feasibility of filtering prospective compositions for utilization in energy storage devices. This will enable the use of high-throughput simulations to supplement experimental work in the future. Additionally, this thesis delved into the study of topological objects in pure BT using the effective Hamiltonian, leading to the theoretical confirmation of antiskyrmions. This area of research presents a wealth of opportunities for future exploration.

# 11 References

[1] H. Ritchie, M. Roser, and P. Rosado, *Energy*, https://ourworldindata.org/energy. Accessed 02.03.2023.

[2] J. Mitali, S. Dhinakaran, and A. A. Mohamad, *Energy Storage Systems: A Review*, Energy Storage Sav. **1**, 166 (2022).

[3] P. A. Tipler and G. Mosca, *Physik*, 7. Aufl. 2 (Springer Spektrum, Berlin, Heidelberg, 2015).

[4] J. Gubbi, R. Buyya, S. Marusic, and M. Palaniswami, *Internet of Things (IoT): A Vision, Architectural Elements, and Future Directions*, Futur. Gener. Comput. Syst. **29**, 1645 (2013).

[5] L. Atzori, A. Iera, and G. Morabito, *The Internet of Things: A Survey*, Comput. Networks **54**, 2787 (2010).

[6] A. Al-Fuqaha, M. Guizani, M. Mohammadi, M. Aledhari, and M. Ayyash, *Internet of Things: A Survey on Enabling Technologies, Protocols, and Applications*, IEEE Commun. Surv. Tutorials **17**, 2347 (2015).

[7] V. Barot and D. Ritesh, *Energy Consumption Optimization in Internet of Things Applications: Concept and Techniques*, Int. J. Adv. Sci. Technol. **29**, 9743 (2020).

[8] S. O. Kasap, *Principles of Electronic Materials and Devices* (McGraw-Hill, 2006).

[9] V. Veerapandiyan, F. Benes, T. Gindel, and M. Deluca, *Strategies to Improve the Energy Storage Properties of Perovskite Lead-Free Relaxor Ferroelectrics: A Review*, Materials (Basel). **13**, 5742 (2020).

[10] V. V Shvartsman and D. C. Lupascu, *Lead-Free Relaxor Ferroelectrics*, J. Am. Ceram. Soc. **95**, 1 (2012).

[11] L. E. Cross, *Relaxorferroelectrics: An Overview*, Ferroelectrics **151**, 305 (1994).

[12] L. E. Cross, *Relaxor Ferroelectrics*, Ferroelectrics **76**, 241 (1987).

[13] A. A. Bokov and Z.-G. Ye, *Recent Progress in Relaxor Ferroelectrics with Perovskite Structure*, J. Mater. Sci. **41**, 31 (2006).

[14] K. M. Rabe, M. Dawber, C. Lichtensteiger, C. H. Ahn, and J.-M. Triscone, *Modern Physics of Ferroelectrics:Essential Background*, in *Physics of Ferroelectrics: A*

*Modern Perspective* (Springer Berlin Heidelberg, Berlin, Heidelberg, 2007), pp. 1–30.

[15] F. Li, A. Bell, D. Damjanovic, W. Jo, Z.-G. Ye, and S. Zhang, *Recent Advances in Piezoelectric Materials for Electromechanical Transducer Applications*, IEEE Trans. Ultrason. Ferroelectr. Freq. Control **69**, 2999 (2022).

[16] F. D. Murnaghan, *The Compressibility of Media under Extreme Pressures*, Proc. Natl. Acad. Sci. **30**, 244 (1944).

[17] L. K. Pradhan and M. Kar, *Relaxor Ferroelectric Oxides: Concept to Applications*, in *Multifunctional Ferroelectric Materials*, edited by D. R. Sahu (IntechOpen, Rijeka, 2021).

[18] W. Kleemann, G. A. Samara, and J. Dec, *Relaxor Ferroelectrics – from Random Field Models to Glassy Relaxation and Domain States*, in *Polar Oxides* (John Wiley & Sons, Ltd, 2004), pp. 275–301.

[19] C.-H. Ma, Y.-K. Liao, Y. Zheng, S. Zhuang, S.-C. Lu, P.-W. Shao, J.-W. Chen, Y.-H. Lai, P. Yu, J.-M. Hu, R. Huang, and Y.-H. Chu, *Synthesis of a New Ferroelectric Relaxor Based on a Combination of Antiferroelectric and Paraelectric Systems*, ACS Appl. Mater. Interfaces **14**, 22278 (2022).

[20] Z. Yu, C. Ang, R. Guo, and A. S. Bhalla, *Ferroelectric-Relaxor Behavior of $Ba(Ti_{0.7}Zr_{0.3})O_3$ Ceramics*, J. Appl. Phys. **92**, 2655 (2002).

[21] R. Farhi, M. El Marssi, A. Simon, and J. Ravez, *Relaxor-like and Spectroscopic Properties of Niobium Modified Barium Titanate*, Eur. Phys. J. B **18**, 605 (2000).

[22] K. M. Rabe and U. V Waghmare, *Localized Basis for Effective Lattice Hamiltonians: Lattice Wannier Functions*, Phys. Rev. B **52**, 13236 (1995).

[23] W. Zhong, D. Vanderbilt, and K. M. Rabe, *First-Principles Theory of Ferroelectric Phase Transitions for Perovskites: The Case of $BaTiO_3$*, Phys. Rev. B **52**, 6301 (1995).

[24] R. D. King-Smith and D. Vanderbilt, *First-Principles Investigation of Ferroelectricity in Perovskite Compounds*, Phys. Rev. B **49**, 5828 (1994).

[25] U. V Waghmare and K. M. Rabe, *Ab Initio Statistical Mechanics of the Ferroelectric Phase Transition in $PbTiO_3$*, Phys. Rev. B **55**, 6161 (1997).

[26] T. Nishimatsu, U. V. Waghmare, Y. Kawazoe, and D. Vanderbilt, *Fast Molecular-*

Dynamics Simulation for Ferroelectric Thin-Film Capacitors Using a First-Principles Effective Hamiltonian, Phys. Rev. B **78**, 104104 (2008).

[27] T. Nishimatsu, M. Iwamoto, Y. Kawazoe, and U. V Waghmare, *First-Principles Accurate Total Energy Surfaces for Polar Structural Distortions of BaTiO₃, PbTiO₃, and SrTiO₃: Consequences for Structural Transition Temperatures*, Phys. Rev. B **82**, 134106 (2010).

[28] A. Paul, J. Sun, J. P. Perdew, and U. V Waghmare, *Accuracy of First-Principles Interatomic Interactions and Predictions of Ferroelectric Phase Transitions in Perovskite Oxides: Energy Functional and Effective Hamiltonian*, Phys. Rev. B **95**, 054111 (2017).

[29] L. Bellaiche, A. García, and D. Vanderbilt, *Finite-Temperature Properties of Pb(Zr₁₋ₓTiₓ)O₃ Alloys from First Principles*, Phys. Rev. Lett. **84**, 5427 (2000).

[30] L. Bellaiche, A. García, and D. Vanderbilt, *Low-Temperature Properties of Pb(Zr₁₋ₓTiₓ)O₃ Solid Solutions near the Morphotropic Phase Boundary*, Ferroelectrics **266**, 41 (2002).

[31] A. R. Akbarzadeh, S. Prosandeev, E. J. Walter, A. Al-Barakaty, and L. Bellaiche, *Finite-Temperature Properties of Ba(Zr,Ti)O₃ Relaxors from First Principles*, Phys. Rev. Lett. **108**, 257601 (2012).

[32] C. Mentzer, S. Lisenkov, Z. G. Fthenakis, and I. Ponomareva, *Phase Evolution in the Ferroelectric Relaxor Ba(Ti₁₋ₓZrₓ)O₃ from Atomistic Simulations*, Phys. Rev. B **99**, 064111 (2019).

[33] T. Nishimatsu, A. Grünebohm, U. V. Waghmare, and M. Kubo, *Molecular Dynamics Simulations of Chemically Disordered Ferroelectric (Ba,Sr)TiO₃ with a Semi-Empirical Effective Hamiltonian*, J. Phys. Soc. Japan **85**, 114714 (2016).

[34] R. E. Cohen and H. Krakauer, *Lattice Dynamics and Origin of Ferroelectricity in BaTiO₃: Linearized-Augmented-Plane-Wave Total-Energy Calculations*, Phys. Rev. B **42**, 6416 (1990).

[35] M. C. Oliveira, R. A. P. Ribeiro, E. Longo, M. R. D. Bomio, F. V Motta, and S. R. de Lazaro, *Temperature Dependence on Phase Evolution in the BaTiO₃ Polytypes Studied Using Ab Initio Calculations*, Int. J. Quantum Chem. **120**, e26054 (2020).

213

[36] G. H. Kwei, A. C. Lawson, S. J. L. Billinge, and S. W. Cheong, *Structures of the Ferroelectric Phases of Barium Titanate*, J. Phys. Chem. **97**, 2368 (1993).

[37] P. R. Potnis, N.-T. Tsou, and J. E. Huber, *A Review of Domain Modelling and Domain Imaging Techniques in Ferroelectric Crystals*, Materials (Basel). **4**, 417 (2011).

[38] C. Ma, J. Yan, Y. Wei, P. Liu, and G. Yang, *Enhanced Second Harmonic Generation in Individual Barium Titanate Nanoparticles Driven by Mie Resonances*, J. Mater. Chem. C **5**, 4810 (2017).

[39] H. Kim, S. Priya, H. Stephanou, and K. Uchino, *Consideration of Impedance Matching Techniques for Efficient Piezoelectric Energy Harvesting*, IEEE Trans. Ultrason. Ferroelectr. Freq. Control **54**, 1851 (2007).

[40] V. K. Veerapandiyan, S. Khosravi H, G. Canu, A. Feteira, V. Buscaglia, K. Reichmann, and M. Deluca, *B-Site Vacancy Induced Raman Scattering in $BaTiO_3$-Based Ferroelectric Ceramics*, J. Eur. Ceram. Soc. **40**, 4684 (2020).

[41] D. Hennings, A. Schnell, and G. Simon, *Diffuse Ferroelectric Phase Transitions in $Ba(Ti_{1-y}Zr_y)O_3$ Ceramics*, J. Am. Ceram. Soc. **65**, 539 (1982).

[42] V. V Kirillov and V. A. Isupov, *Relaxation Polarization of $PbMg_{1/3}Nb_{2/3}O_3$ (PMN)-A Ferroelectric with a Diffused Phase Transition*, Ferroelectrics **5**, 3 (1973).

[43] I. Santos and J. Eiras, *Phenomenological Description of the Diffuse Phase Transition in Ferroelectrics*, J. Phys. Condens. Matter **13**, 11733 (2001).

[44] Y. Imry and S. K. Ma, *Random-Field Instability of the Ordered State of Continuous Symmetry*, Phys. Rev. Lett. **35**, 1399 (1975).

[45] J. Petzelt, D. Nuzhnyy, V. Bovtun, M. Kempa, M. Savinov, S. Kamba, and J. Hlinka, *Lattice Dynamics and Dielectric Spectroscopy of BZT and NBT Lead-Free Perovskite Relaxors – Comparison with Lead-Based Relaxors*, Phase Transitions **88**, 320 (2015).

[46] A. Pramanick, W. Dmowski, T. Egami, A. S. Budisuharto, F. Weyland, N. Novak, A. D. Christianson, J. M. Borreguero, D. L. Abernathy, and M. R. V Jorgensen, *Stabilization of Polar Nanoregions in Pb-Free Ferroelectrics*, Phys. Rev. Lett. **120**, 207603 (2018).

[47] W. Kleemann, J. Dec, and S. Miga, *The Cluster Glass Route of Relaxor Ferroelectrics*, Phase Transitions **88**, 234 (2015).

[48] C. Laulhé, A. Pasturel, F. Hippert, and J. Kreisel, *Random Local Strain Effects in Homovalent-Substituted Relaxor Ferroelectrics: A First-Principles Study of BaTi$_{0.74}$Zr$_{0.26}$O$_3$*, Phys. Rev. B **82**, 132102 (2010).

[49] T. Maiti, R. Guo, and A. S. Bhalla, *Structure-Property Phase Diagram of BaZr$_x$Ti$_{1-x}$O$_3$ System*, J. Am. Ceram. Soc. **91**, 1769 (2008).

[50] A. A. Bokov, M. Maglione, and Z.-G. Ye, *Quasi-Ferroelectric State in Ba(Ti$_{1-x}$Zr$_x$)O$_3$ relaxor*, J. Phys. Condens. Matter **19**, 092001 (2007).

[51] C. Laulhé, F. Hippert, J. Kreisel, M. Maglione, A. Simon, J. L. Hazemann, and V. Nassif, *EXAFS Study of Lead-Free Relaxor Ferroelectric BaTi$_{1-x}$Zr$_x$O$_3$ at the Zr K Edge*, Phys. Rev. B **74**, 014106 (2006).

[52] Q. Xu and Z. Li, *Dielectric and Ferroelectric Behaviour of Zr-Doped BaTiO$_3$ Perovskites*, Process. Appl. Ceram. **14**, 188 (2020).

[53] A. Bootchanont, J. Jutimoosik, S. Chandarak, M. Unruan, S. Rujirawat, R. Yimnirun, R. Guo, and A. Bhalla, *Investigation of Local Structure in BaTiO$_3$–BaZrO$_3$ System by Synchrotron X-Ray Absorption Spectroscopy*, Ceram. Int. **39**, 579 (2013).

[54] L. Dong, D. S. Stone, and R. S. Lakes, *Enhanced Dielectric and Piezoelectric Properties of xBaZrO$_3$-(1−x)BaTiO$_3$ Ceramics*, J. Appl. Phys. **111**, 084107 (2012).

[55] I. Levin, E. Cockayne, V. Krayzman, J. C. Woicik, S. Lee, and C. A. Randall, *Local Structure of Ba(Ti,Zr)O$_3$ Perovskite-like Solid Solutions and Its Relation to the Band-Gap Behavior*, Phys. Rev. B **83**, 094122 (2011).

[56] J. Rödel, W. Jo, K. T. P. Seifert, E.-M. Anton, T. Granzow, and D. Damjanovic, *Perspective on the Development of Lead-Free Piezoceramics*, J. Am. Ceram. Soc. **92**, 1153 (2009).

[57] J. Petzelt, V. Bovtun, D. Nuzhnyy, M. Kempa, M. Savinov, M. Paściak, S. Kamba, G. Canu, and V. Buscaglia, *Broadband Dielectric, Terahertz, and Infrared Spectroscopy of BaTiO$_3$–BaZrO$_3$ Solid Solution: From Proper Ferroelectric over Diffuse and Relaxor Ferroelectrics and Dipolar Glass to Normal Dielectric*, Phys. Status Solidi B **258**, 2100259 (2021).

[58] J. E. Jones and S. Chapman, *On the Determination of Molecular Fields. —II. From the Equation of State of a Gas*, Proc. R. Soc. London. Ser. A, Contain. Pap. a Math. Phys.

Character **106**, 463 (1924).

[59]   J. E. Jones and S. Chapman, *On the Determination of Molecular Fields.—I. From the Variation of the Viscosity of a Gas with Temperature*, Proc. R. Soc. London. Ser. A, Contain. Pap. a Math. Phys. Character **106**, 441 (1924).

[60]   P. M. Morse, *Diatomic Molecules According to the Wave Mechanics. II. Vibrational Levels*, Phys. Rev. **34**, 57 (1929).

[61]   M. Paściak, T. R. Welberry, A. P. Heerdegen, V. Laguta, T. Ostapchuk, S. Leoni, and J. Hlinka, *Atomistic Modeling of Diffuse Scattering in Cubic PbZrO$_3$*, Phase Transitions **88**, 273 (2015).

[62]   M. Pasciak, T. R. Welberry, J. Kulda, S. Leoni, and J. Hlinka, *Dynamic Displacement Disorder of Cubic BaTiO$_3$*, Phys. Rev. Lett. **120**, 167601 (2018).

[63]   H. Azuma, S. Ogata, R. Kobayashi, M. Uranagase, T. Tsuzuki, D. Durdiev, and F. Wendler, *Microscopic Structure and Migration of 90° Ferroelectric Domain Wall in BaTiO$_3$ Determined via Molecular Dynamics Simulations*, J. Appl. Phys. **133**, 104101 (2023).

[64]   T. Hashimoto and H. Moriwake, *Structure of Amorphous BaTiO$_3$ by Molecular Dynamics Simulations Using a Shell Model*, Phys. B Condens. Matter **579**, 411799 (2020).

[65]   J. M. Vielma and G. Schneider, *Shell Model of BaTiO$_3$ Derived from Ab-Initio Total Energy Calculations*, J. Appl. Phys. **114**, 174108 (2013).

[66]   L. Bellaiche and D. Vanderbilt, *Virtual Crystal Approximation Revisited: Application to Dielectric and Piezoelectric Properties of Perovskites*, Phys. Rev. B **61**, 7877 (2000).

[67]   L. Walizer, S. Lisenkov, and L. Bellaiche, *Finite-Temperature Properties of (Ba,Sr)TiO$_3$ Systems from Atomistic Simulations*, Phys. Rev. B **73**, 144105 (2006).

[68]   R. Hemphill, L. Bellaiche, A. García, and D. Vanderbilt, *Finite-Temperature Properties of Disordered and Ordered Pb(Sc$_{0.5}$Nb$_{0.5}$)O$_3$ Alloys*, Appl. Phys. Lett. **77**, 3642 (2000).

[69]   S. Prosandeev, S. Prokhorenko, Y. Nahas, J. Grollier, D. Talbayev, B. Dkhil, and L. Bellaiche, *Ultrafast Activation and Tuning of Topological Textures in Ferroelectric*

*Nanostructures*, Adv. Electron. Mater. **8**, 2200808 (2022).

[70]   S. Prosandeev and L. Bellaiche, *THz-Induced Activation of Hidden States in Rare-Earth-Doped BiFeO₃ Solid Solutions*, Phys. Rev. Mater. **6**, 116201 (2022).

[71]   S. Prosandeev, S. Prokhorenko, Y. Nahas, Y. Yang, C. Xu, J. Grollier, D. Talbayev, B. Dkhil, and L. Bellaiche, *Hidden Phases with Neuromorphic Responses and Highly Enhanced Piezoelectricity in an Antiferroelectric Prototype*, Phys. Rev. B **105**, L100101 (2022).

[72]   S. Prosandeev, J. Grollier, D. Talbayev, B. Dkhil, and L. Bellaiche, *Ultrafast Neuromorphic Dynamics Using Hidden Phases in the Prototype of Relaxor Ferroelectrics*, Phys. Rev. Lett. **126**, 027602 (2021).

[73]   P. Hohenberg and W. Kohn, *Inhomogeneous Electron Gas*, Phys. Rev. **136**, B864 (1964).

[74]   W. Kohn, *Nobel Lecture: Electronic Structure of Matter---Wave Functions and Density Functionals*, Rev. Mod. Phys. **71**, 1253 (1999).

[75]   D. S. Sholl and J. A. Steckel, *Density Functional Theory: A Practical Introduction* (Wiley, 2011).

[76]   W. Kohn and L. J. Sham, *Self-Consistent Equations Including Exchange and Correlation Effects*, Phys. Rev. **140**, A1133 (1965).

[77]   A. D. Becke, *Perspective: Fifty Years of Density-Functional Theory in Chemical Physics*, J. Chem. Phys. **140**, 18A301 (2014).

[78]   J. P. Perdew, J. A. Chevary, S. H. Vosko, K. A. Jackson, M. R. Pederson, D. J. Singh, and C. Fiolhais, *Atoms, Molecules, Solids, and Surfaces: Applications of the Generalized Gradient Approximation for Exchange and Correlation*, Phys. Rev. B **46**, 6671 (1992).

[79]   A. D. Becke, *Density-Functional Exchange-Energy Approximation with Correct Asymptotic Behavior*, Phys. Rev. A **38**, 3098 (1988).

[80]   D. C. Langreth and M. J. Mehl, *Beyond the Local-Density Approximation in Calculations of Ground-State Electronic Properties*, Phys. Rev. B **28**, 1809 (1983).

[81]   J. P. Perdew, K. Burke, and M. Ernzerhof, *Generalized Gradient Approximation Made*

*Simple*, Phys. Rev. Lett. **77**, 3865 (1996).

[82]  G. I. Csonka, J. P. Perdew, A. Ruzsinszky, P. H. T. Philipsen, S. Lebègue, J. Paier, O. A. Vydrov, and J. G. Ángyán, *Assessing the Performance of Recent Density Functionals for Bulk Solids*, Phys. Rev. B **79**, 155107 (2009).

[83]  N. W. Ashcroft and N. D. Mermin, *Solid State Physics* (Cengage Learning, 2011).

[84]  L. Verlet, *Computer "Experiments" on Classical Fluids. I. Thermodynamical Properties of Lennard-Jones Molecules*, Phys. Rev. **159**, 98 (1967).

[85]  M. Griebel, S. Knapek, G. Zumbusch, and A. Caglar, *Numerische Simulation in Der Moleküldynamik* (Springer Berlin Heidelberg, 2004).

[86]  S. D. Bond, B. J. Leimkuhler, and B. B. Laird, *The Nosé-Poincaré Method for Constant Temperature Molecular Dynamics*, J. Comput. Phys. **151**, 114 (1999).

[87]  D. S. Kleinerman, C. Czaplewski, A. Liwo, and H. A. Scheraga, *Implementations of Nosé-Hoover and Nosé-Poincaré Thermostats in Mesoscopic Dynamic Simulations with the United-Residue Model of a Polypeptide Chain.*, J. Chem. Phys. **128**, 245103 (2008).

[88]  S. Nosé, *A Unified Formulation of the Constant Temperature Molecular Dynamics Methods*, J. Chem. Phys. **81**, 511 (1984).

[89]  S. Nosé, *A Molecular Dynamics Method for Simulations in the Canonical Ensemble*, Mol. Phys. **52**, 255 (1984).

[90]  W. G. Hoover, *Canonical Dynamics: Equilibrium Phase-Space Distributions*, Phys. Rev. A **31**, 1695 (1985).

[91]  E. Hairer, *Variable Time Step Integration with Symplectic Methods*, Appl. Numer. Math. **25**, 219 (1997).

[92]  K. Zare and V. Szebehely, *Time Transformations in the Extended Phase-Space*, Celest. Mech. **11**, 469 (1975).

[93]  J. Paul, T. Nishimatsu, Y. Kawazoe, and U. V Waghmare, *Ferroelectric Phase Transitions in Ultrathin Films of BaTiO₃*, Phys. Rev. Lett. **99**, 077601 (2007).

[94]  D. M. Hatch and H. T. Stokes, *INVARIANTS: Program for Obtaining a List of Invariant Polynomials of the Order-Parameter Components Associated with*

*Irreducible Representations of a Space Group*, J. Appl. Crystallogr. **36**, 951 (2003).

[95]   J. Kolafa and J. W. Perram, *Cutoff Errors in the Ewald Summation Formulae for Point Charge Systems*, Mol. Simul. **9**, 351 (1992).

[96]   P. P. Ewald, *Die Berechnung Optischer Und Elektrostatischer Gitterpotentiale*, Ann. Phys. **369**, 253 (1921).

[97]   G. Kresse and J. Hafner, *Ab Initio Molecular-Dynamics Simulation of the Liquid-Metal–Amorphous-Semiconductor Transition in Germanium*, Phys. Rev. B **49**, 14251 (1994).

[98]   G. Kresse and J. Furthmüller, *Efficient Iterative Schemes for* Ab Initio *Total-Energy Calculations Using a Plane-Wave Basis Set*, Phys. Rev. B **54**, 11169 (1996).

[99]   G. Kresse and J. Furthmüller, *Efficiency of Ab-Initio Total Energy Calculations for Metals and Semiconductors Using a Plane-Wave Basis Set*, Comput. Mater. Sci. **6**, 15 (1996).

[100]  G. Kresse and D. Joubert, *From Ultrasoft Pseudopotentials to the Projector Augmented-Wave Method*, Phys. Rev. B **59**, 1758 (1999).

[101]  P. E. Blöchl, *Projector Augmented-Wave Method*, Phys. Rev. B **50**, 17953 (1994).

[102]  T. Hashimoto, T. Nishimatsu, H. Mizuseki, Y. Kawazoe, A. Sasaki, and Y. Ikeda, *Ab Initio Determination of Total-Energy Surfaces for Distortions of Ferroelectric Perovskite Oxides*, Jpn. J. Appl. Phys. **43**, 6785 (2004).

[103]  F. Birch, *Finite Elastic Strain of Cubic Crystals*, Phys. Rev. **71**, 809 (1947).

[104]  A. Togo and I. Tanaka, *First Principles Phonon Calculations in Materials Science*, Scr. Mater. **108**, 1 (2015).

[105]  T. Atsushi, *First-Principles Phonon Calculations with Phonopy and Phono3py*, J. Phys. Soc. Japan **92**, 012001 (2023).

[106]  S. Mühlbauer, B. Binz, F. Jonietz, C. Pfleiderer, A. Rosch, A. Neubauer, R. Georgii, and P. Böni, *Skyrmion Lattice in a Chiral Magnet*, Science **323**, 915 (2009).

[107]  U. K. Rößler, A. N. Bogdanov, and C. Pfleiderer, *Spontaneous Skyrmion Ground States in Magnetic Metals*, Nature **442**, 797 (2006).

[108]  C. Heo, N. S. Kiselev, A. K. Nandy, S. Blügel, and T. Rasing, *Switching of Chiral*

*Magnetic Skyrmions by Picosecond Magnetic Field Pulses via Transient Topological States*, Sci. Rep. **6**, 27146 (2016).

[109] N. Nagaosa and Y. Tokura, *Topological Properties and Dynamics of Magnetic Skyrmions*, Nat. Nanotechnol. **8**, 899 (2013).

[110] P. Shafer, P. García-Fernández, P. Aguado-Puente, A. R. Damodaran, A. K. Yadav, C. T. Nelson, S.-L. Hsu, J. C. Wojdeł, J. Íñiguez, L. W. Martin, E. Arenholz, J. Junquera, and R. Ramesh, *Emergent Chirality in the Electric Polarization Texture of Titanate Superlattices*, Proc. Natl. Acad. Sci. **115**, 915 (2018).

[111] R. Zhu, Z. Jiang, X. Zhang, X. Zhong, C. Tan, M. Liu, Y. Sun, X. Li, R. Qi, K. Qu, Z. Liu, M. Wu, M. Li, B. Huang, Z. Xu, J. Wang, K. Liu, P. Gao, J. Wang, J. Li, and X. Bai, *Dynamics of Polar Skyrmion Bubbles under Electric Fields*, Phys. Rev. Lett. **129**, 107601 (2022).

[112] S. Das, Z. Hong, V. A. Stoica, M. A. P. Gonçalves, Y. T. Shao, E. Parsonnet, E. J. Marksz, S. Saremi, M. R. McCarter, A. Reynoso, C. J. Long, A. M. Hagerstrom, D. Meyers, V. Ravi, B. Prasad, H. Zhou, Z. Zhang, H. Wen, F. Gómez-Ortiz, P. García-Fernández, J. Bokor, J. Íñiguez, J. W. Freeland, N. D. Orloff, J. Junquera, L. Q. Chen, S. Salahuddin, D. A. Muller, L. W. Martin, and R. Ramesh, *Local Negative Permittivity and Topological Phase Transition in Polar Skyrmions*, Nat. Mater. **20**, 194 (2021).

[113] Y. Nahas, S. Prokhorenko, L. Louis, Z. Gui, I. Kornev, and L. Bellaiche, *Discovery of Stable Skyrmionic State in Ferroelectric Nanocomposites*, Nat. Commun. **6**, 8542 (2015).

[114] M. A. P. Gonçalves, C. Escorihuela-Sayalero, P. Garca-Fernández, J. Junquera, and J. Íñiguez, *Theoretical Guidelines to Create and Tune Electric Skyrmion Bubbles*, Sci. Adv. **5**, eaau7023 (2019).

[115] S. Das, Y. L. Tang, Z. Hong, M. A. P. Gonçalves, M. R. McCarter, C. Klewe, K. X. Nguyen, F. Gómez-Ortiz, P. Shafer, E. Arenholz, V. A. Stoica, S.-L. Hsu, B. Wang, C. Ophus, J. F. Liu, C. T. Nelson, S. Saremi, B. Prasad, A. B. Mei, D. G. Schlom, J. Íñiguez, P. García-Fernández, D. A. Muller, L. Q. Chen, J. Junquera, L. W. Martin, and R. Ramesh, *Observation of Room-Temperature Polar Skyrmions*, Nature **568**, 368 (2019).

[116] M. A. P. Gonçalves, M. Paściak, and J. Hlinka, *Antiskyrmionic Ferroelectric Medium*, ArXiv:2303.07389 [Cond-Mat.Mtrl-Sci] (2023).

[117] B. Berg and M. Lüscher, *Definition and Statistical Distributions of a Topological Number in the Lattice O(3) σ-Model*, Nucl. Phys. B **190**, 412 (1981).

# List of Equations

# List of Figures

# List of Tables